



HAL
open science

Towards a squeezing-enhanced atomic clock on a chip

Konstantin Ott

► **To cite this version:**

Konstantin Ott. Towards a squeezing-enhanced atomic clock on a chip. Physics [physics]. Université Pierre et Marie Curie - Paris VI, 2016. English. NNT : 2016PA066287 . tel-01452767

HAL Id: tel-01452767

<https://theses.hal.science/tel-01452767>

Submitted on 2 Feb 2017

HAL is a multi-disciplinary open access archive for the deposit and dissemination of scientific research documents, whether they are published or not. The documents may come from teaching and research institutions in France or abroad, or from public or private research centers.

L'archive ouverte pluridisciplinaire **HAL**, est destinée au dépôt et à la diffusion de documents scientifiques de niveau recherche, publiés ou non, émanant des établissements d'enseignement et de recherche français ou étrangers, des laboratoires publics ou privés.

**THÈSE DE DOCTORAT
DE L'UNIVERSITÉ PIERRE ET MARIE CURIE**

Spécialité : Physique

École doctorale : "Physique en Île-de-France"

réalisée au

Laboratoire Kastler Brossel et SYRTE

présentée par

Konstantin Thomas OTT

pour obtenir le grade de :

DOCTEUR DE L'UNIVERSITÉ PIERRE ET MARIE CURIE

Sujet de la thèse :

Towards a squeezing-enhanced atomic clock on a chip

soutenue le 30 septembre 2016

devant le jury composé de :

M.	Philippe BOUYER	Rapporteur
M.	Matthias KELLER	Rapporteur
M ^{me} .	Agnès MAÎTRE	Examineur
M.	François-Xavier ESNAULT	Examineur
M.	Tilo STEINMETZ	Examineur
M.	Jean-Marc LESAGE	Membre invité
M.	Jakob REICHEL	Directeur de thèse

Abstract

This thesis describes the conception and construction of an “entanglement-enhanced” trapped atom clock on an atom chip (TACC). The key feature of this new experiment is the integration of two optical Fabry-Pérot micro resonators which enable generation of spin-squeezed states of the atomic ensemble via atom-light interactions and non-destructive detection of the atomic state.

It has been shown before that spin-squeezed states can enhance the metrological performance of atomic clocks, but existing proof-of-principle experiments have not yet reached a metrologically relevant level of precision. This is the first goal of the new setup.

To retain the compactness and stability of our setup, we chose the optical resonator to be a fiber Fabry-Pérot (FFP) resonator where the resonator mirrors are realized on the tip of optical fibers. To meet the requirements of our experiment, a new generation of FFP resonators was developed in the context of this thesis, demonstrating the longest FFP resonators to date. For this purpose, we developed a “dot milling” procedure using a focused CO₂-laser that allows shaping of fused silica surfaces with unprecedented precision and versatility. Beyond the TACC experiment these long FFP resonators open up new applications in other fields as in the ion trapping community or for frequency filtering.

Incorporating optical resonators in the TACC system necessitates a new atom chip design, allowing transportation of the atom cloud into the resonator. We present the design and the fabrication of this atom chip.

The completed setup will enable investigations of the interplay of spin-dynamics in presence of light mediated correlations and spin-squeezing at a metrologically relevant stability level of 10^{-13} at 1 s.

Résumé

L'objet de cette thèse de doctorat est la conception et la construction d'une horloge atomique réalisée sur un microcircuit à atomes (TACC) et améliorée par l'intrication.

L'élément principal de cette nouvelle expérience est un micro-résonateur Fabry-Pérot qui permet la génération d'états de spin comprimés de l'ensemble atomique grâce aux interactions entre la lumière et les atomes. Il a déjà été montré que ces états peuvent améliorer les performances métrologiques des horloges atomiques. Cependant, les expériences ayant permis cette démonstration de principe n'ont pas encore atteint un niveau de précision présentant un intérêt métrologique. C'est précisément l'objectif de la nouvelle configuration expérimentale que nous proposons ici.

L'intégration du résonateur optique au dispositif expérimental TACC nécessite une conception nouvelle du microcircuit à atomes, qui doit permettre le transport du nuage atomique jusqu'au résonateur. Nous présenterons donc la conception et la fabrication de ce microcircuit à atomes.

Afin de conserver la compacité et la stabilité de notre installation, nous avons choisi d'utiliser une cavité Fabry-Pérot fibrée (fibered Fabry-Pérot, FFP) comme résonateur optique, dans lequel les miroirs du résonateur sont réalisés sur la pointe de fibres optiques. Pour répondre aux exigences de notre expérience, une nouvelle génération de résonateurs FFP a été développée au cours de cette thèse, les plus longs réalisés à ce jour.

A cette fin, nous avons développé une procédure d'ablation par tirs multiples à l'aide d'un laser CO₂ focalisé, qui permet la mise en forme des surfaces de silice fondue avec une précision et une polyvalence sans précédent

Contents

Introduction	ix
1 Trapped Atom Clock on a Chip	1
1.1 Atomic clocks	1
1.1.1 Rabi and Ramsey spectroscopy	2
1.1.2 Clock stability	4
1.2 Trapped atom clock on a chip (TACC)	5
1.2.1 Magic traps	5
1.2.2 Density shifts in trapped atom clouds	5
1.2.3 ^{87}Rb for TACC	6
1.2.4 TACC clock transition	6
1.3 Magnetic trapping and manipulation of neutral atoms	7
1.3.1 Basic principle	7
1.3.2 Majorana losses	8
1.4 Atom chip technology	9
1.4.1 Basic principle	9
1.4.2 Trap types	10
1.4.3 Trap depth	13
1.4.4 Gravitational sag and rotation	14
2 Spin-Squeezing for Metrology	17
2.1 Spin-squeezing	17
2.2 Atom-light interaction	20
2.3 Spin-squeezing for TACC 2	23
2.3.1 Cavity feedback squeezing	24
2.3.2 Squeezing by QND measurement	25
2.4 Requirements for the new experiment	27
2.5 Conclusion	31
3 CO₂ Machining with Multiple Pulses	33
3.1 CO ₂ machining of fused silica	34
3.2 Limiting factors in single-pulse machining	34
3.3 Dot milling setup	36
3.3.1 In situ profilometry	37
3.3.2 Multi-fiber holder for mass production	40

3.4	Dot milling with CO ₂ laser pulses on fiber end facets	44
3.4.1	Fiber preparation	44
3.4.2	Multiple shots	46
3.4.3	Machining large spherical structures by CO ₂ dot milling	51
3.5	Conclusion	54
4	Long Fiber Fabry-Pérot Resonators	55
4.1	Optical Resonators	55
4.1.1	Resonance, transmission and finesse	55
4.1.2	Mode geometry	57
4.1.3	Fiber Fabry-Pérot resonators	58
4.1.4	Resonator losses	59
4.1.5	Coupling to the resonator	61
4.1.6	Photonic-crystal fibers for FFP cavities	62
4.1.7	Conclusion	63
4.2	Experimental realization and results	63
4.2.1	Finesse and transmission measurements	64
4.2.2	Analytical model: clipping loss	65
4.2.3	Full simulation of the cavity mode using reconstructed mirror profiles	67
4.2.4	Cavity transmission	69
4.2.5	Higher order modes	70
4.2.6	Double λ -Resonators	78
4.2.7	A compact FFP resonator mount	82
4.2.8	Resonators for TACC2	89
4.3	Conclusion	91
5	Atom Chip for TACC 2	93
5.1	Requirements catalogue	93
5.2	Layout of the atom chip	94
5.2.1	Atom transport	96
5.2.2	Three-wire trap	103
5.2.3	Effect of the bias field inhomogeneity on the trap position	105
5.2.4	Stand-alone chip trap	107
5.2.5	MW coplanar wave guide	110
5.3	Fabrication	114
5.3.1	Base chip	116
5.3.2	Science chip	117
5.3.3	“Marriage” of chip and resonator	120
	Conclusion and Outlook	121
A	Appendix	127
A.1	Calculation of the cavity shift	127
A.2	Microclamps fabrication recipe	128
A.3	Additional material	131
A.3.1	CO ₂ machining with multiple pulses	131

A.3.2	Long fiber Fabry-Pérot resonators	131
A.3.3	Atom chip for TACC 2	134
A.4	Chip fabrication recipe	134
A.5	French summary	139
A.5.1	Chapter 1: Trapped Atom Clock on a Chip	139
A.5.2	Chapter 2: Spin Squeezing for Metrology	140
A.5.3	Chapter 3: CO ₂ machining with multiple pulses	140
A.5.4	Chapter 4: Long Fiber Fabry-Pérot Resonators	141
A.5.5	Chapter 5: Atom Chip for TACC 2	142
List of Figures		145
Bibliography		149

Introduction

We are currently in the midst of a second quantum revolution. The first quantum revolution gave us new rules that govern physical reality. The second quantum revolution will take these rules and use them to develop new technologies.

- J. P. Dowling and G. J. Milburn in [1]

Only three months ago, the European Commission launched a one-billion euro “flagship” program on quantum technologies, motivated by the expected “second quantum revolution” [2].

One century after the foundation of quantum mechanics by Planck, Bohr, Einstein, Schrödinger, Heisenberg and others, developments in science and technology allow us to harness quantum mechanics for unprecedented applications. Two fundamental principles of quantum mechanics are responsible for the potential of new quantum technologies: *quantum superposition* and *entanglement*, both of which are non-existent in classical physics.

The linearity of the Schrödinger equation, the central equation of quantum mechanics which describes the dynamics of a quantum state [3], allows *superpositions of quantum states*. This has the unintuitive consequence that a physical system can be in several states at the same time, which Schrödinger himself underlined with his famous gedankenexperiment of Schrödinger’s cat [4]. The fact that these states are not observed in the macroscopic world is due to decoherence, a process in which observation by the environment projects the quantum states and destroys the superposition [5]. The quantum superposition principle holds nonetheless for isolated, microscopic systems, and experiments push the frontier more and more to the macroscopic realm [6, 7].

In 1935, Schrödinger named two subsystems *entangled*, if their global state cannot be described by a product state of the subsystems [8]. This leads to non-classical correlations of potentially separated objects. It was in the same year that Einstein, Podolsky and Rosen attempted to describe this entanglement as a consequence of hidden variables, defining a physical quantity before its measurement, and thus showing the incompleteness of quantum theory [9]. Starting from these assumptions, John Bell formulated in 1964 a set of inequalities, whose violation would prove the contrary: the physical reality cannot be determined by hidden variables [10]. Aspect et al. realized in 1984 an experiment that violated the Bell inequality [11] (with a recent loophole-free confirmation [12]), proving the absence of hidden variables and establishing the “spooky action at a distance” [13], provided by entanglement, as the physical reality.

The impossibility to experience these phenomena in the macroscopic world of everyday life render them the most unintuitive properties of quantum mechanics. It is these revolutionary concepts, that lead to unprecedented technology, not only advancing existing methods, but founding truly new approaches.

Among the possible future quantum technologies, the most well-established ones are the following, but may only represent the tip of the iceberg:

- *Quantum communication*: More than 30 years after the presentation of the first provable secure cryptography protocol [14, 15], quantum cryptography found its way to commercially available encryption equipment [16, 17]. Here, the encryption key is encoded in a quantum state of photons for which the no-cloning theorem [18] makes it impossible to eavesdrop the key without detection of the eavesdropper.
- *Quantum computers*: Quantum computers use superposition and entanglement as a resource to surpass the possible performance of classical computers [14], which allow general simulations of quantum mechanical systems [19]. Furthermore, distinct quantum algorithms for classical problems exist, leading to quadratic [20] or even exponential [21] speed-up. Especially the Shor-algorithm is of great interest, since it renders current encryption methods vulnerable, spurring the development of the ultimate safe quantum cryptography.
- *Quantum simulators*: The main idea of quantum simulators is to use well controllable quantum systems to simulate the properties of inaccessible quantum systems [22]. The exponential scaling of the systems' complexity makes it impossible to simulate even systems of moderate size with classical computers [23]. A simulator does not claim the generality of a quantum computer, but could be designed for distinct purposes ranging from condensed matter [24] over chemistry [25] to cosmology [26]. The specialization to a well-defined set of problems lowers the tremendous amount of technological challenges set by the realization of an universal quantum computer.
- *Quantum sensors*: Depending on the definition, quantum sensors can be seen as the most mature quantum technology. Devices such as atomic clocks use the interference of superposition states to enable the most precise measurements and define the second since nearly 50 years [27]. Until today, sensors based on highly sensitive superposition states are under constant development and lead to numerous applications ranging from magnetic field measurements with solid-state quantum sensors [28] to commercialized gravimeters [29].

A more restricted definition defines quantum sensors as devices that overcome the standard quantum limit [30]. We will pursue this exciting trail in the following, as it brings us closer to the content of this work.

The standard quantum limit (SQL) is imposed by the statistical nature of quantum physics, where the measurement of a superposition state projects it into one of its eigenstates. This discrete outcome of measuring a continuous variable leads to an uncertainty that can only be reduced by repeating the same experiment again and again or by realizing it in parallel with N identical test objects. This is in direct

analogy to a coin-tossing game, where the knowledge of the coin's balance can be increased only by flipping it multiple times.

The continuous variable that is measured with atomic clocks is the frequency difference between the atomic reference and a local oscillator. Due to the projection of N uncorrelated atoms, the uncertainty of the measurement scales as $1/\sqrt{N}$, setting the SQL.

The mastery of theory and experiment enabled Santarelli et al. to push the performance of their atomic clock to this SQL [31], where the clock stability was not limited by technical noise, but by the statistics describing the uncorrelated atoms used. Since then, further clocks have reached this level [32].

Fortunately, quantum mechanics also provides the resource to overcome this statistical limitation: entanglement. The entanglement of particles, such as atoms in an atomic clock or photons in an interferometer, leads to correlations that can reduce the statistical uncertainty of the state measurement [30, 33] and is in principle only limited by the fundamental Heisenberg limit, where the uncertainty scales as $1/N$ [34]. Besides its conceptual interest, the direct impact of entanglement on metrology has motivated many proof-of-principle experiments that successfully overcame the SQL.

To date, the most suitable states for quantum metrology are so-called *squeezed states*, that owe their name to the *squeezing* of the pictorial representation of their uncertainty region. The most prominent example is squeezed light, ready for the use in the next generation of gravitational wave detectors [35–37].

In analogy to squeezed photonic states, *spin-squeezed* states can be prepared in atomic ensembles. After pioneering experiments [38, 39], spin-squeezing had its “*annus mirabilis*” in 2008/2009, when spin-squeezing was demonstrated in several experiments based on different mechanisms [40–47]. Not all of the listed experiments showed metrologically relevant improvement or could be of use for atomic clocks, nonetheless the first proof-of-principle experiment of a squeezed atomic clock was presented the same year [48].

Since then, the field evolved, leading to further reductions of the measurement uncertainties [49], with the impressive record 100 times below the SQL, reported recently in [50]. In most of these experiments, spin-squeezing was realized by use of an optical resonator. Despite this advancement in the production and control of squeezed states, no atomic clock or other quantum sensor was presented to date that showed squeezing enhanced performance at a metrologically relevant level. This remaining challenge is one of the central motivations for the experiment presented here.

In parallel to the advancements of engineered quantum states for metrological application, the ultimate stability and accuracy of atomic clocks was constantly improved. In particular the higher absolute frequency of optical transitions, compared to the current standard microwave transitions, boosted the advancements [51]. This led to the development of optical lattice clocks with the world record in precision and accuracy at the 10^{-18} level [52], which could lead to a redefinition of the SI second in the future [53].

Aside from the approach to tackle the fundamental limitation of precision, the atomic clock community showed tremendous success in making their clocks more compact. This process is driven by the large number of applications for portable clock

systems. It ranges from fundamental research, starting from the first test of the famous “clock paradox” [54], to applications in communication and navigation, since every GPS satellite is equipped with a set of atomic clocks. Especially the operation in space shows many interesting applications [55], but puts the highest demands on small size and weight. A remarkable milestone is the launch of the first *cold* atom clock in space for the operation at the international space station, scheduled for 2017 [56].

Despite the efforts on miniaturization, optical clocks are not always the best candidates for compact design, particularly because they need a frequency comb to connect to a radiofrequency signal. Many applications gain from trading stability and accuracy for compactness, especially in sectors like geophysics, meteorology and navigation, where nonetheless the $\sim 10^{-12}\text{s}^{-1/2}$ stability of the best existing commercial frequency standards is insufficient [57].

Several compact microwave clock-projects were motivated by this need. The goal was to reach the 10^{-13} stability level in one second, which was accomplished successfully with several different technologies [58–62]. One of the projects is the trapped atom clock on a chip (TACC), proposed in [63] and started 2006 in our collaboration between the LKB and SYRTE. While TACC is not the most lightweight approach in terms of its laser system, the atom chip technology [64] makes it an attractive module for compact atomic sensors, including integrated atom interferometers. Furthermore, the high degree of control provided by the atom chip made it a productive testbed for the many-body physics occurring in trapped atom clocks. It has enabled the discovery of spin-self rephasing [65] and clarified the role of collisional frequency shifts in trapped atom clocks, including lattice clocks [66]. The clock performance was continuously improved [67, 68], bringing it closer and closer to the SQL, although some work remains to be done to overcome technical fluctuations of the atomic temperature. Presently, the stability is 5.8×10^{-13} at one second [62].

We plan to use this highly versatile cold atom setup in an environment meeting strict metrological standards, to investigate the effects of squeezing on a metrologically relevant level.

The aim of this work is hence to upgrade the TACC experiment and to enable the investigation of squeezing at the stability level of 10^{-13} and below. Therefore, the goal of this thesis is to extend the TACC experiment by an optical resonator, as in the hallmark squeezing experiments in [48, 50]. The role of the resonator is to increase the atom-light interaction, and thus the squeezing, without revealing the state of the individual atoms, since this would destroy the superposition state and lead to signal loss.

In addition to squeezing, a resonator allows for efficient quantum non-demolition (QND) detection of the atomic state, which can be used to reduce the dead time of the clock and therefore increase its stability [69]. Furthermore, the non-destructive detection is ideal to realize weak measurements that can be used in quantum feedback schemes, as proposed in [70] and demonstrated in [71]. This allows mobile clock operation with low grade local oscillators.

The fiber Fabry-Pérot (FFP) micro resonators developed in our group [72, 73] are optimal candidates for the realization of the optical resonator. Their compact design allows the implementation in the existing TACC system, without enlarging the physics

package, and is furthermore well suited for the combination with atom chips. Future application in mobile devices will benefit from the stability provided by the direct fiber coupling and compact resonator setup. The advantage of this technological innovation led to many successful experiments in the cold atom community [74, 75] and beyond [76–78]. In [79], QND measurement of even a single atom could be realized.

Since the resonators employed in the listed experiments were a factor 4-10 times shorter than the length of the typical atom clouds used in TACC, a new generation of FFP resonators was developed in the context of this work, which led to unprecedented resonator lengths in the millimeter regime and an octave spanning frequency range [80]. These technological advancements could also be of great use in other fields, such as quantum communication [81, 82].

The development of the new FFP resonator generation is finished successfully and fulfills the requirements of TACC. A new atom chip was designed and fabricated for the operation of TACC2 and assembled with the resonator. Thus, the new physics package is ready, which allows clock experiments in the near future.

Organization of the manuscript:

- We begin the manuscript with a short introduction to metrology with atomic clocks in chapter one. The concept of magnetic trapping is presented and the atom chip technology, central to our approach, is discussed. Furthermore, a short derivation of the crucial angles of the atomic cloud axis and the quantization axis in chip traps is given.
- Chapter two is dedicated to the theory of spin-squeezing. To introduce the underlying principles, light-mediated squeezing is presented, where the advantages of an optical resonator become apparent. The main requirements for our new experiment (TACC2) arise from the considerations in this chapter, and are summarized in the last subsection.
- The previously stated requirements for the new TACC2 experiment make high demands on the performance of the FFP resonators. To meet these demands, a novel CO₂ laser dot milling method is developed in chapter three. The improvements of the CO₂ laser milling setup and the obtained structures are demonstrated.
- The fabricated large spherical structures demonstrated in the previous chapter and the use of photonic crystal fibers (PCF) lead to a new generation of millimeter long FFP resonators, presented in chapter four. First, the basic theory of optical resonators is established and fiber Fabry-Pérot (FFP) resonators are introduced. Then, the experimental studies of the critical parameters of the resonator, the finesse and the transmission, are discussed in detail for the fundamental resonator mode, as well as for higher order modes. Numerical simulations are presented, predicting very well the performance of the experimentally realized resonators. The design of a compact and stable resonator mount is presented, leading to the construction of the resonators for the new experiment.

- Finally, in the fifth chapter, we present the design and fabrication of an atom chip that combines the necessary features for clock operation in presence of an optical resonator. Magnetic field simulations are performed to validate the design. The chip fabrication and assembly with the resonator mount is presented.
- This work is concluded with an outlook on future experiments with TACC2 and possible applications of the technologies developed during this work.

Trapped Atom Clock on a Chip

This chapter provides a short introduction to metrology with atomic clocks. We then present the building blocks necessary for our implementation, a trapped atom clock, with an emphasis on atom chip technology. Finally, a short derivation of the crucial angles of the atomic cloud axis and the quantization axis in chip traps is given.

1.1 Atomic clocks

Atomic clocks are highly accurate and stable frequency standards, separable in two classes:

- Active devices, like the hydrogen maser [83], where the atoms emit electromagnetic radiation of a well defined frequency.
- Passive devices, like fountain clocks, where an atomic transition is used to correct the frequency of a local oscillator (LO), as depicted in Fig. 1.1.

Since the trapped atom clock presented here is part of the second class, we will focus on the principle of passive devices: A signal of a local oscillator with frequency ν_{LO} is used to interrogate a transition frequency ν_{at} of an atomic system. The response of the atomic system can then be used to derive the detuning of the two frequencies $\Delta = \nu_{LO} - \nu_{at}$. By regulating the local oscillator frequency, the detuning Δ is minimized, locking the LO frequency to the atomic reference. By reproducing the atomic frequency, the LO benefits from the three main advantages of atomic transitions as a frequency reference:

- The frequencies of atomic transitions are stable, if external influences are excluded. There is no experimental evidence that the transition frequency ν_{at} itself changes with time [84, 85].
- The linewidth of the clock transition is orders of magnitude smaller than the absolute frequency, giving small relative errors (cf. Eq. 1.1.5), an advantage fully exploited with optical clocks [51].

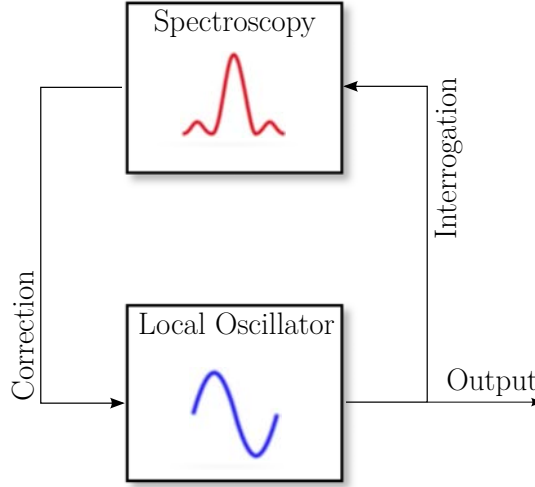


Figure 1.1: Atomic clock schematic. The LO is corrected by the spectroscopic signal of the atoms. The corrected signal is the output and serves as the frequency reference.

- Atoms of the same species are identical, ruling out the reference itself as an error source in comparison experiments

The advantages of atomic transitions are compromised by numerous effects separable in technical and fundamental limitations leading to an altered local oscillator signal

$$\nu_{LO} = \nu_{at} (1 + \epsilon + y(t)) \quad (1.1.1)$$

where the noise $y(t)$ with $\langle y(t) \rangle = 0$ is a measure of the stability of the clock, important for primary and secondary frequency standards. The systematic deviation ϵ is called the accuracy of a clock and is of importance for primary frequency standards only.

1.1.1 Rabi and Ramsey spectroscopy

Before we describe the interrogation of the atomic system with the local oscillator, we introduce the Bloch vector, that maps the atomic state on the Bloch sphere [86] with

$$|\theta, \phi\rangle = \cos(\theta/2)e^{-i\phi/2} |2\rangle + \sin(\theta/2)e^{i\phi/2} |1\rangle. \quad (1.1.2)$$

The two angles θ, ϕ fully describe the quantum state of the atomic system. To now describe the interrogation of the atoms with the LO signal, one of the two following methods are commonly used [87]

Rabi spectroscopy: When applying a near-resonant pulse of electro-magnetic radiation of constant amplitude for a time t , the population of the upper clock state $|2\rangle$ evolves following [88]

$$P_2(\Omega_R, \Delta, t) = \frac{\Omega_R^2}{\Omega_R^2 + \Delta^2} \sin^2\left(\frac{\sqrt{\Omega_R^2 + \Delta^2}}{2}t\right) \quad (1.1.3)$$

with Ω_R being the Rabi frequency and the atom being in the ground state $|1\rangle$ for $t = 0$. Fig. 1.2 a) shows the dependence of the measured atomic state on the detuning of the LO.

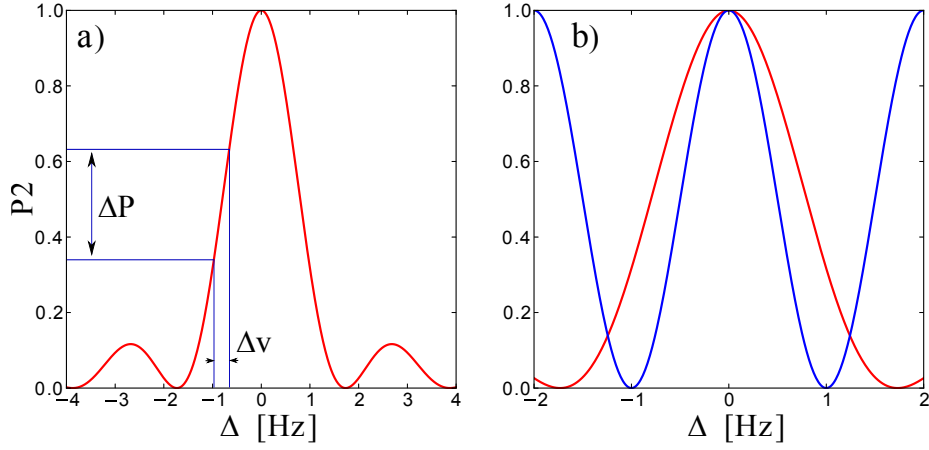


Figure 1.2: a) Rabi pulse following Eq. 1.1.3 with $\Omega_R = 1$ and $t = \pi$. For $\Delta = 0$, the atomic state is fully transferred to $|2\rangle$. A pulse realizing the full transfer is referred to as a π -pulse. b) Comparing the spectroscopic response of the Rabi pulse from a) (red) with a Ramsey sequence (blue) with the same duration $T_R = \pi$.

Ramsey spectroscopy: A more sophisticated sequence consisting of two resonant pulses is used. The first pulse transfers the atomic state to $|\Psi\rangle = \frac{1}{\sqrt{2}}(|1\rangle + |2\rangle)$ with a pulse area of $\Omega_R t = \pi/2$ (called a $\pi/2$ -pulse). After the *Ramsey time* T_R , a second $\pi/2$ -pulse is applied to the atomic system, mapping the phase difference of the two states onto a population difference as depicted in Fig. 1.3. Neglecting the time for the

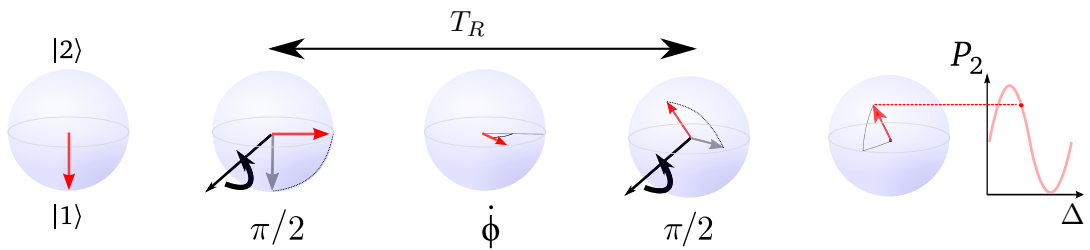


Figure 1.3: The Ramsey sequence depicted on the Bloch sphere. The grey (red) arrows depict the state before (after) the manipulation of each step. The speed of the dephasing is given by $\dot{\phi} = 2\pi\Delta$. Figure adapted from [89].

$\pi/2$ -pulses (valid for $T_R, 1/\Delta \gg 1/\Omega_R$), the population of the upper clock state $|2\rangle$ is given by

$$P_2(\Delta, T_R) = \frac{1}{2} (1 + \cos(\Delta T_R)), \quad (1.1.4)$$

leading to a higher sensitivity for the same cycle time (see Fig. 1.2 b)). Another advantage is that the atoms evolve during the Ramsey time without being disturbed by external fields. With this reduced coupling to the environment, the ideal case of a fully isolated frequency reference is approached.

1.1.2 Clock stability

The standard deviation σ_y of the frequency fluctuation of Eq. 1.1.1 is used as the figure of merit for the clock stability and can be related to the noise of the population σ_{P_2} via the spectroscopic response

$$\sigma_{y,1 \text{ cycle}} = \frac{\sigma_\nu}{\nu_{at}} = \frac{\sigma_{P_2}}{\nu_{at} |dP_2/d\nu|}. \quad (1.1.5)$$

Given a clock cycle time T_C and a total interrogation time τ , the standard deviation for a series of $N_{cyc} = \tau/T_C$ cycles decreases for uncorrelated experiments as

$$\sigma_y(\tau) = \sigma_{y,1 \text{ cycle}} \sqrt{1/N_{cyc}} = \sigma_{y,1 \text{ cycle}} \sqrt{\frac{T_C}{\tau}}. \quad (1.1.6)$$

The measurement performed on the atomic superposition state

$$|\Psi\rangle = \frac{1}{\sqrt{2}} (|1\rangle + \exp(-i\phi) |2\rangle) \quad (1.1.7)$$

projects the atomic state on one of the clock states $|1\rangle, |2\rangle$ with the probability of $P_2 \approx 1/2$ for a Bloch vector close to the equator of the Bloch sphere. A more precise value of P_2 can only be extracted by multiple repetitions of the same experiment or by interrogating multiple atoms at once. In both cases, the shot noise or projection noise σ_{P_2} decreases with the atom (or repetition) number as $\sigma_{P_2} = 1/\left(2\sqrt{N_{at(rep)}}\right)$ [90]. Inserting this expression into Eq. 1.1.6, the clock stability is given by

$$\sigma_y(\tau) = \frac{1}{2\sqrt{N_{at}}\nu_{at} |dP_2/d\nu|} \sqrt{\frac{T_C}{\tau}}. \quad (1.1.8)$$

For a coherent state, the quantum projection noise is the fundamental limit for the clock stability [31]. It can be overcome using entangled ensembles, as will be discussed in chapter 2.

1.2 Trapped atom clock on a chip (TACC)

The TACC experiment is presented in great detail in [89, 91, 92] but as it is the foundation of TACC2, a brief overview is provided in the following. The characteristic feature of TACC is that the atoms are trapped during the Ramsey time. This allows to increase the interrogation time without increasing the system size, as it is the case for fountain clocks. Since it is the main difference compared to conventional atom clocks, we begin this section with a description of the effects that arise from the trapping.

1.2.1 Magic traps

Using trapped atoms as a frequency reference might appear contradictory at first glance. Trapping, independent of the force or the object, requires a position dependent potential with a local minimum. Ideally, a frequency reference should not couple to external fields and if it does, the shift of the frequency should not be position or time dependent. Since in our case the trapping is realized by a magnetic field, which shifts the atomic energy levels via the Zeeman-effect, we violate both points. Fortunately, the level structure of ^{87}Rb holds a solution to this contradiction. Here, the energy shift of the two clock states is the same to first order for a specific magnetic field strength, called “magic field” B_m . A similar approach is taken for dipole traps for optical clocks where specific wavelengths (*magic wavelengths*) are used for trapping [93].

Trapping the atoms in a magnetic trap with the *magic field* $B_{min} = B_m = 3.229 \text{ G}$ as the trap minimum, the transition frequency between the clock states reads as [94, 95]

$$f_{|1\rangle \rightarrow |2\rangle} = \frac{\Delta E_{hfs}}{h} + \Delta\nu_{at} + \underbrace{\beta (B(\mathbf{r}) - B_m)^2}_{\Delta\nu_B(\mathbf{r})}, \quad (1.2.1)$$

where $\frac{\Delta E_{hfs}}{h} = \nu_{at}$ is the atomic reference frequency in the unperturbed case, $\Delta\nu_{at} = -4497.31 \text{ Hz}$ and $\beta = 431.35 \text{ Hz G}^{-2}$. With $\Delta\nu_{at} \neq 0$ our trap is a *pseudo-magic trap*, since it shows an effective frequency shift with respect to the free atom [96]. Still, the first order insensitivity of the atomic frequency to the magnetic field is ensured and dephasing of the atomic spin states in the trap is reduced.

1.2.2 Density shifts in trapped atom clouds

A second position dependent frequency shift is experienced by the atoms due to atom-atom interactions. The interactions are strongly enhanced by the high densities of trapped clouds compared to the typical densities in fountain clocks. By using a mean field approach, the frequency shift due to s-wave collisions can be written as [95]

$$\Delta\nu_C = \frac{\hbar}{m} n [a_{22}a_{22} - a_{11}a_{11} + f(2a_{12}a_{12} - a_{11}a_{11} - a_{22}a_{22})] \quad (1.2.2)$$

with $f = (n_1 - n_2)/n$ and $n = n_1 + n_2$ being the atom number density, m the atom mass, and $a_{11} = 100.44 a_0$, $a_{22} = 95.47 a_0$ and $a_{12} = 98.09 a_0$ the scattering lengths of the respective states with a_0 the Bohr radius. As the density profile of the trapped cloud has Gaussian shape, the collisional shift is position dependent, as depicted in

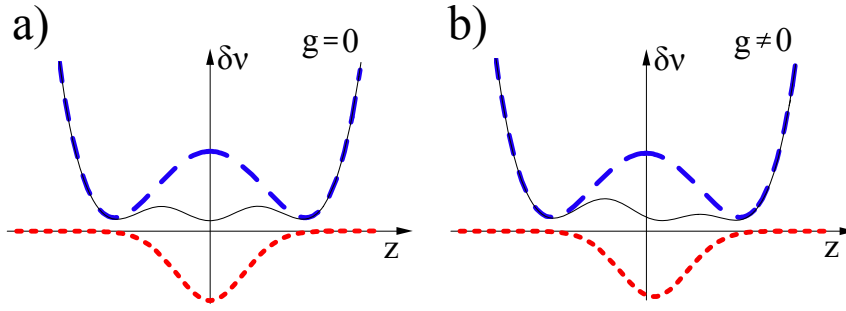


Figure 1.4: Mean field and second order Zeeman shift. a) shows the near cancellation of the total shift (solid black line) by the addition of the negative mean field shift (dotted red line) and the positive second order Zeeman shift (blue dashed line) in zero gravity. b) shows the same situation including the gravitational sag (cf. Sec. 1.4.4). Adapted from [97].

Fig. 1.4. The spatial variation of the clock frequency can be canceled to first order by detuning the magnetic field minimum slightly from $B_{min} = B_m$, as sketched in Fig. 1.4 and shown in [98]. This reduced spatial inhomogeneity is of great assistance for atomic clocks with magnetically trapped atoms [97].

1.2.3 ^{87}Rb for TACC

Due to several reasons ^{87}Rb is an attractive choice for TACC:

- ^{87}Rb is the work horse of the cold atom community and thus a lot of methods and experience are available to cool, trap and manipulate the atoms.
- As shown in Sec. 1.2.1, it is possible to realize a magic trap for ^{87}Rb , an indispensable tool for the operation of a magnetically trapped frequency reference. Furthermore, it allows the first order cancellation of line broadening due to density shifts, as discussed in Sec. 1.2.2.
- The hyperfine splitting is relatively large, yielding with Eq. 1.1.5 a low relative frequency error for a microwave frequency standard.
- The clock states we use have similar scattering lengths [95] which leads to spin-self rephasing, increasing the coherence time, as discussed in [65].
- The collisional shift for ^{87}Rb atoms is at least 50 times lower than for ^{133}Cs [99].

The listed favorable properties of ^{87}Rb lead to the endorsement of the unperturbed ground-state hyperfine transition of ^{87}Rb by the *Comité international des poids et mesures* (CIPM) as a secondary representation of the second [100].

1.2.4 TACC clock transition

Only particular Zeemann sub-levels can be trapped magnetically, as will be seen in the next section 1.3. This rules out the conventional choice of states for Rb fountain

clocks, where $|F = 2, m_F = 0\rangle$, $|F = 1, m_F = 0\rangle$ are used.

To be able to trap the atoms and to benefit from the magic field (cf. Sec. 1.2.1), we use as clock states $|1\rangle = |F = 1, m_F = -1\rangle$ and $|2\rangle = |F = 2, m_F = 1\rangle$. These states cannot be coupled with a single photon transition since $\Delta m_F = 2$. Therefore we use a two-photon transition consisting of a radio-frequency (RF) photon and a micro-wave (MW) photon, leading to an effective Rabi frequency [91]

$$\Omega = \frac{\Omega_{RF}\Omega_{MW}}{2\Delta}, \quad (1.2.3)$$

where $\Delta \approx 500$ kHz is the common detuning of both frequencies to the intermediate state $|F = 2, m_F = 0\rangle$. The two-photon transition and the clock states are presented in the level diagram in Fig. 1.5. Further information on the ^{87}Rb D-line can be found in [101].

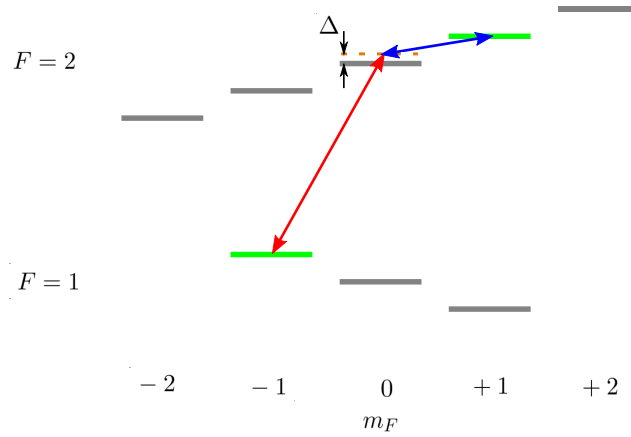


Figure 1.5: Zeeman sub-level diagram of the $5^2S_{1/2}$ manifold of ^{87}Rb . The degeneration of the hyperfine levels is canceled by an external quantization magnetic field and the Zeeman sub-levels are visible (grey lines). The clock-states used in TACC are marked green and the RF (MW) transition is indicated by a blue (red) arrow.

1.3 Magnetic trapping and manipulation of neutral atoms

The unique properties of ^{87}Rb allow clock operation in a magnetic trap, as we have seen in the previous section. In this section we provide the general principles of magnetic trapping of neutral atoms, to prepare for the discussion of the atom chip technology.

1.3.1 Basic principle

For neutral atoms, the interaction energy U of their magnetic dipole $\boldsymbol{\mu}$ with an external magnetic field \mathbf{B} can be written as

$$U = -\boldsymbol{\mu} \cdot \mathbf{B} = \mu_B g_F \mathbf{F} \cdot \mathbf{B} = \mu_B g_F m_F |B|, \quad (1.3.1)$$

if U is smaller than the hyperfine splitting of the atomic structure. In our experiment we will work with ^{87}Rb , where this approximation holds for $|B| < 200$ Gauss [102], met by our chip traps. Here, \mathbf{F} is the total angular momentum of the atom, μ_B the Bohr magneton and g_F the Landé factor. Since the Maxwell equations forbid the existence of local maxima of the magnetic field [103], *high-field-seekers* with a magnetic moment parallel to the magnetic field cannot be trapped. The two clock states used in the experiment, $|1\rangle = |F = 1, m_F = -1\rangle$ and $|2\rangle = |F = 2, m_F = 1\rangle$, are thus *low-field-seekers* with their magnetic moment antiparallel to the magnetic field and can therefore be trapped in magnetic minima. The creation of magnetic minima will be discussed in Sec. 1.4.1.

1.3.2 Majorana losses

Spin-flips, transforming *low-field-seekers* into untrapped atoms (*high-field-seekers* or to states with $m_F = 0$), have to be avoided, since they lead to atom loss. To ensure this, the magnetic field orientation has to change much slower than the precession of the magnetic moment around the magnetic field axis [104]:

$$\frac{d}{dt} \frac{\mathbf{B}}{|\mathbf{B}|} \ll \omega_L = \mu_B |g_F| B / \hbar, \quad (1.3.2)$$

where ω_L is defined as the Larmor frequency.

The Majorana losses can become the main loss channel particularly for magnetic traps with a vanishing magnetic field in the center, like the quadrupol trap (see Sec. 1.4.1). The loss rate for ^{87}Rb atoms with a magnetic moment $\mu = g_F m_F \mu_B$ scales with [105]

$$\Gamma_m \propto \frac{\hbar}{m} \left(\frac{\mu B'}{k_B T} \right)^2 \quad (1.3.3)$$

where B' is the gradient close to the trap center, T the temperature of the atom cloud and m the mass of the atom. Bringing the atoms closer to the trap center by steepening the gradient or lowering the temperature increases the loss rate. In [105] the atoms are prepared in the same state as in our experiment ($|F = 1, m_F = -1\rangle$) and they find experimentally the lifetime

$$\tau_m = 1/\Gamma_m = 5.8 \times 10^{-3} \frac{\text{s}}{\mu\text{K}^2} T^2. \quad (1.3.4)$$

Dividing by the fixed magnetic gradient of $B' = 155 \text{ G cm}^{-1}$ in [105] we get, following Eq. 1.3.3:

$$\tau_m = 139 \frac{\text{s G}^2}{\mu\text{K}^2 \text{cm}^2} \frac{T^2}{B'^2} \quad (1.3.5)$$

as an empirical formula. Note that in [106] the proportionality factor is smaller by a factor of 2, showing that these formulas can only be used as a first estimation, but they will supply an orientation for choosing the trap parameters in the following chapters. For Ioffe-Pritchard traps (see Sec. 1.4.1) with non-vanishing magnetic field B_0 in the center, condition 1.3.2 restricts the choice of the transversal trapping frequency ω_\perp [102]. This can be expressed with the adiabaticity coefficient

$$\alpha_{adiab} = \frac{\omega_{L,min}}{\omega_{\perp}} = \frac{\mu_{BGF} B_{min}}{\omega_{\perp}}. \quad (1.3.6)$$

For $\alpha_{adiab} \gg 1$ the orientation of the magnetic moment $\boldsymbol{\mu}$ follows adiabatically the external magnetic field and Eq. 1.3.2 is fulfilled.

1.4 Atom chip technology

The trapping and manipulation of the atoms is realized by an atom chip. The basic principle of creating versatile magnetic traps close to the chip surface will be described in the following, limited to the use for TACC2. An in-depth presentation of the atom chip technology, from production to future applications can be found in [64] and a recent overview in [107].

1.4.1 Basic principle

Following Eq. 1.3.1, a local minimum of the magnetic field strength $B = |\mathbf{B}|$ is needed to trap neutral atoms. One possibility is to create the minimum by use of a coil pair in anti-Helmholtz configuration, as realized in the early days of magnetic trapping [108]. More sophisticated trap geometries and high trap gradients with relatively small currents can be realized by superimposing a static magnetic bias field with the near-field of a current carrying wire

$$\vec{B}(r) = \frac{\mu_0 I}{2\pi r} \hat{\mathbf{e}}_I \times \hat{\mathbf{e}}_r \quad (1.4.1)$$

as depicted in Fig. 1.6. This is the central building block of all magnetic traps used in this experiment. With a current I in the (infinitely thin) wire along $\hat{\mathbf{e}}_x$ and a bias

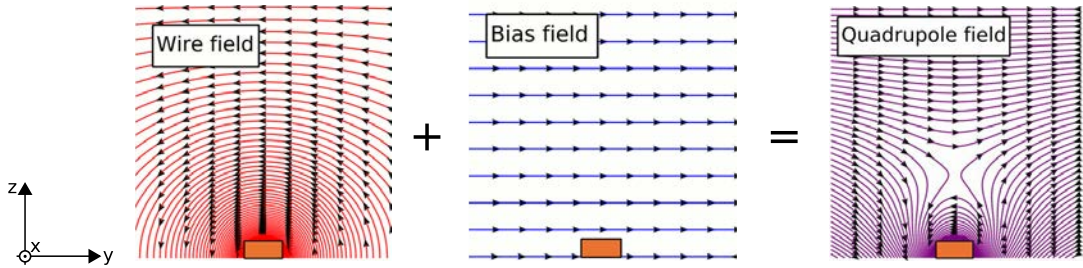


Figure 1.6: Basic principle of wire traps. Taken from [91].

field B_y , a 2D-quadrupole trap is created at the distance

$$z_0 = \frac{\mu_0 I}{2\pi B_y}, \quad (1.4.2)$$

where the wire field cancels the bias field. At this position the gradient of the magnetic field perpendicular to $\hat{\mathbf{e}}_x$ is given by

$$B'(z) = -\frac{\mu_0 I}{2\pi z^2} \Big|_{z=z_0} = -\frac{2\pi B_y^2}{\mu_0 I}. \quad (1.4.3)$$

The approximation of infinitely thin wires holds only if the distance of the wire z_0 is large compared to the wire width w . Since $z_0 \gg w$ can easily be violated by chip traps, the more accurate formulas for finite wire widths have to be used when $z_0 \lesssim w$, where the field created by the wire of width w is given by [102]

$$\mathbf{B}(x=0, y=0, z) = \hat{e}_y \cdot \frac{\mu_0 I}{\pi w} \operatorname{arccot} \frac{2z}{w} \quad (1.4.4)$$

with the gradient along z

$$\frac{\partial B}{\partial z} = \frac{2\mu_0 I}{\pi w^2 + 4z^2}. \quad (1.4.5)$$

While the gradient for large z converges to the infinitely thin wire case (Eq. 1.4.3) it shows a very different behavior for small z and converges against a fixed value dependent on the wire width w .

1.4.2 Trap types

The basic principle of the wire trap confines the atoms in two dimensions. To generate a trap with full 3D-confinement, additional steps have to be taken. Here we present three different approaches, resulting in the trap types we will need for the TACC2 experiment.

Dimple Trap: A realization of a three dimensional Ioffe-Pritchard trap is shown in Fig. 1.7. The current I_0 with the magnetic field $B_{0,y}$ form a 2D-quadrupole, as presented in Sec. 1.4.1. With an additional field along $B_{0,x}$ the field in the trap center is lifted to $B_{min} = |B_{0,x}|$ and the potential takes quadratic form. A current $I_1 \ll I_0$ in a second wire along \hat{e}_y , creates a ‘‘dimple’’ in the field magnitude along x , leading to confinement. This creates a three dimensional Ioffe-Pritchard trap. For $I_1 \ll I_0$, the

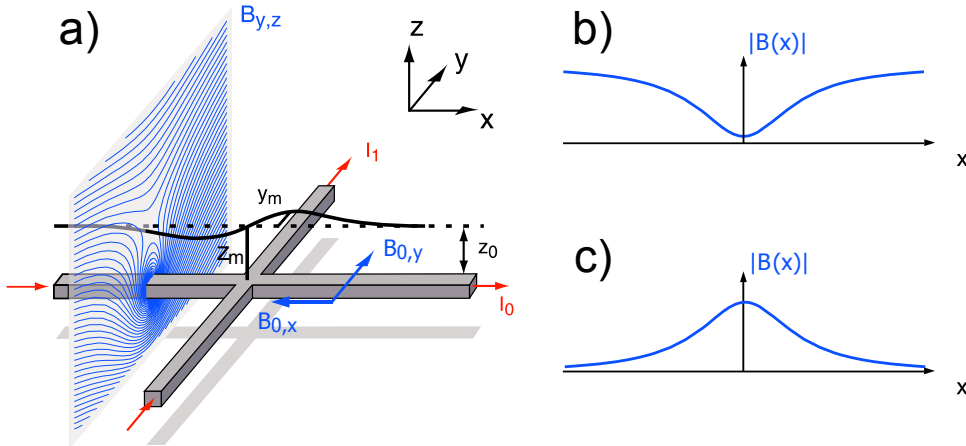


Figure 1.7: Dimple trap of two crossing wires. a) shows the current, wire and bias field configuration with the resulting field in the y - z plane. The field strength minimum is shown as a black line, the minimum line for $I_1 = 0$ is shown as the dashed line. b) shows the potential along x for $I_1 > 0$. c) shows the potential for $I_1 < 0$ and $B_{0,x} = 0$ used for the H,U and Z traps. Adapted from [109].

gradient given in Eq. 1.4.3 is still valid in first approximation and the field on the trap bottom is given by

$$B_0 = \left| B_{0,x} + \frac{\mu_0 I_1}{2\pi z_0} \right| \quad (1.4.6)$$

with the trap frequencies

$$\omega_x = \sqrt{\frac{\mu_m}{m} B''} \quad \text{and} \quad \omega_\perp = \sqrt{\frac{\mu_m}{m} \frac{B'^2}{B_0}} \quad (1.4.7)$$

where $B'' = \frac{\partial^2 B_{1,x}}{\partial x^2}$ is the curvature of the magnetic field created by I_1 .

H/U/Z-Trap: Using several crossed wires can lead to another type of magnetic micro trap: changing the sign of current I_1 for the dimple trap the confinement along x gives way to a maximum depicted in Fig. 1.7 c). Using two parallel wires perpendicular to the initial one creates the widely used H-shape with which two different current configurations can be chosen: if the two currents are parallel, their magnetic fields add up in the center and a Ioffe-Pritchard trap is created. A simplified version of this trap can be realized by a Z-shape, following two arms of the H-layout (see Fig. 1.8). With this configuration the atoms can be trapped with only one current and a bias field. If the currents in the parallel H wires have opposite direction, their magnetic fields cancel in the center, creating a quadrupole trap. Again, by removing two arms to form a “U” as depicted in Fig. 1.8, a “one-wire”-version of the trap can be created, realizing a quadrupole trap with the bias field. This U-trap is widely used in our experiment, to create the magnetic field for the MOT and, in a modified scheme, the atom transport, as will be presented in Sec. 5.2.1.

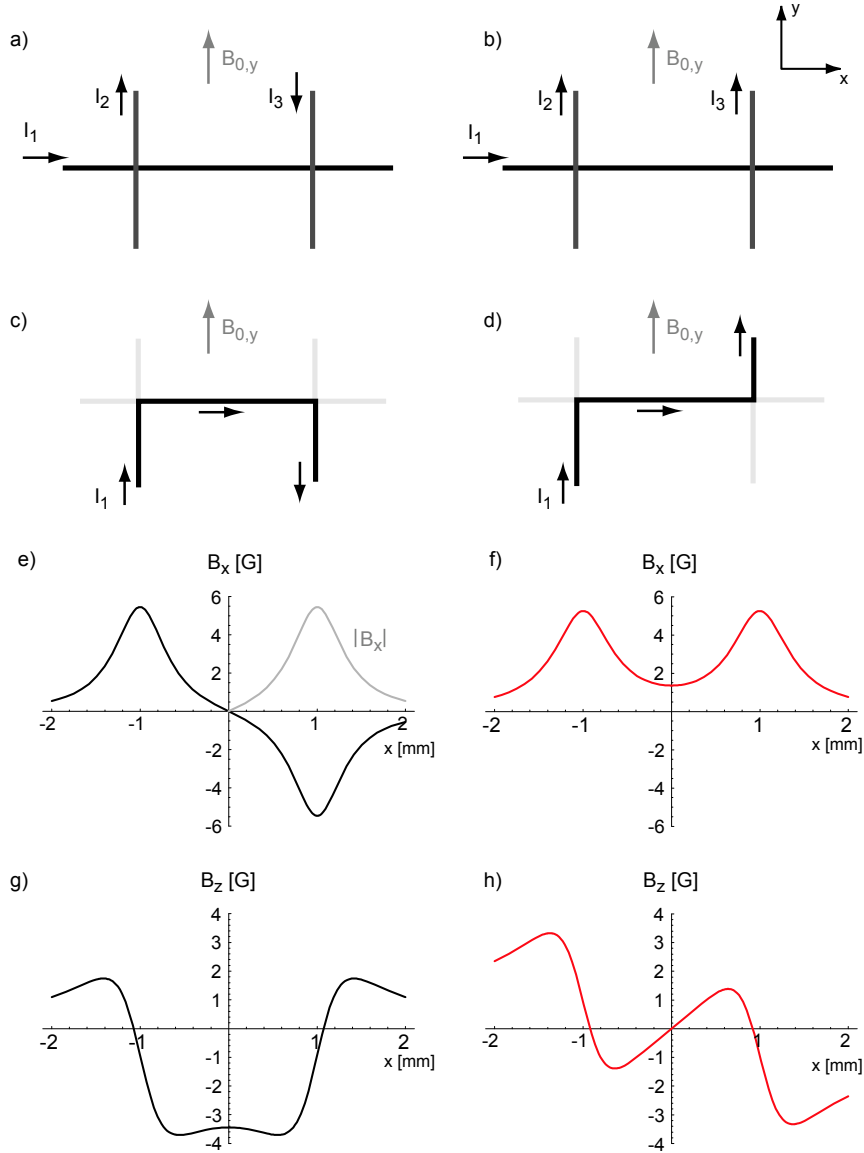


Figure 1.8: H/U/Z-trap. The left column shows the generation of a quadrupole trap with three wires (a) or one wire (c) and a bias field. The right column shows the generation of a IP trap with three wires (b) or one wire (d) and a bias field. e)-h) shows the calculated magnetic fields along x and z for $B_y = 10$ G, $I_1 = I_2 = I_3 = 2$ A and a wire width of $50 \mu\text{m}$ and a distance of the wires along y of 2 mm. Taken from [102].

1.4.3 Trap depth

The trap depth is defined as the energy an atom needs to escape the trap and is given by the lowest potential wall around the local minimum of the potential. For the 2D-confinement of a simple wire trap (see. Fig. 1.6) the trap depth along the confining axis is given by the magnetic bias field B_0 as depicted in Fig. 1.9¹. The potential is given by Eq. 1.3.1 and approaches $U = g_F m_F \mu_B B_0$ for $z \rightarrow \infty$. The effective potential

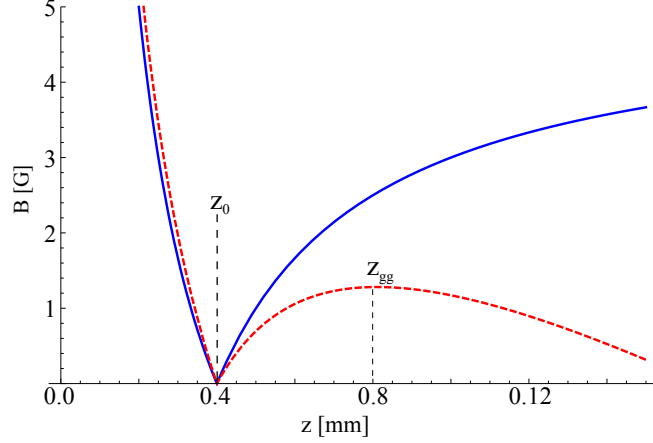


Figure 1.9: Effect of gravity on trap depth. Shown is the magnetic potential for a trap as in Fig. 1.6 with $I=1$ A and $B_0 = 5$ G as the blue line. Taking gravity into account (red dashed line, gravity points along z), the effective potential the atom sees is modified.

the atom experiences is not only created by the magnetic dipole force but as well by gravity. If the trap position lies below the current carrying wire, so that gravity points away from the wire to the trap center, the final trap position is pulled away from the wire (see Sec. 1.4.4) and the trap depth is reduced to [91]

$$\Delta E = g_F m_F \mu_B B(z_{gg}) - mg(z_{gg} - z_0) \quad (1.4.8)$$

with

$$z_{gg} = \sqrt{\frac{g_F m_F \mu_B \mu_0 I}{2\pi mg}} \quad (1.4.9)$$

being the position where the magnetic field gradient is canceled by gravity. With Eq. 1.4.1 the magnetic field below the trap position is given by

$$B = B_y = B_0 - \frac{\mu_0 I}{2\pi z} \quad (1.4.10)$$

and yields with Eq. 1.4.8

$$\Delta E = -2\sqrt{\frac{g_F m_F \mu_B \mu_0 I mg}{2\pi}} + g_F m_F \mu_B B_0 + \frac{\mu_0 I}{2\pi B_0} mg. \quad (1.4.11)$$

¹Since there is no confinement along the wire direction, the 2D-quadrupole has a trap depth $\Delta E = 0$. To obtain a real trap, adding H wires is one possibility to provide confinement along the 2D-quadrupole center line.

Evaluating Eq. 1.4.11 for a chosen gradient $B'_{fix} = \frac{2\pi B_0^2}{\mu_0 I}$, it can be found that the trap depth scales with $\propto \sqrt{I}$ (resp. $\propto B_0$).

The lower the magnetic field gradients are, the more important is the trap depth reduction due to gravity. Working with the atomic states with $m_F = 1$ reduces again the effective gradient by a factor of 2 compared to $m_F = 2$ and thus the trap depth, as can be seen in Eq. 1.4.11. Since we will furthermore use shallow traps in our experiments, the finite trap depth is of particular importance, for which reason we took gravity into account for all performed magnetic trap simulations.

1.4.4 Gravitational sag and rotation

Besides the reduction of the trap depth, gravity pulls the atoms out of the magnetic minimum. Considering a 2D-Ioffe trap at height z_0 with the magnetic field [102]

$$\mathbf{B} = \begin{pmatrix} B_0 \\ b \cdot (z - z_0) \\ b \cdot y \end{pmatrix} \quad (1.4.12)$$

with $b = \partial_z B_y = \partial_y B_z$, the field magnitude is given by

$$|\vec{B}(\vec{x})| \approx B_0 + \frac{1}{2} \frac{b^2}{B_0} y^2 + \frac{1}{2} \frac{b^2}{B_0} (z - z_0)^2. \quad (1.4.13)$$

To account for the influence of gravity on the potential, we parametrize gravity as an effective gravitational gradient $b_g = \frac{m}{g_F m_F \mu_B} g$, which is $b_g \approx 33 \text{ G/cm}$ for ^{87}Rb atoms in $|1, 1\rangle$. This gives the effective magnetic field magnitude

$$|\vec{B}(\vec{x})| \approx B_0 + \frac{1}{2} \frac{b^2}{B_0} y^2 + \frac{1}{2} \frac{b^2}{B_0} (z - z_0)^2 - b_g (z - z_0) \quad (1.4.14)$$

with the new minimum shifted by gravity along z to

$$z_g = z_0 + \frac{b_g B_0}{b^2} \quad (1.4.15)$$

including the *gravitational sag*

$$\Delta z = \frac{b_g B_0}{b^2} = \frac{g}{\omega_z^2}, \quad (1.4.16)$$

where ω_z is the trap frequency along z of the potential in Eq. 1.4.14. In addition to the displacement, the field at the atom position is rotated by an angle $\alpha_{B,x}$ in the x-y-plane, as depicted in Fig. 1.10. The magnetic field of Eq. 1.4.12 at the new trap position $\vec{x}_t = (0, 0, z_g)$ yields

$$\mathbf{B} = \begin{pmatrix} B_0 \\ b \cdot (z_g - z_0) \\ 0 \end{pmatrix} = \begin{pmatrix} B_0 \\ \frac{b_g B_0}{b} \\ 0 \end{pmatrix}. \quad (1.4.17)$$

This can be understood by looking at Fig. 1.6, where the bias field B_y dominates over the wire field above the magnetic minimum. With this field along y , the angle of the field at the trap center with respect to the x -axis is given by

$$\alpha_{B,x} = \tan^{-1} \left(\frac{B_y}{B_x} \right) = \tan^{-1} \left(\frac{b_g}{b} \right). \quad (1.4.18)$$

By applying an additional magnetic gradient b_m to counteract gravity, the effect can be reduced, yielding

$$\alpha_{B,x} = \tan^{-1} \left(\frac{b_g - b_m}{b} \right). \quad (1.4.19)$$

The gradient b_m has to be realized as $b_m = \frac{\partial B_x}{\partial z}$ to not interfere with the gradient $b = \partial_z B_y = \partial_y B_z$. This can be accomplished with a stand-alone chip trap as will be shown in Sec. 5.2.4.

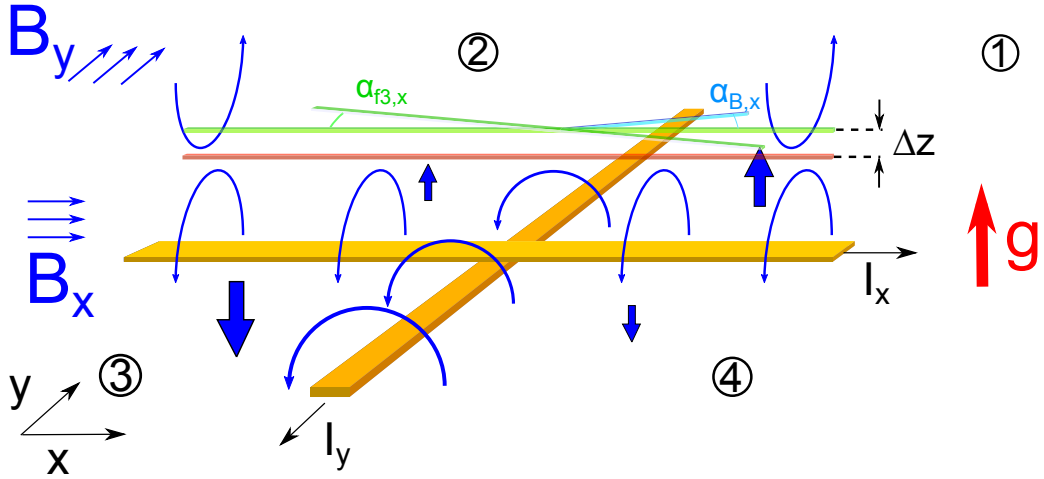


Figure 1.10: Gravitational sag in a dimple trap. The red line marks the center of the 2D-quadrupole trap created by the current I_x and B_y . The green line marks the potential minimum taking gravity into account. As this position is above the zero line of the magnetic potential, the bias field along y dominates over the wire field and the residual magnetic field at the trap position has an additional component along y .

While the field at the trap center is rotated by the effect of gravity, the trap axis itself is rotated by an angle $\alpha_{f3,x}$ in the x - y -plane due to the dimple trap configuration, as depicted in Fig. 1.7. The rotation can be understood intuitively by looking at the z -component of the magnetic fields created by the currents I_y and I_x . In the first and third quadrant in Fig. 1.10, the z -component of the field created by the wires points in the same direction, leading to an increased component B_z , depicted as a thick blue arrow. In quadrant 2 and 4 the fields are anti parallel which leads to a reduction of the stronger field created by I_x depicted as a smaller blue arrow. The z -component adds to the overall magnetic field magnitude $|\vec{B}|$, so the traps eigenaxis points to the quadrants with the reduced z -component (2 and 4) as depicted by the rotated green

line in Fig. 1.10. Describing the dimple trap as two crossed 2D-quadrupoles, we get for the magnetic field [91]

$$\mathbf{B} = b_l \begin{pmatrix} z \\ 0 \\ x \end{pmatrix} + b \begin{pmatrix} 0 \\ z - z_0 \\ y \end{pmatrix} \quad (1.4.20)$$

where b is the gradient of the upper quadrupole as in Eq. 1.4.12 and $b_l \ll b$ is the gradient of the lower quadrupole. The minimum line is parametrized as

$$b_l x + b y = 0; \quad z = \frac{b^2}{b^2 + b_l^2} z_0 \quad (1.4.21)$$

leading to a rotation in the xy -plane of

$$\alpha_{f3,x} = \tan^{-1} \left(\frac{y}{x} \right) = \tan^{-1} \left(-\frac{b_l}{b} \right). \quad (1.4.22)$$

Unfortunately, the situation presented in Fig. 1.10 shows the general behavior for a dimple trap, which traps the atoms below the chip (i. e. gravity points away from the chip towards the trap center). For all four configurations ($B_x > 0, B_y > 0$), ($B_x > 0, B_y < 0$), ($B_x < 0, B_y > 0$), ($B_x < 0, B_y < 0$) with the corresponding currents I_x and I_y , the bottom field is rotated in the opposite direction of the trap eigenaxis. The resulting angle between the bottom field and the trap axis is then

$$\alpha = \alpha_{B,x} - \alpha_{f3,x} = \tan^{-1} \left(\frac{b_g - b_l}{b} \right) + \tan^{-1} \left(\frac{b_l}{b} \right) \quad (1.4.23)$$

where the gradient of the lower quadrupole b_l takes the role of the gradient b_m along z in Eq. 1.4.19. For $b_g - b_l \ll b$, $b_l \ll b$ the angle simplifies to

$$\alpha = \frac{b_g}{b}, \quad (1.4.24)$$

where it gets evident that strong confinement along the transverse direction reduces α . In the absence of gravity² $\alpha = 0$ and perfect alignment of the trap axis and the magnetic field at the trap center can be achieved. If furthermore $b_l = 0$, the magnetic field at the trap center and the trap axis are aligned with the x -axis. This cannot be achieved for the dimple trap where the gradient along z is given by

$$b_l = \left. \frac{\partial B_z}{\partial x} \right|_{x=0} (z = z_0) = -\frac{\mu_0 I_d}{2\pi z_0^2} \neq 0, \quad (1.4.25)$$

which leads with Eq. 1.4.22 to a rotation of the trap. Alignment with the x -axis can be realized with the stand-alone trap presented in Sec. 5.2.4.

The misalignment of the trap axis with the magnetic field at the trap center has to be considered for the atom-light interaction in an optical resonator, as discussed in Sec. 2.4. In the presence of gravity, the atom cloud cannot be perfectly aligned with the cavity mode, while the quantization field points along the optical axis.

Having introduced the general concept of atomic clocks and the current TACC experiment, including the atom chip technology, we move on to discuss spin-squeezing, to give the theoretical background for an entanglement enhanced atomic clock.

²This hypothetically sounding condition is already reality in some chip experiments [110].

Spin-Squeezing for Metrology

Since the goal of TACC2 is to study the influence of quantum correlations on the clock stability in a metrologically relevant regime, we use this chapter to present the link between quantum correlations and time measurement. We restrict the discussion to spin-squeezed states, which describe only one class of entangled quantum states interesting for metrology. Other quantum states for metrology beyond the standard quantum limit can be found in [33, 111], where quantum logic operations are used for the state creation. These concepts are not suitable for entangling a large number of particles, a requisite for our experiment. Therefore we focus on the fundamental concepts of squeezing, using our system of spin- $\frac{1}{2}$ particles as an example. We then present two possible implementations of spin-squeezing, which are envisaged for the new TACC experiment. Both implementations rely on atom-light interaction amplified by optical resonators, whose principles will therefore be recapitulated in Sec. 2.2. The presented spin-squeezing methods define the requirements on the experimental setup which will be summarized in the last section.

2.1 Spin-squeezing

The atoms used in our experiment can be described as a two level system with the two clock states $|1\rangle = |F=1, m_F=-1\rangle$ and $|2\rangle = |F=2, m_F=1\rangle$ (see Fig. 1.5). A convenient way to describe the system is the mapping of the state on the Bloch sphere [86] with $|\theta, \phi\rangle = \cos(\theta/2)e^{-i\phi/2}|2\rangle + \sin(\theta/2)e^{i\phi/2}|1\rangle$, where the two angles θ, ϕ fully describe the quantum state. To describe the large number of atoms in our system, we use a collective pseudospin operator defined as the sum of the spin- $\frac{1}{2}$ vectors: $S_k = \sum_{i=1}^N s_{k;i}$, $k = x, y, z$. Note that the full description of the quantum state on the Bloch sphere, given for a single particle, does not hold any longer for $N > 1$. To keep the ability to describe the system with a N -particle Bloch sphere, we have to restrict ourselves to the states symmetric under particle exchange, so that the length of the vector \mathbf{S} is given by

$$|\langle \mathbf{S} \rangle| \approx S_0 = N/2. \quad (2.1.1)$$

A coherent superposition of the atomic ensemble, named *coherent spin state* (CSS) [112], shows an equally distributed uncertainty along the coordinates transversal to

the direction of \mathbf{S} and is depicted in Fig. 2.1 a). As an example we prepare the atoms in state $|1\rangle$ and excite them with a $\pi/2$ -pulse (as at the start of a standard Ramsey sequence, see Fig. 1.3). Choosing x as the rotation axis, we get the CSS along y

$$|\text{CSS}_y\rangle = \left(\frac{|1\rangle + |2\rangle}{\sqrt{2}} \right)^{\otimes N}. \quad (2.1.2)$$

When the state is measured, every atom gets projected to $|1\rangle$ or $|2\rangle$ with equal probability $p = 0.5$, leading to an uncertainty in the state readout called the *quantum projection noise* [90]. This statistical process is modeled by a binomial distribution giving the variance $\langle \Delta S_x^2 \rangle = \langle \Delta S_z^2 \rangle = N/4 = S_0/2$, saturating the Heisenberg uncertainty relation

$$\langle \Delta S_x^2 \rangle \langle \Delta S_z^2 \rangle \geq |\langle S_y \rangle|^2 / 4 = N^2 / 16. \quad (2.1.3)$$

This implies directly that $\langle \Delta S_x^2 \rangle = \langle \Delta S_z^2 \rangle = N/4$ are the minimal uncertainties for measuring a transverse spin component, if the uncertainty is distributed symmetrically. We could have prepared the coherent spin state $|\text{CSS}_x\rangle$ along x as well, or with an arbitrary phase ϕ , rotating the state around the z axis. To generalize the notation we introduce the transverse variance ΔS_\perp , which is the variance along the equator of the Bloch sphere.

The observable of metrological interest is the angle ϕ that measures the detuning Δ of the local oscillator to the atomic frequency (see Fig. 1.3). The uncertainty of this angle, $\Delta\phi$, depends on the pseudo spin length $|\langle \mathbf{S} \rangle|$ and the uncertainty along the equator as

$$\langle \Delta\phi^2 \rangle = \langle \Delta S_\perp^2 \rangle / |\langle \mathbf{S} \rangle|^2 = 1/(2S_0) = 1/N \quad (2.1.4)$$

leading to the $1/\sqrt{N}$ dependence of the standard deviation already discussed in Eq. 1.1.8 and setting the *standard quantum limit*. In Fig. 2.1 a) the coherent spin state with an arbitrary phase ϕ is shown. The uncertainty of the transversal spin components is depicted as the blurred disc perpendicular to \mathbf{S} . For the application in a clock only

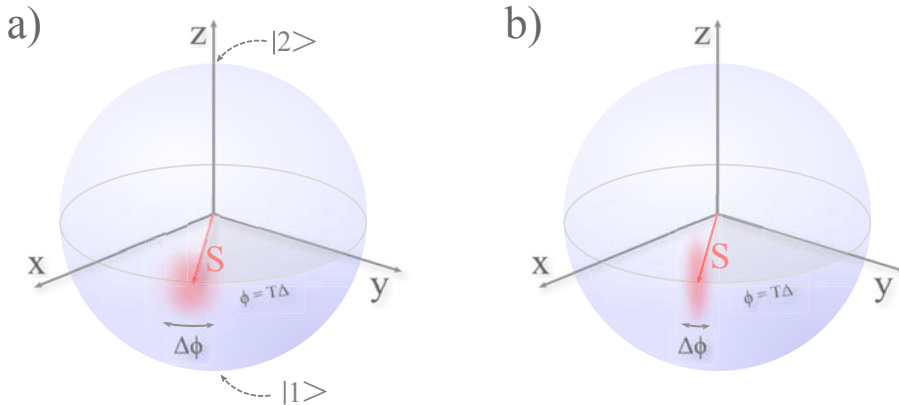


Figure 2.1: a) Coherent and b) squeezed spin state on Bloch sphere. The red shaded region at the tip of the atomic state vector depicts the uncertainty region of the transversal spin components.

a reduction of $\Delta\phi^2$ and thus ΔS_{\perp}^2 is of interest, as can be seen above. Furthermore the length of the vector $|\langle \mathbf{S} \rangle|$ should be maximized, as can be seen in Eq. 2.1.4. To quantify the useful reduction in the variance $\Delta\phi^2$ we compare the sensitivity of the state of interest with the sensitivity of the CSS, which is the limit for uncorrelated atoms. The ratio of the sensitivity of the investigated state to the CSS sensitivity was introduced in [113] as the spin squeezing criterion

$$\begin{aligned}\xi &= \langle \Delta\phi^2 \rangle / \langle \Delta\phi_{\text{CSS}}^2 \rangle \\ &= \frac{\langle \Delta S_{\perp}^2 \rangle}{|\langle \mathbf{S} \rangle|^2} / \frac{\langle \Delta S_{\perp, \text{CSS}}^2 \rangle}{|\langle \mathbf{S}_{\text{CSS}} \rangle|^2} \\ &= \frac{\langle \Delta S_{\perp}^2 \rangle}{|\langle \mathbf{S} \rangle|^2} 2S_0.\end{aligned}\tag{2.1.5}$$

To get an idea of the effects at hand and their influence on ξ we take a look at different exemplary states and their usefulness for metrology:

- **Coherent spin state (CSS):** Discussed in the text above, with $\langle \Delta S_{\perp}^2 \rangle = \langle \Delta S_z^2 \rangle = S_0/2$ and $|\langle \mathbf{S} \rangle| = S_0$. This gives per definition $\xi = 1$ and defines the maximal sensitivity for uncorrelated atoms.
- **Mixed state:** A mixed state without coherence, where half the atoms are in state $|1\rangle$ and the other half in $|2\rangle$. The variances of all components are given by $\langle \Delta S_{x,y,z}^2 \rangle = S_0/2$, the same as for the transversal variance of the CSS, but with the difference that $|\langle \mathbf{S} \rangle| = 0$, a vanishing vector length. It is therefore a state of no use for metrology, with $\xi = \infty$.
- **Squeezed spin state (SSS):** A state where the variance of the transversal component is reduced, by entangling the particles. This allows for a partial cancellation of the fluctuation of the transverse spin measurement of the individual atoms. If the concurrent reduction of the spin vector length is sufficiently small, this leads to $\xi < 1$ and therefore to an effective improvement of the sensitivity. The Heisenberg relation (Eq. 2.1.3) has to be satisfied and demands an increase of the variance of the conjugate operator S_z for a possible reduction of the transverse variance ΔS_{\perp} . This results in the elongated shape of the uncertainty region depicted in Fig. 2.1 b), leading to the denotation *squeezed* spin state.

An explanation why most of the created quantum states have a symmetrical distributed uncertainty is given by the fact that squeezing is a consequence of correlations of the individual particles [114]. Without intentionally engineering the quantum state no ab initio correlations are present, therefore the symmetric uncertainty distribution of a CSS is obtained.

In the following sections we will describe how a correlation of atoms can be realized and how spin-squeezed atomic states are prepared. The main tool for the quantum state engineering is the optical resonator, which is why we will start by introducing the physics of an atom cloud in such a resonator.

2.2 Atom-light interaction

The Hamiltonian governing the atom-light interaction of a two level atom at rest inside an optical resonator can be split up in three parts, describing the photon energy, the energy of the atom and the interaction energy

$$H = H_{at} + H_{res} + H_{int}. \quad (2.2.1)$$

Making use of the rotating wave approximation [88, 115] and eliminating the excited state [116]¹ we get the *Jaynes-Cummings Hamiltonian* [117]

$$H = \hbar\omega_a\sigma^+\sigma^- + \hbar\omega_c c^\dagger c + \hbar g_0 (\sigma^+ c + \sigma^- c^\dagger) \quad (2.2.2)$$

where $\omega_c/2\pi$ is the resonance frequency of the resonator, $\hbar\omega_a$ the energy difference of the atomic levels, $\sigma^+ = |2\rangle\langle 1|$, $\sigma^- = |1\rangle\langle 2|$ are the atomic state transition operators, c (c^\dagger) the annihilation (creation) operators for a photon in the resonator mode and g_0 the atom-resonator coupling. In the dispersive regime (detunings $\Delta_F = \omega_c - \omega_F = \pm\omega_a/2$ of cavity resonance to atomic transitions of hyperfine state F larger than all other frequencies at hand $\Delta \gg \kappa, \Gamma, g$) this Hamilton leads to three main effects [88, 115]:

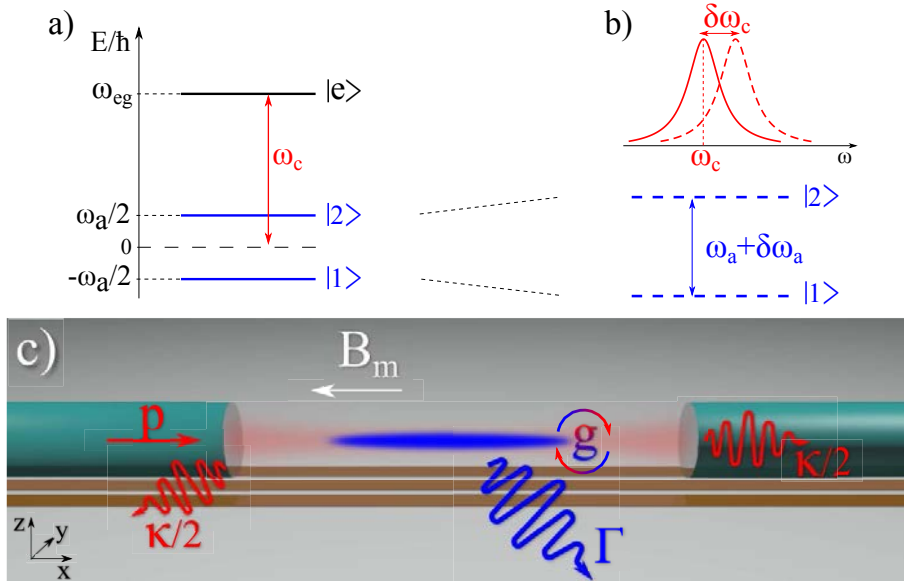


Figure 2.2: Atom-light-interaction. a) Level scheme of a two-level atom with an additional excited state $|e\rangle$ and the cavity resonance frequency tuned in between the two atomic transition frequencies. b) Effect of the atom-resonator coupling described in the text, shifting the resonator frequency and the energy levels of the atom. c) Situation in our experiment, where the resonator mirrors are realized on fiber (green) end surfaces above a three wire waveguide (orange) in the presence of a magnetic bias field B_m . The elongated atom cloud is sketched in blue and the resonator mode in red, pumped with the pump rate p .

¹Legitimate for low intracavity photon number $\langle c^\dagger c \rangle \ll (\lambda/g)^2$

- The light in the resonator leads to an AC-stark shift of both atomic levels $|1\rangle$ and $|2\rangle$, leading to a frequency shift

$$\delta\omega_a = 2 \langle c^\dagger c \rangle \frac{g^2}{\Delta} \quad (2.2.3)$$

of the atomic transition frequency ω_a with $\Delta = |\Delta_F|$.

- The atom interacts dispersively with the resonator mode changing the effective refractive index in the cavity and thereby the optical path length. This leads to a resonator frequency shift per atom

$$\delta\omega_c = \frac{g^2}{\Delta} \quad (2.2.4)$$

- The absorptive interaction of the atom with the light mode leads to scattering of photons into free space with rate

$$\Gamma_{sc} = \langle c^\dagger c \rangle \frac{g^2}{\Delta^2} \Gamma. \quad (2.2.5)$$

These effects already show the principal mechanisms enabling atomic state manipulation with optical resonators and are depicted in Fig. 2.2. The approximations yielding Eq. 2.2.2 are justified in our case and simplify the following treatment, but it should be mentioned that the full Hamiltonian in Eq. 2.2.1 is as well solvable [118].

The Hamiltonian can be further adapted to our case of N atoms for a large detuning $\Delta \gg \Gamma, \kappa$ [119]. If the detuning of the intra cavity light to the atomic transitions $|1\rangle \rightarrow |e\rangle$ ($|2\rangle \rightarrow |e\rangle$) is chosen to be $\Delta_{F=1} = -\omega_a/2$ and $\Delta_{F=2} = \omega_a/2$ (cf. Fig. 2.2 a)), we get

$$H/\hbar = \omega_c c^\dagger c + \Omega c^\dagger c S_z + \omega_a S_z \quad (2.2.6)$$

with $S_z = \sum_{i=1}^N (|2\rangle_i \langle 2|_i - |1\rangle_i \langle 1|_i) / 2$ being the z component of the N -atom pseudo spin introduced in Sec. 2.1 and Ω being the interaction strength $\Omega = 2g_0^2/\Delta$. Here the situation is simplified and all atoms are maximally coupled to the resonator mode. This is not our case of a position dependent coupling, which we will treat in the following.

Effective coupling (following [46, 119]): The need for an effective coupling arises from the fact that each atom couples differently to the resonator mode, depending on its position in the standing wave of the resonator, described by

$$g(\vec{r}) = g_0 \psi(\vec{r}) \quad \text{with } g_0 = \sqrt{\frac{\omega_{eg}}{2\hbar\epsilon_0 V}} \mu_{eg} \quad (2.2.7)$$

where $V = \pi w_0^2 L / 4$ is the mode volume of the resonator mode, with w_0 being the waist radius of the mode and L the resonator length. $\mu_{eg} = \sqrt{\frac{2J+1}{2J'+1}} \cdot 3.58 \cdot 10^{-29} \text{Cm}$ [101] denotes the reduced electric dipole matrix element, ω_{eg} the frequency of the atomic transition and ϵ_0 is the vacuum permittivity. $\psi(\vec{r})$ accounts for the spatial dependence of the light intensity of the mode and we have for the TEM₀₀-mode of a resonator

$$\psi(\vec{r}) = \cos\left(\frac{2\pi}{\lambda_c} x\right) \exp\left(-\frac{\sigma^2}{w_0^2}\right) \quad (2.2.8)$$

with λ_c the wavelength of the light.

A useful parameter to describe the atom-resonator interaction is the cooperativity²

$$C(\vec{r}) = \frac{4g(\vec{r})^2}{\kappa\Gamma} \quad (2.2.9)$$

which denotes the ratio between the photon scattering rate into the cavity mode g and the scattering into freespace with the empty cavity decay rate κ (FWHM) and the atomic decay rate Γ (FWHM). This yields with $\Gamma = \omega_{eg}^3 \mu_{eg} / (3\pi\epsilon_0 \hbar c^3)$, $k = \omega_{eg}/c$ and Eq. 2.2.7

$$C(\vec{r}) = \frac{24\mathcal{F}}{\pi k^2 w_0^2} \exp\left(-2\rho^2/w_0^2\right) \sin^2(kx), \quad (2.2.10)$$

where $\mathcal{F} = \frac{\pi c}{\kappa L}$ is the finesse of the resonator. Expressing the resonator frequency shift due to the atoms (Eq. 2.2.4) with help of the cooperativity we get [46]

$$\delta\omega_c^{(F)} = fC(\vec{r}) \frac{\Gamma\kappa}{4\Delta_F} \quad (2.2.11)$$

where f is the oscillator strength of the transition and Δ_F an effective detuning of the resonator to the nearby atomic transitions. To eliminate the spatial dependence on the coupling we introduce an effective coupling $C_{\text{eff}} = f \langle C^2 \rangle_e / \langle C \rangle_e$. This compares to the cooperativity of an maximally coupled atom $C_0 = 24\mathcal{F}/(\pi k^2 w_0^2)$ as [46]

$$\frac{C_{\text{eff}}}{C_0} = f \frac{\langle \sin^4 kx \rangle_e w_0^2 + 4\sigma_r^2}{\langle \sin^2 kx \rangle_e w_0^2 + 8\sigma_r^2}, \quad (2.2.12)$$

where $\langle O \rangle_e = \iiint dV O \exp\left(\sum_{i=1}^3 x_i^2/\rho_{i,0}^2\right)$ is the average over the atom cloud, with $\rho_{i,0}$ being the cloud radii along the 3 main axes of the trap (see as well Eq. 2.4.2). Furthermore we define the effective atom number $N_0 = N_{\text{at}} \langle C \rangle_e^2 / \langle C^2 \rangle$ in compliance with the statistics of a balanced binomial distribution

$$\Delta N_0^2 = N_0. \quad (2.2.13)$$

Using these quantities the mode shift of Eq. 2.2.11 becomes for N_0 effective atoms

$$\delta\omega_c^{(F)} = N_0 C_{\text{eff}} \frac{\Gamma\kappa}{4\Delta_F} \quad (2.2.14)$$

which we will use in Sec. 2.3 to derive suitable resonator parameters.

Spontaneous emission: The decay rate of the excited state Γ (with the resonator decay rate κ) limits the timescale on which coherent interaction has to take place to allow coherent evolution of the system [120]. Coherent evolution of the system is only possible, if the collective cooperativity of N_0 atoms in a resonator satisfies $N_0 C_{\text{eff}} \gg 1$.

As expressed in Eq. 2.2.5, the finite decay rate Γ leads to the dissipative process of photon scattering into free space, where the scattering events can be classified into two categories:

²We use here the definition predominantly present in the spin-squeezing community. In the previous CQED-publications of our group the cooperativity was defined as $C = g^2/(2\kappa'\gamma)$, where $\gamma = \Gamma/2$ and $\kappa' = \kappa/2$ denote the atomic and cavity HWHM linewidths [75].

- **Rayleigh scattering:** An elastic scattering process, where the atom returns to its initial state after scattering a photon. It leads to decoherence of the system, even though the atomic state is not changed [121].
- **Raman scattering:** An inelastic scattering process, that changes the atom and photon state. This leads to an entanglement of the internal state of atom and photon, resulting in a projection of the atomic internal state, when the photon is measured. Therefore the Raman scattering completely destroys the atomic superposition state of the scattering atom [122].

The projection of single atoms in their eigenstates leads to loss of coherence contrast of the atomic ensemble, expressed by a reduction of the pseudo-spin length $|\langle \mathbf{S} \rangle|$. This leads to a diminished signal-to-noise ratio for the phase measurement and therefore reduces the metrological gain (cf. Eq. 2.1.5). The spontaneous emission thus hinders the use of, in principle favorable, strong probe intensities in the squeezing procedure. To balance this restriction with the gain of the squeezing mechanism, an optimum probe strength can be found, as we will see in Eq. 2.3.8 and in the reported experiments [46, 49, 50] and theory [123, 124].

Having introduced the necessary tools to describe the atom-light interaction inside an optical resonator, we will proceed by using them in the following to present two implementations of spin squeezing.

2.3 Spin-squeezing for TACC 2

Spin-squeezing can be implemented in various different ways, the most common ones being squeezing by quantum-nondemolition (QND) measurement, squeezing by resonator feedback and squeezing by atomic interactions [43, 47, 125]. The latter is of less interest for metrology applications since the atomic interaction can not be switched off easily, which is highly desirable for the Ramsey interrogation following the squeezing. For this reason we will focus the discussion of the subsequent sections on the former two methods using light mediated squeezing. In Tab. 2.1 we give a review of the squeezing achieved so far in various experiments. Note that this table only reviews

Method	Atom number	Resonator	Squeezing $1/\xi$ [dB]	Ref.
Cavity feedback	$3.2 \cdot 10^4$	yes	5.6	[45]
Cavity feedback	$5 \cdot 10^5$	yes	7.0	[50]
QND measurement	$1 \cdot 10^5$	no	3.4	[41]
QND measurement	$5 \cdot 10^4$	yes	3.0	[46]
QND measurement	$8.5 \cdot 10^5$	no	2.0	[126]
QND measurement	$4.8 \cdot 10^5$	yes	10.2	[49]
QND measurement	$5 \cdot 10^5$	yes	20.1	[50]

Table 2.1: Spin-squeezing overview. The table gives an non-exhaustive summary of experiments implementing spin-squeezing in atomic ensembles. The gray shading is only applied to guide the eye (As for all further tables in this document).

the spin-squeezing in atomic ensembles. The standard quantum limit was also overcome in other physical systems. A prominent example is the use of squeezed light in gravitational wave detectors [35].

2.3.1 Cavity feedback squeezing

Cavity feedback squeezing, first proposed in [123] and demonstrated in [45], squeezes the collective spin of the atomic ensemble unconditionally. Its inherent advantage is the independence of the squeezing procedure of a detection of the transmitted photons. In this section we will briefly present the mechanism. Resonator parameters suitable for our implementation are discussed in Sec. 2.4.

As presented in Sec. 2.2 the interaction between the resonator and the atomic ensemble is twofold: The presence of the atoms, acting as a medium of variable index of refraction, shifts the resonance frequency of the resonator (Eq. 2.2.4), while the light in the resonator acts on the energy levels of the atom by an AC-stark shift (Eq. 2.2.3). If we now choose a setting as depicted in Fig. 2.2 a) the atoms in state $|1\rangle$ and $|2\rangle$ shift the cavity resonance in opposite directions, rendering the resonance frequency sensitive to the effective atomic population difference $S_{z,0}$ with

$$\begin{aligned} \delta\omega_c &= \delta\omega_c^{(1)} + \delta\omega_c^{(2)} = C_{\text{eff}}\Gamma\kappa \left(\frac{N_1}{4\Delta_1} + \frac{N_2}{4\Delta_2} \right) \\ &\stackrel{\Delta_2 = -\Delta_1}{=} C_{\text{eff}} \frac{\Gamma\kappa}{4\Delta} (N_2 - N_1) \\ &= C_{\text{eff}} \frac{\Gamma\kappa}{2\Delta} S_{z,0}. \\ &\stackrel{\Delta_2 = \omega_a/2}{=} C_{\text{eff}} \frac{\Gamma\kappa}{\omega_a} S_{z,0}. \end{aligned} \tag{2.3.1}$$

Adding a laser with a fixed frequency $\omega_L = \omega_c + \kappa/2$ as depicted in Fig. 2.3 leads to an intra cavity power I depending on the atomic state. For $S_z < 0$ (case 1 in Fig. 2.3) the intra cavity power is reduced, for $S_z = 0$ (case 2) the intracavity power is unchanged and for $S_z > 0$ (case 3) the resonance frequency is shifted to a higher value leading to a higher intra cavity power. The intracavity power changes the precession speed of each single atom via the Stark shift given in Eq. 2.2.3. The linear dependence of I on S_z for $\delta\omega_c \ll \kappa$ renders the precession speed of each individual spin dependent on the overall spin state through S_z , entangling the transverse components S_y and S_z of the collective spin [124]. This can be understood by decomposing the coherent spin state in the Dicke basis [127]

$$|\theta, \phi\rangle = \sum_{N_1=0}^N \cos(\theta/2)^{N-N_1} \sin(\theta/2)^{N_1} e^{i\phi} \left[\frac{N!}{(N-N_1)!N_1!} \right]^{1/2} |N_1, N\rangle, \tag{2.3.2}$$

where $|N_1, N\rangle$ is the Dicke state with N_1 atoms in state $|1\rangle$ and N being the total atom number. Each Dicke state shifts the cavity resonance depending on N_1 (Eq. 2.3.1) and therefore experiences a different intra cavity intensity and thus a different light shift. For a CSS on the equator, this leads to a linear shearing of the uncertainty region, as depicted in Fig. 2.3 b) and realizes hereby a *one axis twisting Hamiltonian* as in one

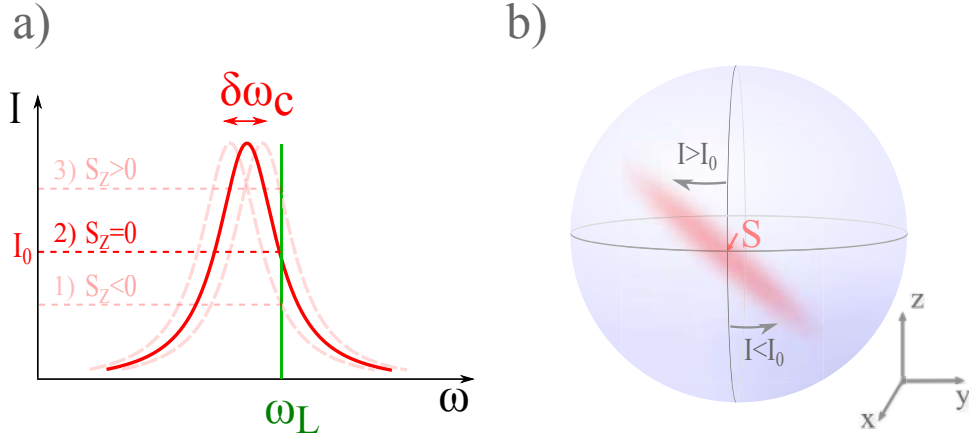


Figure 2.3: Cavity feedback squeezing. a) The cavity resonance is depicted in red for three different values of S_z (1: $S_z < 0$; 2: $S_z = 0$; 3: $S_z > 0$) shifting its frequency with respect to a laser of fixed frequency ω_L shown as a green vertical line. b) the circular uncertainty region of a CSS is sheared on the Bloch sphere, creating a squeezed spin state.

of the first proposals for squeezing in atomic systems [128]. The feedback procedure acts as a replacement of direct spin-spin interactions by light-mediated interactions, allowing squeezing to appear in dilute gases. For the idealized case of low Raman scattering rates $r = \Gamma_{sc}/2$ [129] and neglecting effects from the Bloch sphere curvature [128, 130] we get a reduced variance of S_z depending only on the pseudo spin length S_0 , the effective cooperativity and the Raman scattering rate r [123]

$$\Delta S_{\perp}^2 \approx \frac{1}{4S_0 r C_{\text{eff}}} + \frac{4r}{3}, \quad (2.3.3)$$

with the minimum $\Delta S_{\perp}^2 = 2/\sqrt{3S_0 C_{\text{eff}}}$. It can be seen that the minimum variance reduces with increasing cooperativity. For a given mode waist of the resonator one could be tempted to increase the resonator finesse to reach higher cooperativity for optimum squeezing. However, for our resonator parameters we run quickly in the limit where $\delta\omega_c \ll \kappa$ is no longer satisfied, leading to restrictions to the resonator finesse discussed in Sec. 2.4.

The highest amount of spin-squeezing reported so far [50] was achieved by a combination of cavity feedback squeezing with subsequent squeezing by QND measurement - as well a promising procedure for TACC2. Consequently, we continue by presenting QND-measurement squeezing in the next section.

2.3.2 Squeezing by QND measurement

As we have seen in Sec. 2.2 and summarized in Eq. 2.2.14, the atom-resonator coupling shifts the resonator frequency, as depicted in 2.2 b). In the case of N atoms and a symmetric detuning of the resonator frequency to the two atomic transitions of interest as depicted in 2.2 a) the light shift depends on the z component of the pseudo spin as calculated in Eq. 2.3.1. By measuring the shift of the resonance frequency, we

get information on $S_{z,0}$. This can be accomplished by measuring the photon number transmitted through the cavity p_t given by a Lorentzian function

$$\frac{p_t}{p_i} = \mathcal{L} = \frac{1}{1 + (2\delta/\kappa)^2} \quad (2.3.4)$$

where p_i is the incoming photon number and δ the detuning of the interrogation laser to the cavity resonance $\delta = (\omega_L - \omega_c)/2\pi$. This leads for a detuning $\delta = \kappa/2$ to a measurement variance of $S_{z,0}$ [129]

$$\langle \Delta S_{z,0}^2 \rangle = \frac{\langle \Delta \delta \omega_c^2 \rangle}{\kappa^2} \left(\frac{\kappa S_{z,0}}{\delta \omega_c} \right)^2 = \frac{1}{4p_t} \frac{1}{C_{\text{eff}}^2} \left(\frac{2\Delta}{\Gamma} \right)^2 \quad (2.3.5)$$

decreasing with the photon number p_t . Scattering of photons into free space (Eq. 2.2.5) happens at the rate [129]

$$2r = p_t \frac{\Gamma_{sc}}{\kappa \langle c^\dagger c \rangle / 2} = 2p_t C_{\text{eff}} \left(\frac{\Gamma}{2\Delta} \right) \quad (2.3.6)$$

leading to

$$\langle \Delta S_{z,0}^2 \rangle = \frac{1}{4C_{\text{eff}} r} \quad (2.3.7)$$

only depending on the photon scattering probability and the effective cavity cooperativity. Furthermore, scattering into free space shortens the spin vector, which reduces signal contrast, nicely described in [129]. The interplay of reduced variance and contrast can again be expressed with the squeezing parameter given in Eq. 2.1.5 and leads for large collective cooperativity $N_0 C_{\text{eff}} \gg 1$ to

$$\xi \approx \frac{1}{N_0 r C_{\text{eff}}} + \frac{4r}{3} \quad (2.3.8)$$

which is the same scaling as for squeezing with cavity feedback [123]. We neglected again effects of the Bloch phase curvature. The minimum can be found for $2r = \sqrt{3/2S_0 C_{\text{eff}}}$ and gives

$$\xi_{\text{min}} \approx \sqrt{\frac{16}{3N_0 C_{\text{eff}}}} \quad (2.3.9)$$

only depending on effective atom number and cooperativity and shown in Fig. 2.4. In a more elaborate method, the cavity detuning can be measured via the phase shift [49, 50] leading to a higher optimum enhancement of the measurement of [50, 131]

$$\chi^2 = 1/\xi \approx \frac{\sqrt{3/2\epsilon N_0 C_{\text{eff}}}}{1 + N_0 C_{\text{eff}} (\Gamma/\omega_a)^2} \quad (2.3.10)$$

with ϵ being the overall detection efficiency of the probe photons. The two readout methods are compared in Fig. 2.4, where it can be seen that both benefit from a high cooperativity. Note that both measurement methods rely on the fact that the cavity shift $\delta\omega_c$ does not surpass the linear range of the transmission, so that

$$\delta\omega_c \ll \kappa \quad (2.3.11)$$

should be ensured.

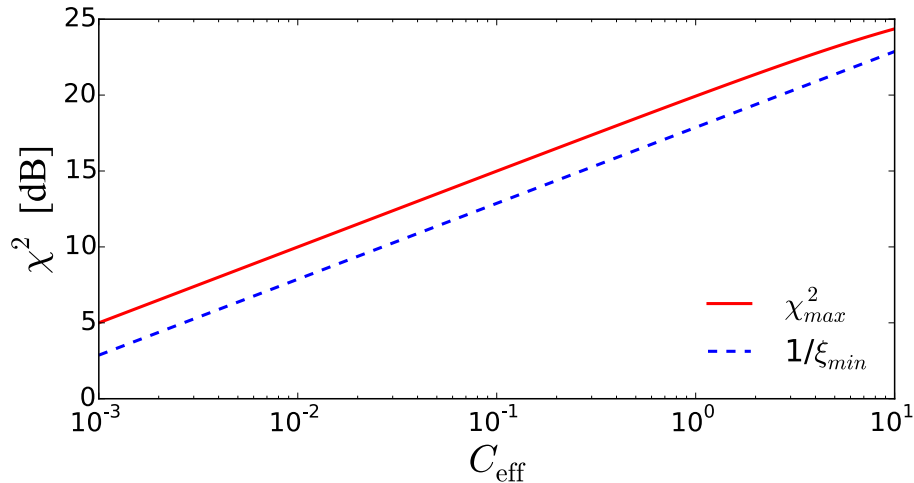


Figure 2.4: Optimal enhancement by QND-measurement squeezing. We chose $N = N_0 = 2 \cdot 10^4$, a typical value for the TACC experiment. The derivation of ξ_{min} neglects all photon loss in the optical path and a perfect detector, but accounts for the photon collection on only one side of the cavity. To account for this we chose $\epsilon = 0.5$ for calculating χ^2_{max} . Both values overestimate the enhancement accessible in the experiment by assuming 100% efficiency of the photon detection at the resonator output, which we will address later. The values for ^{87}Rb are $\Gamma = 2\pi \cdot 6.07 \text{ MHz}$ and $\omega_a = 2\pi \cdot 6.834 \text{ GHz}$ [101].

2.4 Requirements for the new experiment

With the enhancement factor χ^2 we now have a useful tool at hand to find optimum parameters for our resonator, which have to meet several requirements:

Resonator length: Our approach is to realize the optical resonator with fiber Fabry-Pérot resonators for optimal compactness and mechanical stability. This leads to a new challenge previous cQED experiments did not encounter with centimeter size optical resonators [46, 49, 50]: The resonator length must be long enough to accommodate the elongated atom cloud.

The finite size of the mirrors on fiber tips sets a limit to the achievable length of this resonator type, which will be discussed in detail in Sec. 4.1.4. We achieved best clock performance in the previous TACC experiment for a dilute cloud in a magnetic trap with the parameters [62]: $(\omega_x, \omega_y, \omega_z) = 2\pi \times (2.7, 92, 74) \text{ Hz}$ with $N = 4 \cdot 10^4$ non-condensed atoms at temperature $T \approx 80 \text{ nK}$. This leads to an atomic density distribution of Gaussian shape given by

$$n(\vec{x}) = n_0 \exp\left(-\sum_{i=1}^3 \frac{x_i^2}{\rho_i^2}\right) \quad (2.4.1)$$

with the cloud radius along the i -th eigenaxis of the trap $\rho_i = \sqrt{\frac{2k_B T}{m} \frac{1}{\omega_i}}$ [104]. For the trap frequencies and temperature given above we get $\rho_{x,y,z} = (231, 6.8, 8.4) \mu\text{m}$.

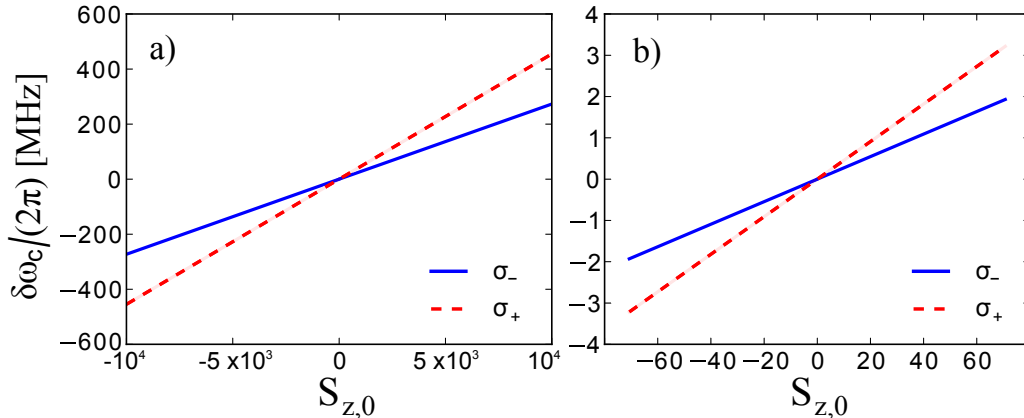


Figure 2.5: a) Shows the cavity shift given by Eq. A.1.1 for an effective atom number $N_0 = 2 \cdot 10^4$, $w_0 = 13.4 \mu\text{m}$ and $L=1.2 \text{ mm}$ for the two transitions possible with the resonator mode. b) shows a zoom to the central part, spanning the standard deviation of the shot noise ($S_{z,0,max} = -S_{z,0,min} = \sqrt{\Delta S_{z,0}^2} = \sqrt{S_0/2}$). The reduction of 3/4 from the mode overlap is taken into account (see Eq. 2.4.2).

To maximize the coupling, the cigar shaped atom cloud has to be aligned with the resonator mode. The cloud length of $2\rho_x = 462 \mu\text{m}$ surpasses the typical lengths of FFP resonators in cQED experiments so far (several tens of micrometers [72, 132] or more recently in the range of $170 \mu\text{m}$ [78]).

To estimate roughly the atom loss due to collisions with the nearby resonator mirrors, we calculate the overlap of the atom cloud with the mirrors in Fig. 2.6, giving the ratio of atoms lost to the total atom number N_{lost}/N . At a cavity lengths $L > 1.1 \text{ mm}$ $N_{\text{lost}} < 10^{-3}N$, which we take as a threshold. Note that this mechanism removes first the high energy atoms from the ensemble, which can be used in a controlled way to evaporatively cool the cloud [133–135]. With the given minimum length, the only way to minimize the mode radius on the fiber mirror is to optimize the mirror ROC R . A minimum can be found for a confocal cavity with $R = L$. A disadvantage of the confocal cavity is the higher sensitivity to imperfections in the mirror ROC as discussed in Sec. 4 and the degeneracy of the transversal resonator modes, which can lead to increased coupling to transversal resonator modes of higher order. This leads to our choice of a near-confocal design with $L = 1.2 \text{ mm}$ and $R = 1.5 \text{ mm}$, giving a waist of $w_0 = 13.5 \mu\text{m}$ and a mode radius on the mirrors of $w_m = 17.4 \mu\text{m}$ for the wavelength of $\lambda = 780 \text{ nm}$ used.

Having fixed the resonator geometry, we can directly calculate the resonator shift depending on $S_{z,0}$ for a given effective atom number, shown in Fig. 2.5.

Atom cloud - mode overlap: Only placing an atomic ensemble between resonator mirrors does not automatically generate a useful cQED experiment. As we have seen in Eq. 2.2.12 the cooperativity of the system depends strongly on the atom cloud - resonator-mode overlap, which we will examine in this section. The effective coopera-

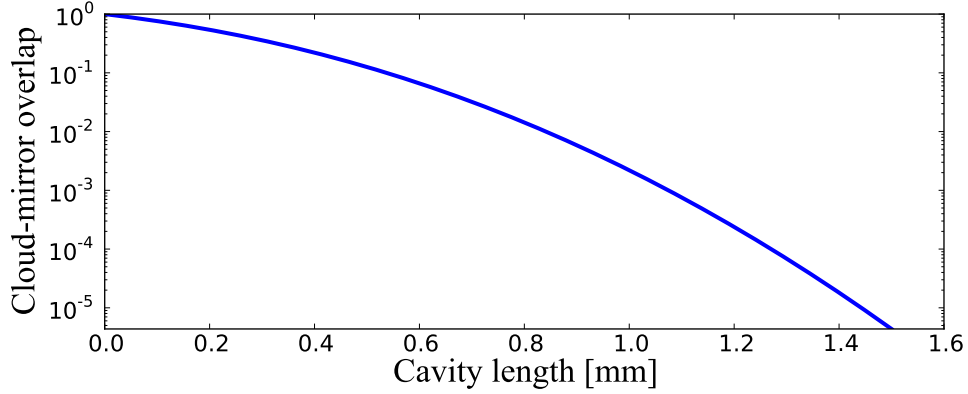


Figure 2.6: Cloud-mirror overlap. The proportion of atoms colliding with the mirrors (here both mirrors in a symmetrical configuration are taken into account) is plotted over the cavity length for a cloud radius $r_{x,0} = 231 \mu\text{m}$ and a cloud temperature $T = 80 \text{ nK}$.

tivity is given by

$$\begin{aligned}
C_{\text{eff}} &= f \frac{\langle C^2 \rangle_e}{\langle C \rangle_e} \\
&= f \frac{\iiint dV C^2 \exp\left(-\sum_{i=1}^3 x_i^2 / \rho_{i,0}^2\right)}{\iiint dV C \exp\left(-\sum_{i=1}^3 x_i^2 / \rho_{i,0}^2\right)} \\
&= f \frac{\int_0^{2\pi} d\phi \int_0^\infty r dr \int_{-\infty}^\infty dx \exp(-4r^2/w_0^2) \sin^4(kx) \exp(r^2/\rho_r^2) \exp(x^2/\rho_x^2)}{\int_0^{2\pi} d\phi \int_0^\infty r dr \int_{-\infty}^\infty dx \exp(-2r^2/w_0^2) \sin^2(kx) \exp(r^2/\rho_r^2) \exp(x^2/\rho_x^2)} C_0 \\
&= f \frac{3 w_0^2 + 4 \rho_r^2}{4 w_0^2 + 8 \rho_r^2} C_0
\end{aligned} \tag{2.4.2}$$

with $C_0 = 24\mathcal{F}/(\pi k^2 w^2)$. Here we neglect the variation of the mode field radius w with x , which plays a minor role since it varies less than 10% over the extend of the atom cloud ($w(x = \rho_x = 231 \mu\text{m}) = 13.8 \mu\text{m}$). It can be seen that the transversal extension of the cloud, parametrized by the radial cloud radius ρ_r , reduces the effective cooperativity. For typical values of the atomic cloud in the previous TACC experiment $\rho_r = 6.9 \mu\text{m}$ and the waist radius $w_0 = 13.5 \mu\text{m}$ as motivated in the previous section, we get $\frac{w_0^2 + 4\rho_r^2}{w_0^2 + 8\rho_r^2} = 0.66$. Doubling the transversal trap frequency, readily achievable with our atom chip, yields already 0.83 with $\rho_r = 3.5 \mu\text{m}$. This makes the radial cloud radius an interesting parameter for controlling the effective cooperativity in the experiment.

Due to the integration over a range much larger than the period of the standing wave we get the same pre-factor $\frac{3}{4}$ as for the situation in [46], where the atoms are trapped in a 1-d lattice with non-perfect overlap with the standing wave of the probe light. Apart from the same pre-factor for the effective coupling, the two different trapping methods lead to very different situations, as discussed in the next paragraph.

Elongated magnetic trap vs. 1-d optical lattice: A drawback of trapping the atoms in far-off resonant optical traps (FORTs [136]) as in [46] is that a large part of the atoms is not or only weakly squeezed, depending on their fixed position in the incommensurate standing wave of the probe inducing the spin-squeezing. The presence of un-squeezed atoms limits the readout to resonator based methods, where the read-out light couples equally to the ensemble as the squeezing light. Consequently the detection is weighted as the squeezing, thus un-squeezed atoms are not detected. This has the disadvantage that the atoms cannot be released from the dipole trap, which prohibits the use of time of flight detection methods and various interesting interferometer experiments. Since our clock relies on a low atomic density during the Ramsey time, we are obliged to release the atoms for the Ramsey time in the magnetic trap, rendering the partly squeezed approach of [46] insufficient for our application.

An approach to circumvent the partial squeezing is to trap the atoms in such a way that all atoms couple identically to the squeezing light, as realized by a commensurate double- λ lattice in [50], which will be also to realizable with our cavities (cf. Sec. 4.2.6). Since the trapping in the 1D lattice and the following release of the atoms could lead to heating, we plan to trap instead the atoms in a shallow magnetic trap during the interaction with the resonator mode. This leads to an averaged coupling, which we assume to be homogeneous for all atoms, if the barrier height created by the squeezing-light lattice is well below the average cloud temperature. This sets a strict constraint to the maximum intra-cavity power, since our ensembles have typical temperatures of around 100 nK. Furthermore, the interaction time has to be long enough for the averaging to take place, setting a minimum duration of the squeezing pulse. In absence of a trapping lattice no reference for the resonator length is available. We therefore plan to stabilize the resonator length with the help of an auxiliary resonator in close vicinity, as in [72, 135]. This has the advantage, that we avoid the considerable light shifts of the 1560 nm light [137].

Mirror loss: The enhancement factor Eq. 2.3.10 depends on the ability to detect the photons used in the QND measurement. This is parametrized by the detection efficiency ϵ , directly proportional to the light leaving the resonator expressed by the resonant transmission T_c . The resonant transmission and the finesse of an optical resonator depend on the transmission of the individual mirrors \mathcal{T} and the loss in the mirror \mathcal{L} and are given in Eq. 4.1.5 and Eq. 4.1.9. One possibility to increase the cooperativity is the enhancement of the finesse by decreasing \mathcal{T} . By doing so, the cavity transmission T_c will decrease in a realistic scenario with $\mathcal{L} > 0$, which leads to a decrease of the detection efficiency ϵ . To weigh the influence of finesse and transmission on the enhancement factor, we show in Fig. 2.7 χ^2 in dependence of the mirror transmission \mathcal{T} . The interplay of the finesse and the detection efficiency lead to a maximum achievable squeezing around $\mathcal{T} \approx 100$ ppm depending on the atom number. Additional photon loss along the optical path from the cavity to the detector, reduces ϵ further and limits the maximum enhancement. This means for the case of a FFP resonator, that maximizing the coupling of the resonator mode to the fiber mode is of crucial importance for the accessible squeezing.

To account for the large uncertainties related to a new experiment, ranging from

the final atom number achievable to the specifications of the long FFP resonators not realized before, we opted for the safe way and decided to install two resonators with largely different finesse (low finesse: $\mathcal{F}_{LF} = 3,000$ and high finesse $\mathcal{F}_{HF} = 50,000$) and transmissions, indicated as red dashed lines in Fig. 2.7. Note that only the low finesse resonator fulfills $\delta\omega_c \ll \kappa$ and respects the linear regime³. For the high finesse resonator we envisage a different scheme, where the probe laser is scanned across the (shifted) cavity resonance and the peak position is detected with single photon counting modules⁴ of high quantum efficiency $> 50\%$, as in the atom number detection in [72].

2.5 Conclusion

We showed that an upgrade of the existing TACC experiment with an optical resonator opens up several possibilities to create spin-squeezed states. This allows to study spin-squeezing for the first time in a metrological environment, with the goal to show quantum enhanced metrology on a metrologically relevant stability level.

It was emphasized that the atom cloud length in an optimized clock trap demands for FFP resonator lengths exceeding the state of the art at the beginning of the project by nearly one order of magnitude. For this reason we developed a novel generation of FFP resonators that accounts for the requirements compiled in this chapter, namely: long resonator length, good optical coupling to the resonator and the possibility to create double- λ lattices. The resonators will be presented in chapter 4, after we introduce their fabrication process in the following chapter.

³ $\kappa_{LF} = 2\pi \cdot 41.5$ MHz for $L = 1.2$ mm and $\mathcal{F}_{LF} = 3,000$, more than $10\times$ the maximal shift expected for $N_0 = 2 \cdot 10^4$ (see Fig.2.5)

⁴Excelitas SPCM-AQRH-14

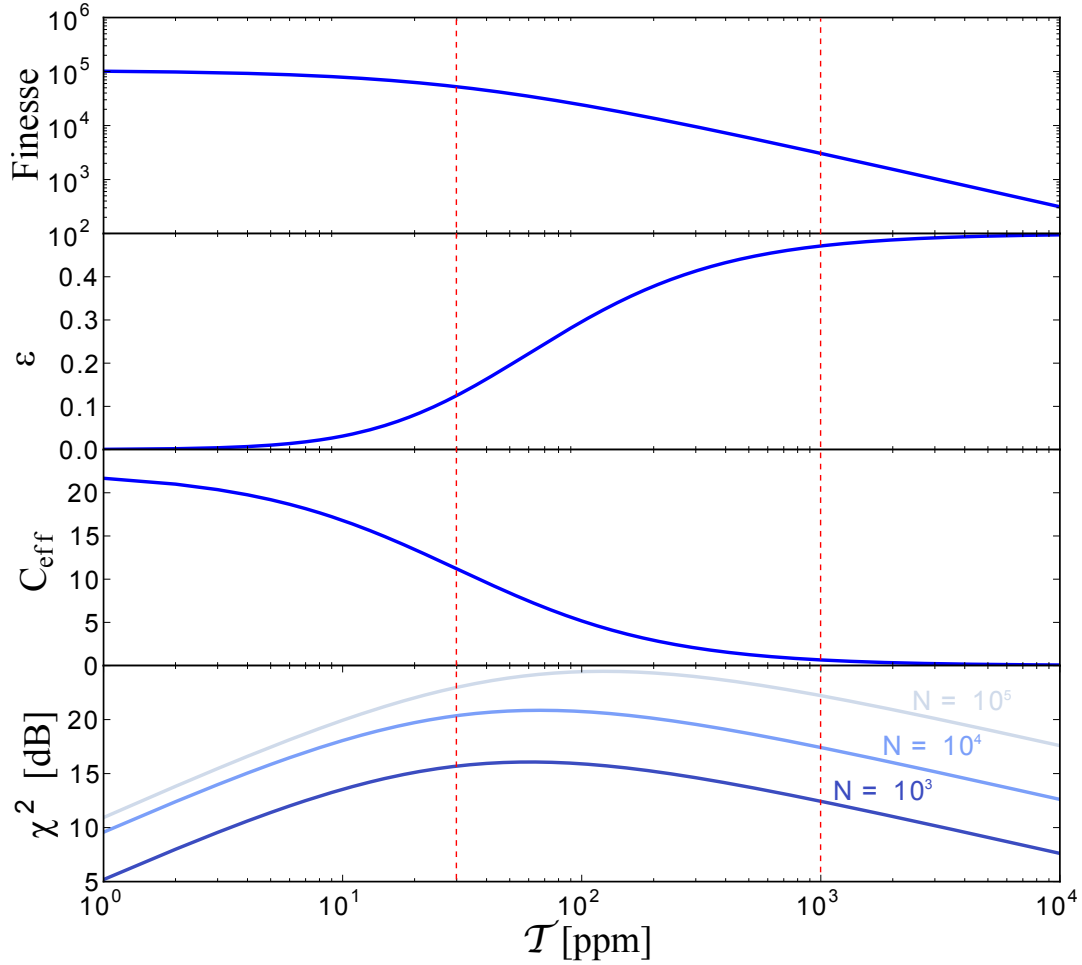


Figure 2.7: Influence of the mirror transmission \mathcal{T} for a mirror loss of $\mathcal{L} = 30$ ppm, a typical value for double-wavelength coatings. ϵ converges to 0.5 assuming a read out on only one side of the resonator and no additional photon loss. The resonator mode waist used is $w_0 = 13.5 \mu\text{m}$, the atom cloud diameter $\sigma = 6.9 \mu\text{m}$. The red dashed lines indicate the values chosen for our experiment (see Sec. 4.2.8).

CO₂ Machining with Multiple Pulses

Fiber Fabry-Pérot (FFP) microresonators with CO₂ laser-machined concave mirrors, developed in our group [72, 73], are being used in a fast-growing number of applications, ranging from cavity quantum electrodynamics with atomic, molecular and solid-state emitters [72, 78, 138–142] and optomechanical systems [143] to Raman spectrometers for atmospheric gases [144] and new scanning microscopy techniques [77].

As mentioned in the introduction, FFP cavities are also the technology of choice for realizing spin squeezing and nondestructive detection in TACC2. However, the experiments discussed in chapter 2 require an increased mirror distance to accommodate elongated atomic ensembles in the resonator. This is our main motivation to generalize our method to produce FFP mirrors, using multiple CO₂ pulses, presented in this chapter.

Beyond TACC2, increasing the optical length L to the millimeter range while maintaining the FFP advantages (built-in fiber coupling, small mode waist, high finesse and high passive stability) fills a gap in micro-optical technology and opens up new applications.

Development towards this goal has been initiated by the ion trap community [145, 146], where FFP cavities are now arguably the most promising candidate for realizing a high-fidelity light-matter quantum interface. In this application, increased cavity length will mitigate or even remove the perturbation of the trapping potential induced by the dielectric mirrors [147].

Furthermore, because of the reduced free spectral range, larger L will also make it possible to use laser-machined concave mirrors in telecom applications of FFP cavities, where planar mirrors [148] are currently being used in commercial solutions¹.

The CO₂ machining method, presented in the following, allows for the fabrication of more complex structures, surpassing the limitations of simple concave depressions opening new applications for CO₂ machined fused silica.

The results presented in this chapter and chapter 4 are summarized in [80].

¹see for example www.micronoptics.com

3.1 CO₂ machining of fused silica

The strong absorption of fused silica in the far infrared makes CO₂ laser light with $\lambda_{CO_2} = 10.6 \mu\text{m}$ the perfect tool for its machining [149]. The absorption of the light melts a fused silica layer of several microns to several tens of microns, depending on the laser parameters and the target geometry [150]. If sufficient energy is provided, the fused silica evaporates, creating a depression and surface tension leads to formation of a smooth surface of the molten layer. The smoothing of the surface by surface tension is used for CO₂ laser polishing [150–152] and leads to a small residual surface roughness of $\sigma_r \sim 0.2 \text{ nm}$, necessary for high finesse resonators (cf. Sec. 4.1.4) [153]. The surface tension of the molten fused silica allows the fabrication of microlenses [154] and toroid microcavities [155], where the exceptional small surface roughness led to ultra high quality factors.

Besides CO₂ machining, other methods exist that allow the creation of concave structures in the micrometer regime. Examples are focused ion beam (FIB) milling [156, 157] or femtosecond laser ablation [158]. Both methods do not reach the low surface roughness of the CO₂ machining method, but the FIB method approaches it with $\sigma_r = 0.3 \text{ nm}$ for small structures of $\varnothing = 10 \mu\text{m}$ [159].

On the other hand, superpolishing of fused silica can yield surface roughness below 0.1 nm, a factor of 2 better than the CO₂ machining process [160]. Unfortunately, the mechanical polishing limits this method to macroscopic substrates and the inability to produce the radii of curvatures $R = 0.01 \text{ mm} - 2 \text{ mm}$, interesting for our applications.

CO₂ machining represents therefore a versatile tool that reaches high surface quality on microscopic structures, a regime, to our best knowledge, not accessible with any other technology. This enabled the production of concave, low-roughness features in fused silica [153], used for the construction of micro resonators of finesse up to $\mathcal{F} = 190.000$ [161].

Single or multiple CO₂ laser pulses to the center of the fiber facet were used so far for the fabrication of micro mirrors. We summarize in the following the limitations of this “single shot” method and then present the “dot milling” method, that increases further the application range of CO₂ machining.

3.2 Limiting factors in single-pulse machining

Two factors have limited L in earlier FFP implementations. First, a disadvantage arises from the insufficient mode coupling for increasing cavity length. This is caused by the given mode diameter in the fibers and will be discussed later in Sec. 4.1.6.

The much more severe limitation is the non-spherical profile generated by a single CO₂ laser pulse: The profile of the depression generated by a single CO₂ laser pulse is Gaussian rather than spherical [73], so that the effective mirror diameter is significantly smaller than the diameter of the depression. Additionally, due to boundary effects in heat transport during the laser machining, it is difficult to machine depressions that extend over the full fiber surface [153], even with a very large CO₂ beam diameter [161]. The small effective mirror size causes clipping loss when the transverse mode size on the mirror becomes comparable to the effective mirror diameter (see Fig. 4.3). This typically happens long before L reaches to the stability limit [73, 145, 146, 162].

Finally, it is known that the milling profile of a given laser pulse is affected by the doping profile of the fiber [146]. The effect is most pronounced for single-mode (SM) fibers, where it leads to a circular ridge at the core-cladding interface, as shown in Fig. 3.1, but it is present also for multi-mode (MM) fiber machining, see Fig. 3.13.

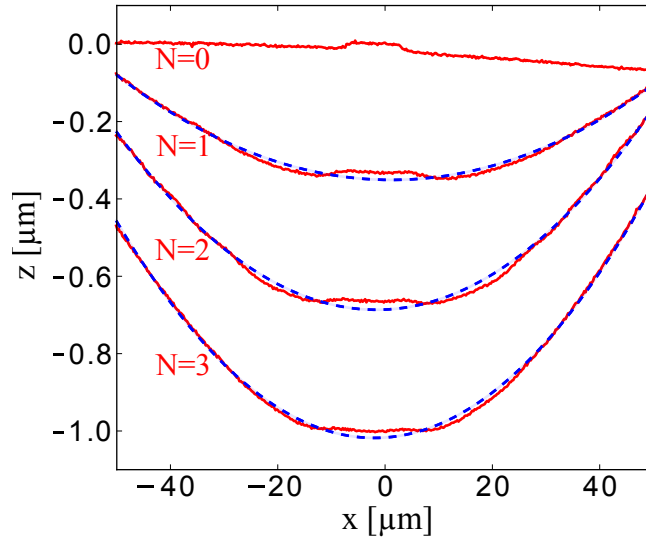


Figure 3.1: Ridge at the core-cladding interface. The red line shows a cut through a 3D-profile of the central part of a depression after $N=0,1,2, 3$ CO_2 -pulses to the center of the fiber. The lines are vertically shifted by $1/3 \mu\text{m}$ for clarity. The blue dashed line shows a parabolic fit to the cut over the full $100 \mu\text{m}$, giving the ROCs $R_{N=1} = 4838 \mu\text{m}$, $R_{N=2} = 2551 \mu\text{m}$, $R_{N=3} = 2060 \mu\text{m}$. The power on the fiber is $P = 2300 \text{ mW}$ and the pulse lengths are $T_{N=1} = 60 \text{ ms}$, $T_{N=2} = 55 \text{ ms}$, $T_{N=3} = 65 \text{ ms}$. The core can be seen clearly in the cleaved surface ($N = 0$) and remains visible after the machining. Similar results were found in [146] with AFM measurements.

Concerning the mirror profile, a natural approach is to use multiple CO_2 laser pulses on the same fiber, instead of a single pulse. A first application of this approach was demonstrated recently in [146], where the fiber was rotated about its axis between pulses. The main purpose of this rotation was to reduce mirror ellipticity, but the technique also resulted in larger mirror profiles, enabling values of L up to $400 \mu\text{m}$ before the finesse dropped by 50%, for cavities with one SM fiber. However, the mirror profile still remained Gaussian. To address the mirror shape limitation, we apply a newly developed CO_2 dot milling technique, where a large number of weak individual pulses sequentially address an optimized pattern of target points on the substrate surface. This method gives access to a wide range of shapes with extremely precise control over the surface profile, while maintaining the excellent surface roughness that is characteristic of CO_2 machining. In Sec. 3.4.3 we show that it enables fabrication of large, spherical structures, as required for long cavities, with a shape deviation of less than $\lambda/20$. Beforehand, we present the setup that enables the micro machining.

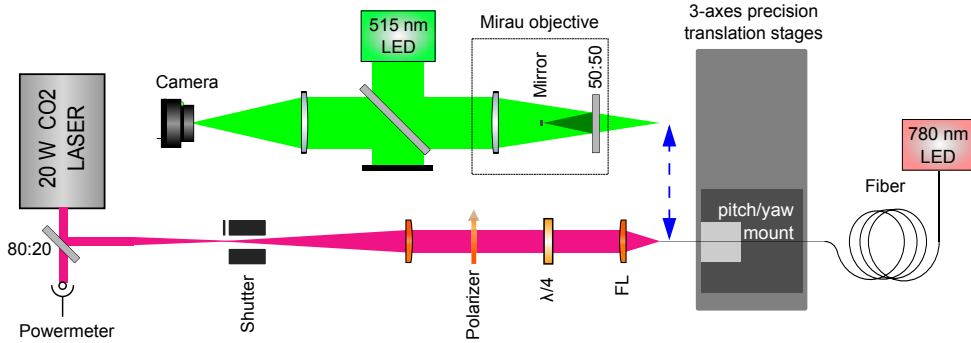


Figure 3.2: CO₂ dot milling setup: Precision translation stages are used to control the CO₂ beam position on the fiber and to translate the fiber to the optical profiler position for surface characterization. Light coupled into the fiber core allows a precise centering of the mirror profile. The CO₂ focusing lens (FL) is a $f = 25$ mm asphere illuminated with a beam diameter of 7 mm.

3.3 Dot milling setup

During the work for this thesis, we build a new CO₂ machining setup that is designed to enable surface machining with multiple, precisely positioned CO₂ pulses (“shots”) and analysis of the results on the fly². It has three main components: the CO₂ laser with external pulsing and focusing optics, a high-precision, three-axis translation stage, and an in-situ optical profilometer (Fig. 3.2). The complete setup is enclosed in a temperature-stabilized laminar flow box. A home-made motorized tilt stage³ (pitch and yaw) was mounted on the translation stages to align the fiber cleave surface perpendicular to the CO₂ beam axis before machining. The CO₂ part is similar to our earlier setups [73, 153]. Pulses are generated using a combination of pump switching and mechanical shutters [73]; pulse-to-pulse power fluctuations are on the order of 0.5%. The CO₂ focusing lens is a $f = 25$ mm asphere illuminated with a beam diameter of 7 mm. In contrast to [73, 153], however, the CO₂ and profilometry beam paths are kept separated, with the translation stages ensuring reproducible travel between the two locations. The stages⁴ have optical encoders for repeatable absolute positioning. The step size of the transverse stages is 50 nm. The optical profilometer is based on a Mirau objective⁵ with a nominal transverse resolution of $0.8 \mu\text{m}$. To achieve best height (z) resolution, we use phase-shifting profilometry [164]. The measured noise for a reference surface is 1.4 nm rms for a single profile [163], which can be further reduced to the sub-nm level by averaging several profiles (see Sec. 3.3.1). To localize the fiber core of SM fibers, weak light is coupled into the fiber, so that the core appears as a bright spot on the microscope image. The whole system is software-controlled [163] and allows for automated centering of SM fibers.

²Special thanks to Sebastien Garcia and Klemens Schüppert (Universität Innsbruck) who build major parts of the setup and did a great job in programming the control software [163].

³Consisting of a mirror mount and two Z825B stepper motors from Thorlabs.

⁴Newport GTS150 and GTS30V, Attocube ECS5050NUM

⁵Nikon CF IC EPI Plan DI 20 \times

In the following, we will describe in more detail the three major improvements making the creation and analysis of large spherical profiles possible.

3.3.1 In situ profilometry

To characterize the produced structures we use a Mirau-objective, which takes an interferogram of the structure of interest with the Mirau-mirror as the reference plane (see Fig. 3.2). Typical interferograms are shown in Fig. 3.10 or Fig 3.17 a). From a single interferogram it is impossible to deduce the height information of the profile without further assumptions, even the sign of the surface curvature is not accessible.

For this reason, we use a phase-shifting algorithm to gain the full 3D information of the structures [164], which allows to extract the profile height z at each point. Six interferograms are taken in succession with a phase offset of $\pi/2$, which translates for our profilometer light of $\lambda_P = 512 \text{ nm}$ to $\lambda_P/8 \approx 64 \text{ nm}$. This can be realized with the high precision stage in use along the z -direction⁶, which has a nominal resolution of 1 nm. The tangent of the phase $\phi(z(x, y)) = 2\pi \frac{z(x, y)}{\lambda_P}$, and with that the height information $z(x, y)$, is then given by the intensities of the six interferograms $I_{1-6}(x, y)$ as

$$\tan(\phi(x, y)) = -\frac{3I_2(x, y) - 4I_4(x, y) + I_6(x, y)}{I_1(x, y) - 4I_3(x, y) + 3I_5(x, y)}. \quad (3.3.1)$$

The hereby created 3D-profiles, depicted in Fig. 3.17 b) are used throughout this thesis to deduce the critical structure parameters as the radius of curvature or the ellipticity of the structure. Furthermore, we can use the 3D-profiles to perform a full simulation of the resonator consisting of the reconstructed mirror surfaces, as will be discussed in Sec. 4.2.3. For this purpose, the noise of the profile height has to be reduced, which depends strongly on the distance of the surface to the Mirau-objective. First, the finite depth of field of the objective reduces the contrast on a scale of a few micrometers, see Fig. 3.3. Second, the initial phase of the first image leads to an erroneous residual in the 3D-reconstruction, see Fig. 3.4. To overcome the depth of field limitation we perform a scan of the z position before each profilometry and use the data as in Fig. 3.3 to determine the optimum distance giving the highest contrast. The contrast then only depends on the reflectivity of the scanned surface at λ_P , which can differ strongly, depending on the surface material. The depth of field limits the maximum scannable height of a structure.

To get a full profile as in Fig. 3.17 b) spanning a depth of $\Delta z \approx 3.5 \mu\text{m}$, the optimum profilometer distance is only assured for the positions with a medium height $z \approx \Delta z/2$, leading to higher noise for the positions of extreme depth or height, furthest from the optimum. The dependence of the profile noise to the profilometer distance can be seen in Fig. 3.5.

To characterize the noise of a profile, we use the RMS surface roughness

$$\sigma = \sqrt{\frac{1}{A} \iint_A (z - \bar{z})^2 dA} \quad (3.3.2)$$

⁶Attocube ECS5050NUM

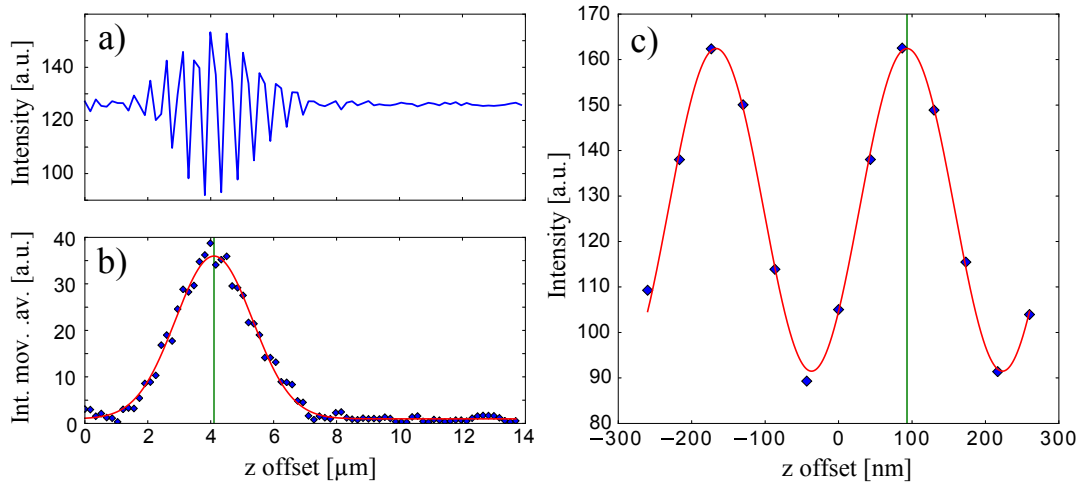


Figure 3.3: Contrast of the profilometry. a) shows the intensity of the central pixel, while the fiber facet is moved along z , with step size $\Delta z = \lambda_P/3$. b) A moving average is used to determine the maximum contrast (green vertical line) with a Gaussian fit (red line). It showed that this is much more robust than a sinusoidal fit with a Gaussian envelope. c) We use then a sinusoidal fit (red line) to the central region, to always start the profilometry at a defined phase (green vertical line).

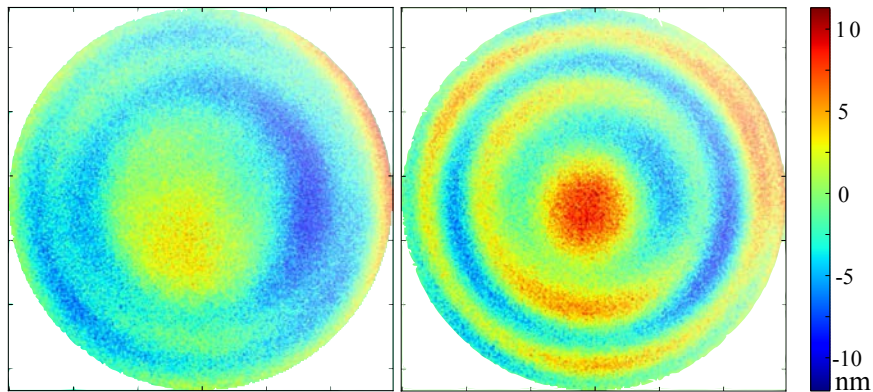


Figure 3.4: Residuals depending on profilometry position. The same surface was scanned twice with a distance offset of $\lambda_P/8$ and fitted with a 2D-paraboloid, the edge length is $60 \mu\text{m}$. The residuals shown have a sinusoidal modulation, dependent on the initial profilometry position. Averaging two profiles with such a distance offset reduces strongly the spurious effects of the reconstruction algorithm.

with \bar{z} the mean profile height and z the local profile height⁷. This is justified only if the expected roughness of the profile is well below the noise, which is the case for CO₂-machined fused silica with a surface roughness of $\sigma_{RMS} \approx 0.22$ nm [153].

A straight forward way to reduce the profile noise is to average N profiles of roughness σ_1 . As presented in Fig. 3.4, two consecutive profiles are taken with a profilometer distance offset of $\lambda_P/8$ to average out errors from the reconstruction algorithm. The averaging over N profiles leads to the averaged roughness of

$$\sigma_{\text{profilo}} = \sigma_1 / \sqrt{N}. \quad (3.3.3)$$

To take into account the real roughness of the substrate, we add the roughness due to noise and the real roughness of the profile σ_{RMS} yielding the effective profile roughness

$$\sigma_r = \sqrt{\sigma_{RMS}^2 + (\sigma_1 / \sqrt{N})^2}. \quad (3.3.4)$$

This equation is fitted to the roughness extracted of averaged profiles consisting of different numbers N of single profiles, shown in Fig. 3.5. It can be seen that the

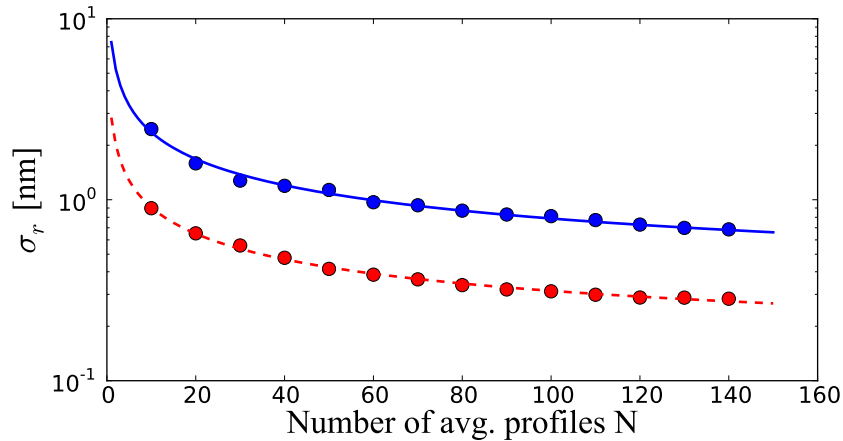


Figure 3.5: Noise reduction due to averaging. The same fiber is scanned twice, once at the optimum profilometry distance (red circles) and with an offset of $-1.9 \mu\text{m}$ (blue circles). The surface roughness is calculated as the RMS of the residual after fitting a polynomial of order 25 over a central cut of length $100 \mu\text{m}$. Eq. 3.3.4 is fitted to the data giving $\sigma_{RMS,opt} = 0.13$ nm (red dashed line), $\sigma_{RMS,off} = 0.26$ nm (blue solid line).

expected $1/\sqrt{N}$ reduction of the roughness takes place, saturating against the value of σ_{RMS} . Unfortunately the extracted value σ_{RMS} cannot be interpreted as the real surface roughness due to several reasons: First, the transversal resolution of the microscope of $\sim 0.8 \mu\text{m}$ is of the same size as the wavelengths later used in the resonator experiments $\lambda \approx 0.7 - 1.6 \mu\text{m}$. This is why it cannot resolve all details important for scattering processes. Furthermore, the data acquisition for $N=100$ profiles takes

⁷Both values have to be taken exclusive of the macroscopic shape to make a statement on the microscopic surface roughness and not the overall topography.

~30 minutes⁸. This leads to thermal drifts in the order of a few microns, shifting the transversal surface position and also averaging out the real irregularities on the surface. We reduce this effect drastically by determining the profile position with a parabolic fit every 10 profiles and use the extracted center position to recenter the surface. The precision of the fit-center determination diminishes with shallower profiles, but the standard deviation of the center position of the consecutive fits is below 0.1 μm for our typical structures with a ROC of $R \approx 1500 \mu\text{m}$.

The profilometer, especially boosted by multi-profilometry, remains nonetheless an instrument of remarkable precision, well below a nanometer for the $z(x, y)$ -information and around one micrometer in the transversal axes. For the evaluation of the structures and for simulations of high finesse cavities of a finesse up to $\mathcal{F} = 50.000$, we could not reveal a deficiency arising from the profilometry.

3.3.2 Multi-fiber holder for mass production

For the profilometry and the shooting of the fibers sub-micrometric precision is necessary, posing the need to minimize position drifts of the fibers and the optics. Furthermore, the whole process has to be carried out in clean room conditions, to avoid a contamination of the machined fiber surfaces prior to coating. For this purpose, the optical table with the fiber machining setup is enclosed in a temperature stabilized laminar flow box, with temperature fluctuations $< 0.2^\circ\text{C}$.

In the previous setup, every fiber had to be handled individually to be placed in the shooting range and then mounted in a holder for the shipping to the coating company. Especially in this last step, the experimenter risks a contamination of the fiber surface. Furthermore, the controlled temperature in the flow box cannot be maintained if the box is opened every few minutes to load a new fiber.

To eliminate these short comings, we decided to design a multi-fiber holder that allows to machine a multitude of fibers without handling, once loaded and placed in the shooting range. The requirement catalog for the holder consists of the following points

- A capacity of more than 10 fibers
- Placing and take out of individual fibers
- Compatibility with holders of the coating company to minimize handling of machined fibers
- Compact design to maximize the number of fibers in one coating run
- Vacuum compatibility for coating company
- Compatible with temperatures of 100°C ⁹ used in the coating process
- Exact positioning of the fiber end facets ($\pm 50 \mu\text{m}$) for identical vapor deposition in the coating process to ensure identical mirror properties on every fiber surface
- Parallel alignment of the fibers to ensure the same incident angle of the CO₂ laser and reduce the misalignment of the structure positions due to an angled fiber surface. The limit to parallelism of the fiber surfaces is given by the state

⁸The duration is composed of the time the Attocube needs to stabilize its position for each of the 6 images, the readout and the de-wrapping algorithm. Furthermore the optimum profilometer position is determined every 5 profiles taken, to cancel drifts.

⁹For later annealing of the fibers at 300°C the fiber will be released from the holder

of the art cleave technology¹⁰, allowing for cleave angles $< 0.3^\circ$ which we take as an upper limit for the accepted angle imprecision of the holder.

A widely used concept for aligning and holding fibers in telecommunications and research are *v-grooves*, as depicted in Fig. 3.6. Here the fiber is pressed in the v-shaped groove, which leads to only three contact lines enabling reproducible placement of the fiber. We developed two fiber holders based on the v-groove concept, presented in the following:

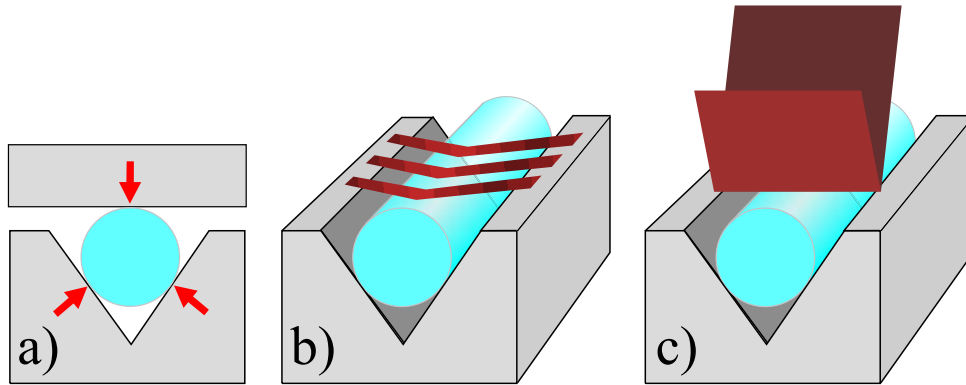


Figure 3.6: Multi fiber holder with v-grooves. a) shows the widely used principle of v-grooves for fiber fixation. The three red arrows mark the contact lines that align the fiber. The gray rectangle on top depicts the glass or silica piece that is normally glued on top. b) shows the possibility of fixing the fiber temporarily with metallic micro clamps and c) shows the solution with macroscopic clamps not directly attached to the groove substrate.

Microfabricated nickel clamps:

To meet the requirements of high alignment precision and compactness, we turned to optical lithography and processes common in the MEMS (micro-electro-mechanical systems) community [165]. In [166] microfabricated nickel clamps are presented to hold optical fibers in silicon v-grooves for integration in photonic devices. The v-grooves are wet-etched with a KOH solution in silicon, where the parallelism of neighboring grooves is determined by the quality of the optical mask.

We adapted the configuration to our needs of a multitude of parallel fibers and simplified the fabrication process slightly. An overview over the fabrication is given in Fig. 3.7 and the detailed recipe in the appendix A.2. The fabricated clamps and grooves are presented in Fig. 3.8. The fibers can be inserted by hand and are held by the nickel clamps with an astonishing force, largely sufficient for all handling such as mounting in the CO₂ shooting setup. The drawback of the method is depicted in Fig. 3.8 d) and e), where the fiber facet is shown before and after being inserted into a groove with nickel clamps. The picture shows a particularly bad example, where a lot of debris can be found on the surface, rendering subsequent CO₂ machining impossible. Even though the typical insertion gives a cleaner result, the risk for contamination and

¹⁰NYFORS Autocleaver, Stockholm, Sweden

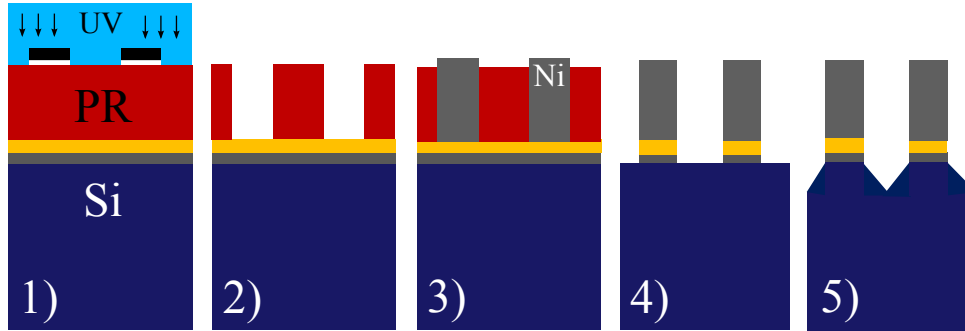


Figure 3.7: Microclamp fabrication (dimension not to scale). The principle is similar to the method we use for the fabrication of the atom chip (see Sec. 5.3). 1) On the Si-wafer (blue squares) a 50-100 nm Au-seed layer is evaporated with a 3 nm adhesion layer of chrome (gray and yellow stripes). A $7\mu\text{m}$ thick photo resist layer is applied and locally exposed with UV light in a mask aligner. The black squares depict the mask, which gives the desired pattern. 2) The photo resist is developed removing the resist on the beforehand exposed areas, revealing the seed layer. 3) The nickel is grown with an electro plating process on the seed layer. 4) The photo resist and the seed layer is removed. 5) With a wet-etching process in a KOH solution the grooves are etched in the silicon. For details see App. A.2.

the laborious production procedure led us to the decision to search for a cleaner option, which we found with the following solution.

Aluminum v-grooves with spring fixation:

The drawback of the previous design is the fact that the delicate fiber facet has to be pushed through the groove leading to debris and damage on the fiber facet. To eliminate this constructional defect, we use macroscopic clamps that can be opened before the fiber is put in the groove, leaving the fiber facet untouched. The design idea is sketched in Fig. 3.6 c) where a metal strip acts as a spring and presses the fiber in the groove. To be able to maintain the tight tolerances for the fiber alignment, the grooves are machined with a precision CNC-mill¹¹. To improve the attachment of the mirror material deposited in the coating process, the aluminum holders are sandblasted before the fragile grooves are machined. This reduces dust creation during handling after the coating process. The springs are realized as a comb made of 0.13 mm thick sheets of gilding-metal¹² and are shown in Fig. 3.9 b) and incorporated in the holder in Fig. 3.9 a).

We found experimentally that the CO₂ machining produces asymmetric structures, if the fiber facet is too close to the holder. We did not investigate if this effect is related to an asymmetric heat transport in the aluminum v-groove below the fiber or is due to reflections of the laser on the holder. To eliminate this effect for the shot parameters used in Sec. 3.4.3, the fiber facet should stick out at least 3 mm.¹³ To test

¹¹<http://www.magafor.com/article.php?grp=433&famille=8088>

¹²An alloy of high elasticity made of copper, zinc, tin and nickel. Normal spring steel works as well.

¹³For smaller structures/fibers presented in [163] a protrusion of 1 mm was sufficient.

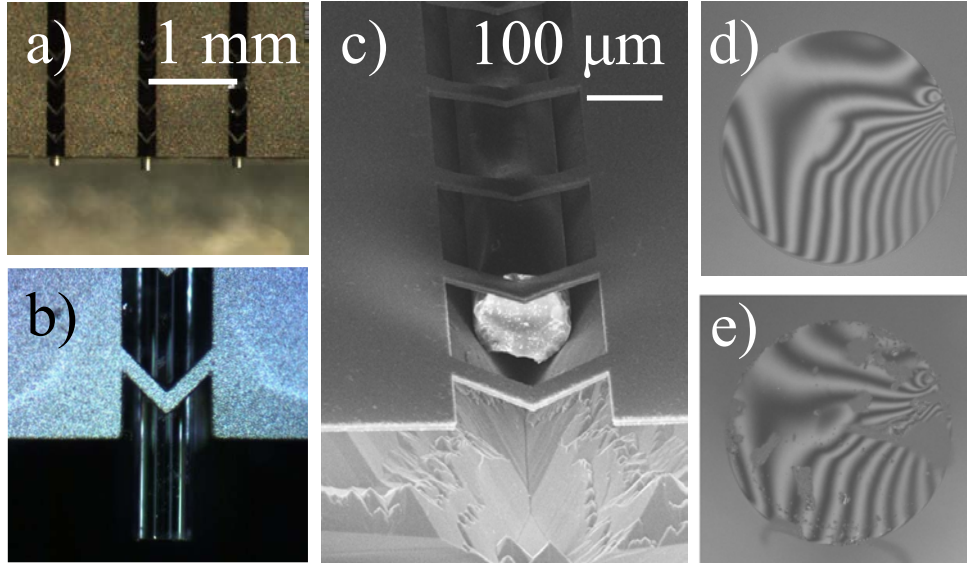


Figure 3.8: Microfabricated nickel clamps. a) and b) show microscope images of fibers ($\varnothing = 125 \mu\text{m}$) held by nickel clamps. c) shows a SEM picture of the Si v-groove with a non-cleaved fiber. d) shows a fiber facet before and e) after inserting it into a groove with nickel clamps, showing debris accumulated on the surface.

the parallelism of the grooves, we loaded the holder with fibers and determined the fiber facet angle by help of the 3D reconstruction presented in Sec. 3.3.1 and a planar fit. To distinguish the cleave angle of the fiber itself and the angle of the groove, we rotate the fibers in the groove as shown in Fig. 3.10. This allows us to determine the groove angle α_G of each groove and the fiber cleave angle with a precision well below 0.05° , enough to characterize the holder. We find for one exemplary holder a standard deviation of the groove angle of 0.1° in the x and y direction. This shows that the fiber facet angle is dominated by the cleave angle of $\sim 0.2^\circ$ and not the fiber alignment in the holder.

Besides the fulfillment of the requirement catalog, the multi holder allows to correct the displacement of a CO_2 machined depression to the fiber core from fiber to fiber. This feedback leads to the measured average centering error of a CO_2 shot with respect to the fiber core of $0.9 \mu\text{m}$, which is a significant improvement over the earlier setup. The remaining error has contributions from the translation stages (thermal drifts in particular), and possibly from the CO_2 laser's beam pointing stability. The relative positions of the multiple shots making up the dot milling pattern (see Sec. 3.4) have much better accuracy because they do not require the ~ 4.5 cm translation between the profiler and the CO_2 beam, which is needed in the centering procedure.

The holder design was adopted for now by the teams of J. Harris, Yale University, M. Köhl, University of Bonn and C. Voisin of the Laboratoire Pierre Aigrain, Paris as well as by the subgroups of our team and used to successfully produce several hundred fiber mirrors.

Unfortunately, the remaining angle of the surface to the profilometer of $\alpha < 0.3^\circ$ was still too high for the fabrication of the shallow spherical profiles presented in

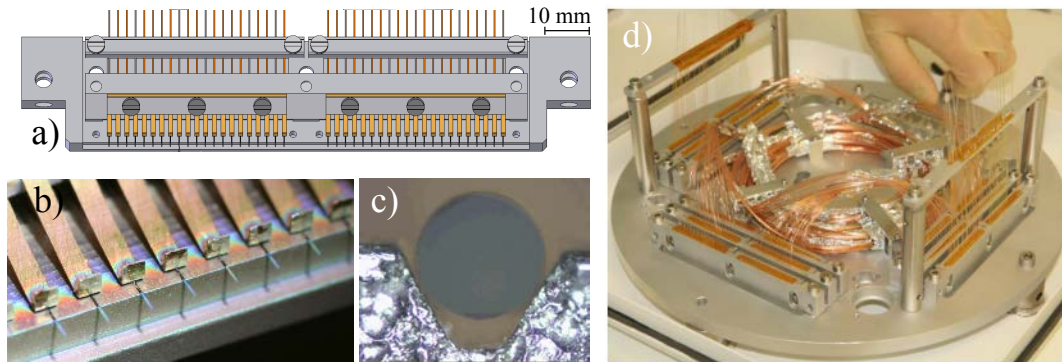


Figure 3.9: Multi fiber holder. a) shows the design of the fiber holder from the top holding 42 fibers. The copper coated fiber tails leave the holder on the upper edge, fixed by two additional bars. On the lower edge the stripped fiber sticks out of the holder, letting the fiber surface in free air ready for CO₂ machining. b) shows the spring comb pushing several fibers into grooves. c) shows a microscope image of a fiber ($\varnothing = 200 \mu\text{m}$) in an aluminum groove, focused on the groove. The high quality of the groove machining and the structured surface of the sandblasting is visible. d) shows 9 multi fiber holders carrying ~ 320 fibers mounted on a support for the coating process.

Sec. 3.4.3, posing the need to align the angle of every fiber individually. For this purpose, we installed a tilt stage for single fibers, at that moment not compatible with the multi fiber holder. To profit in the future from the multi fiber holder for the fabrication of large shallow structures, the system will be upgraded with a pitch/yaw stage compatible with the fiber holder.

3.4 Dot milling with CO₂ laser pulses on fiber end facets

With the presented setup we have the possibility to machine surfaces with submicrometric precision. Although a multitude of materials can be machined with a CO₂ laser [167, 168], we focus on the ablation of small volumes ($\approx 1 - 100 \mu\text{m}^3$) of fused silica, needed for the machining of optical fibers. The machining depends strongly on the surface quality of the prepared fibers, which is why we start this section with the fiber preparation.

3.4.1 Fiber preparation

We have machined three different fiber types, presented in Table 3.1. For good reproducibility of the machining results, it is important to control the cleave angle to tight tolerances. We have used a pneumatic cleaver¹⁴ with a specified typical cleave angle of less than 0.3° . Our measured mean cleave angle deviation was less than 0.4° throughout, and below 0.2° for the SM fibers. To achieve these results, the cleaver has to be calibrated carefully and the copper-coated fibers have to be straightened by

¹⁴NYFORS Autocleaver, Stockholm, Sweden

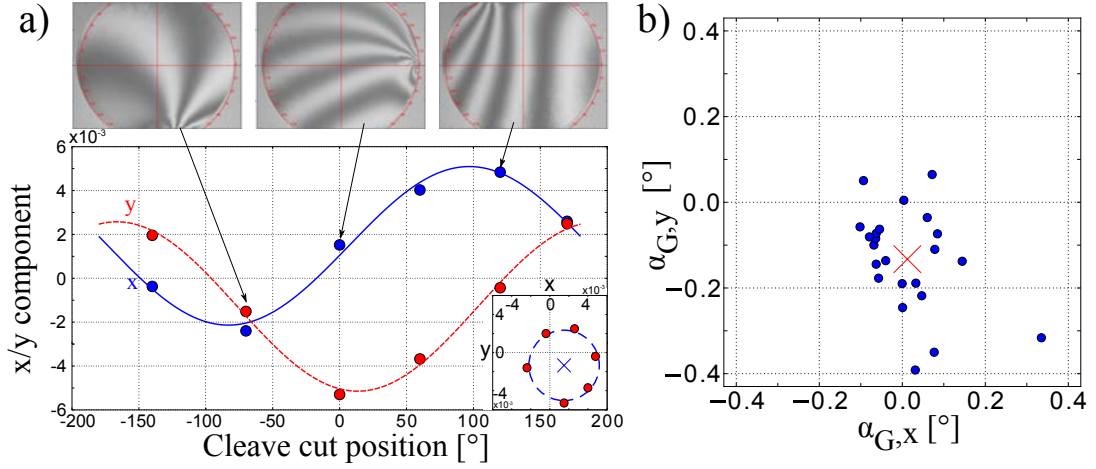


Figure 3.10: Cleave and groove angle estimation. a) The top row shows interferograms of the surface of the same fiber in one v-groove rotated around the fiber axis by three different angles. The damage due to the blade intrusion, best seen on the right side of the central image, is used as an indicator of the rotation angle. We extract the fiber surface angle by fitting a plane to the reconstructed 3D-profile of the surface. The x and y component of the normal vector of the fitted plane is plotted as red and blue circles, fitted by two sinusoidal functions 90° phase shifted. The inset shows the same data as red points on a polar plot, visualizing the fiber rotation. The blue dashed circle represents the parameters deduced from the sinusoidal fits. The circle center (blue x) shows the obtained groove orientation. The circle radius contains the information on the cleave angle. For the cleave angle of this fiber we get $\alpha_c = 0.21^\circ \pm 0.01^\circ$, for the groove angle $\alpha_G = 0.11^\circ$. b) The groove angles estimated as in a) for 21 neighboring grooves, marked as blue circles. The mean value $\alpha_{G,x} = (0.01 \pm 0.10)^\circ$, $\alpha_{G,y} = (-0.13 \pm 0.11)^\circ$ (red cross), shows the small tilt of the holder in the y -direction. The standard deviation of only 0.1° proves the parallelism of the single grooves. The outliers on the bottom right are most likely due to dust particles in the groove, bending the fiber slightly.

Type	Supplier	Ref.	MFD μm	Wavelength range nm	Coating
MM	IVG Fiber	Cu200/220 IR	200±3	700–1700	copper
SM	IVG Fiber	Cu800-200	6±0.5	800–1000	copper
PC	NKT Photonics	LMA 20	16.4±1.5	700–1700	acrylate

Table 3.1: Fiber Types Used in the Experiments. The mode field diameter (MFD) indicated here is the nominal value specified by the manufacturer. The actual value depends on wavelength. For the MM fiber, the core diameter is specified instead of the MFD.

hand before cleaving. We found, that the mean cleave angle of the copper coated fibers could be improved by more than a factor of three, if the fiber is pulled and released by the cleaver once before the real cleaving process, depicted in Fig. 3.11.¹⁵ For the PC

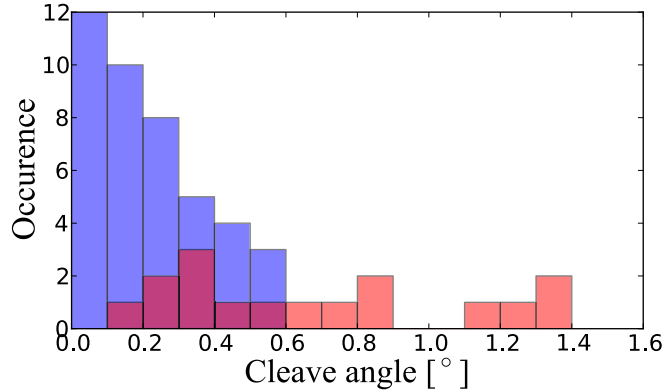


Figure 3.11: Pre-pull method for small cleave angles. The red histogram shows the occurrences of cleave angles with the normal cleaving procedure on a SM fiber. The blue histogram shows a significant improvement, when the fiber is pulled and released by the cleaver, prior to the real cleaving. The cleave angles are measured with a fusion splicer (Fujikura FSM-45 PM/PM LDF). The same improvement could be found for the MM fibers. The fibers with cleave angles $> 0.3^\circ$ are recleaved, leading to a smaller average cleave angle for the following CO₂ machining.

fiber (see Sec. 4.1.6 for more details), simple cleaving exposes the holes of the photonic crystal. We found that direct machining on that structure was possible for profiles with $R \lesssim 300 \mu\text{m}$. For the much shallower profiles of our targeted $R > 1000 \mu\text{m}$ mirrors, this simple approach turned out to be problematic. Therefore, we have collapsed the holes before cleaving using the arc of a fusion splicer as described in Ref. [170]. The cleave was positioned at a distance $d_c \sim 50 - 100 \mu\text{m}$ from the onset of the collapsed region as shown in Fig. 3.12.

Excellent results were achieved with the fibers prepared in that way. For shorter d_c , residues of the six-fold symmetry of the PC hole pattern remained visible in the machined structure. The PC fiber was only available with an acrylate coating, not accepted in the machines of the coating company. For this reason we replaced the acrylate coating with a polymer coating¹⁶. The prepared fibers are then mounted in the tilt mount in the shooting range ready for the CO₂ machining.

3.4.2 Multiple shots

To create structures by multiple single shots, we started with general tests on the reaction of the material on the new machining procedure. The experiences made

¹⁵An interesting alternative is shown in [169], where the fiber is cleaved with a CO₂ laser with cleave angles $< 0.06^\circ$. Especially interesting for the PC fibers, where a simultaneous collapsing of the PC structure and cleaving could be achieved.

¹⁶PI-2525, HD-Microsystems

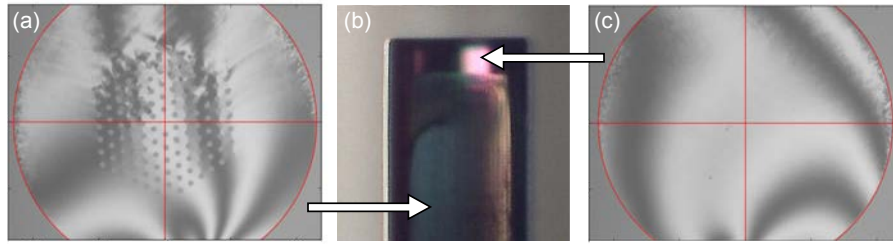


Figure 3.12: a) Profilometer image of the surface of a PC fiber (NKT LMA 20) cleaved in the non-collapsed region, indicated by the arrow. b) Side view of a PC fiber, showing the transition between the non-collapsed and collapsed regions. c) Profilometer image of the surface for a cleave in the collapsed region. (The red crosshairs in a) and c) mark the center of the fiber.)

are presented in this section and lead to the fabrication of large spherical structures presented in the following section 3.4.3.

As stated before, the goal is to create structures by use of a multitude of single CO₂ shots. The first question at hand is if a simple model can be found to predict the structure shape after multiple shots. Unfortunately, the strong nonlinearity of the ablation process [153] and the high sensitivity to the target material properties shown in Fig. 3.13 made it for now impossible to model the multi shot process. Even for single shots on a fiber facet, the structure predicted by the model in [153] deviates strongly from the experimental findings.¹⁷ A central problem for the multi shot sequence is the fact that the fused silica is not only ablated but a considerable amount is melted and moved, as can be seen in Fig. 3.14. In Fig. 3.14 a) it is shown that the shooting raises walls of a comparable height as the depth of the created depression. This moving of the material leads to a strong dependence of the created structure on the shot order as can be seen in Fig. 3.14 b), c). Recent publications present theoretical models verified with experimental data for short ($\tau \leq 100 \mu\text{s}$) [171] and long ($\tau \sim 1 \text{ s}$) [172] pulse durations. The latter shows a good prediction for the morphology of the created structures. It could be an interesting project to investigate, whether the model can be extended to substrates of small radius (fibers) and our range of pulse durations in the 1 – 100 ms regime. Both models were published after our CO₂ fabrication, so that the nonexistence of a model led us to an empirical approach, where we optimized the shot pattern by minimizing the deviation of the desired shape. This is presented for the spherical structures in Sec. 3.4.3.

Beyond that, the versatility of the setup allows to produce structures deviating far from the single concave shapes needed for micro mirrors. Two examples are presented in Fig. 3.15. Similar structures are fabricated with a FIB in [173], but note that the FIB fabrication produces significantly higher surface roughness (more than a factor 3 in [156]), which is disadvantageous for high finesse resonators, as we will see in Sec. 4.1.4.

¹⁷The much better agreement for structures machined on macroscopic samples led the authors to the conclusion that the small diameter of the fiber restricts the transverse heat flow and thus causes heat accumulation, not covered by the model.

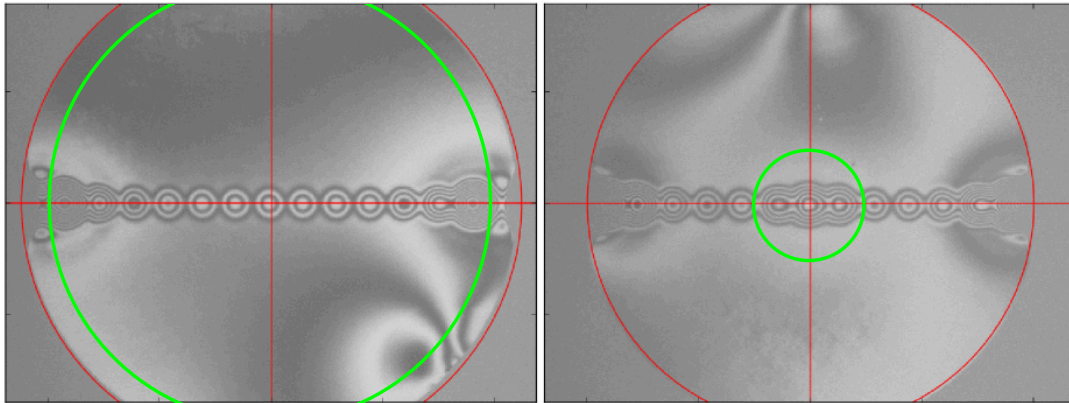


Figure 3.13: Effect of doping on the CO₂ machining. On the left a step-index MM fiber (IVG Cu200/220 IR) is shown with an non-doped core ($\varnothing = 200 \mu\text{m}$, green circle) and on the right a graded index MM fiber (IVG Cu50-200) with a germanium doped core with $\varnothing = 50 \mu\text{m}$. Both fibers were shot 13 times with identical parameters and scanning the x -position. It is clearly visible that the ablation process is highly position and material dependent. More fused silica is removed at the fiber edges and in the germanium doped center.

Especially the possibility to create *convex* structures on macroscopic substrates or fiber end facets opens the possibility to produce freeform optics [174] with inexhaustible applications. The efficient and precise machining of fused silica with CO₂ laser light leads to a wide spread use of the technology for polishing [152, 177], machining [178–183], cutting [169] and fusion splicing [184], both in research and industry. Even the creation of freeform optics already found the way to industry¹⁸. Our method of laser dot milling expands this listing to our best knowledge to an unprecedented level of precision in the nanometer range, with the lowest reported surface roughnesses of $\sim 0.2 \text{ nm}$. We will make full use of this precision in the following section 3.4.3, to create spherical depressions for micro mirrors.

¹⁸<http://www.powerphotonic.com>

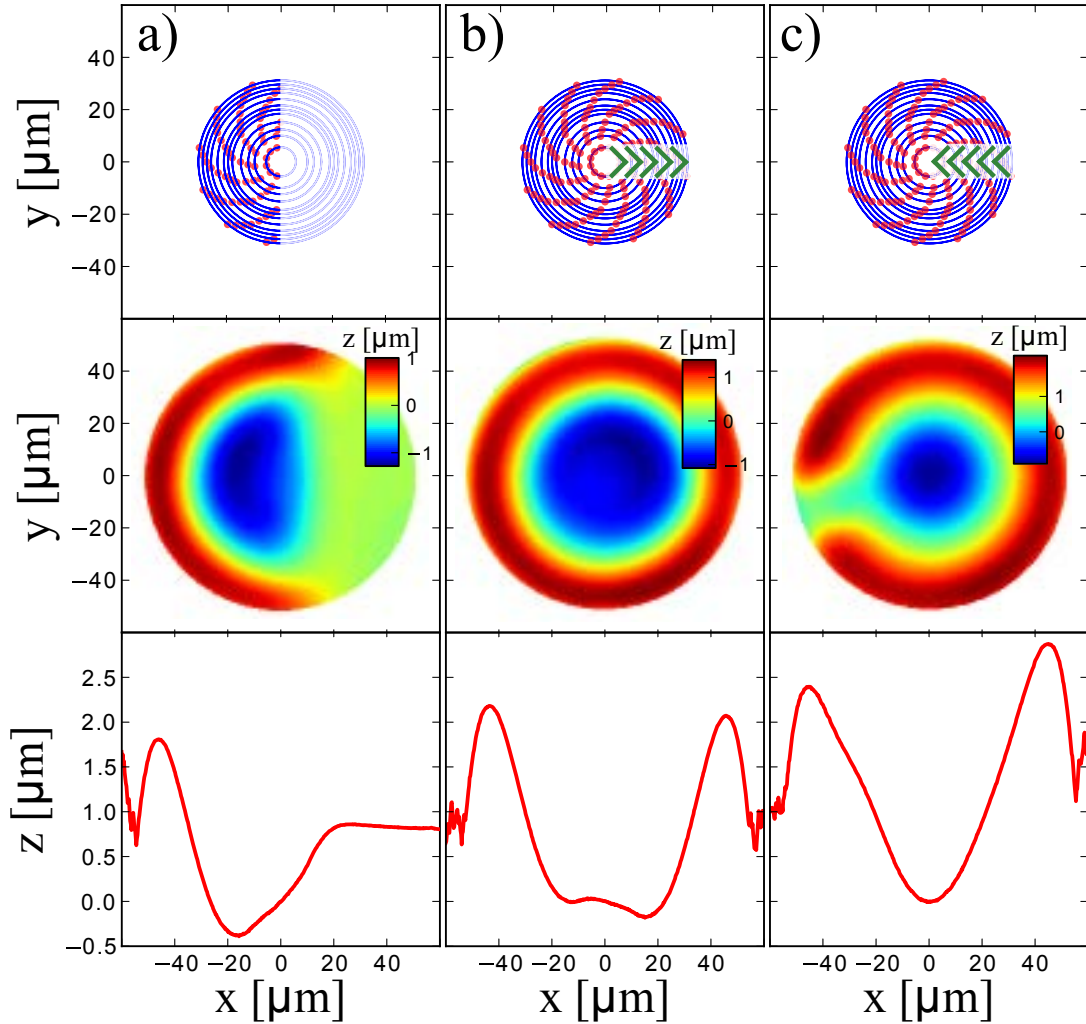


Figure 3.14: Initial tests for multi shots. a), b), c) show three different shot procedures on individual fibers ($\varnothing = 125 \mu\text{m}$). The first row shows the shot positions, the second row the reconstructed profiles and the third row cuts along x at $y = 0$. All single shots have identical parameters of $\tau = 14.5 \text{ ms}$, $P = 2250 \text{ mW}$ with a CO₂ radius of $\sim 60 \mu\text{m}$ on the fiber. a) uses only the left half of the shots, to preserve the cleaved surface on the right as a reference. It can be seen that the shots are not only digging, but also create a wall of $\sim 1 \mu\text{m}$. b) and c) are realized with identical shot number (144) and shot positions, only the order in which the rings are shot is inverted. In b) the inner ring is shot first (as in a)), in c) the inner ring is shot last. A strong effect of the shot order can be seen.

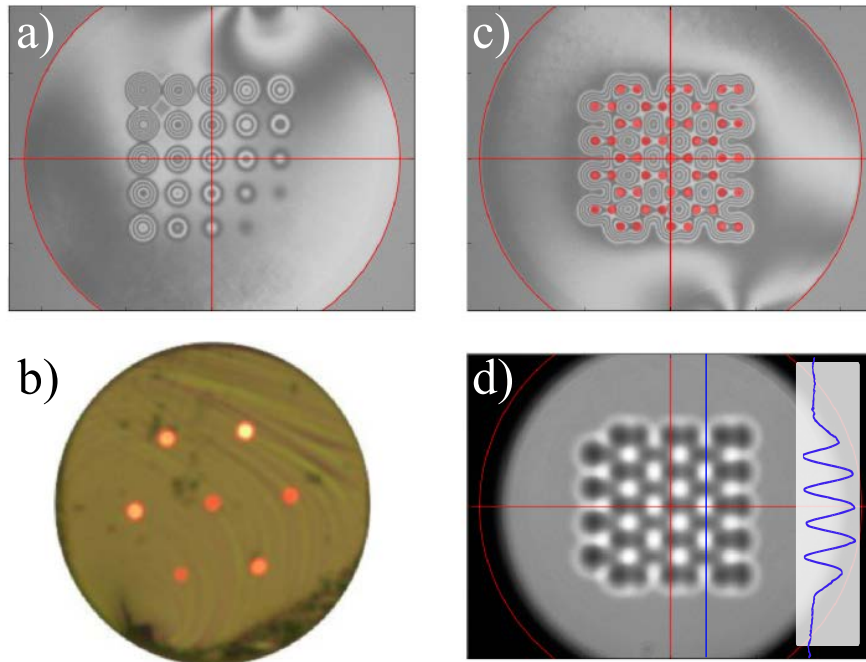


Figure 3.15: Mirror and lens array. a) Interferogram of a multi mirror array on a MM fiber facet ($\varnothing = 220 \mu\text{m}$). In combination with a planar mirror or a second mirror of this kind a large array of resonators with different geometries can be realized. To address the single cavities multicore fibers as in b) (taken from [175]) or methods as in [176] could be used. c) shows a interferogram of a lens array on a MM fiber, created by multiple shots marked as red points. The ROCs of the aspheric lenses are $R_{1/2} \approx 67/26 \mu\text{m}$. A 3D-representation can be found in Fig. 5.3.3. d) shows a microscope picture of the lens array illuminated with a LED through the MM fiber. The inset shows a cut along the blue line, illustrating the strong spatial intensity modulation by the microlenses.

3.4.3 Machining large spherical structures by CO₂ dot milling

Our fabrication goal was to obtain spherical mirror profiles with ROCs in the 1 mm range, and with a useful diameter of 100 μm . We have achieved good results using identical CO₂ beam parameters for all dots in the pattern. For the results shown below, the beam had a $1/e^2$ radius $w = 140 \mu\text{m}$, and its power was $P = 2.3 \text{ W}$. The pulse length τ was adjusted such that an individual milling pulse near the center of a flat (cleaved) MM fiber yielded a depression with depth $t \sim 100 \text{ nm}$ and diameter (2σ of a Gaussian fit) of $\sim 30 \mu\text{m}$. This led to $17 \text{ ms} \leq \tau \leq 25 \text{ ms}$ depending on the fiber type. This dot size is small enough to produce features with the required resolution and using about one hundred pulses, while a smaller beam diameter would require more pulses with no obvious advantage. The milling process is highly nonlinear, so

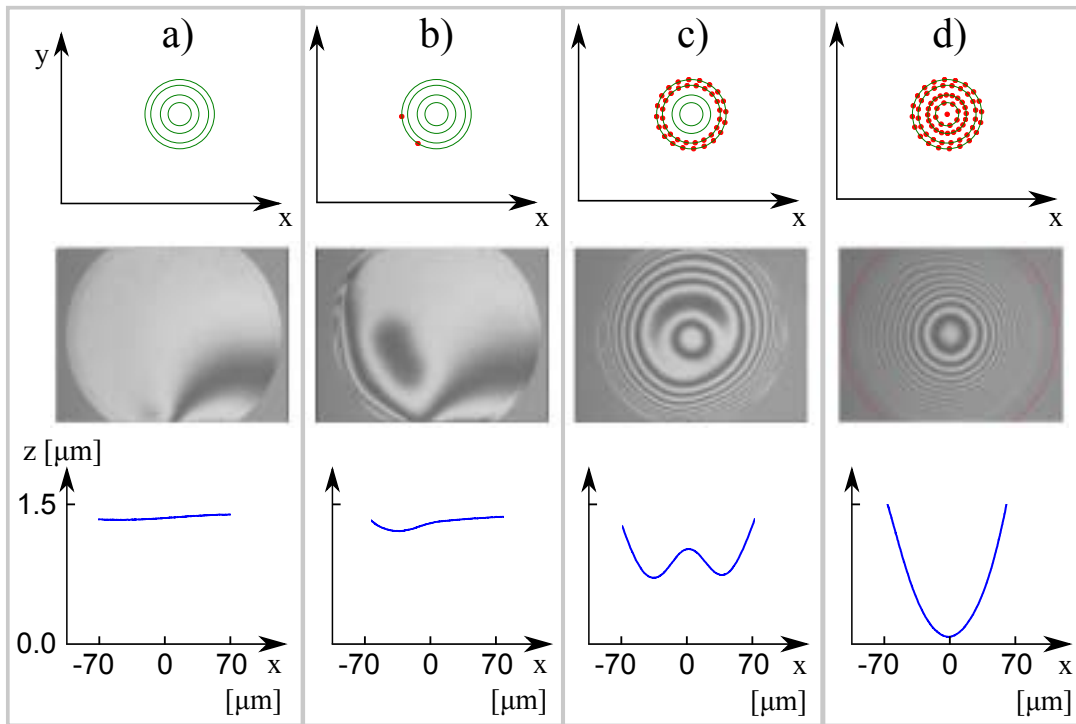


Figure 3.16: Multi shot sequence. The first row shows the shot positions, the second interferograms of the fiber facet and the third a cut along x through the 3D profile at $y = 0$. The different columns show the fiber facet after a) 0, b) 2, c) 40 and d) 69 shots. After inspection the shape can be fine tuned with an additional shot of reduced pulse length to the center.

that the time order of the pulses also affects the result. Furthermore, due to the finite size of the fiber, the effect of a given pulse also depends on its distance from the center of the fiber surface. Therefore, finding a suitable milling pulse pattern requires some empirical testing to reduce the parameter space before a systematic optimization can be done.

We have used the following strategy: as the desired shape has rotational symmetry, the milling pulses are placed on concentric circles. The outmost circles are shot first.

The number of pulses is limited to ~ 100 , because this range was empirically found to give good results and higher numbers brought no obvious improvements. To reduce effects of the shot order, neighboring pulse positions are not shot consecutively. The number and diameters of the circles are optimized experimentally by minimizing the difference between the measured profile and a spherical surface over a circular region of interest. A typical pulse pattern and a shot sequence are shown in Fig. 3.16. Once the pattern is optimized, processing and characterizing a single fiber with a typical 70-dot pattern takes less than 2 minutes. Using this type of pattern, we have produced mirror

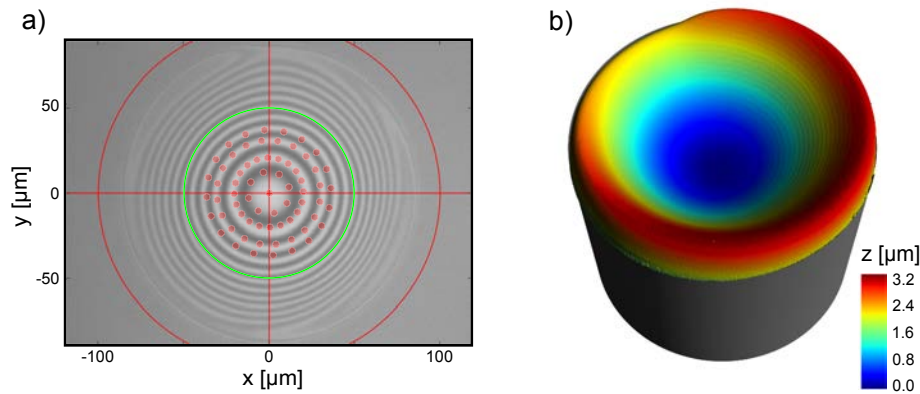


Figure 3.17: Large spherical surface machined on a 200 μm diameter SM fiber. a) Interferogram of the surface after processing. The red circle shows the initial fiber diameter, the green circle shows the area over which the structure was optimized. The crosshairs indicate the center of the fiber. The red circles indicate the positions of the CO₂ pulses. b) Surface profile measured by phase-shifting interferometry. (The grey area was added to indicate the fiber orientation.)

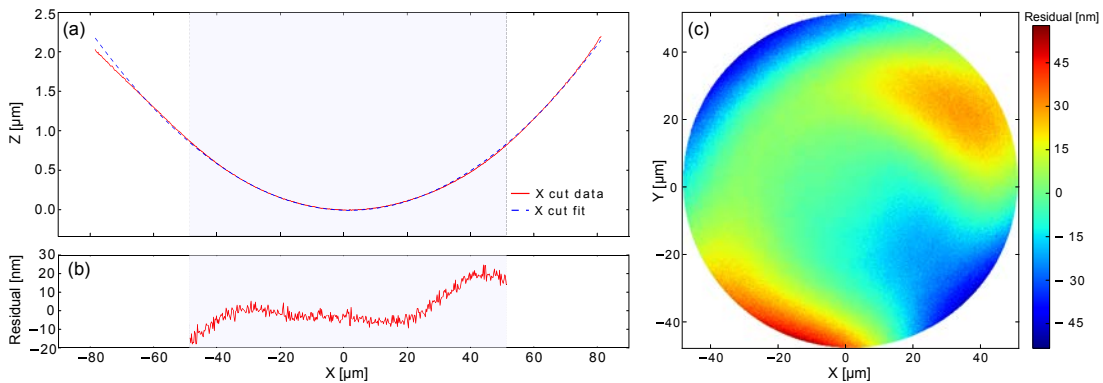


Figure 3.18: (a) Cut along the x -axis of a spherical profile on a 220 μm diameter MM fiber and corresponding cut of a two-dimensional spherical fit ($R = 1475 \mu\text{m}$) on a circular region with a diameter of 100 μm . (The shaded area in (a) and (b) indicates the fit region.) (b) Cut along the x -axis of the fit residuals. (c) 2D fit residuals.

profiles on SM, MM and PC fibers. Figures 3.17 and 3.18 show sample results. The shot

positions and parameters were optimized for $R = 1500 \mu\text{m}$, where the mean deviation from a 2D spherical fit is smaller than 12 nm, and the maximum deviation smaller than 40 nm, over a circular region of interest with a diameter of $100 \mu\text{m}$. Between samples processed with identical parameters, the measured R varies by about $\pm 10\%$ on SM and MM fibers, and by about $\pm 20\%$ on PC fibers. Within some limits, larger and smaller profiles can be machined by simply changing the pulse length and scaling the shot positions, without optimizing anew. When machining smaller R with the pattern of Fig. 3.17, the mean deviation increases up to 59 nm for $R = 330 \mu\text{m}$. When producing $R > 1500 \mu\text{m}$, the mean deviation does not increase significantly, but cleave imperfections start to compromise the symmetry of the structure. The ellipticity $(R_a - R_b)/R_a$ is below 10%, where R_a and R_b are the radii of the large and the small axis, respectively, of a 2D parabolic fit to the measured profile over a region of $100 \mu\text{m}$ diameter. This ellipticity could in principle be further reduced by adapting the milling pattern. However, ellipticity-induced birefringent splitting of the cavity resonance frequencies scales as $1/R$ [161], making it a small effect for the cavities considered here. Therefore, we did not attempt such an optimization here.

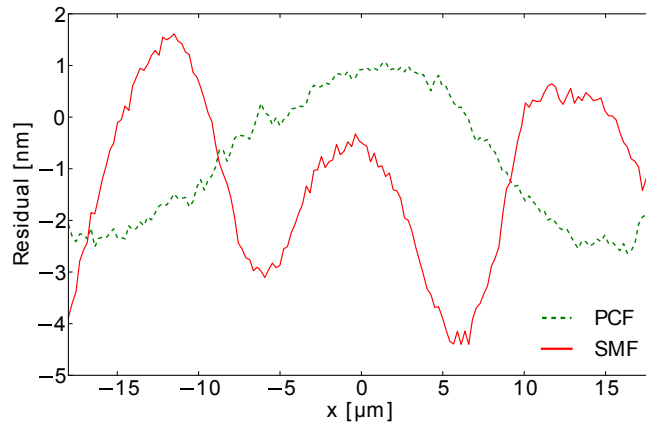


Figure 3.19: Influence of the doped core region. Shown are the residuals of a 2D spherical fit for machined SM and PC fiber surfaces. The milling patterns are very similar for both fibers and are close to the one shown in Fig. 3.17(a). 73 pulses were used for the SM fiber and 70 for the PC fiber; the pulse length is $\tau = 17.6$ ms for the SM fiber and $\tau = 20$ ms for the PC fiber. The data is the average of 120 profile measurements for each fiber (see Sec. 4.2.3). The radius of the fit region was chosen to be $18 \mu\text{m}$ because this is the mode radius on the fiber for a cavity of length $L = 1200 \mu\text{m}$ and a ROC $R = 1650 \mu\text{m}$. The fit for the PC fiber gives $R = 1492 \mu\text{m}$ and the residual shows only a slow modulation, which could probably be further reduced by fine-tuning the pulse length of the last, central pulse. By contrast, the residual of the standard SM fiber (fitted $R = 1508 \mu\text{m}$) shows a strong variation at the fiber center at the interface between core and cladding material.

With SM fibers, we also observe a shape deviation of 20-40 nm height located near the interface between the cladding and doped core, similar to that reported in [146] for several pulses on the fiber center. It can be compensated to some extent by slight

adjustments in the milling pattern, with the resulting residual shown in Fig. 3.19. Collapsed PC fibers do not experience this effect, which makes them particularly suitable for CO_2 processing. Likewise, large-core MM fibers are also easy to process because of their large, homogeneous central region.

3.5 Conclusion

We showed that the CO_2 dot milling method is well controllable and enables the production of large spherical structures. These can be used for the creation of long high finesse FFP resonators, presented in the next chapter. Furthermore, the versatility of the machining process enables the creation of freeform optics with excellent surface properties and high precision on the macroscopic shape, which promises a wide range of applications in the future.

Long Fiber Fabry-Pérot Resonators

The CO₂ dot milling method presented in the previous chapter allowed the realization of the longest FFP resonators to date. In this chapter we will present these resonators and characterize their properties. Before we do so, we start with introducing the central concepts of optical resonators.

4.1 Optical Resonators

The goal of this section is to establish all parameters and formulas that characterize the resonators presented in this work. We will focus on Fabry-Pérot resonators [185] with an emphasis on fiber Fabry-Pérot (FFP) resonators, which will be introduced. Further implementations of optical micro resonators, as micro spheres or photonic crystals, will not be treated here but we recommend [186] and the references therein.

4.1.1 Resonance, transmission and finesse

An electric field resonates in an optical system if it reproduces itself after one round trip. This leads to a constructive interference and hence a build-up of the field intensity in the resonator. The reproduction criterion can be subdivided into two conditions: first the field has to reproduce its shape, which leads for a Fabry-Pérot resonator in the paraxial approximation to the following *stability condition* [187]

$$0 < \left(1 - \frac{L}{R_1}\right) \left(1 - \frac{L}{R_2}\right) < 1 \quad (4.1.1)$$

where R_1, R_2 are the radii of curvature (ROC) of the two mirrors and L is the resonator length. The condition is visualized in the stability diagram in Fig 4.1.

Secondly, the *resonance condition*

$$kL = q\pi, \quad q \in \mathbb{N} \quad (4.1.2)$$

with the wave vector $k = 2\pi/\lambda$, ensures that the phase of the electric field is the same after one round trip. From Eq. 4.1.2 the resonance frequencies for a given length L are

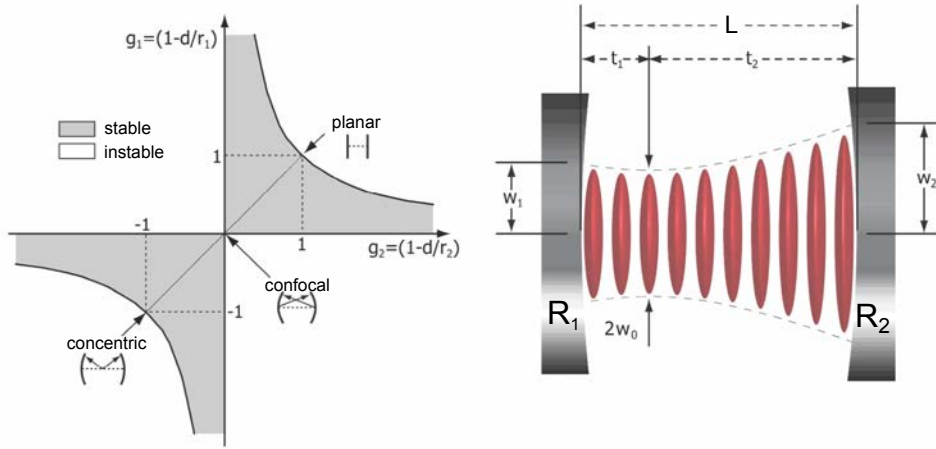


Figure 4.1: Stability diagram and resonator configuration. Taken from [135].

given by

$$\nu_q = q \frac{c}{2L} \quad (4.1.3)$$

with the frequency distance $\nu_{q+1} - \nu_q$ called the *free spectral range*

$$\nu_{FSR} = \frac{c}{2L}. \quad (4.1.4)$$

The constructive interference of the intra cavity field yields a maximum of the transmitted intensity for all $\nu = \nu_q$ of

$$T_c = \frac{\mathcal{T}^2}{(\mathcal{T} + \mathcal{L})^2}, \quad (4.1.5)$$

defined by the intensity transmission \mathcal{T} and the losses \mathcal{L} of each of the two mirrors. Here we assume the same properties for both mirrors $\mathcal{T} = \mathcal{T}_1 = \mathcal{T}_2$, $\mathcal{L} = \mathcal{L}_1 = \mathcal{L}_2$. Furthermore, the intensity reflected from the resonator is minimized on resonance to

$$R_c = \frac{\mathcal{L}^2 (1 - \mathcal{T} - \mathcal{L})}{(\mathcal{T} + \mathcal{L})^2}. \quad (4.1.6)$$

For each mirror the conservation equation $1 = \mathcal{R} + \mathcal{T} + \mathcal{L}$ holds, with \mathcal{R} being the mirror reflectivity. It can be seen that the resonator transmission depends strongly on the ratio of mirror transmission and mirror losses, which is of importance for high finesse cavities where $\mathcal{T} \approx \mathcal{L}$. Besides its height, the transmission peak is defined by its line width (FWHM), given by

$$\delta\nu = \frac{\kappa}{2\pi} \approx \frac{(1 - \mathcal{R})}{\pi\sqrt{\mathcal{R}}} \nu_{FSR} \quad (4.1.7)$$

depending on the mirror reflectivity and with Eq. 4.1.4 on the resonator length. To eliminate the length dependence, we introduce the *finesse* as a characteristic parameter of the resonator:

$$\mathcal{F} = \frac{\nu_{FSR}}{\delta\nu} \approx \frac{\pi\sqrt{\mathcal{R}}}{1 - \mathcal{R}} \quad (4.1.8)$$

that can be approximated for high reflectivity (for us $\mathcal{R} > 0.999$) by

$$\mathcal{F} = \frac{\pi}{\mathcal{T} + \mathcal{L}}. \quad (4.1.9)$$

The damping of the resonator can be characterized by the Q-factor, which describes the ratio of the stored energy to the energy loss per cycle and is given by

$$Q = \frac{\nu}{\delta\nu} \quad (4.1.10)$$

which is proportional to the photon lifetime in the resonator

$$\tau = \frac{1}{2\pi\delta\nu}. \quad (4.1.11)$$

4.1.2 Mode geometry

The resonator parameters L, R_1, R_2 define the resonator mode characterized by the mode waist radius

$$w_c(L, R_1, R_2) = \sqrt{\frac{\lambda}{\pi} \sqrt{\frac{L(R_1 - L)(R_2 - L)(R_1 + R_2 - L)}{(R_1 + R_2 - 2L)^2}}} \quad (4.1.12)$$

and the waist distance to the two mirrors

$$t_{1,2} = \frac{L(R_{2,1} - L)}{R_1 + R_2 - 2L}. \quad (4.1.13)$$

The mode radius along the cavity axis can then be calculated using the standard Gauss beam formulas [188]

$$w(z) = w_0 \sqrt{1 + \left(\frac{2(z - z_0)}{kw_0^2}\right)^2} \quad (4.1.14)$$

$$R(z) = (z - z_0) \left(1 + \left(\frac{kw_0^2}{2(z - z_0)}\right)^2\right). \quad (4.1.15)$$

where z_0 is the waist position and here $w_0 = w_{0,c}$. The finite size of the mirrors of a FFP resonator raises particular interest in the resonator mode radii on the mirrors

$$w_{m;1,2}(R_1, R_2, L) = \sqrt{\frac{\lambda R_{1,2}}{\pi} \sqrt{\frac{R_{2,1} - L}{R_{1,2} - L} \frac{L}{R_1 + R_2 - L}}}. \quad (4.1.16)$$

The situation is depicted in Fig. 4.1 b) for an asymmetric resonator with $R_1 > R_2$.

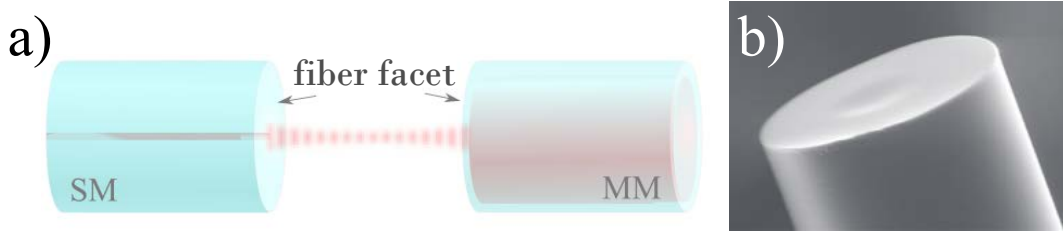


Figure 4.2: a) shows a FFP resonator, where the high reflective mirror coating is applied directly on the machined fiber facets. The light is guided to the cavity in a single mode (SM) fiber to guarantee stable mode coupling. The output light is collected by a multimode (MM) fiber to increase the collection efficiency. The red standing wave pattern depicts the resonator mode. b) shows a typical concave structure created with CO_2 laser ablation on a fiber of $\varnothing = 125 \mu\text{m}$ (taken from [73]).

4.1.3 Fiber Fabry-Pérot resonators

One possible realization of microscopic Fabry-Pérot resonators was demonstrated in [73], where the resonator mirrors are realized directly on the end facet of optical fibers. A concave depression is fabricated with CO_2 laser ablation on the fiber end facet, to satisfy the stability condition 4.1.1. The machining with CO_2 laser ablation will be discussed in detail in Sec. 3 and an exemplary result is shown in Fig. 4.2 b). A high-reflective coating is evaporated on the created concave structures, realizing mirrors with low losses, discussed in Sec. 4.1.4. Aligning two fibers with mirrors on the end facets as in Fig. 4.2 realizes a fiber Fabry-Pérot (FFP) resonator, showing a set of interesting properties:

- Thanks to the CO_2 fabrication process, very small radii of curvature ($R < 50 \mu\text{m}$) can be realized in combination with short resonators ($L < 5 \mu\text{m}$). This leads to a small mode volume, advantageous in cavity quantum electrodynamics (cQED) experiments (see Sec. 2.2)
- Another advantage for cQED experiments is the open geometry, that allows to place atoms in the intensity maximum of the resonator mode, in contrast to resonators where the mode maximum lies inside the optical guide (e.g. [189]), not accessible for the atoms.
- The small size of the resonator and the direct coupling to an optical fiber renders this resonator type particularly interesting for applications in hardly accessible environments such as cryostats or close to other devices.
- The reduced size decreases furthermore the sensitivity to external influences such as acoustic noise and misalignment due to thermal stresses.

The mentioned properties make FFP resonators the perfect tool for cQED experiments. Due to their compactness, they are particularly well suited for the combination with atom chips, which is the goal of this thesis. Next to the advantages listed above, two major problems have to be addressed: the fixed coupling of the resonator mode to the fiber mode reduces the possibilities of mode matching, while the small mirror diameters may lead to additional losses in the resonator. Since a large part of this work

was dedicated to solve these problems, both effects will be discussed in the following sections.

4.1.4 Resonator losses

The loss in a resonator is a combination of the loss in the resonator medium and the losses of the resonator mirrors. Here we will discuss the case of an empty resonator and thus focus on the mirror losses. The mirror losses are composed of the absorption loss \mathcal{L}_A in the mirror coating, the scatter loss \mathcal{L}_S on the mirror surface and the clipping loss \mathcal{L}_C due to a non-sufficient mirror diameter. We will discuss the different loss mechanisms in the following, with exemplary parameters for our application of CO₂ machined fused silica fibers.

Absorption loss \mathcal{L}_A : The absorption loss is given by the mirror material. For standard metal mirrors the penetration of the evanescent field leads already to an absorption loss of several percent not suitable for high finesse resonators. Substantially lower loss in the 1 ppm range [190] can be achieved with distributed Bragg reflectors. Here, the reflection is generated by a stack of thin layers of materials with alternating high and low indexes of refraction, such as Ta₂O₅ and SiO₂, showing low loss in the visible spectrum and the near infrared. For our application, several layers have to be added to the mirror to adjust the phase of two different wavelengths present in the resonator, as discussed in Sec. 4.2.6. This leads to additional absorption, giving $\mathcal{L}_A = 15$ ppm at 780 nm and $\mathcal{L}_A = 3$ ppm at 1560 nm, estimated by the coating company of our choice¹.

Scatter loss \mathcal{L}_S : The dependence of the scattering loss on the RMS surface roughness given in Eq. 3.3.2, is usually estimated to be [191]

$$\mathcal{L}_S = \left(\frac{4\pi\sigma}{\lambda} \right)^2. \quad (4.1.17)$$

The application of the mirror coating by ion beam sputtering follows the form of the substrate, conserving the imperfections of the substrate surface. This puts high requirements on the surface quality of the substrate, in our case the machined fiber surface. In [153] the surface roughness of a CO₂-machined fiber surface was measured to be $\sigma = 0.22$ nm, leading to an estimated scatter loss of $\mathcal{L}_S = 11$ ppm at 780 nm and $\mathcal{L}_S = 3$ ppm at 1560 nm. This proves the suitability of our fabrication method for high finesse resonators.

Clipping loss \mathcal{L}_C : A problem arises when the resonator mode diameter is of the same order of magnitude as the mirror diameter. Considering a mirror of finite radius r_{clip} , only the part of the mode of intensity $I(r)$ that hits the mirror will be back reflected, leading to the clipping loss

$$\mathcal{L}_C = 1 - \frac{\int_0^{r_{clip}} I(r)rdr}{\int_0^\infty I(r)rdr}. \quad (4.1.18)$$

¹LASEROPTIK GmbH, Garbsen, Germany

For a Gaussian resonator mode, with the mode radii $w_{m;1,2}$ (Eq. 4.1.16) on the mirrors of diameter $D_{1,2}$ this leads to a loss of

$$\mathcal{L}_C(w_i, D_i) = \exp\left(-2(D_i/2)^2/w_{m,i}^2\right). \quad (4.1.19)$$

In Fig. 4.3 the clipping loss depending on the ratio of the mirror diameter and the mode field radius is shown. It can be seen that the mirror diameter has to be ~ 5 times

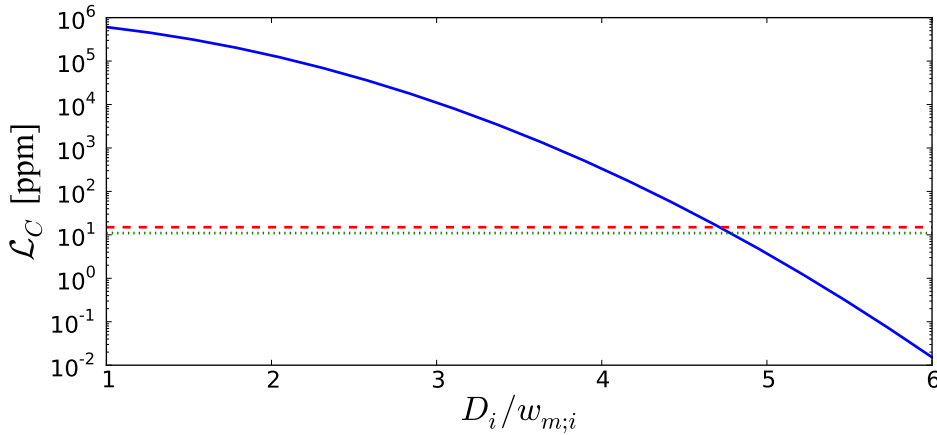


Figure 4.3: Clipping loss for finite mirror diameters (blue line). The clipping loss is reduced by increasing the ratio of the mirror diameter to the beam radius on the mirror. For comparison, the red dashed line indicates the expected absorption loss $\mathcal{L}_A = 15$ ppm and the green dotted line the expected scatter loss $\mathcal{L}_S = 11$ ppm at 780 nm.

the mode radius on the mirror to reduce the clipping losses to the range of \mathcal{L}_A and \mathcal{L}_S .

The finesse of a symmetric high-finesse resonator with identical mirrors given in Eq. 4.1.9 has to be generalized for non-identical mirrors to

$$\mathcal{F} = \frac{2\pi}{\sum_{i=1}^2 \mathcal{L}_{A,i} + \mathcal{L}_{S,i} + \mathcal{L}_C(w_{m;i}, D_i) + \mathcal{T}_i}, \quad (4.1.20)$$

where $\mathcal{L}_{A,i}$ are the absorption losses in the coatings, $\mathcal{L}_{S,i}$ the scattering losses, \mathcal{T}_i the transmissions, $\mathcal{L}_{C,i}$ the clipping losses of the individual mirrors. If the mirrors are applied in the same coating run, it is reasonable to assume that the coating properties are identical and so $\mathcal{L}_{A,1} = \mathcal{L}_{A,2}$, $\mathcal{L}_{S,1} = \mathcal{L}_{S,2}$ and $\mathcal{T}_1 = \mathcal{T}_2$. Then, the mirror losses differ only due to the different effective sizes of the mirrors and the differing mode field diameters on the mirrors, determined by the resonator geometry, as will be shown in Sec. 4.2.2.

4.1.5 Coupling to the resonator

The coupling of the fiber mode with a Gaussian transverse mode profile to the resonator mode is described by the mode overlap of two Gaussian modes [192],

$$\epsilon = \frac{4}{\left(\frac{w_f}{w_c} + \frac{w_c}{w_f}\right)^2 + \left(\frac{\lambda}{\pi w_f w_c}\right)^2 s^2}, \quad (4.1.21)$$

w_f being the waist radius of the fiber mode entering the cavity, w_c the waist radius of the cavity mode as before, and s the distance between the two waist positions. The lensing effect of the concave mirror structure, as well as the additional phase mismatch due to the wavefront curvature of the cavity mode can be neglected for the long FFP resonators presented in this thesis. (A treatment including these effects can be found in the appendix of [73].) For a symmetric cavity, $s = L/2$. We find it convenient to introduce the dimensionless factor

$$\alpha \equiv \frac{L}{2z_R} = \frac{1}{\sqrt{2\frac{R}{L} - 1}}, \quad (4.1.22)$$

such that $\alpha = 1$ for a confocal cavity, $\alpha \rightarrow 0$ for a short cavity, and $\alpha \rightarrow \infty$ when approaching the concentric limit $L = 2R$. The power coupling efficiency can then be written as

$$\epsilon = \frac{4}{\left(\frac{w_f}{w_c} + \frac{w_c}{w_f}\right)^2 + \left(\frac{w_c}{w_f}\right)^2 \alpha^2}, \quad (4.1.23)$$

which depends only on the ratio w_f/w_c and α . Figure 4.4(a) shows this coupling efficiency for different α . The optimum coupling ϵ_{max} for a given α is reached for $w_f/w_c = \sqrt[4]{1 + \alpha^2}$. For configurations with $0 \leq \alpha \lesssim 1$, this corresponds to $1 \leq w_f/w_c \lesssim 1.2$: for cavity lengths up to the confocal length, the optimum fiber mode radius is always close to the waist of the cavity mode. To keep the ratio of the mode waists close to one, fibers of large mode field diameter have to be found for increasing resonator waist radii. In Fig. 4.4, we show the gain of using a large mode area photonic crystal (PC) fiber (see Sec. 4.1.6 for details) compared to a single mode fiber for long FFP resonators.

A coupling efficiency rigorously equal to 1 can only be reached for $\alpha = 0$, but high coupling efficiencies $\epsilon > 0.8$ are possible for a wide range of α values, as shown in Fig. 4.4 b). Whether these efficiencies can actually be realized experimentally depends on the availability of a suitable fiber. As we have seen in Sec. 4.1.4, the clipping loss renders small mode field radii on the mirrors advantageous. Therefore, a good working point for symmetric cavities is close to the confocal configuration $\alpha = 1$, where w_m is smallest. As can be seen in Fig. 4.4, the mode coupling benefits from a decreasing $\alpha < 1$, so that a compromise between reduced clipping loss and maximized coupling has to be found. Note that further optimization is possible in situations where asymmetric cavities can be employed, notably for plano-concave configurations with asymmetric reflectivity.

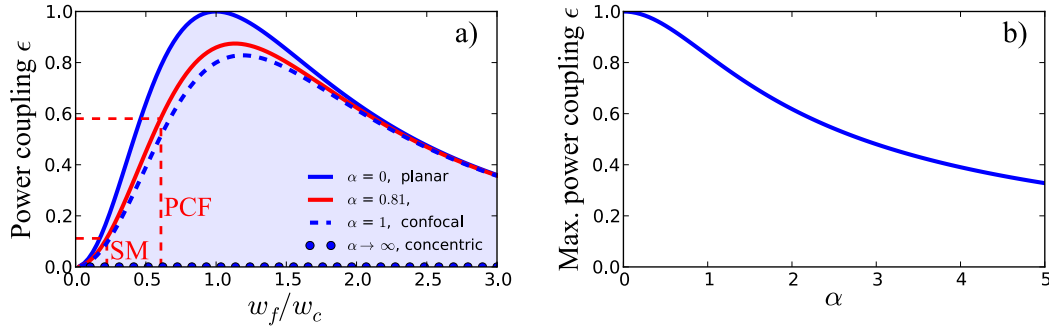


Figure 4.4: a) Power coupling between the incoupling fiber mode and the mode of a symmetric cavity for different values of α (the cavity length normalized to the Rayleigh range of the cavity mode). The red dashed lines indicate the increased power coupling expected from the use of a PC fiber ($w_f = 8.2 \mu\text{m}$) with respect to a standard SM fiber ($w_f = 3 \mu\text{m}$) for an example cavity with $w_0 = 13.5 \mu\text{m}$ and $L = 1.2 \text{ mm}$, chosen to meet the requirements of our experiment, discussed in 2. The blue shaded area shows the stability region of the symmetric cavity. b) Maximum achievable power coupling for a given α . The figure can be found as well in [80].

4.1.6 Photonic-crystal fibers for FFP cavities

As we have seen in Eq. 4.1.23, the mode field diameter of the fiber determines the coupling efficiency between fiber and cavity mode. With typical mirror curvatures, the standard single-mode (SM) fibers used in earlier FFP implementations provide near-perfect mode matching to short cavities, and are used with great success in cavity quantum electrodynamics experiments. Resonant cavity transmission T_c rapidly drops, however, when L is increased beyond a few hundred μm [73, 145]. The discussion in Sec. 4.1.5 shows that mode matching for long fiber cavities can be substantially improved by using a fiber with larger mode field diameter. The need for a well-defined, stable coupling excludes large core MM fibers on the input side of the cavity.² A promising alternative, which we explore here, is to use single-mode fibers with large mode area³. Such fibers are available based on different technologies. Here we use photonic-crystal (PC) fibers. Let us evaluate the power coupling that can be expected for $L = 1.2 \text{ mm}$, which is the targeted cavity length in our application. In practice, at the confocal point itself, stability is compromised by the fact that the mirror ROCs have some tolerance from sample to sample (see Sec. 3.4.3), so we choose not to work at the confocal configuration but with a slightly larger ROC of $R = 1.5 \text{ mm}$, giving with Eq. 4.1.22 $\alpha = 0.81$. The calculated cavity mode waist for these parameters is $w_c = 13.5 \mu\text{m}$ at 780 nm . The red dashed lines in Fig. 4.4 show the expected power coupling efficiency of this mode to a standard SM fiber with $w_f = 3 \mu\text{m}$, $\epsilon \approx 11\%$, and to the NKT LMA20 photonic crystal fiber which we have used in our experiments,

²In principle, this problem can be overcome by the use of time-reversal techniques to achieve the desired mode at the output of the multimode fiber [176]. However, a suitable scheme to obtain an error signal remains to be found.

³The expanded diameter of the core leads to an increased sensitivity to bending losses, as shown in Fig. A.3

which has a specified near-field mode field radius of $w_f = (8.2 \pm 0.8)\mu\text{m}$ at 780 nm (see Tab. 3.1 for more information). This w_f value leads to $\epsilon \approx 58\%$, nearly a factor 6 higher than with the SM fiber. Note however that this idealized calculation neglects effects such as the non-Gaussian shape of the PC fiber mode, so its result should be considered as an upper limit. Experimental details of preparing these fibers for CO₂ machining are discussed in Sec. 3.4.1.

In addition to the improved mode coupling, these PC fibers are “endlessly single mode” [193], allowing stable single-mode guiding over a large wavelength range which can span more than an octave. Here, we will use them with a dual-wavelength coating optimized for 780 nm and 1560 nm.

4.1.7 Conclusion

We have seen that FFP resonators are well described by the standard Fabry-Pérot resonator theory. Their crucial difference is given by the small dimensions of the resonator, leading to small mode radii and robust and stable operation close to devices like an atom chip but give also rise to effects like clipping loss. In the following sections, we will use the introduced theory to analyze the fabricated mirrors and the realized resonators.

4.2 Experimental realization and results

To measure the performance of the improved mirrors presented in Sec. 3.4.3, we have built cavities and performed finesse and transmission measurements. $L > 1.6$ mm is reached before the finesse drops by 50%. This is a significant increase to previous long FFP resonators [145], where the Finesse drops to 50% for $L \sim 200 \mu\text{m}$. In parallel to this work, a different multi-shot CO₂ method was developed in [146], that enabled SM-MM resonator lengths of $L \sim 400 \mu\text{m}$. It is worth noting that the previous resonators used by our group have typical lengths of $L = 40 \mu\text{m}$.

We present measurements of finesse as a function of L for different cavities and compare them to simulations that use the measured mirror profiles, finding good agreement. These simulations also clarify the impact of doping-related shape variations. We also measure cavity transmission over the full length range and directly compare the results of a PC-multimode (MM) fiber cavity to a SM-MM cavity with similar mirror parameters. Subsequently, we present the first⁴ high finesse FFPs simultaneously resonant at 780 nm and 1560 nm and discuss a compact resonator mount optimized for the TACC2 experiment.

For the here presented resonators, two different coatings were applied to the fiber facets, both reflective at 780 nm and 1560 nm, as motivated in Sec. 2.4. One coating was designed for cavities of high finesse of $\mathcal{F} \sim 50.000$ and thus, we will refer to it as the high-finesse (HF) coating, while the second coating enables resonators of moderate finesse of $\mathcal{F} \sim 3.000$ at 780 nm and we will refer to it as the low-finesse (LF) coating.

⁴With the resonators presented in [163]

4.2.1 Finesse and transmission measurements

We have machined a large number of SM, MM and PC fibers and had them coated with an ion-beam sputtered (IBS), dual-wavelength high-reflectivity coating⁵ for 780 nm and 1560 nm. For the HF-coating presented here, the nominal transmission is $\mathcal{T} = 30$ ppm at 780 nm and 1560 nm; the sum $\mathcal{T} + \mathcal{L}$ is 66 ± 2 ppm at 780 nm and 34 ± 2 ppm at 1560 nm, as determined from finesse measurements on short FFP cavities. We have built high-finesse cavities from fiber pairs of different fiber types using a three-axis translation stage equipped with piezo actuators (Thorlabs MAX311D/M) and a two-axis rotation stage (Thorlabs PR01/M, GNL10/M). Several PC-MM cavities were tested at both wavelengths. Compared to cavities with the standard Gaussian-shaped fiber mirrors, the difference was striking. With mirror ROCs on the order of 1 mm, we could readily achieve stable cavities with sizeable transmission for lengths $L > 1$ mm – a length never achieved with the Gaussian-shaped mirrors (Fig. 4.5(a)).

The optical measurements presented below were performed using an external-cavity diode laser at 780 nm. The cavity length L was measured with a simple video microscope⁶. The free spectral range (FSR) was calculated from L as $\nu_{\text{FSR}} = c/2L$. The cavity length was then scanned around this position using the piezo. The linewidth $\delta\nu$ of the TEM₀₀ mode was measured using an electro-optic modulator to generate sidebands for frequency calibration.

These measurements were repeated for different cavity lengths over the full stability range. Cavity transmission on resonance was also measured for every length. In order to eliminate the uncertainty associated with coupling a free-space beam into the cavity fiber, we have first injected the free-space beam into an open-ended fiber and measured the power emerging from the open end before splicing it to the mirror fiber. In this way, the uncertainty is only given by the splice. Based on previous splices, we estimate splice transmission to be $T_{\text{splice}} \gtrsim 0.97$ for SM fibers, and $T_{\text{splice}} \gtrsim 0.9$ for PC fibers. (The typical value for the PC case is closer to 0.95, but is very sensitive to all splice preparations, such as the cleave angle.)

Figure 4.5(b) and (c) show the finesse $\mathcal{F} = \nu_{\text{FSR}}/\delta\nu$ and resonant transmission T_c measured at 780 nm as a function of cavity length for two different cavities: one with an SM fiber (ROC measured by optical profilometry: $R_1 = 1508 \pm 65 \mu\text{m}$) on the incoupling side and a MM fiber ($R_2 = 1629 \pm 73 \mu\text{m}$) for outcoupling; the other with the same MM fiber, but a PC fiber ($R_1 = 1492 \pm 110 \mu\text{m}$) on the incoupling side. Since the ROCs are not exactly equal, an unstable region exists for both cavities where $R_1 < L < R_2$. This is clearly visible in the finesse and transmission data. Comparing the performance of the two cavities, the PC-MM configuration is superior in every respect. It shows higher transmission, especially for large L . This was expected and validates the choice of the PC fiber, although the experimental values do not reach the theoretical optimum yet (see Sec. 4.2.4 below). Furthermore, with this cavity, \mathcal{F} is almost constant up to $L \sim 1.5$ mm, whereas with the SM-MM cavity, it decreases significantly with L , even for short lengths. Such a decrease has been observed for all FFP cavities involving SM fibers [145, 146, 162]; the authors of [146] have conjectured that it is likely to be caused by the ridge in the mirror profile (cf. Fig. 3.19). We confirm

⁵LASEROPTIK GmbH, Garbsen, Germany

⁶Veho VMS-004

this quantitatively using a numerical simulation that takes into account the measured mirror profile, as described below in Sec. 4.2.3. This adverse effect is virtually absent with PC fibers, giving them an additional advantage in FFP cavities.

4.2.2 Analytical model: clipping loss

Clipping loss for Gaussian cavity modes can be described with a simple analytical model (Sec. 4.1.4). In Fig. 4.5(b), the finesse including the loss model of Eq. (4.1.19) was fitted to the data of the PC-MM cavity (solid blue line), leaving $R_{1,2}$ and $D_{1,2}$ as free parameters. The total losses $\mathcal{L}_A + \mathcal{L}_S + \mathcal{T} = 66$ ppm of each mirror were measured independently by short-cavity finesse measurements (see Eq. (4.1.9)) and are used as fixed parameters. Since all our fiber mirrors were coated in the same run, and all substrates are CO₂-machined fused silica, we assume that all loss terms are the same for the two mirrors except for clipping loss. In a perfectly symmetric cavity, it would be difficult to attribute clipping loss values to the individual mirrors, since an overestimation of one value could be compensated by the other. Here, due to the slight difference of the ROCs, the beam radius is diverging on the PC fiber mirror for $L < 1650 \mu\text{m}$ and on the MM mirror for $L > 1650 \mu\text{m}$, and individual \mathcal{L}_{cl} values are obtained with good confidence. (To test the reliability of the fit, we have tried to fix D_2 to a value 5% larger than the best fit, and refit the data with this restriction. This leads to an increase of χ^2 by 46%.) The result (solid blue curve in Fig. 4.5(b)) fits the data well, explaining the sharp drop of \mathcal{F} for $L \sim 1.5$ mm and the decrease for $L \gtrsim 1.8$ mm: in these regions, the mode radii on the mirrors $w_{m;1,2}$ diverge, explaining the decreasing finesse by a rise of the clipping losses. The ROC values $R_{1,2}$ and the effective mirror diameters D_i , resulting from the fit, are shown in Table 4.1 together with the ROCs obtained from the 3D optical profilometry of the mirrors. All values

	clipping loss model		profilometry
	D_m [μm]	R [μm]	R [μm]
PC (m1)	94	1645 ± 60	1492 ± 110
MM (m2)	97	1665 ± 60	1629 ± 73

Table 4.1: Mirror Diameters and ROCs Deduced from the Finesse Data (see Fig. 4.5(b)). The last column shows the ROCs deduced from 2D spherical fits to the mirror profiles.

agree within the error margins, which shows the reliability of our 3D reconstruction, and confirms that the mirrors are well described by spheres. The initial goal of creating mirror structures with $D_m \approx 100 \mu\text{m}$ is reached for both fiber types. Note that this diameter was chosen to meet our requirements. It was not investigated which maximal diameter the multi-shot method can create.

For the SM-MM cavity, \mathcal{F} drops linearly with increasing L (red dots in Fig. 4.5(b)). The simple clipping loss model of Eq. (4.1.19) does not fit this data with any reasonable parameters. This indicates that the loss is not related to clipping on the mirror edges, but has its origin in irregularities of the machined structures shown in Fig. 3.19. This is confirmed by the numerical simulations which we will now describe.

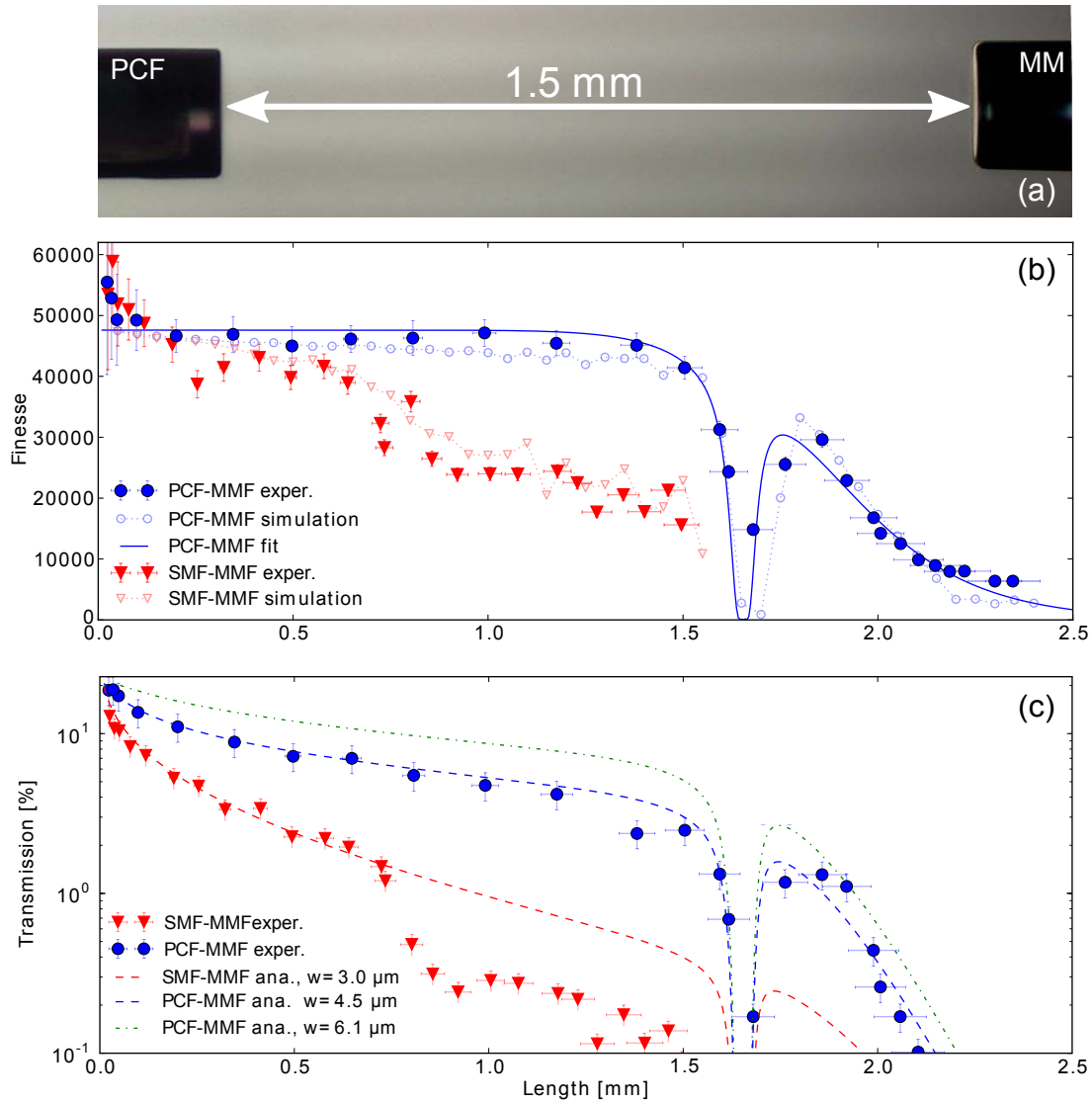


Figure 4.5: (a) Microscope image of a fiber Fabry-Pérot cavity with a PC fiber (left) and a MM fiber (right). The fibers were illuminated from the back to obtain a high contrast for cavity length measurement. The collapsed region of the PC fiber is visible. (b) Experimental results (filled symbols) and simulations (empty symbols with dotted lines, see 4.2.3) for the finesse as a function of length. Results are shown for an SM-MM cavity (red triangles) with $R_1 = 1508 \pm 65 \mu\text{m}$ and $R_2 = 1629 \pm 73 \mu\text{m}$ and for a PC-MM cavity (blue circles) with $R_1 = 1492 \pm 110 \mu\text{m}$ and R_2 as before. (The MM fiber is the same in both cavities.) The blue solid line shows the result of the analytical clipping loss formula (4.1.19) fitted to the PC-MM data. The fit parameters are given in Table 4.1. (c) Transmission of the cavities. The PC fiber improves transmission by more than an order of magnitude for $L > 1 \text{ mm}$. The lines show the calculated transmission using Eq. (4.2.1) and the mode field radius w_f given in the legend. $w_f = 6.1 \mu\text{m}$ is the mode field radius measured independently for the PC fiber (see Sec. 4.2.4). The blue dashed line for $w_f = 4.5 \mu\text{m}$ fits the PC data well, but the large deviation from the nominal value of the PC mode field radius remains unexplained. The sharp drop in finesse and transmission around $L = 1650 \mu\text{m}$ corresponds to the unstable region $R_1 < L < R_2$ of the slightly asymmetric cavity.

4.2.3 Full simulation of the cavity mode using reconstructed mirror profiles

To gain further insight into the role of structure imperfections, and to be able to predict the performance of the machined structures without building a cavity or even applying a coating, we have performed numerical simulations of the cavity eigenmodes using the measured surface profiles. We have used the FFT toolbox OSCAR [194]. This toolbox simulates cavity eigenmodes for arbitrary mirror profiles, which are represented as 2D arrays of height information. Each of the profiles used in the simulations presented in Fig. 4.5 is the average of 120 profiles of the same fiber taken in succession to reduce noise.

The effect of the averaging on the simulated losses is presented in Fig. 4.6 and Fig. 4.7. The surface roughness of ~ 1 nm of a single profile is dominated by noise of the acquisition and overestimates the real roughness manifold (cf. Sec. 3.3.1). This surface noise leads to additional scatter loss in the simulation, not distinguishable from real surface roughness, thus described by Eq. 4.1.17. In Fig. 4.6, a clear distinction between the additional scatter loss for all resonator lengths and the clipping loss for large L can be made. Only for very short resonators with $L \leq 50 \mu\text{m}$ the scatter loss is drastically reduced. Here, the short mirror distance promotes a backreflection on the opposite mirror, which counteracts the loss process. This could be a possible explanation for the higher finesse for short cavities measured in Fig. 4.5 b).

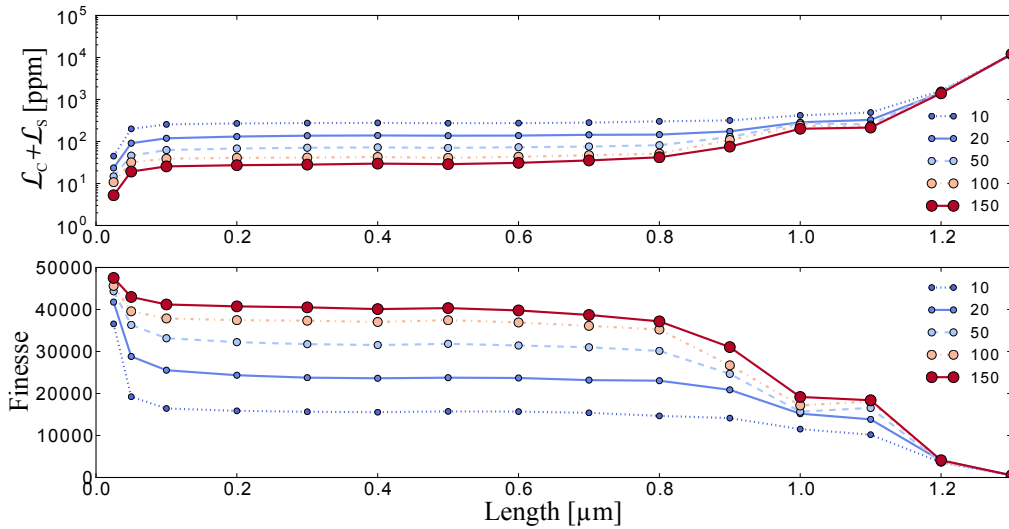


Figure 4.6: Simulated cavity length scan with different numbers of averaged profiles. a) shows the clipping/scattering losses for a cavity consisting of a plane mirror (without roughness) and a reconstructed profile of a machined PC fiber. The mirrors were not aligned, so their orientation is given by the fiber alignment during profilometry. b) shows the calculated finesse if an additional loss of $\mathcal{L} = 33$ ppm and a Transmission of $\mathcal{T} = 30$ ppm is assumed for each mirror. The legend indicates the number of profiles used for the averaged profile.

The surface noise leads to an overestimation of the losses for small numbers of

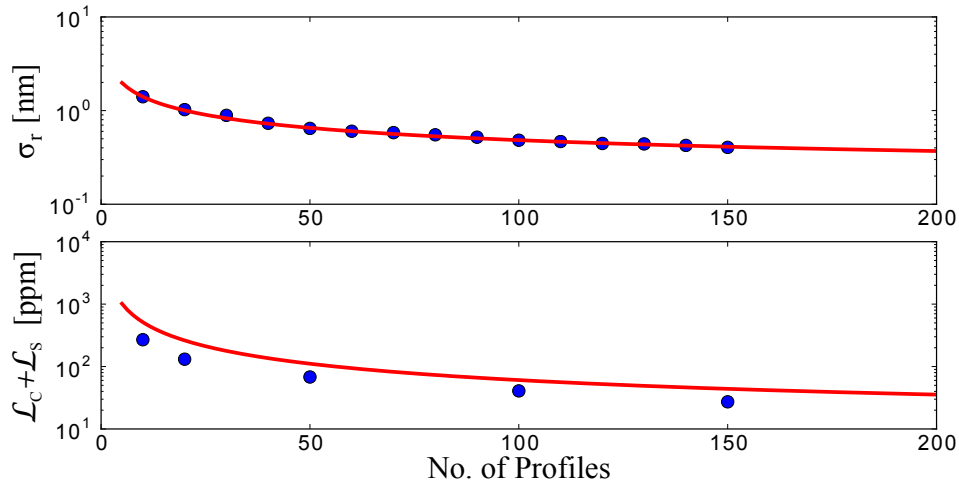


Figure 4.7: Simulated losses with different numbers of averaged profiles. a) The points show the surface roughness (Eq. 3.3.2) for different numbers of averaged profiles of the same PC fiber shown in Fig. 4.6. The red line represents a fit to Eq. 3.3.4. b) The points show the simulated clipping loss for a cavity of length $L = 200 \mu\text{m}$ of the same profile as in a) and a planar mirror (without surface roughness). The line is the expected scattering loss calculated from the values of a) and Eq. 4.1.17. It can be seen that the calculated loss from the deduced surface roughness overestimates the losses in the simulation.

averaged profiles. and drops with the expected $1/N$ dependence, shown in Fig. 4.7. A further reduction of the surface noise and thus the losses can be expected for higher profile numbers, but for an average of 120 profiles absorption loss and transmission already dominate the expected finesse for our coatings.⁷ Apart from this averaging, no fit or filter was used to process the profile data. The profiles here were taken after coating, but no significant deformation with respect to the profiles of the uncoated structures could be seen.

The simulations covered the full fiber diameter with a grid resolution of $1.17 \mu\text{m}$, which is sufficient, as shown in Fig. 4.8. The alignment procedure for the simulation is analogous to that of a real cavity: the two profiles are spaced by a fixed distance L , and the resonance closest to the target cavity length is found. By tilting and translating one of the profiles, the transmission signal is optimized. In our simulations, we have not attempted to rotate the profiles around the cavity axis. Their relative angle is left at an arbitrary value and is not changed in the optimization. This is justified when the deviation from rotational symmetry is small, as it is the case here. The computation time for a single cavity length, including the alignment procedure, was on the order of one hour on a generic desktop PC. To reach such a reasonable time, the simulations were carried out with higher mirror transmission ($\mathcal{T}_{sim} = 0.01$) compared to the experiment. This has no effect on the simulated clipping and scattering losses of

⁷This depends as well on the quality of the single profile (cf. Fig. 3.5), which should be taken at optimal profilometry conditions.

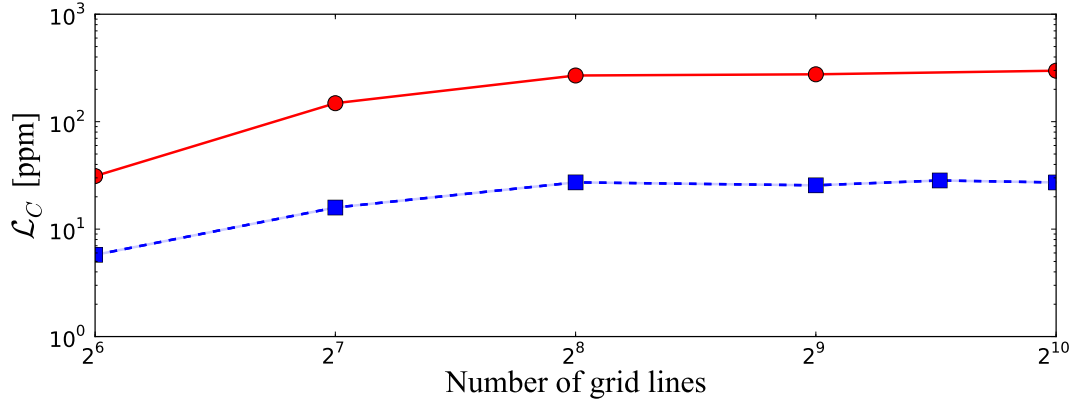


Figure 4.8: Simulated losses depending on grid resolution. The simulated scatter losses are shown for a cavity of $L = 200 \mu\text{m}$ consisting of a plane mirror and a reconstructed profile with an average over $N=10$ profiles (red circles) and for $N=150$ (blue triangles) for changing grid resolution. The window size for the simulation is $300 \times 300 \mu\text{m}^2$, giving a grid resolution of $4.7 \mu\text{m}$ for the lowest and $0.29 \mu\text{m}$ for the highest grid line number shown. The stagnation at $2^8 = 256$ grid lines makes this our chosen grid resolution of $1.17 \mu\text{m}$ for the simulations shown in this thesis.

the mirrors. The losses and transmission of the coating, which are not contained in the simulation, are experimentally determined by short-cavity finesse measurements and added to the simulated diffraction losses to determine the finesse using Eq. (4.1.9). The results of the simulated finesse for one mirror pair are shown in Fig. 4.5 b) as empty symbols connected by dotted lines for both cavities. Simulation and experiment are in excellent agreement, which confirms that the linear decay of the finesse for the standard single-mode fiber is explained by the structure itself. Additional loss effects from coating variations (as discussed in [145, 195]) are not significant here. Furthermore, this remarkable agreement means that such simulations could be used to optimize structures produced by laser dot milling without laborious iterations of coating and cavity construction.

4.2.4 Cavity transmission

To compare the measured cavity transmissions to theoretical expectations, we have used the simple model described in [73]. The power coupling efficiency ϵ between the input fiber and the cavity mode (Eq. (4.1.21)) limits the resonant transmission T_c of a symmetric FFP cavity as

$$T_c = \epsilon \frac{\mathcal{T}^2}{(\mathcal{T} + \mathcal{L})^2}, \quad (4.2.1)$$

where $\mathcal{L} = \mathcal{L}_S + \mathcal{L}_A + \mathcal{L}_C$ is the sum of all mirror losses. (We are assuming that the coupling to the MM output fiber is perfect, which is reasonable because of the large mode area and high acceptance angle of the MM fiber.) The lines in Fig. 4.5(c)

are calculated using this equation. The \mathcal{T} values are the same for all three curves and are those of the multilayer coating (see Sec. 4.2.2). The length-dependent \mathcal{L} values are deduced from the finesse measurements and take the additional loss with increasing L into account. The coating properties determine the maximum $T_c = 0.207$, achieved for short cavity length. The red dashed line uses the nominal mode field radius $w_f = 3 \mu\text{m}$ of the SM fiber and fits the SM-MM data well for lengths up to $L \approx 770 \mu\text{m}$. The sharp drop at this length is not expected from Gaussian mode overlap and could be due to imperfections of the mirror profile discussed above. In that case, optimization of this profile would bring T_c into agreement with the prediction also for larger L . However, this would still be more than five times smaller than the measured T_c of the PC-MM cavity. This confirms the advantage of the PC fiber. Nevertheless, headroom for further improvement remains: indeed, the PC-MM result falls below the expected value if we assume the catalog value for the mode field radius of the PC fiber ($w_f = 8.2 \mu\text{m}$). A good fit is obtained for a much smaller $w_f = 4.5 \mu\text{m}$ (blue dashed line in Fig. 4.5). To investigate the disagreement more closely, we have measured the mode field radius of the PC fiber independently. The beam profile was imaged with a camera at several distances (1.5 mm - 2.5 mm) from the fiber output, to determine the divergence θ of the beam. By using $w_f = \lambda/(\pi\theta)$, we found $w_f = (6.1 \pm 0.2) \mu\text{m}$, significantly smaller than the catalog value. The calculated transmission for this w_f is shown in Fig. 4.5 (green dash-dotted line), it remains above the measured values. The fact that the PC fiber mode is not strictly Gaussian may explain some of the deviation. To investigate other possible sources, we have tentatively added tilt and displacement in the calculation of ϵ following [196], but no parameter set could be found which fits the experimental data as well as the model without displacement or angle and $w_f = 4.5 \mu\text{m}$. Simple propagation of the outcoupled beam in the collapsed part (assumed homogenous) changes the coupling to the cavity mode only slightly and does not explain the difference between theory and experiment. Further possible effects of wavefront distortions, diffraction or lensing at the position of the melted holes of the PC fiber remain to be investigated. Understanding these effects may lead to further improvements of coupling and transmission.

4.2.5 Higher order modes

To fully characterize the cavities, we studied as well the behavior of higher order transversal modes. As the mirrors are not rotationally symmetric the higher order resonator modes are well described by Hermite-Gauss modes, a family of solutions of the paraxial Helmholtz equation [188]. The wavefront curvatures of the higher order modes are the same as for the transversal 0^{th} order mode (Eq. 4.1.15) - the earlier discussed Gaussian mode. The field of the TEM_{ml} mode is then described by

$$E_{ml}(\vec{r}) = \frac{A_{m,l}}{\sqrt{w_x(z)w_y(z)}} \mathcal{H}_m\left(\frac{\sqrt{2}x}{w_x(z)}\right) \mathcal{H}_l\left(\frac{\sqrt{2}y}{w_y(z)}\right) \times \exp\left[-\frac{x^2}{w_x(z)} - \frac{y^2}{w_y(z)} - \frac{ikx^2}{2R_x(z)} - \frac{iky^2}{2R_y(z)} - i(kz - \phi_{ml}(z))\right] \quad (4.2.2)$$

with $\vec{r} = (x, y, z)$, $w_{x/y}(z)$ and $R_{x/y}(z)$ being the radii and the wavefront ROCs of the mode in x and y direction at position z. The ellipticity of the cavity mode splits up the degeneracy of the higher order modes via the Gouy-phase

$$\begin{aligned}\phi_{m,l}(z) &= (m + 1/2) \phi_{0;x}(z) + (l + 1/2) \phi_{0;y}(z) \\ \phi_{0;x/y}(z) &= \arctan \frac{\lambda z}{\pi w_{0,x/y}^2}.\end{aligned}\quad (4.2.3)$$

The normalization constant

$$A_{m,l} = \sqrt{\frac{2}{2^{m+l} m! l! \pi}} \quad (4.2.4)$$

ensures $\int \int dS |E_{ml}(\vec{r})|^2 = 1$. The frequencies of the resonator modes are given by [162]

$$\nu_{q;ml} = \nu_F \left(q + \frac{l + 1/2}{\pi} \Delta\phi_x + \frac{m + 1/2}{\pi} \Delta\phi_y \right) \quad (4.2.5)$$

where $\Delta\phi_{x/y} = \phi_{0;x/y}(z_1) - \phi_{0;x/y}(z_2)$ is the Gouy-phase difference⁸ at the two mirror positions z_1 and z_2 and $q = 0, 1, 2, \dots$ is the longitudinal mode number of the cavity mode, fulfilling the resonance condition $2kL - 2(m + l + 1) \Delta\phi = 2\pi q$.

Besides the different resonance frequencies, their main characteristic is the transverse mode profile given by the Hermite polynomials, depicted in Fig. 4.9.

Mode overlap: The transverse mode profile leads to an individual coupling of each cavity mode $E_{ml}(\vec{r})$ to the incoming fiber mode $E_f(\vec{r})$ [197].

$$\epsilon = \left| \int \int E_{ml}^*(\vec{r}) E_f(\vec{r}) dS \right|^2 \quad (4.2.6)$$

For the TEM₀₀ mode the overlap can be calculated analytically for elliptical beams under the assumption that the mode factors as [192]

$$E_{00}(x, y) = E_{00}(x, w_x, \kappa_x) E_{00}(y, w_y, \kappa_y) \quad (4.2.7)$$

leading to

$$\tau_{a,x} = \frac{2}{[\bar{w}_x/w_x + w_x/\bar{w}_x + (1/2k\bar{w}_x w_x)^2 (\bar{\kappa} - \kappa)^2]^{1/2}} \quad (4.2.8)$$

giving the coupling

$$\epsilon = \tau_{a,x} \cdot \tau_{a,y}. \quad (4.2.9)$$

Here, $w_{x,y}$ and $\kappa_{x,y} = 1/R_{x,y}$ are the mode radii and curvatures of the incoming mode at a chosen intersection plane. $\bar{w}_{x,y}$ and $\bar{\kappa}_{x,y} = 1/\bar{R}_{x,y}$ are the radii and curvatures of the second mode (here cavity mode) at the same intersection plane, depicted in Fig. 4.10. The radii and curvatures at a given position z_{int} can be calculated from the mode waists $w_{0,c/f}$ and the waist position $z_{0,c/f}$ with the standard Gauss beam formulas Eq. 4.1.14, 4.1.15, leading to the earlier presented representation in Eq. 4.1.21.

⁸The Gouy-phase difference in [162] is given for one planar mirror with $R = \infty$

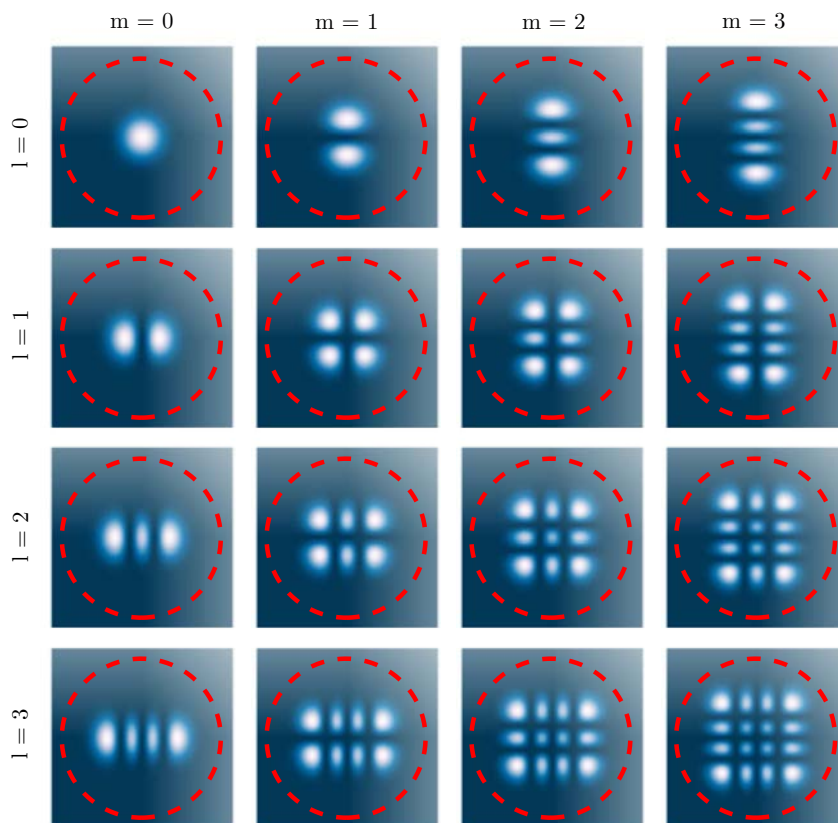


Figure 4.9: Intensity distribution of the Hermite-Gauss modes on a cavity mirror of a cavity with length $L = 1.22$ mm and ROC $R = 1.56$ mm. The edge length is $130 \mu\text{m}$. The red circles indicate a clipping radius of $r_{clip} = 58 \mu\text{m}$.

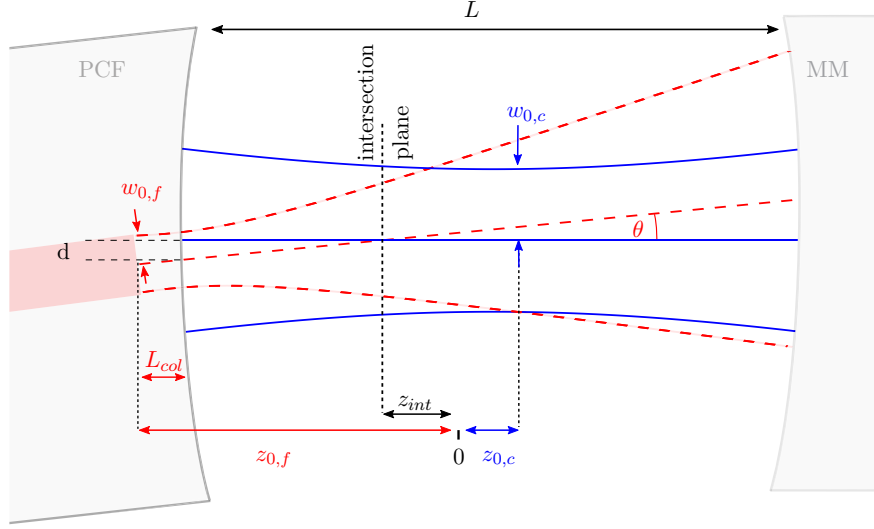


Figure 4.10: Cavity mode (blue, straight) with input fiber mode (red dashed). Shown are the critical parameters for the mode coupling. The transversal displacement d of the two modes at the PCF-mirror position and the relative angle θ of the two modes. For different $R_{PCF} \neq R_{MM}$ of the two mirrors, the cavity mode waist is not centered, so $z_{0,c} \neq 0$. The crossing position z_{int} of the two modes is crucial for the mode overlap calculation.

The analytical formula can be generalized so that the two modes show a transversal misalignment d and an angle θ , shown in Fig. 4.10. The angle θ can be introduced by adding to the exponent in Eq. 4.2.2 an additional phase angle $k\theta x$, yielding the coupling in the $x - z$ plane as [192]

$$\tau_x = \tau_{a,x} \exp [-(\theta/\theta_e)^2] \quad (4.2.10)$$

with

$$\theta_e = \frac{2^{3/2}}{k\tau_{a,x}(\bar{w}^2 + w^2)}. \quad (4.2.11)$$

With $\theta \neq 0$, the mode overlap calculated with Eq. 4.2.9 is dependent on the chosen intersection plane. This can be interpreted as the choice of the center of rotation, which evidently alters the coupling. The intersection plane chosen defines then the center of rotation, which is the crossing point of the optical axes of the two modes, as depicted in Fig. 4.10. By deliberately shifting the crossing point by $\Delta z_{int} = d/\tan(\theta)$ an additional transversal translation d is generated. Using $\Delta z_{int} \rightarrow \infty$, $\theta \rightarrow 0$ a translation without tilt can be realized [192].

For the higher order transversal modes with $m, l \neq 0$, we calculate the mode overlap numerically using Eq. 4.2.6, where again Eq. 4.2.2 is extended by the additional phase angle $k\theta x$ in the exponent. The resolution of the mesh for the calculation is typically $\sim 2 \text{ px}/\mu\text{m}$ and is chosen so that the numerical simulation for the TEM_{00} mode reproduces the analytical calculations of Eq. 4.2.9. The size of the integration region is chosen to be $\sim 10 \times w_{max}$, the biggest encountered mode radius.

Since in our typical cavities the deviation of the two radii $w_{0,x/y}$ is below 5%, the effect on the amplitude profile can be neglected and we use for the numerical calculations the simplification $w(z) = w_x(z) = w_y(z)$. Note, that this cannot be neglected in the calculation of the resonance frequencies in Eq. 4.2.5.

Fig. 4.11 shows the coupling of the first few higher order resonator modes to the incoming fiber mode. It can be seen that for a long resonator, the higher order modes with even m and l show a stronger coupling to the incoming TEM_{00} mode for small translations $d < w_f$, explained by their non-zero amplitude in the center.

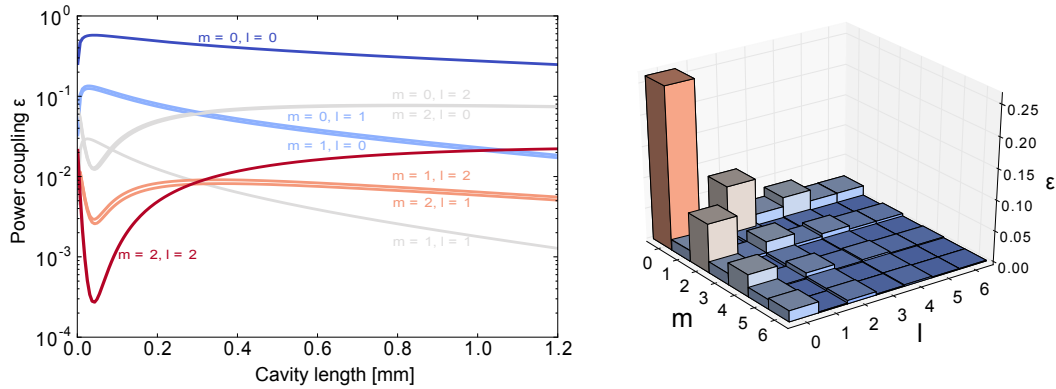


Figure 4.11: Higher order mode coupling. The graphs show the coupling of the fiber mode with waist $w_f = 5.3 \mu\text{m}$ and a collap length of $L_{col} = 60 \mu\text{m}$ to the first few higher order modes of a cavity with a ROC of $R = 1.56 \text{ mm}$. The transverse misalignment is $d_x = 2.6 \mu\text{m}$ and $d_y = 2.7 \mu\text{m}$. On the left the length of the cavity is varied, on the right the coupling is shown for the cavity length $L = 1.22 \text{ mm}$.

Clipping loss: Besides the different coupling to the incoming mode, the fact that the intensity distribution for the higher order modes is not as well centered as for the TEM_{00} mode, leads to increased clipping losses with higher l and m (see Fig. 4.9). The clipping loss per mirror is given by Eq. 4.1.18 to be

$$\mathcal{L}_C = 1 - \frac{\int_0^{r_{clip}} I_{ml}(\vec{r}) r dr}{\int_0^\infty I_{ml}(\vec{r}) r dr} \quad (4.2.12)$$

but cannot be simplified to Eq. 4.1.19 for higher order transversal modes. Here $I_{ml}(\vec{r}) = E_{ml}^*(\vec{r})E_{ml}(\vec{r})$ is the intensity of the according mode and r_{clip} the size of the mirror. Fig. 4.12 shows the clipping loss for a cavity with the same parameters as the one presented in Fig. 4.11 and a LF-coating. The clipping loss leads to a reduction of the finesse and transmission of the cavity, presented in Fig. 4.12 b), c). One can see that the higher order modes show higher clipping loss for a given length and the loss increases faster with the cavity length.

Taking the mode coupling and the clipping loss into account, we modeled the transmission of the cavities: Fig. 4.13 shows the measured spectrum of a low finesse

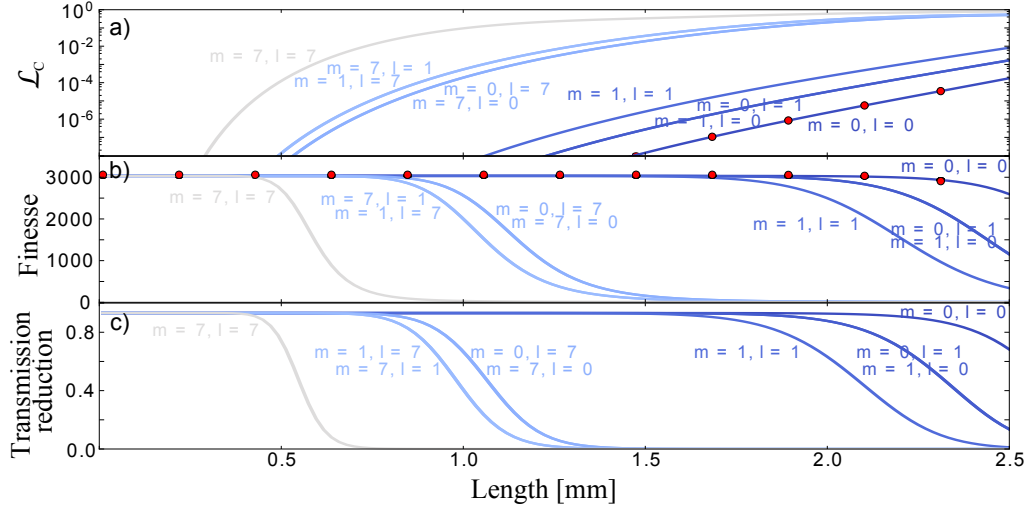


Figure 4.12: Clipping loss for higher order modes. a) shows the calculated clipping loss for some selected modes of a cavity of length $L = 1.22$ mm, a ROC of $R = 1.56$ mm and a clipping radius of $r_{clip} = 58 \mu\text{m}$. The red dots show the result of the analytical formula in Eq. 4.1.19, the lines the result of the numerical integration following Eq. 4.1.18. b) shows the resulting finesse assuming the LF-coating with a mirror transmission of $\mathcal{T} = 1000$ ppm and losses $\mathcal{L} = 33$ ppm at 780 nm. c) shows the expected reduction of the transmission with the same \mathcal{T} and \mathcal{L} .

cavity ($F \approx 3000$) with the calculated frequencies (Eq. 4.2.5) and the according mode overlap with the incoming fiber mode (Eq. 4.2.6). The cavity length and the collaps length were measured with a microscope to be $L = 1.22$ mm and $L_{col} = 60 \mu\text{m}$. The measured spectrum was linearly stretched to meet the calculated free spectral range. Subsequent, the two radii of curvature R_1 , R_2 of each mirror were chosen to reproduce the frequency splitting of the higher order modes ($R_1 = 1.56$ mm, $R_2 = 1.52$ mm). Note that we simplified the situation by assuming the two cavity mirrors to be identical and having both the ROCs R_1 , R_2 .⁹ Thereby, the cavity mode was calculated to reproduce the coupling of each individual mode. The spectrum calculated in this way shows already a good qualitative agreement with the data. The measured transmissions for the modes with $l, m < 3$ were then used to find the translations d_x , d_y and the fiber waist w_f that reproduce the data. The fit to the experimental data gives $d_x = 2.64 \mu\text{m}$, $d_y = 2.77 \mu\text{m}$ and the fiber waist $w_f = 5.33 \mu\text{m}$, again well below the datasheet value of $w_f = 8.2 \mu\text{m}$ (cf. Sec. 4.2.4). The calculated higher order modes with $l + m > 3$ showed systematically a higher transmission than the data, without adding the clipping loss to the model. With the introduced clipping radius $r_{clip} = 58 \mu\text{m}$, the calculated transmissions in Fig. 4.13 reproduce the data very well.

For the mode $m + l = 6$, the clipping loss reduces the transmission of the central

⁹The ROC of the two mirrors of the cavity are measured as well with our profilometer to be: $R_{PCF,1} = 1559$, $R_{PCF,2} = 1468 \mu\text{m}$, $R_{MM,1} = 1612$, $R_{MM,2} = 1523 \mu\text{m}$, agreeing in the error margin with the values deduces from the spectrum. The two values represent the ROC along the two main axis of a 2D paraboloid fitted over a region of interest of radius $r_{ROI} = 18 \mu\text{m}$, close to the cavity mode radius on the mirrors.

modes not strongly enough, while reducing the mode with $m, l = 6$ to the measured value. Most likely, this shows a limit of the clipping loss model, where a sharp mirror edge is assumed, which is not the case for our mirrors. The sharp edge leads to a strong impact on the outlying modes, while the more centered modes are untouched. A smooth decay of the reflectivity at the mirror edge could reduce the disparity of the transmission reduction.

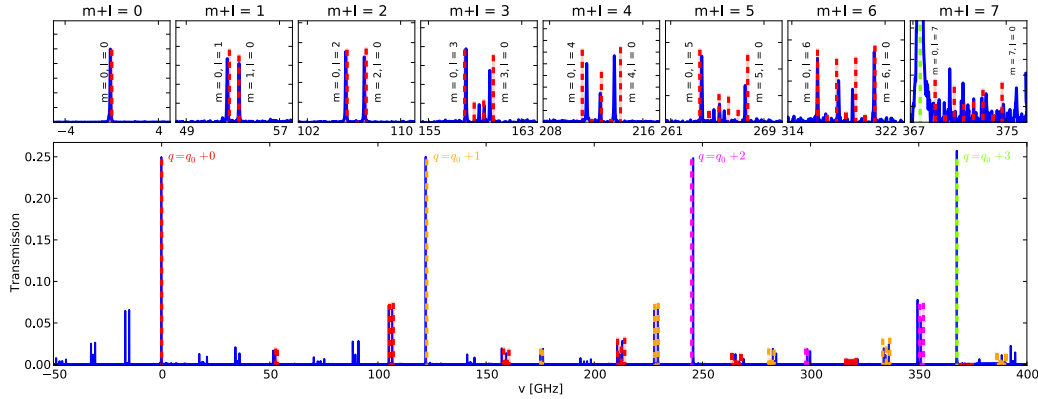


Figure 4.13: The bottom row shows a spectrum of the low finesse cavity (blue line), taken by scanning the laser (Velocity 6312) around 780 nm with a scan speed of ~ 1.5 nm/s. The x -axis was calibrated with the calculated FSR for the cavity length $L = 1.22$ mm, measured with a microscope. The colored dashed lines indicate the calculated frequencies and transmissions for higher order modes. The overlap of the higher order modes is taken into account as well as transmission reduction due to clipping loss. The top row shows the magnification of each higher order mode of the $q = q_0$ transversal mode. To compensate the length jitter of the cavity the data was shifted in each subframe to meet the theory by the following values [0, 1, 0.3, 1, 0.6, -1.6, -0.6, 0] GHz.

Mode crossing: While gluing the low finesse cavity (cf. Sec. 4.2.7), a spurious mode appeared close to the TEM_{00} of interest, shown in a detailed scan in Fig. 4.14 a), since the scan in Fig. 4.13 is too fast to reveal it. Using the analysis above, the mode order could be identified to be $m + l = 7$, most likely the mode with the lowest frequency $m = 0, l = 7$. In [162, 198], the mode coupling of different transversal modes is described, which increases finesse and transmission of the higher order mode in expense of the lower order mode. By approaching the frequency of the TEM_{00} mode of lower longitudinal order the $m+l=7$ mode, that was barely visible before, is gaining strength. Fig. 4.14 b) shows how the mode can change its resonance frequency during the gluing: by changing one of the ROCs by only 1% the resonance frequency of the higher order mode changes by nearly 3 GHz, which is roughly 70 times the resonance line width. Since our mirrors are not perfectly spherical, already a small transversal shift can alter the effective ROC the mode is sampling on the mirror surface.

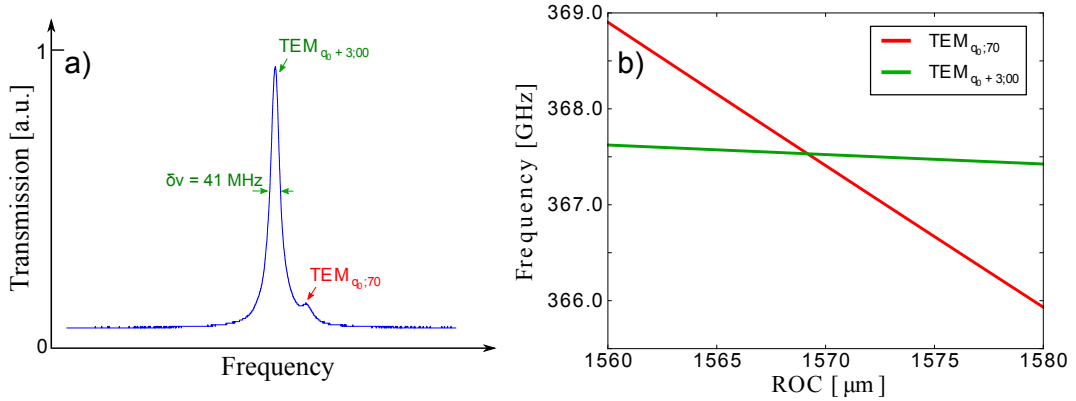


Figure 4.14: Mode crossing. a) shows a zoom in the transmission spectrum of the LF-cavity of length $L=1.22 \text{ mm}$, presented in Fig. 4.13. Close to the TEM_{00} mode, a second peak can be seen, most likely of order $m=0, l=7$. b) shows the sensitivity of the resonance frequency of the higher order mode to the ROC. $R_1 = 1.52 \text{ mm}$ is kept constant, while R_2 is varied by only $\approx 1.3\%$. Note that the role of R_1 and R_2 can be exchanged as well. Here, the avoided crossing [162] is not modeled.

The analysis of the higher order modes confirms again the validity of the mode coupling model, beforehand only applied to the TEM_{00} modes of FFP resonators. It gives an independent measure of the effective mirror curvatures and information on the translation and tilt of the fiber and the resonator mode. Here it confirms the smaller effective fiber mode diameter for the PC fiber found in Sec. 4.2.4. It served our initial motivation to identify the spurious mode shown in Fig. 4.14 a). The coupling of transversal modes renders the frequency and properties of the higher order transversal modes very important, since it can strongly diminish finesse and transmission of the TEM_{00} mode. The fact that in our low finesse resonator the 7th order mode, barely visible in the spectrum, interferes with the fundamental mode, tightens further the resonator alignment restrictions. For future resonator constructions a detailed search for higher order modes around the envisaged resonator length is recommended.

After the full characterization of the long FFP resonators at 780 nm, we will now investigate the functionality of the double- λ coating, enabling high finesse as well for 1560 nm.

4.2.6 Double λ -Resonators

The initial plan for the TACC2 experiment is to trap the atoms in a magnetic trap provided by the chip, presented in chapter 5. If the perturbation by the squeezing light thwarts this approach, an alternative would be to trap the atoms in a far red detuned 1D-lattice as in [50]. In either way, locking of the cavity is necessary, which should evoke minimal light shifts on the atoms. This is again best realized with light far detuned from the atomic transition.

For this reason, we applied a coating highly reflective at 780 nm and 1560 nm to allow for locking (and if necessary trapping) at 1560 nm, while squeezing is performed with light close to 780 nm (cf. 2.3). Locking and stable trapping puts the need of a fixed frequency relation between the light at 780 nm and the light at 1560 nm. A convenient way to obtain this is the frequency doubling of the latter in a PPLN crystal¹⁰, as shown in Fig. 4.16.

The resonance condition has to be fulfilled for both wavelengths at the desired cavity length L , which requires customized reflection phases ϕ_{780}, ϕ_{1560} of the coatings. The resonance condition for double resonance then reads as

$$\begin{aligned}\pi q_{780} &= Lk_{780} - \phi_{780} - 2\phi_G(L, R) \\ \pi q_{1560} &= Lk_{1560} - \phi_{1560} - 2\phi_G(L, R)\end{aligned}\tag{4.2.13}$$

where the sign of the mirror phases follows the convention of the coating company¹¹ and $\phi_G(L, R)$ is the Gouy-phase accumulated over a quarter round trip. To maximize the overlap of the two standing waves, the standing wave at 780 nm has to have an antinode in the cavity center, while the standing wave at 1560 nm can either have a node or an antinode in the center. The wavelength close to 780 nm is determined by the D₂-line of ⁸⁷Rb, setting with $\lambda_{1560} = 2\lambda_{780}$ as well the wavelength close to 1560 nm. For our configuration of $L = 1.2$ mm and the mirror ROC $R = 1.5$ mm, we choose the phase pair $\phi_{780} = 90^\circ, \phi_{1560} = 185.3^\circ$ for our low-finesse coating¹². The expected atom-light coupling and the intensity distribution along the cavity axis are shown in Fig. 4.15. Loading the lattice out of a centered cloud with the expected length of 462 μm (see Sec. 2.4) the coupling varies less than 5%. To test the resonator performance at the two wavelengths and to verify the simultaneous resonance, we carried out a resonator length scan as in Sec. 4.2.1, now with light at 780 nm and 1560 nm in the resonator. For this we used the setup presented in Fig. 4.16. To extract the coating phases we injected light at 1560 nm which we locked via frequency doubling to the $F = 3 \rightarrow F' = 4$ cycling transition of ⁸⁵Rb with $\lambda = 780.2437$ nm.¹³ The cavity length was set to the desired value and then fine-tuned, so that the light at 1560 nm was resonant. The light at 780 nm was provided by a largely tunable ECD laser¹⁴ and the wavelength was set, so that the light at 780 nm was also resonant at the chosen length. The tuned

¹⁰WH-0780-000-F-B-C, NTT Electronics corp., Japan

¹¹LASEROPTIK, Garbsen, Germany

¹²The mirror phases of the high finesse coating were optimized for another experiment [163, 199] and are $\phi_{780} = 207.6^\circ, \phi_{1560} = 99.4^\circ$. To fulfill the double resonance this requires a shift of the 1560 nm light of $\Delta\nu \sim 24$ GHz.

¹³This transition has the advantage of a strong signal in the used modulation transfer spectroscopy [201] and is only ~ 2.2 GHz away from the transition later used in the experiment.

¹⁴Velocity 6312

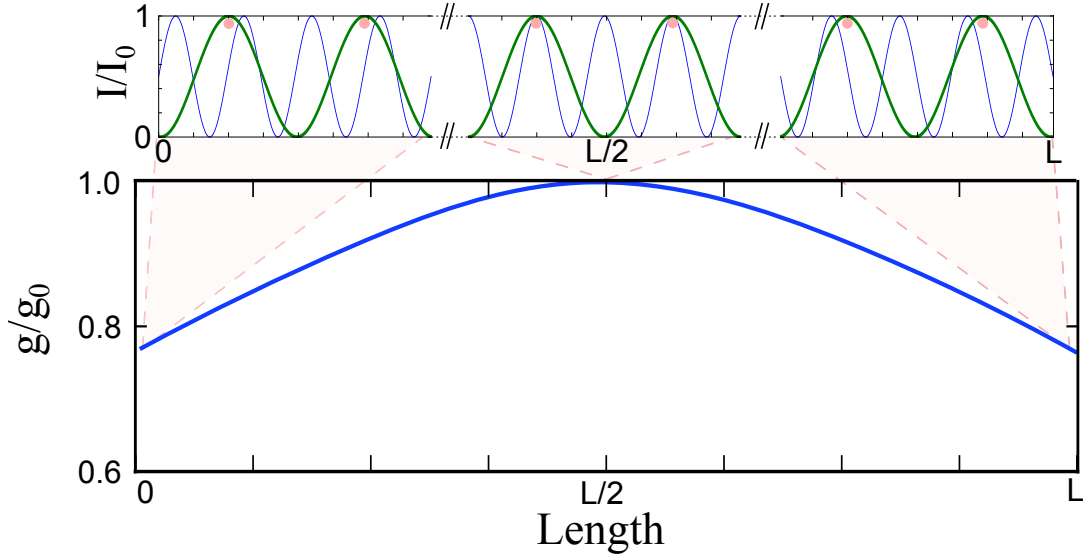


Figure 4.15: $\lambda_{780,1560}$ standing wave configuration. The lower graph shows the modulation of the atom-resonator coupling of Eq. 2.2.7 for atoms at $T = 0$ K due to the non-perfect overlap of the two standing waves, depicted in the insets above. The blue line shows the standing wave close to 780 nm, the green line the standing wave close to 1560 nm. The red dots depict the atom trap positions in the maxima of the standing wave at 1560 nm. To fulfill the resonance condition for $\lambda_{780} = 780.241$ nm and $R = 1.5$ mm the cavity length was set to $L = 1200.37 \mu\text{m}$, with the chosen coating phases of $\phi_{780} = 90^\circ$, $\phi_{1560} = 185.3^\circ$.

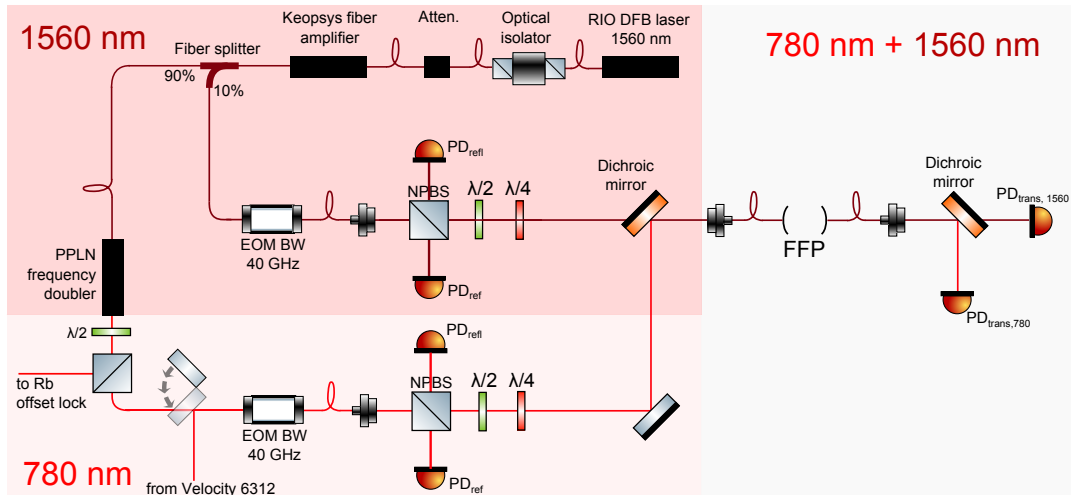


Figure 4.16: Laser setup for 780 nm and 1560 nm. Light at 780 nm and 1560 nm can be coupled simultaneously to the FFP resonator. With the flip mirror we can choose between the widely tunable velocity laser, or use the frequency doubled light. Using components of the free optical component library of [200].

and the locked light at 780 nm were measured with a wavemeter¹⁵. The results are shown in Fig 4.17, where the experimental data is compared to the expected resonant wavelengths. The dependence, providing simultaneous resonance, reads as [163]

$$\nu_1 = 2\nu_2 - \frac{c}{\pi L} (\phi_G(L, R) + \phi_{1560} + \phi_{780}/2) - j\nu_{FSR}, \quad (4.2.14)$$

where j is an even integer. Using $\lambda = c/\nu$, the calculated curves for $R = 1.5$ mm and the mirror phases $\phi_{780} = 90^\circ$, $\phi_{1560} = 185.3^\circ$ are in excellent agreement with the data. The crossing at $L = 1.22$ mm shows that $\lambda_{1560} = 2\lambda_{780}$ for our envisaged resonator length. This enables the use of the frequency doubling technique for the generation of the light at 780 nm, ensuring a stable frequency link of the two wavelengths.

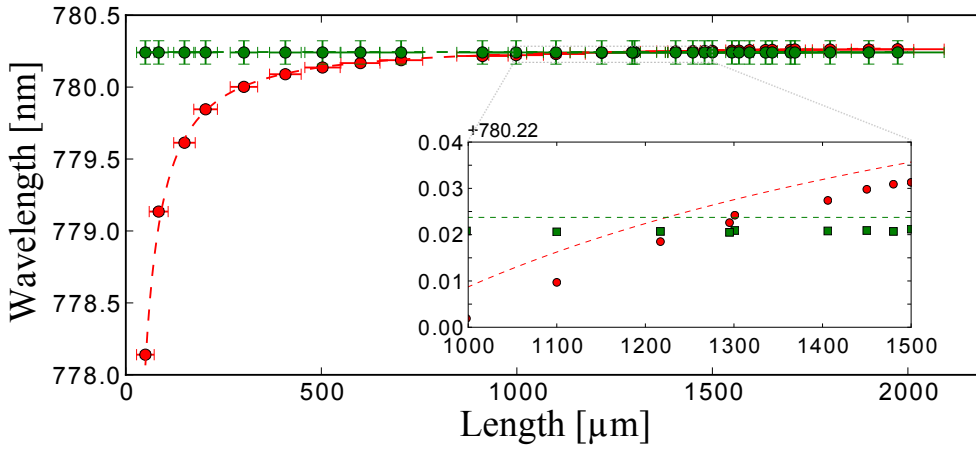


Figure 4.17: Co-resonant length scan. The two wavelengths are shown, which are co-resonant at different lengths of the resonator. The light at 1560 nm is represented by the measured wavelength after frequency doubling (see text). In the inset, the crossing at $L = 1.22$ mm can be seen. The offset of the data to the calculation is most likely due to an outdated calibration of the wavemeter.

In parallel to the wavelength determination, we measured again the transmission and finesse of the resonator, to investigate the performance of the low finesse coating. The measured cavities performed well at both wavelengths, and the measured finesse values were consistent with the coating specifications and the numeric simulations as presented in Fig. 4.18. For the simulation (open triangles) and the analytical clipping loss model (solid line), the nominal mirror transmissions of $\mathcal{T}_{1560} = 80$ ppm and $\mathcal{T}_{780} = 1000$ ppm were used with additional losses (excluding clipping loss) determined by short cavity measurements of $\mathcal{L}_{1560} = 15$ ppm and $\mathcal{L}_{780} = 30$ ppm. The mirror ROCs¹⁶ are extracted from the reconstructed profiles and for 1560 nm the clipping radii are $r_{c,PCF} = 56$ μm and $r_{c,MM} = 65$ μm . The experimental data is again in good

¹⁵Wavelength meter WS-6, HighFinesse

¹⁶ $R_{PCF,1} = 1587$ μm , $R_{PCF,2} = 1500$ μm , $R_{MM,1} = 1525$ μm , $R_{MM,2} = 1580$ μm . For the clipping loss model the mean value for each mirror was taken.

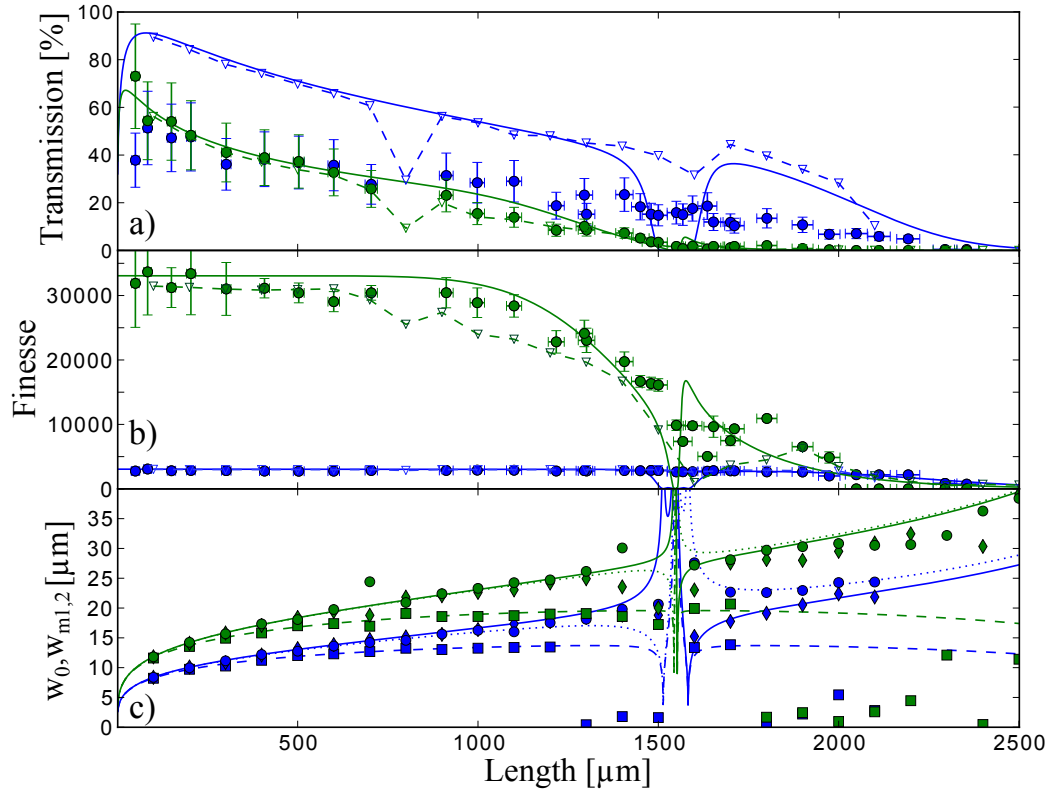


Figure 4.18: Length scan of low finesse resonator. The data at 1560 nm is presented in green, the data at 780 nm in blue. a) shows the transmission of the resonator. The data (filled circles) was rescaled to account for a faulty splice for this resonator. The large error bars of $\pm 30\%$ account for the uncertainty in the splice loss estimation. The open triangles show the results of the numerical simulation, the solid lines the analytical calculation. b) shows the measured finesse (filled circles), the simulation (open triangles) and the analytical model of Eq. 4.1.19 (solid line). c) shows the mode waist radii (squares), the radii on the PCF fiber (diamonds) and on the MM fiber (circles) extracted from the numerical simulation. The solid lines show the correspondent analytical values of Eq. 4.1.16. For the simulated radii close to 0 for $L > 1.2$ mm the initialization of the fit did not succeed.

agreement with the numerical simulations, but for cavity length $L > 900 \mu\text{m}$ the finesse at 1560 nm is systematically underestimated by the simulations. We found later that some dust particles were present on the fiber during the 3D-reconstruction, which could be a possible explanation. For the scan shown, the transmission data is strongly diminished by a faulty splice with a reduced transmission of only $\sim 20\%$ at 780 nm and $\sim 30\%$ at 1560 nm. The data in the plot was rescaled to show the fiber-cavity coupling. The uncertainty in the splice loss results in the large error bars shown. The transmission is again a factor of 2 lower than the value expected from the analytical mode overlap (Eq. 4.1.21), assuming a fiber mode waist radius of $w_{f,780} = 8.2 \mu\text{m}$. For the light at 1560 nm, the transmission matches very well the calculation and is in perfect agreement with the simulation. The specified fiber mode field radius of $w_{f,1560} = 8.3 \mu\text{m}$ is used for calculation and simulation.

We have seen so far, that long high finesse FFP resonators can be build with the fabricated fiber mirrors. The data shown was taken with the resonators mounted and adjusted with macroscopic precision stages. To allow an incorporation of the resonators in a compact vacuum cell, a miniaturized resonator mount is necessary, which we will describe in the following section.

4.2.7 A compact FFP resonator mount

To combine the FFP resonators with an atom chip, a compact resonator mount is needed, which has to fulfill the following requirements:

- Minimal obstruction of the optical access to the chip: Especially the mirror MOT on the chip puts a strong constraint on the height of the mount¹⁷.
- A possibility to scan the resonator length
- Low thermal expansion to reduce the resonator detuning with temperature changes
- A minimal distance of the resonators to maximize their mechanical coupling. Thereby, we hope to enable the length stabilization of both resonators with sending light only to one of them.

The general design presented in Fig. 4.19 was inspired by the impressive work in [135] where the - to date - only FFP resonator is combined with an atom chip. We choose fused silica¹⁸ as the bridge material for its high stability and low coefficient of thermal expansion of $\kappa = 5 \times 10^{-7}/\text{K}$. The later alignment of the resonators with the conductors of the atom chip made it necessary to polish the fused silica to transparency, which could not be accomplished by the supplier¹⁹. To maximize the possible cavity detuning, a piezo stack is used, which will be presented in Sec. 4.2.7. The FFP resonators have to be aligned on the mount and rigidly fixed, which we accomplish by the gluing method presented in Sec. 4.2.7.

¹⁷An interesting option for the future is the use of a *grating chip MOT* [202], which needs no incoming 45°-MOT beams. This technology reduces furthermore the apparatus size and complexity.

¹⁸HSQ300 by HERAEUS

¹⁹Precinet SARL, Neuilly-Plaisance, France, <http://precinet-fr.com>

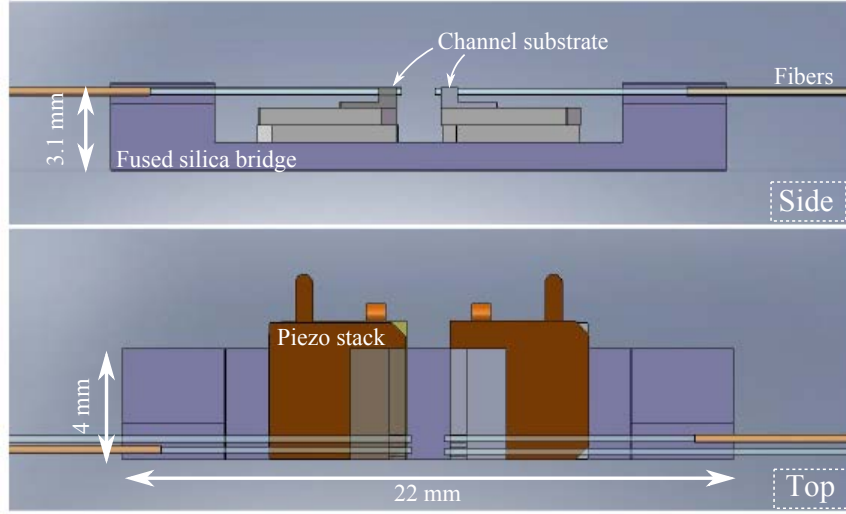


Figure 4.19: Bridge design. The fused silica bridge is shown with shear piezo stacks glued to it. In the top view the electrodes of the piezo stack can be seen. On top of the shear piezos the channel substrates are glued, which hold the fibers.

Optimized piezo configuration

Two factors influence our choice of the piezo configuration. First, the height of the piezo should be kept to a minimum, since it directly determines the bridge height²⁰. Secondly, the applied voltages should be kept to a minimum in order to minimize DC Stark shifts of the atomic transition. As a compromise, we chose a shear piezo stack, composed of two parallel shear piezos²¹. In Fig. 4.20, the electric field created by a single shear piezo is compared to the chosen piezo stack. The simulations were carried out with a commercial finite element simulation tool²² and only take a 2D cut through the piezo electrodes into account.

To estimate the DC Stark shift on the atoms, we use the scalar hyperfine polarizability of the ground state of ^{87}Rb , given in [203]. We neglect the anisotropic effect of the projection of the electric field onto the quantization axis due to its small contribution [204, 205]. This gives the frequency shift of

$$\delta\nu = -kE^2 \cdot 10^{-10}\text{Hz}/(\text{V/m})^2 \quad (4.2.15)$$

with $k = 1.23(3)$ [203] and E being the electric field strength. This shows that the

²⁰The minimum is given by the distance the atoms fall in a typical time of flight measurement. For dense BECs in the previous TACC experiment a minimum time of flight of $\tau_{min} = 20$ ms is needed to image the atom cloud correctly, which translates to a distance of 2 mm.

²¹CSAP02, Noliac, Kvistgaard, Denmark. We ordered customized piezos to guarantee non-magnetic materials for the stack (CuBe for the electrodes). We found recently (after the full assembly) that the stacks show a strong magnetization. A field of 30 mG was measured in direct vicinity of the stack. This is due to a faulty use of Ni instead of Ag to coat the piezo ceramic. **The resulting magnetic field fluctuations close to the atoms will probably diminish the clock performance drastically**, rendering this footnote to the most unfortunate one of this thesis. It remains to be investigated if the present magnetic gradients jeopardize the planned magnetic trapping.

²²COMSOL

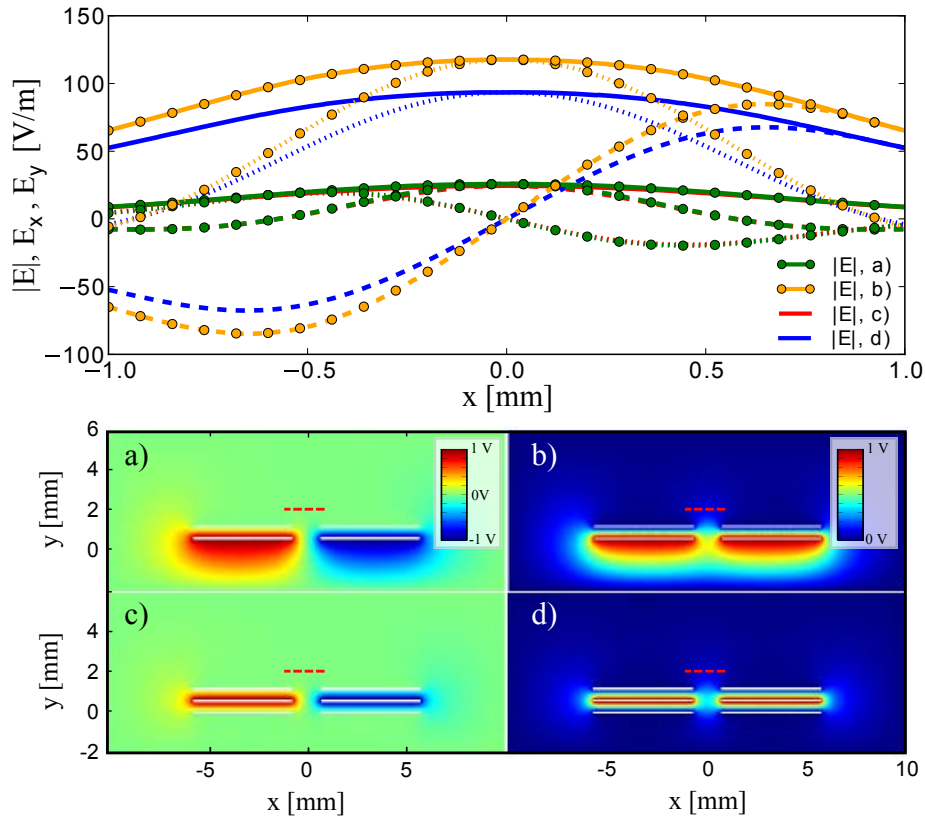


Figure 4.20: Electric field of piezos. The upper graph shows the simulated electric field components E_x (dashed lines), E_y (dotted lines) and the electric field strength $|E|$ (solid lines) along the red dashed line, indicating the atom position in the piezo configurations below. Each color represents one configuration. a) and b) show the electric potential for a single piezo with the upper electrode grounded and the lower electrodes on $U = 1\text{ V}$ or $U = -1\text{ V}$. c) and d) show the potentials for a piezo stack, with the outer electrodes grounded. Note that the field components for a) and c) nearly overlap over the full cut. The electrode length of each piezo is 5 mm, the single piezo height 0.6 mm and the distance of the piezos along x is 1.4 mm.

asymmetric configurations a) and c) in Fig. 4.20 cause the smallest stark shift of

$$\delta\nu \approx -738 \cdot 10^{-10} \text{Hz/V}^2 \cdot U^2 \quad (4.2.16)$$

depending on the applied voltage of $\pm U$ on the electrodes of the opposite piezos. The stack configuration gives an electric field strength 6% smaller than the single piezo, but note that for the same stroke only half the voltage is needed, reducing the DC Stark shift by a factor of 4. To increase the longitudinal mode number of the standing wave at 1560 nm, a voltage of $U = 174 \text{V}$ has to be applied, assuming the nominal stroke of the piezo of $\sim 4.5 \text{nm/V}$. If the voltage is applied to the left and right piezo stack simultaneously (with opposite sign), the voltage can again be reduced by a factor of 2. This maximum voltage of $U = 87 \text{V}$ leads with Eq. 4.2.16 to a DC Stark shift of $\delta\nu \approx 5.5 \cdot 10^{-4} \text{Hz}$. Note, that the expected voltages for the resonator length stabilization are of the order of several tens of mV (cf. [135]), which leads to negligible DC Stark shifts.

Alignment sensitivity

The finesse and especially the transmission of the resonator are very sensitive to the alignment of the two mirrors. Since the position of the incoupling mirror is fixed with respect to the fiber mode, no corrections of the fiber-cavity coupling can be made after gluing the fibers to the resonator mount. Furthermore, the rigid coupling of the incoupling fiber mode and the input mirror leaves only the freedom of changing the resonator mode position on the mirror. This is in contrast to conventional macroscopic cavities, where typically the incoupling beam is scanned over the mirror to optimize the coupling.

In addition, tilting or displacing one mirror, leads to a simultaneous tilt *and* displacement of the cavity mode. To account for all the effects, we use the numerical simulations, presented in Sec. 4.2.3, to estimate the alignment sensitivity of the long FFP resonators, shown in Fig. 4.21. While the finesse with a plateau like behavior allows an angle misalignment of $\pm 0.5^\circ$ and a displacement of $\pm 10 \mu\text{m}$, the transmission puts much tighter constraints. To lose less than 10% of the optimum transmission, the allowed angle misalignment reduces to $\pm 0.2^\circ$ and to $\pm 4.2 \mu\text{m}$ for the displacement. A comparison of the alignment sensitivity for different resonator configurations is presented in Fig. 4.22. It can be seen that the long FFP resonators show the highest sensitivity to angle misalignment, whereas the sensitivity to displacement is minimal. Further insight in the fiber-resonator coupling can be gained by analyzing the line shape of the reflected signal, as presented in the recent publications [163, 206, 207]. This remains to be tested with long FFP resonators, where especially the role of the collapse could be investigated.

We will proceed in the next section with presenting the alignment and gluing method, developed to meet this tolerances.

Channel gluing method

While aligning a FFP resonator with macroscopic translation and tilt stages, is rather straight forward, more care has to be taken, when fixing the resonator to its final

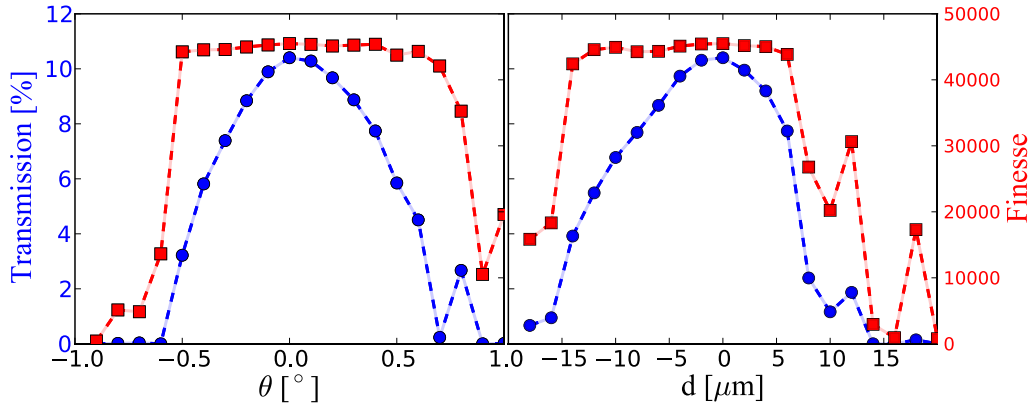


Figure 4.21: Simulated effects of misalignment. For the simulation the profiles and mirror losses of Fig. 4.5 are used at a cavity length $L = 1.2$ mm. The fiber waist is $w_f = 8.2 \mu\text{m}$. In a) the output mirror is tilted, in b) displaced. The blue circles mark the transmission, the red squares the finesse.

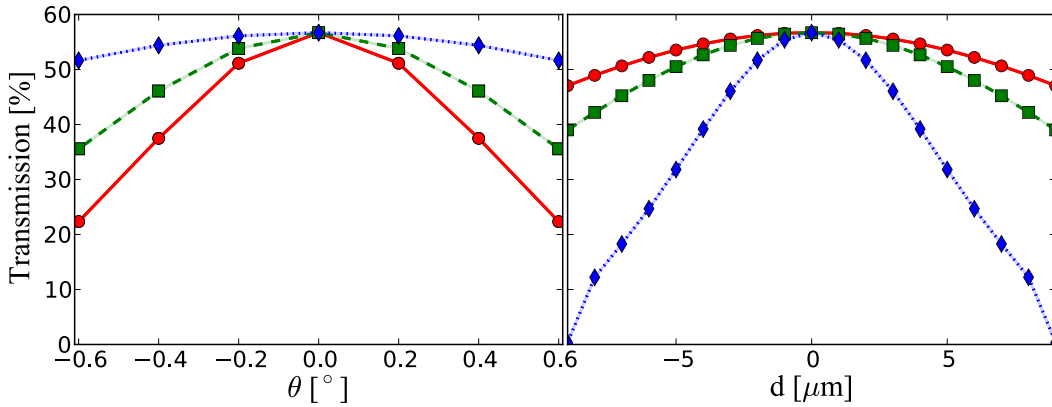


Figure 4.22: Simulated effects of misalignment for different resonator lengths. For the simulations perfectly spherical profiles with ROC of $R = 1.5$, mm (red circles), $R = 0.75$, mm (green squares) and $R = 0.15$ mm (blue diamonds) are used. The resonator length is chosen such, that the ratio α of the resonator to the Rayleigh length (Eq. 4.1.22) is the same for all three configurations: $\alpha = 0.81$. The fiber mode waists are chosen to keep also the ratio w_f/w_c constant. The values read $w_f = 8.2 \mu\text{m}$ for $L = 1.2$ mm, $R = 1.5$ mm; $w_f = 5.8 \mu\text{m}$ for $L = 0.6$ mm, $R = 0.75$ mm and $w_f = 2.6 \mu\text{m}$ for $L = 0.12$ mm, $R = 0.15$ mm. In a) the output mirror is tilted, in b) displaced. The graph shows only the geometrical coupling of a lossless resonator.

mount. To obtain a compact and robust setup the only solution is to glue the fiber mirrors. Here, the central problem is given by the linear shrinkage of the glue, which exerts a pulling force on the glued objects during the curing of the glue [208–211]. The best way to reduce the misalignment due to shrinkage is of course to reduce the thickness of the initial glue layer. This results in a common method for precise optical alignment depicted in Fig. 4.23 a). Here, two auxiliary blocks are mounted around the aligned element, leading to 4 thin glue layers. In [199] this method is used to glue optical elements in a compact laser setup and in [212] for the assembly of a high finesse FFP resonator. Unfortunately this method requires a lot of space and makes it impossible to mount two resonators close to each other. A space-saving alternative is shown in Fig. 4.23 b), where the two blocks are omitted. This has the disadvantage, that a thicker glue layer is needed to allow for alignment of the fiber. This method was nonetheless successfully used for the construction of a single FFP resonator [206], and even a pair of FFP resonators with a distance of 0.5 mm in [135]. Our choice of the atom transport (cf. Sec. 5.2.1) necessitates an even more compact solution: One resonator is placed only 150 μm away from the edge of the resonator mount, as can be seen in Fig. 4.24 a).

Next to the presented methods, a multitude of solutions for the precise alignment of fibers is present in the literature [213–216], motivated by the fabrication of integrated optical devices. Unfortunately, none of the found methods was compact and precise enough for our purpose. For this reason, we developed a method, where the fiber is not

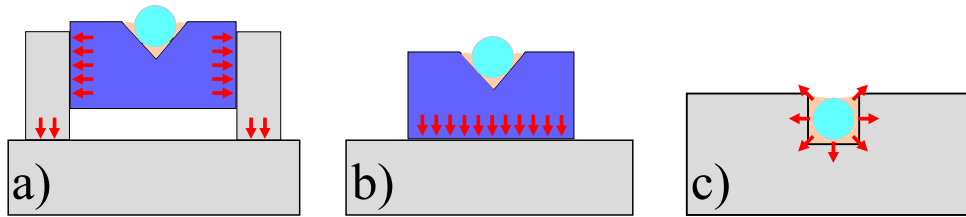


Figure 4.23: Gluing of FFP resonators. Three different methods for highly precise fixation of a fiber (turquoise circle) are presented. In a) and b) the fibers are glued to macroscopic v-groove substrates (blue) prior to the critical alignment. The red arrows mark the faces glued in the critical alignment step and in the same time the expected pull due to glue shrinkage. In c) the fiber is held directly during the critical step and is glued in a channel with a square cross section. This is the method chosen for our setup.

glued onto a macroscopic substrate before alignment, but the fiber itself is held during the alignment and gluing step (Fig. 4.23 c). The nearly full embedding of the fiber in the glue is chosen to balance the forces during curing. The procedure is depicted in Fig. 4.24 and presented in the following: First, the prepared resonator mount, with the contacted²⁵ piezos and the channel substrates, is glued temporarily²⁶ to a tilt stage, see Fig. A.5. To allow for additional heat curing of the glues used, the resonator mount rests on a Peltier element.

²⁵KAP012, MDC vacuum, glued with Epotek H21-D

²⁶DYMAX OP 67-LS. We remove the glue with a self sharpened solder iron at 300°C, after attaching the resonator mount to the atom chip. An easier removable glue remains to be found.

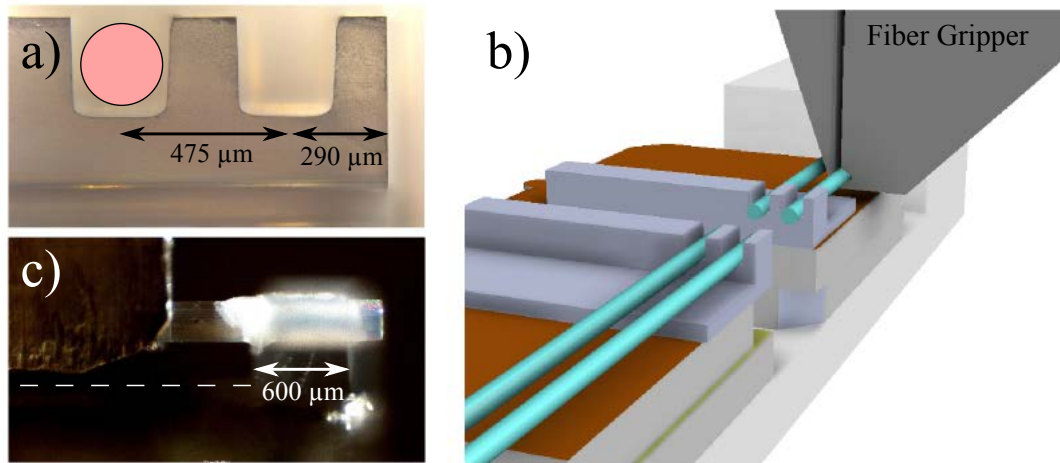


Figure 4.24: Channel gluing method. a) shows a microscope image of channels cut in a fused silica substrate with a dicing saw²⁴. A fiber of $\varnothing = 230 \mu\text{m}$ is sketched in the left channel. b) shows the bridge (white) with the piezos (copper colored upside) with the channel substrates (gray) and all for fibers (blue). The fiber gripper holds the last installed fiber. c) shows the tip of the fiber gripper holding a just glued PC fiber. The white dashed line marks the surface of the channel substrate.

The fiber is held by a piezoelectric gripper stage²⁷, that allows to release the fiber without applying force. The fiber gripper sits on a translation stage, while the opposing fiber is mounted on a tilt mount. After placing and aligning the fibers in the square channel as depicted in Fig. 4.24 a), a small amount of UV curable glue²⁸ is used to fill the channel. If necessary, the resonator can be realigned with the glue present. The length of the channel of $600 \mu\text{m}$ and the width of $280 \mu\text{m}$ allows an angle alignment of a PCF fiber ($\varnothing = 230 \mu\text{m}$) of $\pm 2.4^\circ$. Once the resonator is aligned, the glue is cured by exposing it with UV-light²⁹. We use a syringe tip with an inner diameter of $200 \mu\text{m}$ to get a small UV light spot only on the glue. This reduces the heating of the mount, avoiding misalignment. To reduce the heating further, we pulse the UV light: after 5 s of exposure, we wait until the cavity signal has recovered (typ. 20 – 30 s). Since the glue changes quickly its viscosity, no further alignment is recommended after the first exposure.

For the second fiber³⁰ the procedure is repeated. Now, the bridge, with the first glued fiber is tilted, and the second fiber in the gripper is again translated.

We reduced the free standing length of the fiber tips to below $200 \mu\text{m}$ (see Fig. 4.24 b)), to minimize mechanical vibrations in the final resonator. While gluing the MM-fiber of a high finesse cavity, with a free standing fiber end of only $100 \mu\text{m}$, we observed the

²⁷GRIPPY3, Piezosystem, Jena, Germany, customized with a home build tip

²⁸OPTOCAST 3410 Gen2, EMIUV, chosen for its small linear shrinkage and low coefficient of thermal expansion in the cured state of $14 \cdot 10^{-6}/\text{K}$.

²⁹Blue Wave 50, DYMAX

³⁰We generally glue the MM fiber last, since its smaller diameter compared with the PCF, leads to an increased alignment range in the channel.

appearance of a birefringence, as reported before for macroscopic mirrors [217]. This is explained by the stress the glue exerts on the coating and leads to a mode splitting of 1.1κ at 780 nm and 0.7κ at 1560 nm. This stress should be avoided in future assemblies by allowing longer free standing fiber tips.

After the successful gluing of the resonator, the fibers are fixed by a drop of glue to the feet of the bridge, to serve as a strain-relief for the fibers. After exposing the glue filled channels for effectively ~ 30 minutes³¹, the resonator mount was heated to 150°C for 1 hour³² to fully cure the glue. While the resonator length changed by a few micrometers for elevated temperatures, no transmission or finesse loss could be observed at 150°C , where both resonators were still fully functional. This underlines the suitability of FFP resonators in extreme conditions.

We glued several long FFP resonators with the presented method and for all attempts the transmission and finesse loss stayed well below 10%, proving its suitability for the resonator assembly.

4.2.8 Resonators for TACC2

Using the discussed method a high- and low-finesse resonator were glued to the resonator mount, as shown in Fig. 4.25. The resonator properties are summarized in

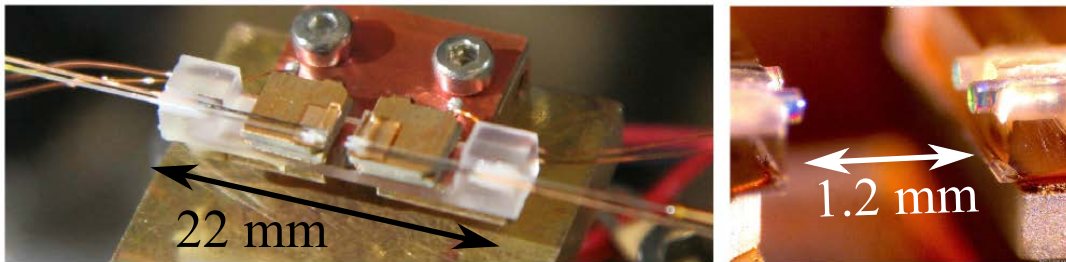


Figure 4.25: Long FFP resonators for TACC2. The left picture shows the assembled resonator mount, still glued to the temporary assembly fixture. The right picture shows a closeup view of the high finesse resonator in the back and the low finesse resonator in the front.

Table 4.2. The difference of the resonance frequencies of the two resonators changes only very little with time. In free air, the two frequencies change in one minute less than the line width of the low finesse resonator κ_{LF} . In one hour the change is still smaller than $3\kappa_{LF}$. We expect a further improvement, when putting the resonators in the ultra high vacuum and a temperature stabilized environment. Therefore we hope, that the envisaged scheme of locking the low finesse resonator by use of the high finesse resonator can be implemented.

³¹The full process took several hours, since we used the described intervals for the curing. The glue showed strong variations in the curing speed from test to test, even if the glue was from the same batch or even the same syringe. The reason is most likely a chemical reaction with humidity, which reduces the activity of the photo initiator.

³²Slow temperature ramps with $< 1^\circ\text{C}/\text{min}$.

	Unit	Low Finesse (LF)		High Finesse (HF)	
Length L	μm	1215 ± 20		1275 ± 20	
ROC_{MM}	μm	1612/1523		1494/1416	
ROC_{PCF}	μm	1559/1468		1513/1437	
ROC_{eff}	μm	1560/1520		1490/1430	
z_R	μm	745/761		711/737	
collapse L_{col}	μm	60 ± 5		50 ± 5	
FSR	GHz	123 ± 2		118 ± 2	
		780 nm	1560 nm	780 nm	1560 nm
$w_{0,c}$	μm	13.6/13.7	19.2/19.4	13.3/13.5	18.8/19.1
w_m	μm	17.5/17.6	24.8/24.9	17.8/17.9	25.2/25.3
$\kappa/(2\pi)$	MHz	41.4 ± 0.6	5.28 ± 0.08	3.08 ± 0.08	2.02 ± 0.06
\mathcal{F}		$2,980 \pm 100$	$23,370 \pm 800$	$38,200 \pm 2,100$	$58,200 \pm 3,600$
bire. split. $\delta\nu/\kappa$		n.a.	n.a.	1.1	0.7
res. trans. T_c		23.2%	9.8%	4.6%	8.4%
res. refl. R_c		70.7%	36.0%	30.7%	34.6%
offres. refl. R_o		33.8%	61.6%	68.6%	79.0%
$g_0/(2\pi)$	MHz	10.9	-	10.9	-
$C_0 = 4\frac{g_0^2}{\kappa\Gamma}$		1.90	-	25.44	-
$\delta\omega_0/(2\pi)$	kHz	34.9	-	34.8	-
C_{eff}		0.63	-	8.37	-
$\delta\omega_{\text{eff}}/(2\pi)$	kHz	11.6	-	11.5	-

Table 4.2: Cavity parameter overview. The table shows the parameters of the two cavities at both resonant wavelengths 780 and 1560 nm. The data was taken after the chip-cavity ensemble was glued to the glass cell. ROC_{eff} are the values deduced from the higher order mode spectra Fig. 4.13, A.4. κ is the FWHM value. The resonant reflection gives the reduction of the offresonant reflection signal in percent. For the calculation of C , we take $\Gamma(\text{FWHM}) = 2\pi \cdot 6.07 \text{ MHz}$ [101]. For the effective values in the last two rows, we assume a typical transversal cloud radius of the existing TACC experiment: $\rho_r = 6.9 \mu\text{m}$ resulting from $T = 80 \text{ nK}$, $\omega_t = 2\pi \cdot 90 \text{ Hz}$, note that the effective coupling can be increased easily with changing the trap frequency. The oscillator strength of the D_2 line is $f = 2/3$ [46].

4.3 Conclusion

We presented the first FFP resonators fabricated with the dot milling method introduced in the previous chapter 3. The finesse and transmission measurements performed, show that CO₂ laser dot milling and large mode area photonic-crystal fibers form a powerful combination. The maximum length for FFP resonators is extended into the millimeter range while maintaining the advantages of a miniature, robust, fiber-based approach and an acceptable overall transmission. The finesse $\mathcal{F} \sim 50000$ reached in our data is limited by the dual-wavelength coating. The surface roughness of the CO₂ process admits still higher values, and it will be interesting to see whether these can also be reached at the length scale introduced here. For a state-of-the-art single-wavelength coating, total absorption and scattering losses $\mathcal{L}_A + \mathcal{L}_S = 2 \times 13.5$ ppm have been measured for a pair of fiber mirrors [161]. Choosing a transmission of the same value, and adding the clipping losses of 5.5 ppm per mirror estimated by the simulations shown above for a cavity of $L = 1$ mm, it should be possible to produce FFP cavities of $L = 1$ mm and a finesse of up to 97,000 with the method presented here. Beyond the cavity QED applications for which we have originally developed it, we note that the free spectral range for a 1.5 mm fiber cavity is 100 GHz, approaching an interesting range for filtering applications.

Besides the increased length the presented FFP resonators work simultaneously at 780 nm and 1560 nm due to a double wavelength coating and the PC fibers. This marks the first FFP resonator with an octave spanning frequency range.

The development of a new FFP resonator gluing method allowed the construction of two resonators, with a distance of only 475 μm of the resonator axes. The compactness of the setup allows a combination with the atom chip, which will be presented in the following chapter.

Atom Chip for TACC 2

With the fiber cavity, the atom chip is the centerpiece of the experiment. In this chapter we will outline the requirements for the chip together with the constraints imposed. To meet these requirements, a chip design was developed which is presented in the following section. The realization of the design in our clean room facilities is documented in the last subsection.

5.1 Requirements catalogue

Every chip experiment has its individual set of requirements that the chip design has to fulfill. Here, we will note the tasks specific to the TACC2 experiment.

Clock performance: The top priority of the chip design is to enable the clock performance as in the preceding TACC experiment [62]. To achieve this, the atoms have to be trapped and transferred to an Ioffe-Pritchard trap with the parameters given in [62]: The best clock performance was found at low atomic density, generated by the trap frequencies $(\omega_x, \omega_y, \omega_z) = 2\pi \times (2.7, 92, 74)$ Hz with a magnetic field of $B_0 \approx 3.229$ G at the trap center (cf. Sec. 1.2.1), allowing atom numbers of up to $4 \cdot 10^4$ atoms at temperature $T \approx 80$ nK in the final trap. The trapping of ultra cold atoms in shallow traps requires high surface quality of the micro fabricated gold wires, as will be discussed in Sec. 5.3

Microwave guide: A two photon transition is used (cf. Sec. 1.2.3) for the interrogation and state preparation. While the RF signal can be guided by one of the standard DC-wires on the chip, the microwave needs a dedicated waveguide. The choice of a coplanar waveguide (CPW) as the MW guide for TACC is motivated in depth in [91]. The main advantage is the focusing of the MW power to the dimension of the CPW cross section, much smaller than the λ^2 for a freely propagating wave, and the precise control of the created MW profile $B_0(x, y)$ by the CPW design. The main disadvantage is the impossibility to cross the CPW with further wires. This is a severe constraint especially for the atom transport to the resonator, as will be discussed in Sec. 5.2.1.

Fiber Fabry-Pérot resonator: To realize the experiments presented in Ch. 2, the atoms have to be placed in the mode of an optical resonator. A fiber Fabry-Pérot resonator (see chapter 4) is chosen for compactness, robustness and high cooperativity. The chip wires must be able to position the atom cloud in the cavity mode. All currents used for the magnetic manipulation of the atoms should be kept as low as possible to reduce heating of the resonator assembly. Given the millimeter size of the resonator, it has to be mounted on the chip surface, which poses problems for the optical access, described in the following.

Optical access: The optical access is crucial for two steps in the experiment cycle. First, the atoms have to be trapped and cooled with light, using a mirror-MOT (mMOT, see [64, 133]). Later, the atoms are detected through resonant absorption imaging [65]. The beam diameter of the mirror-MOT beams are limited by the accessible reflective surface on the chip, which has to be maximized to decrease the MOT loading time. This is in conflict with the mounting of an optical resonator on the chip surface. A very elegant approach was taken in [135], where the mirror MOT is realized on one half of the chip while the cQED experiments are carried out on the opposite half. We adopt this general layout, necessitating atom transport from the trapping zone to the optical resonator.

Compatibility with the previous TACC: To minimize the necessary changes on the existing experiment while replacing the chip, special care has to be taken, to keep the new chip compatible with the existing coil cage and optics around the vacuum cell.

Besides the specific constraints of our experiment, the chip is subject to numerous general restrictions for cold atom experiments, such as UHV compatibility, non-magnetic components and heat management. An exhaustive summary of the topic can be found in [64]. Following the general as well as the specific requirements we developed a new chip design, which will be presented in the next chapter.

5.2 Layout of the atom chip

In this chapter, we present the design of our atom chip depicted in Fig. 5.1. A two-layer chip design was chosen for two reasons: Crossed wires can be realized despite the presence of the MW guide and the optical access to the atoms is improved. The smaller chip is named science chip (SC) in the following, the chip with the connections outside of the vacuum will be referred to as base chip (BC). A general idea was to realize two main interrogation areas on the chip, resulting in the symmetry of the chip design. One side recreates the basic properties of the old TACC experiment. Since the atoms are trapped here initially, we call it trapping region, but the wire layout allows as well clock operation at this position. The second interrogation region is at the position of the fiber cavities, and will therefore be referred to as cavity region (see Fig. 5.2). This duality should allow to compare very efficiently the clock performance with and without the cavity. To ensure the compatibility with the existing optics,

the center of the wire pattern is shifted 1.5 mm with respect to the chip-wafer center. This moves the resonator mount further out of the mMOT zone, increasing the MOT efficiency.

The following subsections describe the task and functionality of each element, supported by numerical simulations¹ of the created magnetic fields. We use a macroscopic copper U [218] and I, identical to the one in the previous TACC experiment [91] for the initial trapping and cooling of the atoms in the mirror MOT. They are glued to the backside of the base chip as shown in Fig. A.8. The bias fields are created by macroscopic coils around the chip, sketched in Fig. A.9.

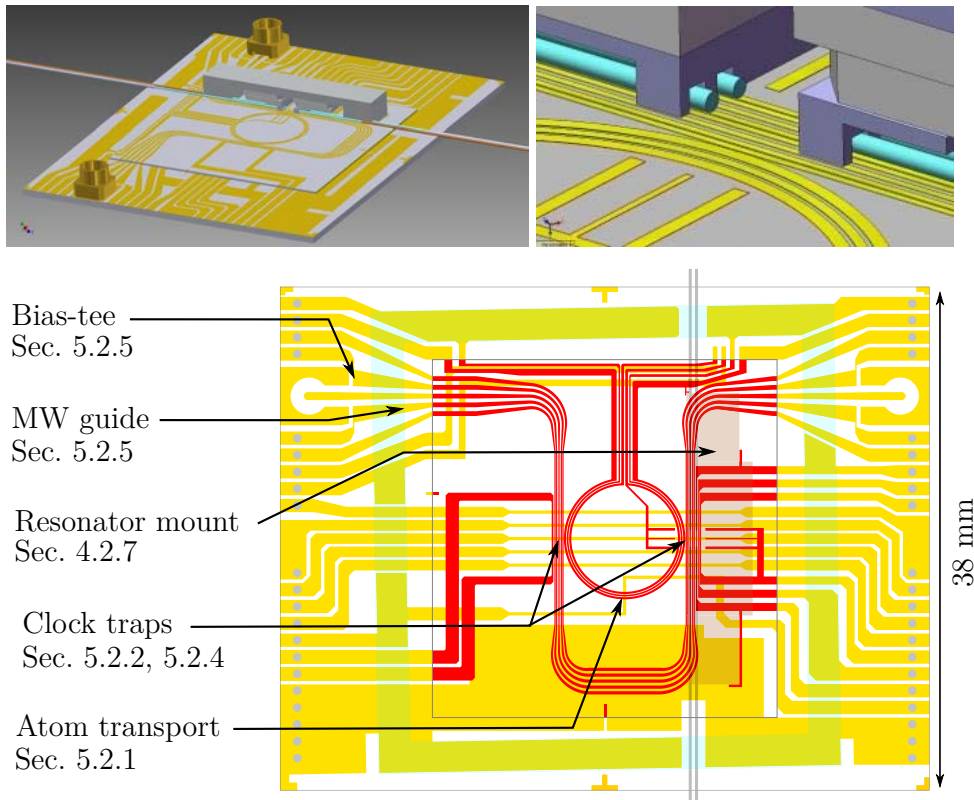


Figure 5.1: Layout of the TACC2 atom chip. The top row shows a 3D-model of the chip, including the bridge and the micro wave connectors. The right image shows a zoom to the cavity region. In the lower row, the science chip wires are depicted in red, the base chip wires in orange. The blue shaded area marks the foot print of the glass cell and the brown shaded area marks the foot print of the bridge with the fibers in dark gray. The bore holes in the base chip substrate are marked as gray cycles. All details that will be presented in the following are marked. A more detailed view can be found in Fig. 5.2.

¹For the calculations a C-program written by Wolfgang Hänsel [102] was used.

5.2.1 Atom transport

After the MOT loading and a short molasses phase, the atoms will be transferred to the first magnetic trap. If the cycle of the previous TACC experiment is chosen, the atoms will stay in the trapping region and a first dimple trap can be created with $I_{B3} = 2.5 A$, $I_{MW} = 3 A$ (cf. Fig 5.2) and a current $I_{\text{mac}} = 11A$ through the macroscopic U and a magnetic bias field created by the coil cage [89]. After increasing the trap frequencies for evaporative cooling the final clock interrogation trap is reached. This sequence is described in detail in [89, 92], which is why we will proceed and present the experimental cycle for an experiment involving the cavity.

Ω -wire transport: As we will see, the atomic transport will be carried out in an quadrupole trap generated by an Ω -shaped wire (S2 in Fig. 5.2). To avoid atom loss due to reduced mode matching of quadrupole and Ioffe-Pritchard traps [104], the transfer trap should be a quadrupole trap as well. This can be realized by using the macroscopic U and a H-trap consisting of the Ω -wire and B1 and B5.

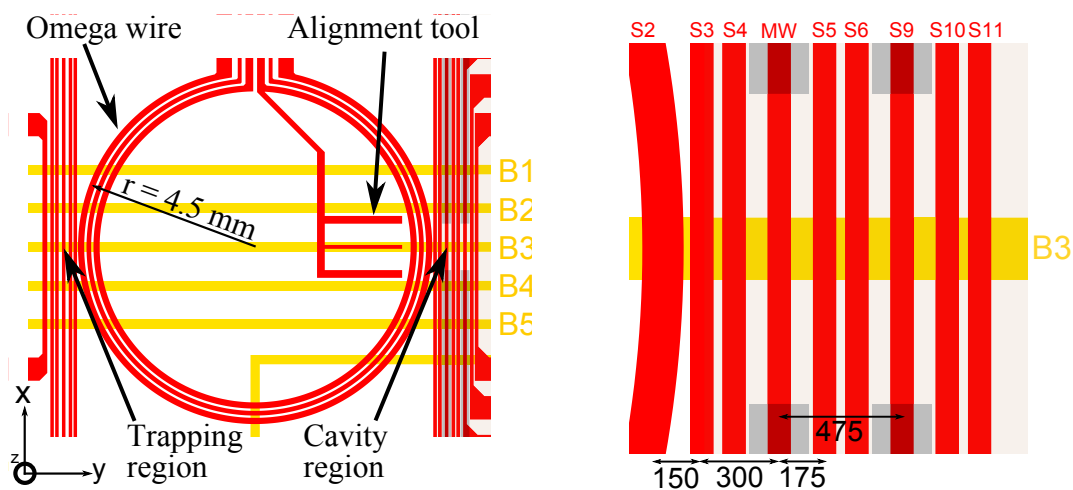


Figure 5.2: Details of the science chip. The left figure shows the central part of the science chip. The Ω -wire is used to transport the atoms from the trapping region to the cavity region, as described in the text. The alignment tool serves only during the gluing of the cavity to the chip, since the base chip wires are not visible. It is connected to the inner Ω -wire to avoid the accumulation of surface charges. The right side shows a detailed view on the cavity region with the crucial center to center distances in μm . All wires besides S2 (= Ω -wire) and B3 have a width of $w = 90 \mu m$. All labels of the wires can be found in Fig. A.6, A.7.

Since the atom cloud will form a cigar shape along x in the first transfer trap due to the geometry of the macroscopic U and the H-trap, the transport trap should have the same orientation at the beginning. At the end of the transport the cigar shaped cloud should be aligned along the optical axis of the cavity, so again parallel to the x -axis. In [135] a similar atom chip with cavity setup is presented. There, the atoms are transported along a linear wire and a shifting magnetic field minimum generated by

external coils. Since the wire is perpendicular to the center piece of the macroscopic U the cloud has to be rotated before the transport to increase the mode matching between the transfer trap and the single wire transport trap.

In our experiment, a second rotation would be necessary at the end to align the cloud with the cavity axis. Every rotation would need a transfer to a rotation trap as realized in [219]. Here, we present a new approach, where the transport is realized by use of the rotation scheme of [219] only. This enables us to simplify the transport scheme and we expect a higher atom number after the transport, since less trap transfers are needed.

The basic principle of the transport uses a quadrupole trap generated by the circular Ω -wire and an external magnetic field. By rotating the external magnetic field \vec{B}_{ext} the magnetic minimum shifts along the Ω -wire, as depicted in Fig. 5.3. The radial

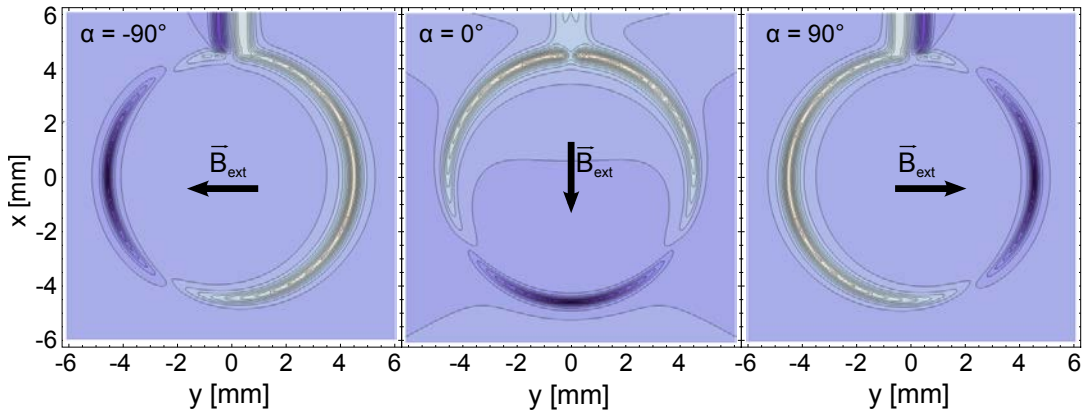


Figure 5.3: Magnetic field strength above Ω -wire for different angles α of the external magnetic field \vec{B}_{ext} . The field created by the simulated coils has a strength of $|\vec{B}_{ext}| \approx 25 \text{ G}$ at the wire position and $I_\Omega = 2 \text{ A}$ with a radius of the omega wire $r_\Omega = 4.5 \text{ mm}$. The cut along the x - y plane is made at $z = z_0$, the height where the magnetic field strength has its minimum. The potential difference of the equipotential lines is 2 G. The darkest region depicts $|\vec{B}| = 0 \text{ G}$, the brightest region $|\vec{B}| = 50 \text{ G}$

gradient B'_R (perpendicular to the Ω -wire) is in first approximation given by the thin wire formula Eq. 1.4.3, while the longitudinal gradient B'_L (along the Ω -wire) is given by the curvature of the Ω -wire and the absolute value of the external magnetic field, but shows no dependence on the current in the Ω -wire². The two main dependencies of B'_L are shown in Fig. 5.4.

While we can reproduce B'_R of the previous atom transport experiments, B'_L will be significantly smaller for our larger r_Ω . In [219, 220], a small P-wire of radius $r_P = 0.9 \text{ mm}$ was used to create a longitudinal gradient $B'_L = 90 \text{ G/cm}$ enabling a transport without losses and heating of curvilinear velocities of up to 1.6 cm/s. The authors mention that a faster transport is not limited by the gradient of the potential,

²This is an untypical behavior for micro traps, where normally all gradients depend on the wire currents.

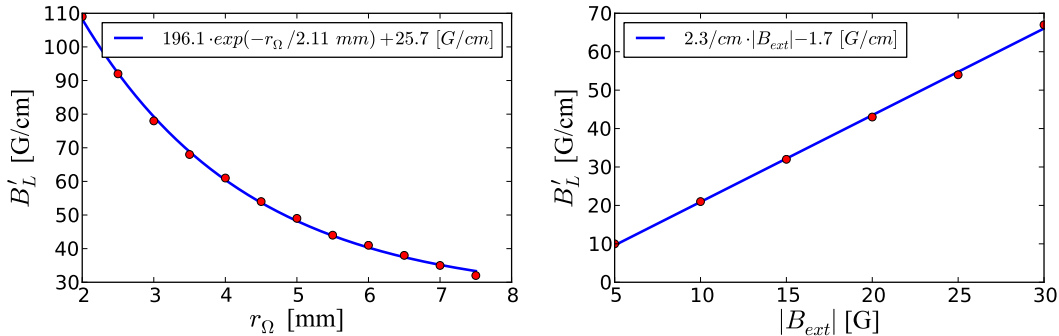


Figure 5.4: Dependence of longitudinal gradient of Ω -wire. The left graph shows the dependence of the longitudinal gradient B'_L of the transport trap on the Ω -wire radius r_Ω . Here $|\vec{B}_{ext}| = 25 \text{ G}$ and an exponential function (blue line) was fitted to the simulation results (red circles). The right graph shows the linear dependence of B'_L on the magnetic field strength of the external field. For all simulations the current was $I_\Omega = 4 \text{ A}$, but since the dependence of B'_L on the current is very weak the graphs are approximately valid for a range of $1 \text{ A} < I_\Omega < 6 \text{ A}$.

but most likely by the potential-shape change over the transport. Since our Ω -wire, unlike the P-wire in [220], does not show any irregularities over the transport distance we assume to not encounter problems due to the potential shape. The limitation for our transport is given by the low longitudinal gradient B'_L ³. The distance of the trapping region to the cavity region d_T sets the available mirror surface for the MOT, while it increases $r_\Omega = d_T/2$. We found as a compromise $d_T = 9 \text{ mm}$, giving a mirror surface comparable to the one in [135], where $20 \cdot 10^6$ atoms can be trapped in 2 s with the mirrorMOT⁴. This gives $r_\Omega = 4.5 \text{ mm}$, leaving only the external magnetic field as a free parameter to chose B'_L .

Fig. 5.4 shows the dependency of B'_L on the external field strength $|\vec{B}_{ext}|$, for magnetic fields realizable with our coil cage. Fig. 5.5 shows the simulated gradients and the trap depth over a full transport, with $|\vec{B}_{ext}| \approx 25 \text{ G}$, generated by the currents in the x and y-coil $I_x = I_{x,max} \cos(\alpha)$ and $I_y = I_{y,max} \sin(\alpha)$ with $I_{x,max} = 2 \text{ A}$ and $I_{y,max} = 4.2 \text{ A}$. The positions during the transport are depicted in Fig. 5.5.

The fluctuation of the gradients during the transport is $\sim 10\%$ which can be reduced to less than 5% by applying an additional modulation $I_{mod,x/y} = I_{x/y} \cdot \frac{1}{20}(1 - \text{Cos}[4\alpha])$ to the current of the coils. The trap depth of approximately 18 G translates to $\Delta E =$

³Note that in [219, 220] the atoms are in the Zeeman level $|F = 2, m_F = 2\rangle$, while in our case the atoms will be pumped to $|F = 1, m_F = -1\rangle$. This lowers the restoring forces felt by the atom for a given magnetic gradient by a factor of 2 (see Eq. 1.3.1). If the magnetic gradients should limit the transport speed, a possibility to circumvent this problem would be to transport the atoms in $|F = 2, m_F = 2\rangle$ and then transfer them after the transport via a two-(MW)-photon transition or a stimulated rapid adiabatic passage [221] to the clock ground state.

⁴Personal communications with G. Barontini and L. Hohmann, who were running the experiment at the time.

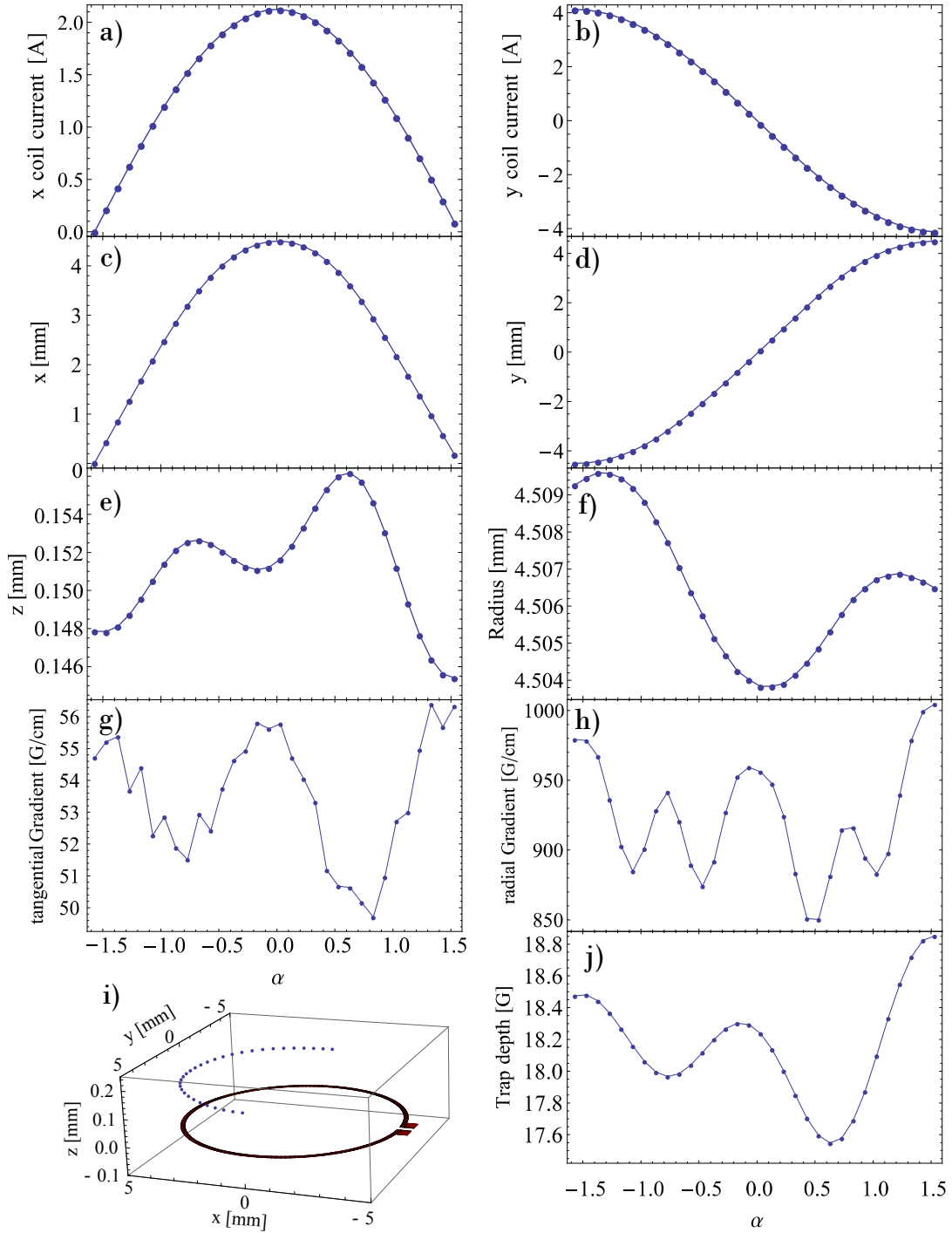


Figure 5.5: Positions and gradients during transport. a), b) show the currents applied to the x- and y-coil of the coil cage, to create $|\vec{B}_{ext}| \approx 25 G$. c)-f) show the positions of the magnetic trap created with $I_{\Omega} = 2 A$. g), h) show the gradients during the transport. The gradient changes around 10% during the transport, due to the geometry and position of the coils. The asymmetry of the start and end position is caused by an offset of the Ω -wire center position to the coil cage of $\Delta y = -1.5 \text{ mm}$. i) shows a 3D representation of the positions and j) the trap depth.

600 μK for the atoms in $|F = 1, m_F = -1\rangle$. This is more than a factor 10 higher than the typical initial temperature of the atom cloud in the transfer trap of $T \approx 50 \mu\text{K}$ [89]. For this temperature and the simulated radial gradient of $B'_R \approx 900 \text{ G/cm}$ Eq. 1.3.5 yields a trap life time $\tau = 0.43 \text{ s}$. An optimal current I_Ω has to be found experimentally that maximizes the trap life time by balancing losses due to the finite trap depth and Majorana losses. Generally loss due to the finite trap depth is favorable compared to Majorana losses, since here the hottest atoms are expelled from the trap and not the coldest in the trap center, which results in an evaporative cooling of the cloud.

To give an estimation for the lower bound of the transport time T_{min} , we calculate the maximum acceleration a_{max} the longitudinal gradient B'_L can withstand.

$$\begin{aligned} m a_{max} &= \nabla U = g_F m_F \mu_B B'_L \\ a_{max} &= \frac{g_F m_F \mu_B}{m} B'_L \\ a_{max} &= 32 \cdot 10^{-2} \frac{m}{\text{s}^2} \frac{B'_L}{\text{G/cm}} \end{aligned} \quad (5.2.1)$$

with m being the mass of a ^{87}Rb -atom. With $B'_L = 50 \text{ G/cm}$ the maximum acceleration is $a_{max} = 16 \text{ m/s}^2$. Using the first half of the transport for acceleration we need the time $t = \sqrt{\frac{2s}{a}}$, where s is the arc length of a quarter of the Ω -wire, and the same time t to decelerate the atoms again. With $s = r_\Omega \pi/2 = 7.07 \text{ mm}$, the lower bound for the transport time results to $T_{min} = 2t = 60 \text{ ms}$. To give a number for a realistic acceleration of $a_{max}/4$ the transport time only doubles and yields $T = 118 \text{ ms}$, for the overall distance of $U/2 = \pi r_\Omega = 14.14 \text{ mm}$. Further gain should arise from optimizing the acceleration sequence with the use of optimal transport functions like the Blackman-Harris curve [222].

Parallel park: At the end of the Ω -transport the atoms have to be transferred to the center of the cavity above the CPW. This will be realized by smoothly ramping the currents in the adjacent wires S2, S3, S4 and MW (cf. Fig. 5.2), so that the trap center moves along y , as shown in Fig. 5.6.

To follow the symmetry of the current in the Ω -wire, the longitudinal confinement (along x) is realized with antiparallel currents in the two base chip wires B2 and B4. This creates a moving H-quadrupole trap. To find a set of currents that realizes a smooth transport, we implemented an algorithm that reduces the difference to a potential with a chosen radial gradient and minimum position. Since the longitudinal gradient is not changed by the currents in the science chip wires, the optimization routine only takes the radial gradient B'_R and the trap position into account. The potential minimum is then translated along the y -axis, and the current configuration is determined which reproduces best the wanted potential. The results of this optimization are shown in Fig. 5.6, where the longitudinal gradient is chosen to be $B'_L \approx 50 \text{ G/cm}$ ($-I_{B4} = I_{B2} = 2 \text{ A}$) to meet the value of the precedent Ω -transport. It can be seen that the trap height is only changing by several μm during the transport, while the radial gradients fluctuate around 10%, which should allow a fast switching of the wire currents. The decline of B'_L for $y < 250 \mu\text{m}$ is caused by the simultaneous confinement along x created by the BC wires and the Ω -wire curvature, which can be avoided by ramping up the BC wire currents with increasing y .

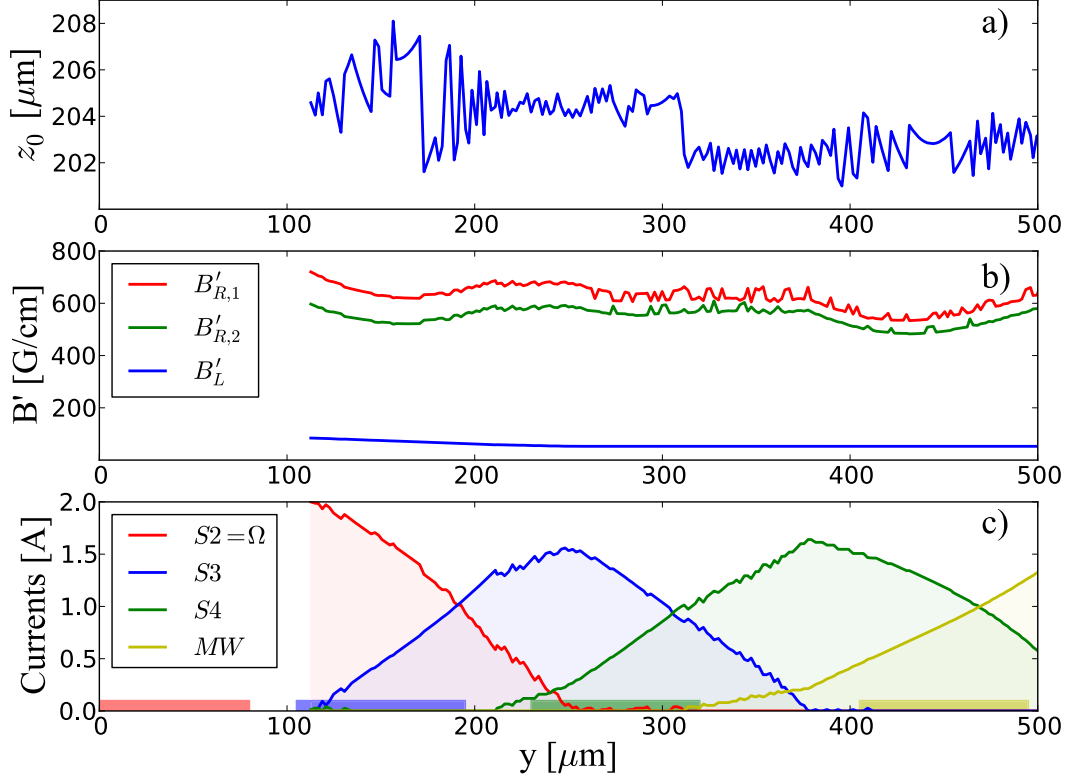


Figure 5.6: Trap properties during parallel park procedure. The current configuration was optimized as described in the text with an external field $\vec{B}_{ext} \approx (0, 15, 0)$ G created by the simulated y -coils (with $\Delta y = -1.5$ mm) and currents in the base chip wires $-I_{B4} = I_{B2} = 2$ A for the longitudinal confinement. The field created by the base chip wires causes the y -displacement of $\sim 112 \mu\text{m}$ for the start configuration, where only $I_{S2} \neq 0$. a) shows the trap height z_0 . The x -position is 0 during the sequence. b) shows the gradients along the three eigenaxes of the trap. The ripples are an artifact of the optimization process. c) shows the currents found in the optimization process realizing the trap properties in a) and b). The wire positions and widths are indicated as colored rectangles.

At the end of the transport the atom cloud is trapped in a quadrupole trap right below the central wire of the CPW. For the experiments, it is necessary to transfer the atoms in a IP-trap at the same position. It is favorable to undertake this transfer before the evaporative cooling, to avoid Majorana losses of cold atoms and to minimize the manipulation of the cooled cloud. The transfer can be realized by ramping down I_{B4} and I_{B2} and replace them by parallel currents of the same strength. Care has to be taken for this step to not change the y -position of the cloud too abruptly. Another possibility would be to ramp up a dimple trap as in the previous TACC experiment ($B_x = 15 G$, $B_y = 29 G$ and $I_{MW} = 1.5 A$, $I_{B3} = 3A$), which is used for the evaporative cooling of the atoms [89].

With the atoms transported to the desired trap position, we will continue with a description of two possible trap realizations for the clock operation, which we call the *interrogation trap*.

5.2.2 Three-wire trap

The main limitation of the clock stability of TACC is caused by temperature fluctuations of the atom cloud and fluctuations of the bias field [62]. Both effects are related to the stability of the applied currents. Therefore it is favorable to reduce the number of individual currents for realizing the interrogation trap. The measurements presented in [62] are carried out in a dimple trap by applying two different currents to the chip and two additional currents to the x- and y-coils.

A tempting alternative is to create the trap only with chip wires and the curvature of the magnetic field created by the x-coil for the confinement in x -direction. By sending the same current but with opposite sign through the MW-wire and the adjacent wire pair S4, S5, a 2D-quadrupole is created at a distance $z_0 = d$ above the MW-wire, where d is the distance of the MW wire to S4, S5, as depicted in Fig. 5.7. Note that the fixed $z_0 = d$ renders this trap type unattractive for the use with the optical resonator, since a fine tuning of the cloud height with the chip currents is not possible but necessary to align the atom cloud with the resonator mode.

It is nonetheless interesting to study the clock performance in a trap that only depends on two independent currents and has a strongly reduced dependence of the trap position on current noise, as we will see in the following.

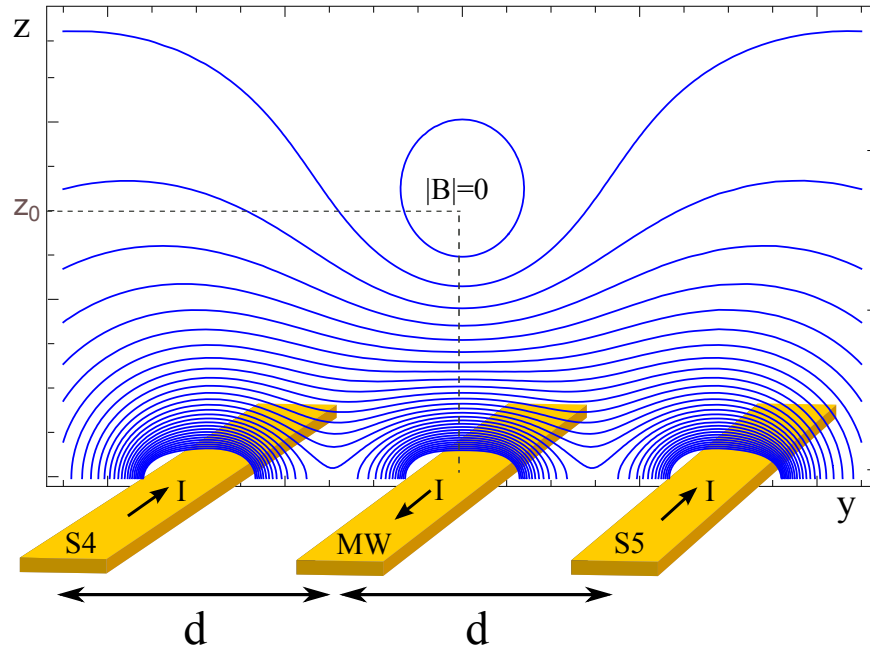


Figure 5.7: Three wire trap configuration. The bias field of the basic 2D-quadrupole trap described in Fig. 1.6 can be as well created by adjacent wires (here S4, S5). If the currents in the three wires are supplied by the same source the trap distance z_0 is immune to current fluctuations. Another interesting advantage of this trap type is the possibility to rapidly switch the bias fields which is used in AC-atom chips to reduce effects of the surface roughness [223].

Using the x-coil to create the Ioffe field which lifts the field minimum in the trap

center to the desired “magic field”, a confinement along x is automatically created by the curvature of the x-coil field. Tab. 5.1 shows the simulated properties of two traps with different wire distances $d = 175 \mu\text{m}$ and $d = 300 \mu\text{m}$, available on the chip. A layout of the geometry used in the simulation can be found in Fig. A.9.

d [μm]	I_{MW} [A]	f_1 [Hz]	f_2 [Hz]	f_3 [Hz]	z_0 [μm]	Trap depth [mG]
175	0.5	146	113	0.9	182	73
300	1.35	144	126	0.9	310	346

Table 5.1: Three-wire-trap properties. The currents in the adjacent wires are of the same amplitude as I_{MW} , but of opposite sign. Because of the gravitational sag away from the chip $z_0 > d$. The bias field was chosen to realize the magic field of $|\vec{B}_{min}| \approx 3.05 \text{ G}$.

The currents in the chip wires are chosen to generate similar trap frequencies for both traps, suitable for clock operation. The current in the x-coils is in both cases the same ($I_{x-coil} = 0.24 \text{ A}$) and generates the a field amplitude in the center of $|\vec{B}_{min}| \approx 3.05 \text{ G}$, close to the magic field. It can be seen, that for given trap frequencies the trap depth profits from the larger distance to the chip, for which reason we added additionally to S4 and S5 the wires S3 and S6 to the science chip. Note that the trap depth of 346 mG ($\equiv \Delta E = 11 \mu\text{K}$) is still small, but seen that the atom temperature at this stage is around 80 nK it is largely sufficient.

In this configuration, only one current source can be used to drive the three chip wires in series, which reduces trap position and frequency fluctuations due to current noise. To estimate the sensitivity of the trap to current fluctuations, we modulated all involved currents and deduced the effect on the trap properties in the simulation. In Tab. 5.2 the presented three-wire trap for $d = 300 \mu\text{m}$ is compared to the dimple trap used in the previous TACC experiment.

	f_1 [Hz]	f_3 [Hz]	z_0 [μm]	Trap depth [mG]	Ioffe field [G]
mean value 3-wire	144	0.9	310	346	3.06
I varied	$+123 \cdot \Delta I/A$	$+0.1 \cdot \Delta I/A$	$-19 \cdot \Delta I/A$	$+1000 \cdot \Delta I/A$	$-0.034 \cdot \Delta I/A$
I_{xCoil} varied	$-344 \cdot \Delta I/A$	$+2 \cdot \Delta I/A$	$+60 \cdot \Delta I/A$	$-2600 \cdot \Delta I/A$	$+12.7 \cdot \Delta I/A$
mean value dimple	92	2.8	353	406	3.07
I_{MW} varied	$-100 \cdot \Delta I/A$	$+2 \cdot \Delta I/A$	$+409 \cdot \Delta I/A$	$+800 \cdot \Delta I/A$	$+0.18 \cdot \Delta I/A$
I_{B3} varied	$+70 \cdot \Delta I/A$	$+134 \cdot \Delta I/A$	$-100 \cdot \Delta I/A$	$+1400 \cdot \Delta I/A$	$+0.03 \cdot \Delta I/A$
I_{xCoil} varied	$-240 \cdot \Delta I/A$	$-0.22 \cdot \Delta I/A$	$+187 \cdot \Delta I/A$	$-3900 \cdot \Delta I/A$	$+12.9 \cdot \Delta B/G$
I_{yCoil} varied	$218 \cdot \Delta I/A$	$2.3 \cdot \Delta I/A$	$-484 \cdot \Delta I/A$	$3430 \cdot \Delta I/A$	$-0.324 \cdot \Delta I/A$

Table 5.2: Effects of current fluctuations on interrogation trap. The upper part shows the simulated values for the 3-wire trap presented above ($d = 300 \mu\text{m}$). The lower part shows the effect of the current modulation on the dimple trap used in TACC. Since the effect on the transversal frequencies f_1 and f_2 are very similar only f_1 is shown. $x_0, y_0 = 0$ is not influenced by the varied parameters. Gravity is taken into account in all the simulations.

While the sensitivity to the current in the x-coil I_{xCoil} is only reduced by a factor

of 2 for the shallow trap axis and by a factor of 3 for z_0 , the sensitivity for a current fluctuation in the MW-wire is reduced by a factor 20 for the two parameters. The variation of the Ioffe-field at the trap center with the x-coil current stays the same, whereas the sensitivity to the current in MW is reduced by a factor of 5. This shows clearly that the three-wire trap configuration could be advantageous for the clock operation.

A drawback of the three-wire trap is the need to place the wires with no x or y -offset with respect to the two x-coils. This is not simple, since the coils are macroscopic constructions and alignment in the micrometer regime would need precision stages for the coil cage. Furthermore, the two interrogation zones on the chip make it even theoretically impossible to have them both in the center of the x-coil pair. In the next subsection we therefore study the effects of the coil misalignment with respect to the chip.

5.2.3 Effect of the bias field inhomogeneity on the trap position

The magnetic bias field \vec{B}_{ext} created by macroscopic coils in the vicinity of the chip are not ideal homogeneous fields as often simplified in text books. The shallower the traps are and the further out of the optimal center of a Helmholtz-coil pair we operate, the more we find effects of the finite field curvature of \vec{B}_{ext} .

In the previous section 5.2.2, we already saw one beneficial application of this field curvature, leading to confinement of the atoms. As we will see in this section, the trap position depends strongly on the position of the chip with respect to the coil cage, as shown in Fig. 5.8. For the three-wire trap, the trap displacement along x with the coil

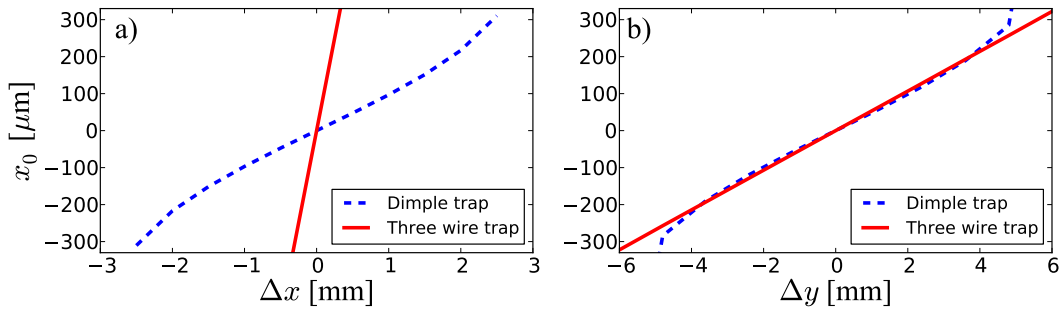


Figure 5.8: Trap position depending on coil cage displacement for the dimple trap and three wire trap discussed in the text. The displacements along y and z are negligible and not shown. a) shows the translation of the trap position for a displacement of the coil cage along x . The three wire trap position shows the same displacement as the coil cage, since the confinement along x is only provided by the coils. b) shows the x -position dependence of the trap on a displacement of the coil cage along y .

cage displacement is trivial, since the magnetic field minimum is at the center of the two coils.

The translation of the trap along x due to a y -displacement of the coil cage is less

evident and will be explained in the following: The magnetic field created by the x-coil has as well components $B_{y,coil}$ and $B_{z,coil}$, as shown in Fig. 5.9.

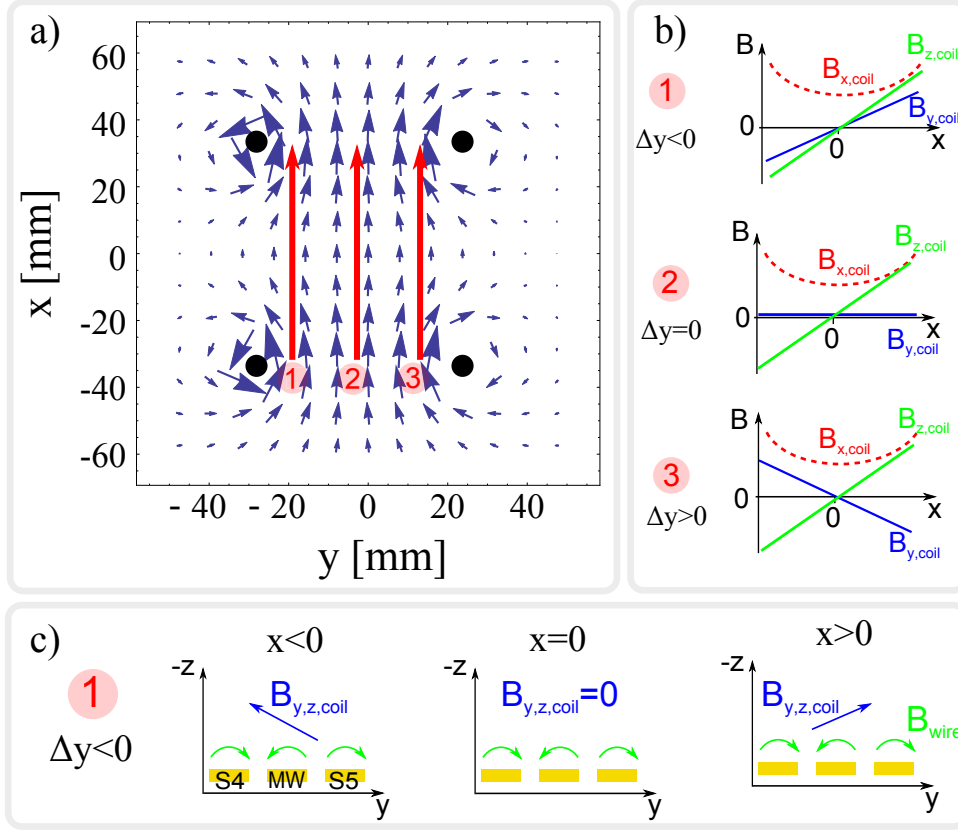


Figure 5.9: Simulated magnetic field of the x-coil pair in xy -plane at height of the chip surface. The cuts through the coil wires are marked as black circles. b) The cuts along 1,2,3 sketch the dependence of the magnetic field components on the y -position. While $B_{x,coil}$ and $B_{z,coil}$ do not change their qualitative behavior along x for the different y positions, $B_{y,coil}$ is 0 for all x for $\Delta y = 0$ and has opposite slopes for the two cases $\Delta y < 0$ and $\Delta y > 0$. c) shows the interaction of the coil field with the wire field for the cut along 1. For $x < 0$ the coil field reduces the bias field created by the wires S4, S5. For $x > 0$ the coil field increases the bias field.

These components interfere with the magnetic field components along y and z created by the chip wires $B_{y,wire}$ and $B_{z,wire}$. In Fig. 5.9, b) it can be seen that $B_{y,coil}(x)$ changes its sign along x for a displacement $\Delta y \neq 0$. This means that $B_{y,coil}$ reduces the bias field created by the wires S4 and S5 for $x < 0$ and increases the bias field for $x > 0$, as depicted in Fig. 5.9, c). Consequently the distance of the 2D-quadrupole minimum to the chip changes with x (compare with Eq. 1.4.2), which can be interpreted as a tilt in the xz -plane. In the presence of gravity, this tilt of the 2D-quadrupole center line in the xz -plane leads to a pull of the atoms along x , as found with the simulation presented in Fig. 5.8.

Since the cavity region is shifted by $\Delta y = 6.45$ mm with respect to the coil cage, the atom cloud is shifted by $\sim 150 \mu\text{m}$ along x . This deviation along the cavity axis

(= x -axis) leads to an decreased coupling of the atoms to the cavity field and increases atom loss due to collisions with the near-by cavity mirrors.

A variety of possible solutions can be found by using chip wires to push or pull the trap minimum along x . The simplest solution is to apply $\sim 4.1\%$ more current in one of the x -coils, which re-centers the atom cloud along x without changing the overall trap properties of the three-wire trap.

Note that this step makes an additional power supply necessary, rendering the trap more prone to current fluctuations. The dimple trap can not be recovered as easily by adjusting the x -coil currents for $\Delta y > 4$ mm. But a trap with similar parameters as shown for the centered dimple trap in Tab. 5.2 can be generated by not using the centered base chip wire to “dig” a dimple, but to use a current of $I_{B5} = -0.14$ A in B5 to create a hill in the magnetic potential, as shown in Fig. 1.7 c). Together with the x -coil curvature this leads to a centered confinement of the atoms with $\omega_{1,2,3} = 2\pi$ (2.1; 78; 96) Hz.

A more elegant way would be to create the interrogation trap only with chip wires, to rely for the trap positioning only on micro fabricated structures with well defined distances, which will be treated in the following subsection.

5.2.4 Stand-alone chip trap

An interesting trap type is a stand-alone chip trap, which resigns completely the external coils. An advantage is that the trap position is only defined by micro fabricated chip wires and is therefore well controllable, in contrast to the effects of the macroscopic coil cage position, described in the previous Sec. 5.2.3. Furthermore, the overall energy consumption can be reduced since the magnetic fields are created in direct vicinity of the trapping position. This is of particular interest for application in mobile devices.

An additional requirement has to be taken into account for the here presented clock, where the atoms have not only to be trapped by the magnetic field, but the field in the trap center has to realize the “magic field” as discussed in Sec. 1.2.1.

The strong transversal confinement can again be realized by the three-wire trap configuration in Fig. 5.7. The longitudinal confinement along x and the “magic field” are then provided by the base chip wires B1-B5, for which we now discuss a suitable configuration.

The magnetic field of two parallel wires along y with the distance $2 \cdot d$, carrying the same current I , is given by

$$\begin{aligned} B_x(x, z) &= \frac{\mu_0 I}{2\pi} \left(\frac{z}{z^2 + (x-d)^2} + \frac{z}{z^2 + (x+d)^2} \right) \\ B_z(x, z) &= -\frac{\mu_0 I}{2\pi} \left(\frac{x-d}{z^2 + (x-d)^2} + \frac{x+d}{z^2 + (x+d)^2} \right) \end{aligned} \quad (5.2.2)$$

and is plotted in Fig. 5.10.

At the center of the two wires ($x = 0$) the field simplifies to

$$\begin{aligned} B_x(x = 0, z) &= \frac{\mu_0 I}{\pi} \frac{z}{z^2 + d^2} \\ B_z(x = 0, z) &= 0 \end{aligned} \quad (5.2.3)$$

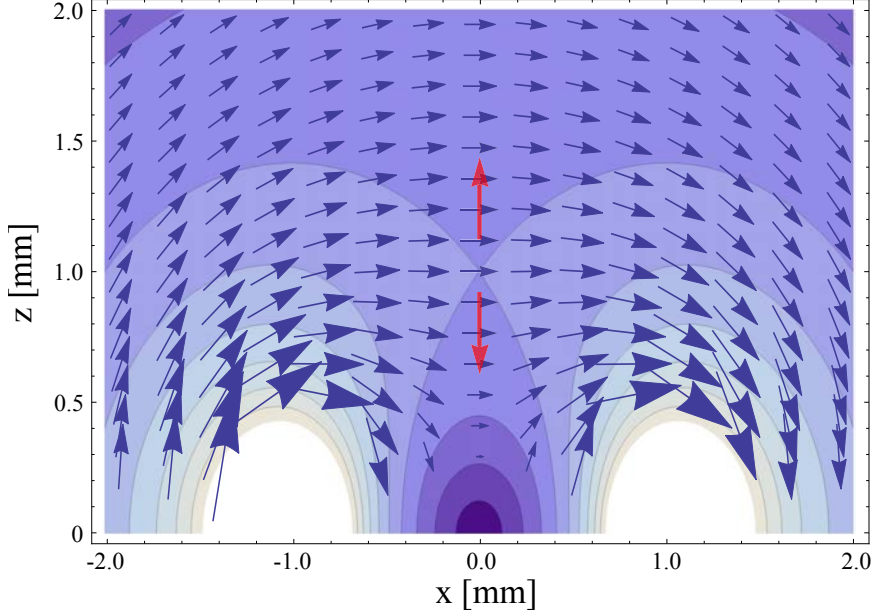


Figure 5.10: Magnetic field of two wires with a parallel current $I=1\text{A}$ and a distance of 2 mm between the two wires. In addition to the vector field, the magnetic field magnitude $|\vec{B}|$ is shown as contours with dark blue for $|\vec{B}| = 0\text{G}$ up and white for $|\vec{B}| > 5\text{G}$. The red arrows show the direction of the field gradient along z above and below the magnetic field maximum along z .

with the derivatives at the center between the two wires

$$\begin{aligned}\frac{\partial B_x}{\partial z}\bigg|_{x=0}(z) &= \frac{\mu_0 I}{\pi} \frac{d^2 - z^2}{d^2 + z^2} \\ \frac{\partial B_z}{\partial x}\bigg|_{x=0}(z) &= \frac{\mu_0 I}{\pi} \frac{d^2 - z^2}{d^2 + z^2}.\end{aligned}\tag{5.2.4}$$

From Eq. 5.2.4 follows (with $B_z(x=0, z) = 0$) that the field has its maximum along z at height $z = d$ and therefore changes the sign of the gradient $\partial B/\partial z$ at this height. This is a first important characteristic of this trap type, since the gradient can either reinforce the effect of gravity for $z > d$ or counteract the gravitational pull for $z < d$.

The trap distance $z_{0,SC}$ to the science chip surface is given by the three-wire trap, which is for our setup $z_{0,SC} \approx 300\ \mu\text{m}$. The thickness of the science chip of $\sim 400\ \mu\text{m}$ gives a distance of $z_0 \approx 0.7\text{ mm}$ from the trap to the base chip wires. To counteract the trap depth reduction by gravity (cf. Sec. 1.4.3) the base chip wire spacing has to be chosen to be $d > 0.7\text{ mm}$. We chose $d=1\text{ mm}$ and $d=2\text{ mm}$ with which we can realize the traps shown in Tab. 5.3.

For increasing d high currents are needed to create the “magic field” of $B_m \approx 3.23\text{ G}$, which can be avoided by using the central BC wire BC3 to lift the bottom field at the trap position. This can also be used to change the rotation of the trap axis and the orientation of the magnetic field at the trap center. Contrary to the case of the dimple trap with gravity (cf. Sec. 1.4.4), the trap axis angle $\alpha_{f3,x}$ and the bottom field angle

d [mm]	I [A]	f₁ [Hz]	f₂ [Hz]	f₃ [Hz]	$\alpha_{f3,x}$ [°]	$\alpha_{B,x}$ [°]	Trap depth [G]
1	1.92	113	108	29	8.6	0.2	0.29
2	6.05	132	121	15	13.5	5	0.8

Table 5.3: Stand-alone chip traps. The transversal confinement is realized by the SC wires S3, MW and S6 with currents (1, -1, 1) A, fixing the trap height to $z_0 \approx 300 \mu\text{m}$. The first row shows the results for parallel currents in B2, B4, the second row for currents in B1, B5. The currents were chosen to realize the bottom field $B_0 = 3.23 \text{ G}$. The distance of the SC to the BC wires is set to 0.4 mm.

α_B can have the same sign, if the gravitational sag is over compensated by the pulling gradient of the BC wires. The rotation of the trap eigenaxis is due to the changing z -components of the magnetic field in the 4 quadrants around the trap center, which is described by the gradient of B_z along x above the BC wire. Contrary to the dimple trap in Sec. 1.4.4 the stand-alone trap can be aligned with the x axis: The atoms are held at the position $y = 0$, $z_0 = d$, where with Eq. 5.2.4

$$b_l = \left. \frac{\partial B_z}{\partial x} \right|_{x=0} (z = d) = 0 \quad (5.2.5)$$

which gives with Eq. 1.4.22 $\alpha_{f3,x} = 0$ and aligns the trap axis with x . Without gravity the atoms are held in the magnetic minimum of the 2D-quadrupole and therefore the bottom field points as well along x , so $\alpha_{f3,x} = \alpha_B = 0$.

The situation is less advantageous in presence of gravity: To align the bottom field with x , the magnetic gradient $b_m = \partial_z B_x = -\frac{m}{g_F m_F \mu_B} g$ has to be used to compensate gravity and pull the atoms back in the 2D-quadrupole center. With $b_m = \partial_y B_z = \partial_z B_y \neq 0$ the trap eigenaxis will be rotated with Eq. 1.4.22. Comparing Eq. 1.4.22 and Eq. 1.4.19, it is evident that either the bottom field or the trap axis can be aligned with x .

The rotation of the trap axis and bottom field direction can be reduced by increasing the transversal confinement (see Eq. 1.4.24), which gives the following exemplary trap configurations in Tab. 5.4. If we calculate analytically the transversal gradient of the strong quadrupole for the wire distance $d = 300 \mu\text{m}$, we get in dependence of the SC current

$$b = 222 \text{ G/cm} \cdot I/\text{A}. \quad (5.2.6)$$

With the gravitational gradient $b_g = 33 \text{ G/cm}$ and Eq. 1.4.24, this leads to an angle between the bottom field and the trap axis of

$$\alpha = 33/222 \frac{\text{A}}{I} = 0.15 \frac{\text{A}}{I}. \quad (5.2.7)$$

This gives $\alpha = 8.6^\circ$ for $I = 1 \text{ A}$ as in Tab. 5.3 and $\alpha = 5.1^\circ$ and 4.2° for $I = 1.7 \text{ A}$ and 2 A in good agreement with the numerically simulated values in Tab. 5.4.

Since the transversal confinement is realized by the three-wire trap, the trap distance to the chip is determined by the wire spacing (cf. Eq. 5.2.2), if the antiparallel currents in S3, MW and S6 have the same amplitude. The trap can be run in this configuration, to investigate the clock stability without use of the macroscopic coil cage.

d [mm]	I_{B3} [A]	I_{B2,B4} [A]	f₁ [Hz]	f₂ [Hz]	f₃ [Hz]	α_{f3,x} [°]	α_{B,x} [°]	Trap depth [G]
1	-0.28	2.13	223	220	31	4.0	0.0	1.4
1	0	1.71	219	212	24	2.0	-2.0	1.2
1	0.283	1.28	216	204	14	0.0	-4.1	1.1
1	0	1.708	186	177	24	-2.4	2.4	0.8

Table 5.4: Stand-alone chip traps. The transversal confinement is realized by the SC wires S3, MW and S6 with currents (2, -2, 2) A, fixing the trap height to $z_0 \approx 300 \mu\text{m}$. The two rows show the results for parallel currents in B2, B3, B4. The currents were chosen to realize the bottom field $B_0 = 3.23 \text{ G}$. The distance of the SC to the BC wires is set to 0.4 mm. The last row shows an interesting configuration where the currents in the SC-wires are set to the same value as the current in the BC-wires $I_{all} = 1.708 \text{ A}$, which creates an interrogation trap that can be realized with only one current source.

This can lead to further insight in the source of the magnetic field noise. Especially the last trap in Tab. 5.4 is interesting in terms of stability and energy consumption, since it can run with only one current source.

The reduction of the number of individual currents prevents again the fine tuning of the trap position, as in Sec. 5.2.2. This is of no importance for the standard clock operation as it was in the previous TACC experiment, but gets crucial for the operation with the optical resonator, since the atom cloud has to be aligned with the resonator mode. This can be only achieved with currents of individual amplitudes in S3, S6 and MW. We therefore propose separated investigation of the clock operation with the “single current chip trap” and the operation with the resonator. Note, that the operation with the resonator is still possible with a standalone chip trap, but the position fine tuning demands $I_{S3,S6} \neq -I_{MW}$.

Thereby, we showed that a wide range of trap parameter is accessible with and without use of the macroscopic coil cage. Furthermore, we have seen that the trap angles can be controlled and that the simulation is in good agreement with the derivation of the trap- and the magnetic field- orientation in Sec. 1.4.4. This finishes our discussion of the DC currents and we can direct our attention to the MW guiding on the chip.

5.2.5 MW coplanar wave guide

The coplanar wave guide is one possible realization of a transmission line which delivers the MW ($f=6.835 \text{ GHz}$) to the atoms. Different transmission line types are available and discussed in [224], but since the performance of the coplanar wave guide in the previous TACC experiment [91] was fully satisfying, we keep the major properties of the design. To pass the two interrogation zones, the CPW is longer than on the previous TACC chip. To counteract the accompanying increase of the DC and MW resistance, and with this heating, we increased the wire width at the atom positions from $g = s = 50 \mu\text{m}$ to $g = s = 90 \mu\text{m}$ but kept the central wire distance $d = g/2 + s/2 + w = 175 \mu\text{m}$ (cf. Fig. 5.11). Since we work at atom cloud to chip distances

of $z_0 \approx 300 \mu\text{m} \gg g = s = 90 \mu\text{m}$, only negligible changes are expected for the MW distribution, seen by the atoms which we verified with DC simulations. To further reduce the resistance of the wire and to have a symmetric wire configuration around the atom positions, the CPW is widened again in between the trapping region and the cavity region (see Fig. 5.1).

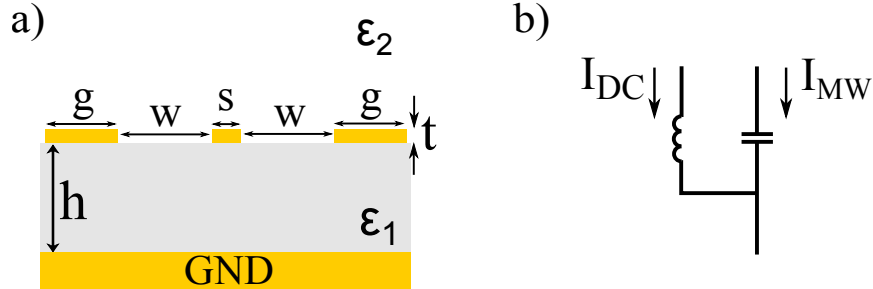


Figure 5.11: Coplanar waveguide and bias-tee

To reduce the CPW dimensions from the connector to the interrogation region, it is tapered linearly so that the impedance change along the line is not abrupt. For an ideal, lossless CPW with $g \rightarrow \infty$ and $t \rightarrow 0$ the impedance only depends on the ratio $\frac{s}{s+2w}$ [225], which means it does not change when s and w are scaled linearly. Since the wires are not lossless and as we have a GND-plane on the backside of the science chip, we calculate⁵ the impedance for the characteristic positions on the chip, shown in Tab. 5.5. It can be seen that the change of the impedance is most dramatic due

Position	s [μm]	w [μm]	h [μm]	t [μm]	GND -plane	Z [Ω]	loss dB/m
MW-connector	600	500	800	12	no	66.1	4.3
Bonding-BC	360	300	800	12	no	63.6	6.2
Bonding-SC	360	300	250	10	yes	41.4	8.6
atom position TACC2	90	85	250	10	yes	58.9	17.6
atom position TACC	50	125	250	10	yes	77	17.7

Table 5.5: Impedance along the CPW. The dimensions are given as sketched in Fig. 5.11. The calculations were made with $\epsilon_{AlN} = 8.7$, $\sigma_{Au} = 4.1 \cdot 10^7 \text{S/m}$, $\tan \delta = 10^{-3}$ and $f=6.8 \text{ GHz}$.

to the GND-plane at the backside of the science chip. We assume that the reduced transmission measured for the previous TACC chip to be -4.75 dB [91] is mostly caused by the impedance jump at this position, enforced by the discontinuity due to the wire bonding. An interesting option would be to change the wire geometry on the science chip to account for the impedance change due to the additional GND-plane. If we

⁵TXline, Freeware. The calculation assumes $g = \infty$, which is not the case for our CPW with $g = s$. A full simulation of the microwave field for our configuration in [91] shows impedance values close to the ones calculated with TXline, justifying the approximation.

<http://www.awrcorp.com/products/optional-products/tx-line-transmission-line-calculator>

chose $s=140\ \mu\text{m}$ instead of $s=360\ \mu\text{m}$ at the position “Bonding-SC” in Tab. 5.5 and keep the other parameters, we get an impedance $Z=63.6\ \Omega$ in continuity with the value on the BC. We decided against this possibility in order to avoid any other unwanted effects e.g. on the mode shape and stayed close to the initial design, but it could be subject of further testing for the next chip generation.

Bias-tee and interdigital capacitors: To be able to realize the magnetic traps with the CPW, it is necessary to feed besides the MW currents DC currents to the wires. Therefore, a *bias-tee* coupler can be used, where the MW is coupled capacitively to the DC carrying wire as depicted in Fig. 5.11 b). For the central wire this can be achieved with commercial MW-components prior to the connection to the atom chip, which is realized in the existing TACC experiment.

A limitation for the carried out interferometer experiments with TACC was the lacking possibility to apply independent DC currents to the outer wires of the CPW [226]. This made it impossible to create trap configurations comparable to the situation in [227], where the quadrupole axis are parallel and orthogonal to the chip, favorable for the applied MW-dressing scheme.

To apply independent currents to the outer wires of the CPW (for us S4, S5) a bias-tee has to be realized on the chip, since the SMP-connector has only one common ground. An elegant solution was found in [228] where a SMD-capacitor realizes the capacitive coupling. To avoid the additional solder step during the chip production and realize a fully integrated system, we investigated the possibility to realize the bias-tee with an interdigital capacitor, integrated in the chip-wire design. The layout of the

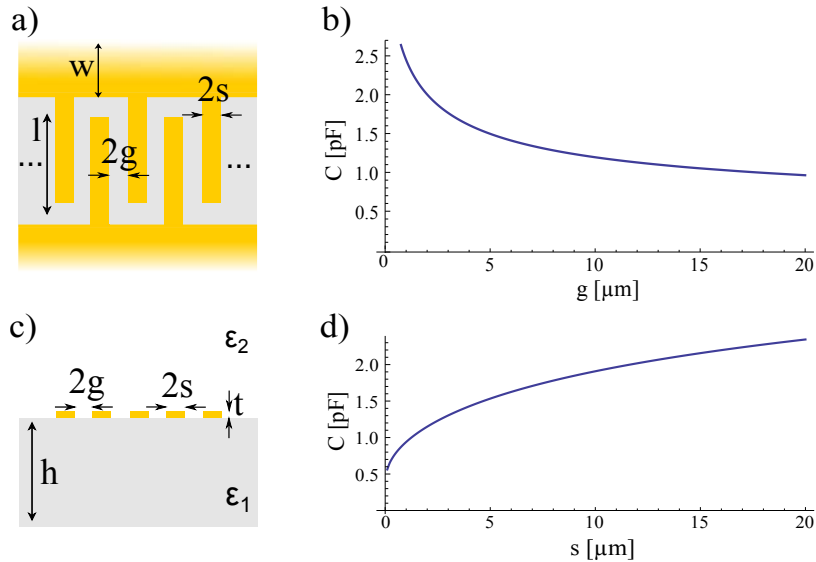


Figure 5.12: Interdigital capacitor. a) shows the geometry from the top, c) the profile. The yellow structures mark the gold wires, the gray area the AlN substrate. b) shows the calculated capacitance over a varying conductor distance g , with $s = 5\ \mu\text{m}$. d) shows the capacitance for varying wire width s , with $g = 5\ \mu\text{m}$. The other parameters for both plots are $w = \infty$, $l = 1\ \text{mm}$, $t = 12\ \mu\text{m}$, $\epsilon_1 = \epsilon_{\text{AlN}} = 8.7$, $\epsilon_2 = 1$, $h = 800\ \mu\text{m}$ and $n = 50$.

interdigital capacitor is shown in Fig. 5.12 for which the capacitance is given by [229]

$$C_n = (n - 3) \epsilon_3 \epsilon_{en} \frac{K(k_0)}{K(k'_0)} l \quad (5.2.8)$$

with

$$\begin{aligned} \epsilon_{en} &= 1 + q_{1n} \frac{\epsilon_1 - 1}{2} \\ q_{1,n}(s, g) &= \frac{K(k_{1,n}) K(k_0)}{K(k'_{1,n}) K(k'_0)} \\ k_0 &= \frac{s}{s + g} \\ k_{1,n} &= \frac{\sinh\left(\frac{\pi s}{2h}\right)}{\sinh\left(\frac{\pi(s+g)}{2h}\right)} \sqrt{\frac{\cosh^2\left(\frac{\pi(s+g)}{2h}\right) + \sinh^2\left(\frac{\pi(s+g)}{2h}\right)}{\cosh^2\left(\frac{\pi s}{2h}\right) + \sinh^2\left(\frac{\pi(s+g)}{2h}\right)}} \end{aligned} \quad (5.2.9)$$

where $K(k)$ is the elliptic integral of the first kind, l is the finger length, n the number of fingers and $k'_i = \sqrt{1 - k_i^2}$. In Fig. 5.12 the capacitance is shown for varying gap size g and finger width s , for a capacitor realized by wires of height $t = 12 \mu\text{m}$ on AlN ($\epsilon = 8.7$ [230]). For simplicity, we neglected the two outmost fingers in the calculation, since their contribution for $n=50$ is small. The overall capacitor width varies for both graphs from 0.5 mm to 2.5 mm, which is the maximum we set to fit to the already crowded surface of the chip. In order to maintain the same requirements for the fabrication, we set the minimum wire distances and widths to $2g = 2s = 10 \mu\text{m}$. For a footprint of $1 \times 1 \text{ mm}^2$, we get with this a capacity of $C = 1.6 \text{ pF}$. This value is 60 times smaller than the capacitance used in [228], where a cutoff frequency of $\sim 0.1 \text{ GHz}$ was measured for the capacitive coupling. A 60 times higher cutoff frequency of $f_c = 6 \text{ GHz}$ is close to the MW frequency our experiment relies on, for which reason we decided against the interdigital capacitor and realized the bias-tee in the tried and tested implementation of [228], depicted in Fig. 5.17.

Herewith, all central components of the chip layout are defined, and the complete layout is shown in Fig. 5.1 and more detailed in Fig. 5.2, A.7, A.6. To reduce the glue layer thickness between vacuum cell and chip, a gold frame was added to the base chip. Furthermore, no DC connection holes and bonding positions were placed in the two optical axes on the chip to not disturb the imaging. Finishing the design considerations, the chip is ready for production.

5.3 Fabrication

The chip production follows the recipe given in [225] and [231, 232] with slight modifications. The steps are shown in Fig. 5.13 and are described in detail in the appendix. In the following, we note only the major steps and the differences to the original recipe: A thin titanium adhesion layer (5 nm) and a 50 nm gold seed layer are deposited by e-beam evaporation on the thoroughly cleaned AlN wafer⁶. With a spin coater we apply a homogeneous layer of positive photoresist,⁷ which is then selectively exposed using a chrome mask⁸ in a mask aligner⁹. The exposed resist is developed¹⁰ and the gold layer is grown in an electroplating process¹¹ on the seed layer.

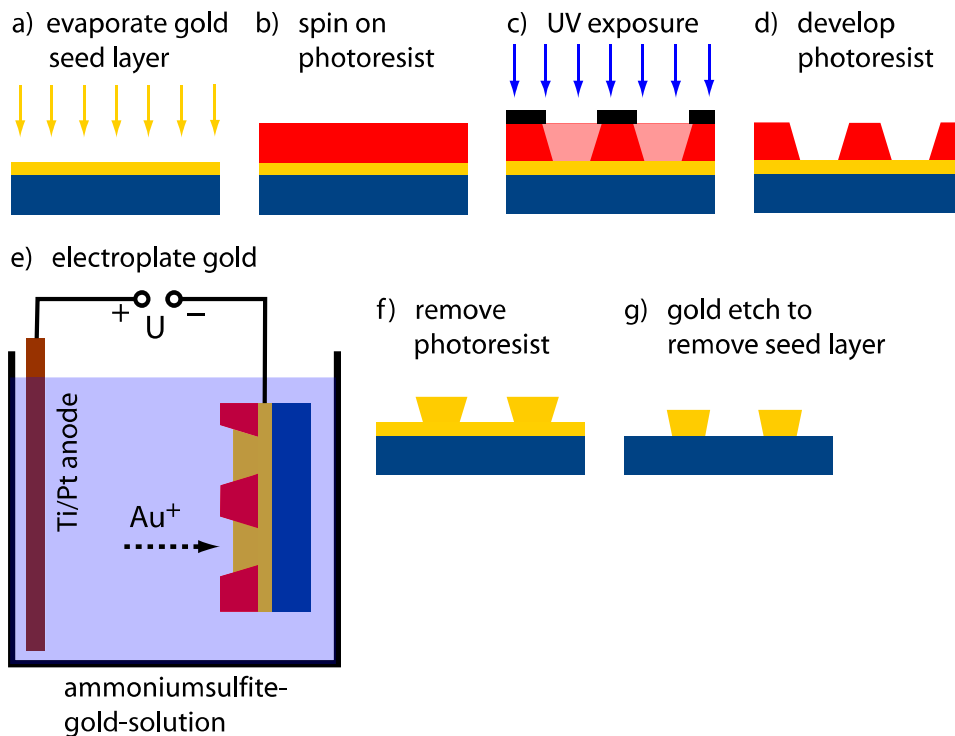


Figure 5.13: Chip fabrication process. The steps are explained in the text. Taken from [225]

After the gold is grown to the desired thickness, the photoresist is removed with acetone. We changed the following step of the seed layer removal like suggested in [232] and replaced the chemical etching with aqua regia by an ion milling process. The advantage of this process is, that it is very clean and reproducible and does not involve dangerous chemicals. Furthermore, the seed layer is attacked everywhere

⁶Plassys MEB550S

⁷ma-P 1240, ma-P 1275, micro resist technology GmbH, Berlin, Germany

⁸Delta Mask B.V., Enschede, Netherlands

⁹MJB4, SÜSS microTec, Germany

¹⁰ma-D 331, micro resist technology GmbH, Berlin; AZ 726 MIF, MicroChemicals GmbH, Ulm, Germany

¹¹Gold-SF-bath, METAKEM GmbH, Usingen, Germany

homogeneously, while the aqua regia etch can be slower in tight channels or corners. In [225, 233] indications for an increase of the surface roughness of the electroplated gold were found during the aqua regia etch. We realized the ion milling with two different machines: one is a reactive ion etcher (RIE)¹² where the gold is machined with SF₆ molecules accelerated by an RF-voltage. The low reactivity of gold does not lead to reactive ion etching but the physical bombardment still attacks and reduces the gold surface. The reflectivity of the machined surface can be observed during the process, depicted in Fig. 5.14. While removing ~ 350 nm of electroplated gold we could

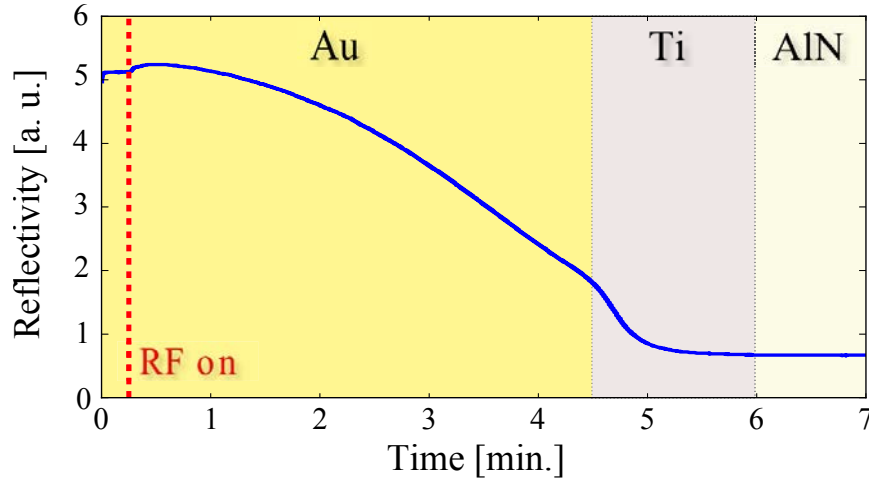


Figure 5.14: Au/Ti removal by reactive ion etching. The graph shows the reflectivity at $\lambda \approx 770$ nm of the gold and titanium coated AlN wafer during the dry etching of the seed layer of $t_{Au} = 50$ nm, $t_{Ti} = 5$ nm. The reason for the slight increase of the reflectivity after switching on the RF is unknown. We attribute the change in the edge speed at 4.5 minutes to the transition from Au to Ti. The reflectivity stagnates after 6 minutes, which signals that the AlN surface is reached.

measure with a DEKTAK profiler¹³ a negligible increase of the surface roughness of $r_a = 28 \pm 3$ nm to $r_a = 30 \pm 3$ nm. Since this measurement may not be sufficient because of the finite tip size of the DEKTAK ($r_{tip} = 5 \mu\text{m}$), we measured the surface with a atomic force microscope (AFM), shown in Fig. 5.15. The surface roughness was estimated over a 2D profile and gives $\sigma_r = 33.7$ nm before the etching and $\sigma_r = 32.3$ nm after the electroplated gold layer was reduced by ~ 350 nm. No increase of the surface roughness can be observed and the small *decrease* of the surface roughness is in the error margin. It is worth noting that we measured on the surface of the AlN wafer an increase of the surface roughness from $r_a = 34 \pm 3$ nm to $r_a = 50 \pm 3$ nm for the same etching process. In [233] an increase of the surface roughness of the electroplated gold due to the aqua regia etch was observed with the same DEKTAK, giving a roughness of $r_a = 66$ nm on some regions of the surface, which is significantly worse than the results of the RIE process.

The second machine we used to remove the seed layer was the e-beam evaporator,

¹²Corial 200R

¹³Veeco, DEKTAK 8

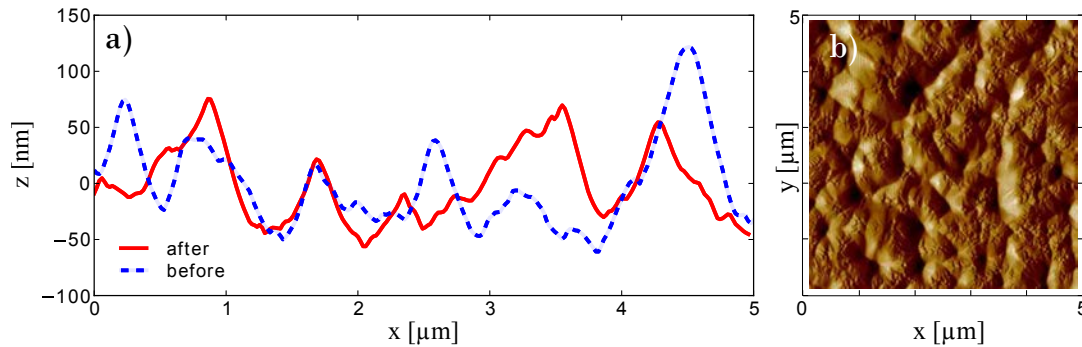


Figure 5.15: Au surface after RIE etch. The electroplated gold surface was measured before and after reducing the gold layer thickness by ~ 350 nm. a) shows a cut along x of a measured 2D profile as shown in b). The measurements were performed on the same position on the chip and show with $\sigma_{r,before} = 33.7$ nm and $\sigma_{r,after} = 32.3$ nm no increase of the surface roughness during the etch process.

which is equipped with an argon-ion gun. Here we got similar results for the surface roughness. Both processes are more convenient and reproducible than the chemical etch. To give a conclusive answer on the effect of the etch method on the surface roughness, the surfaces should be measured with more suited instruments, like the optical profilometer presented in Sec. 3.3.1 or an atomic force microscope.

The DEKTAK profiler gave us the possibility to measure the photoresist and gold profiles during the fabrication process. The results for one science chip are shown in Fig.5.16. It can be seen that the gold grows slower at the center of the chip, where the circle of the Ω -wire meets the legs (Fig.5.16 b)). Furthermore it is apparent that the electroplating process alters strongly the shape of the photoresist and creates walls at the interface of electroplated wires and the photoresist. This effect could be observed for both resists used, maP-1240 and maP-1275. Since the measurement of the wire widths gives systematically values 1-5 μm wider than the initial gap in the photoresist structure, we assume that the gold pushes the photoresist to the outside while growing. This is confirmed by looking at Fig. 5.19 a), where the walls are visible with an optical microscope due to their lensing effect and the photoresist is cracked in the corners. None of the effects pose problems for our chips, but should be taken into account if very accurate wire width and heights are necessary.

With the described recipe, we produced several science and base chips, presented in the following.

5.3.1 Base chip

The final base chip consists of a 0.8 mm thick AlN-180 wafer¹⁶ with a nominal surface roughness of $r_a < 50$ nm. The layout of the electroplated gold structures of 11 – 12 μm thickness is shown in Fig. A.7. Prior to the fabrication, holes of diameter $\varnothing = 0.6$ mm

¹⁶Supplier: CoorsTek Advanced Materials ANCeram

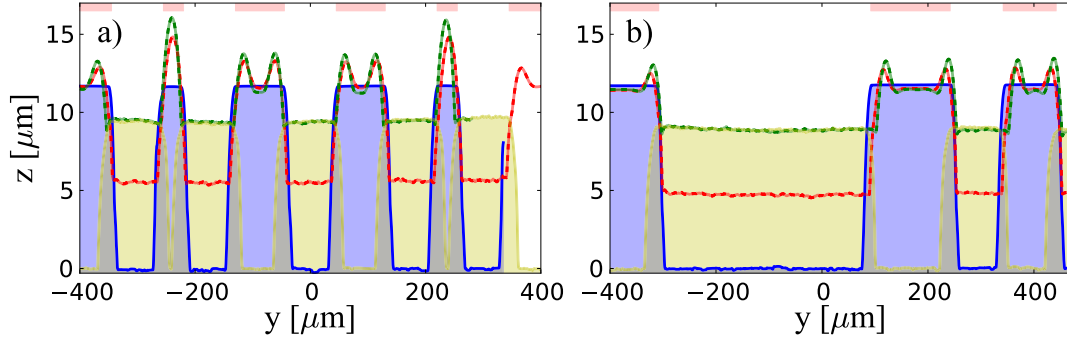


Figure 5.16: Photoresist and Au-Profile. Both pictures show the different steps of the electroplating process on two different positions on the same science chip. a) shows the wires close to the trapping region, with the MW wire in the center. b) shows the Ω -supply wires. All traces are measured with a DEKTAK surface profiler¹⁵ with a tip radius of $r = 12.5 \mu\text{m}$, which leads to the artifact of a large angle of the photoresist and wire walls. The blue line shows the photoresist structure after development, the red line shows the photoresist and the electroplated gold after 35 min. of electroplating. The green line shows the photoresist and gold after 65 min. of electroplating. The yellow line shows the gold wires after the photoresist and the seed layer have been removed. The red rectangles show the mask.

for the DC contacts have been laser drilled¹⁷ in the wafer. The process produces conductive Al droplets in the vicinity (up to 1 mm away) of the holes and would contact neighboring conducting paths. They can be removed with a scalpel, a fiber glass brush¹⁸ and some patience¹⁹. The AlN surface around the holes is scratched during this step, but we could not see any problems arising from this in the following fabrication steps.

After the electroplating, we used indium based reflow solder paste²⁰ to connect the bias-tee capacitors²¹ and the mini-SMP²² connectors to the chip, in order to avoid degradation of the electrical contact over time [228], as shown in Fig. 5.17.

5.3.2 Science chip

The science chip consists of a AlN-180 wafer of thickness $h=0.29 \text{ mm}$ ²³ with a specified surface roughness of $r_a < 50 \text{ nm}$. The layout of the electroplated gold structures of $9 - 10 \mu\text{m}$ thickness is shown in Fig. A.6. We encountered problems during the

¹⁷A.L.L. Lasertechnik GmbH, München

¹⁸e.g. DURATOOL pencil brush

¹⁹Cannot be bought.

²⁰Indalloy #204, Indium Corporation, Chimie Tech Services, Antony

²¹ $C=100 \text{ pF}$, KEMET KONDENSATOR (C0402H101J5GACT500 MLCC C0G/NP0 100PF 50V 0402), unfortunately we found the capacitors to be magnetic so they will be replaced by non-magnetic capacitors, like <http://www.vishay.com/docs/45128/nonmagneticepoxybond.pdf>

²²18S101-40ML5-NM, Rosenberger, Tittmoning

²³We ordered a thickness of $250 \mu\text{m}$ and realized to late that the wafers are to thick.

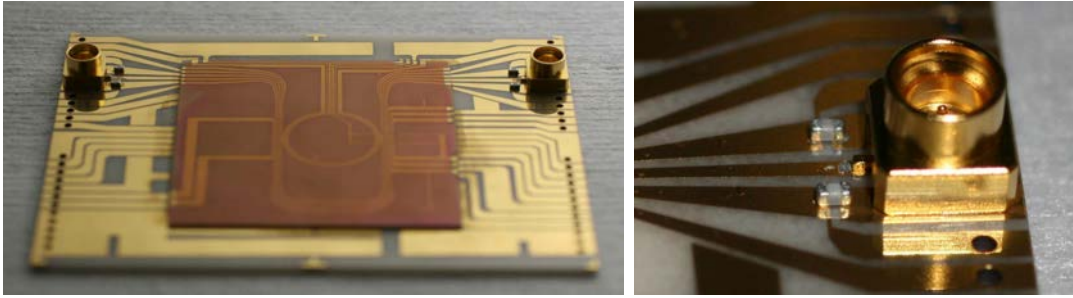


Figure 5.17: Chip assembly with MW connector and bias-tee capacitors soldered and the SC glued to the base chip.

development of the photoresist, which resulted in non-straight resist edges and thereby an increased wire edge roughness, as depicted in Fig. 5.18 a). In [234] it is shown that

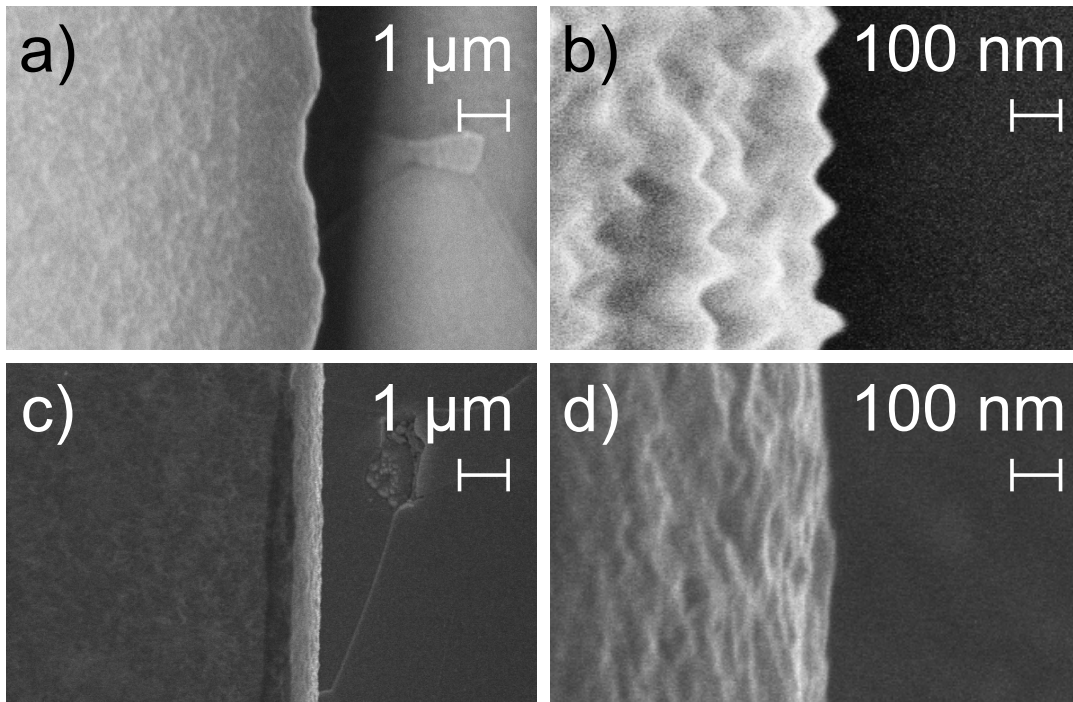


Figure 5.18: SEM pictures of SC wire edges. On all pictures the gold surface is on the left. a) shows the first attempt, where the edge of the chip wire shows irregularities of $\sim 1 \mu\text{m}$ due to problems with the photoresist development. b) shows an old chip of the previous TACC chip production [231] declined by 50° . c) and d) show the wires of the final TACC 2 science chip before RIE etching without inclination.

wire edge roughness leads to a distortion of the trapping potential. This is of particular importance for TACC, since the final temperature of the atoms is below 100 nK, and thereby already minuscule potential corrugations would split the atom cloud.

It was found that the developer we used (expired maD-331) attacked the photoresist very selectively and created “mousebites” at the edge of the resist structures, which could not be improved by different concentrations. By changing to an TMAH based developer (AZ 726 MIF) this effect was effaced, visible in Fig. 5.18 c),d) and Fig. 5.19 c). The selective developing could be related to an increased tendency of NaOH based developers to penetrate micro channels in the resist, which is reduced with TMAH based developers [235]. To avoid coupling of the MW to the base chip wires, we

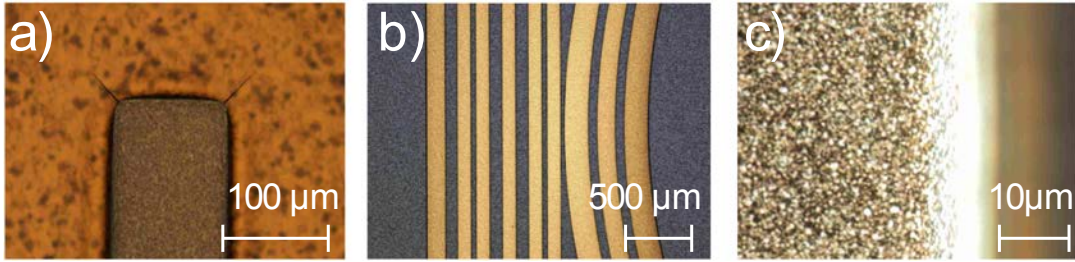


Figure 5.19: Microscope pictures of the science chip. a) shows the cracking of the photoresist during the electroplating as fine diagonal lines in the wire corners. b) shows the wires in the trapping region. c) shows a close-up of a science chip wire edge, where the granularity of the electroplated gold is visible.

applied a $\sim 12 \mu\text{m}$ thick gold ground plane on the back side of the science chip. The backside was not polished and shows a roughness of $r_a \approx 0.8 \mu\text{m}$. The gold adhesion was weaker than on the front side, where the gold cannot be removed mechanically from the AlN. On the backside, the gold adhesion is still mechanically stable but can be damaged with brutal scratching with a scalpel. For future chip productions, we recommend to work with wafers polished on both faces, which should as well increase the thermal contact of the two chips. After the clean room fabrication, the BC and SC were cut to their final size with a dicing saw²⁴ and a high reflective transfer coating²⁵ for the mirror-MOT was glued²⁶ to the science chip. We used four bond wires of diameter $\phi = 25 \mu\text{m}$ as spacers for this gluing step, to ensure a minimal glue layer thickness [236]. The wires were placed on the transfer coating, so that they would not touch any chip wire. The science chip and the base chip were then glued together with thermally conductive epoxy²⁷, while the ground plane on the back side of the science chip was connected to the base chip with one drop of electrically conductive epoxy²⁸, shown in Fig. 5.17. It may be interesting to note for future chip manufacturers that the electrically isolating glue increases its resistivity by more than one order of magnitude during the cure, while the electrically conducting glue is first non-conductive in the uncured state and gets conductive during curing. Finally, base and science chip were connected by 12-14 bond wires ($\phi = 25 \mu\text{m}$, $I_{max} = 0.8 \text{ A}$) per connection and the DC resistances of all wires were tested. As expected, the thinnest wires of the CPW show

²⁴Disco DAD-321

²⁵Optische Interferenz Bauelemente GmbH, Jena

²⁶Epotek 353ND

²⁷Epotek H77

²⁸Epotek H20E

the highest resistance of $R = 1.44 \Omega$ at 1A, as in the previous TACC, measured with a 4-point measurement.

Following the described recipe, three chip ensembles were fabricated and are ready to be combined with the resonator mount described in Sec. 4.2.7.

5.3.3 “Marriage” of chip and resonator

After the successful fabrication of the chip and the resonator ensemble, the resonator mount was glued²⁹ to the chip. Only one side of the bridge is glued to the chip since this strongly reduces the effect of thermal expansion of the chip on the resonator [135]. In Fig. 5.20 a) it can be seen that the polishing of the quartz bridge (see Sec. 4.2.7) allows the alignment of the resonators with the science chip wires with a lateral precision of $\sim 10 \mu\text{m}$. With Fig. 5.20 b) the distance of the fibers to the mirror surface can be estimated to $(250 \pm 20) \mu\text{m}$ leading to a distance from the chip surface to the cavity center of $(370 \pm 30) \mu\text{m}$, which is $70 \mu\text{m}$ further away than planned, mostly due to the imprecise height of the piezo stack. This distance to the chip wires is close to the working distance in the previous TACC experiment ($d \approx 350 \mu\text{m}$) and should not pose any problems for the experiment.

Now, the chip-cavity ensemble is ready to be assembled with the vacuum cell.

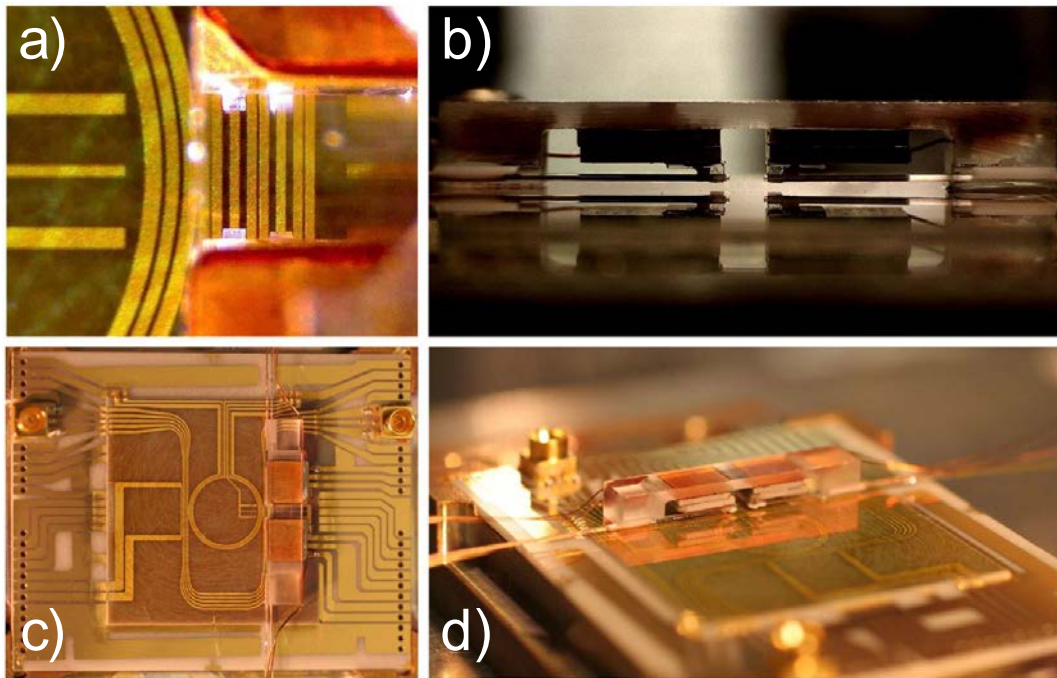


Figure 5.20: Cavity mount glued to chip. a) shows the two resonators above the science chip wires. See Fig. 5.2 for comparison. The view is slightly blurred by the quartz bridge. b) side view on the bridge where the reflection in the mirror coating is visible. c) top view of whole ensemble d) perspective view of the ensemble.

²⁹Epotek 301. This step was skillfully accomplished by Mengzi Huang, while I was already writing this manuscript

Conclusion and Outlook

Experiments with TACC2

In this thesis we have described the conception and successful construction of the new centerpiece of our atomic clock that opens the way for an “entanglement-enhanced” trapped atom clock on a chip.

For this purpose, a new atom chip was designed which allows the trapping and manipulation of the atoms. It is the first atom chip assembly that combines an optical resonator with a MW guide which can be used for CQED experiments with state dependent microwave potentials, besides the clock operation.

During the preparation of this manuscript, the TACC team continued the experimental work by gluing the resonator-chip ensemble to the vacuum cell which is now ready for pumping. Since the whole construction is compatible with the existing TACC setup, first cold atoms on the new chip of TACC2 are expected in the next months.

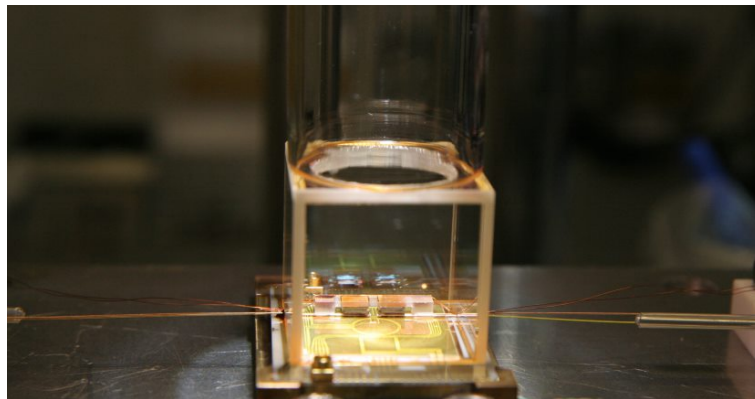


Figure 5.21: TACC2 chip assembly with cell.

After calibration, the FFP resonators will enable a wide range of experiments ranging from Dick-Effect reduction by reuse of the cold atoms to more sophisticated experiments such as spin-squeezing. The unique properties of the TACC2 experiment will allow us to investigate the new physical effects that we expect to arise at this level of precision. We are curious to study the interplay of the spin-self rephasing mechanism (first observed in TACC [65]) with the light-mediated entanglement used for spin-squeezing. This presents an experimental situation that has never been accessed so far and will grant insight into the mechanisms of both effects. Since the long co-

herence times due to the spin-self rephasing and the spin-squeezing are both directly related to the performance of the clock, we expect this study to be of profound interest for metrology, as well as for the fundamental understanding of atomic interactions.

Next steps:

The technological developments carried out during this work open the way for further applications for TACC but also beyond. In the following, we present promising “next steps”.

TACC2:

- The measurements taken during the atom chip production suggest that the use of reactive ion etching for seed layer removal lead to a decreased surface roughness compared to the previous used chemical etching. As surface roughness is a critical parameter for atom chips in general, it deserves being investigated further.
- The new setup will also contain a 2D-MOT, allowing faster loading at lower background pressures. This reduces the dead time of the clock and increases the lifetime of the trapped atoms. The reflective chip surface allows to send a beam nearly antiparallel to the atomic beam coming from the 2D-MOT. One possible application is to slow down the atom beam before reaching the 3D-MOT zone to increase the loading efficiency.
- Depending on the attainable clock stabilities, a further miniaturization of the TACC2 setup should be considered. The centerpiece, consisting of atom chip and FFP resonator, is not the limiting size factor of the current setup and should allow a system size comparable to compact commercial devices [29]. Especially the combination with *single beam MOTs* [202, 237] and atom detection exclusively with the resonator would yield a compact and robust system, requiring only one free-space laser beam. Furthermore, the modularity of atom chips offers the possibility to combine TACC2 with chip-based interferometers already under development [238, 239]. The two trapping sites on our new chip could be used for preliminary tests of running two spatially separated devices (here two clocks) on one chip.
- The investigation of the magnetic traps in Ch. 5 showed that the new chip can create a stand-alone chip trap with only one single current, without need for external coils. The TACC2 setup can be used to investigate its suitability for clock operation. Based on the acquired experience, a dedicated miniaturized chip could be designed, taking another step towards a compact system.

CO₂ machining:

The versatility and precision of our new CO₂ dot milling method now allows the fabrication of large spherical depressions on the end facets of different types of fibers. This has enabled the construction of the longest FFP resonators to date, and several research groups already applied the method for the fabrication of their micro mirrors.

- In addition to the fabrication of simple concave shapes, our method allows one to produce freeform optics with a wide range of possible applications. As a first example, Fig. 5.3.3 shows a lens array fabricated with our new platform that could be used to realize a 2D-array of dipole traps as in [240]. Optical elements with less regular forms, as in [241], are in reach as well.

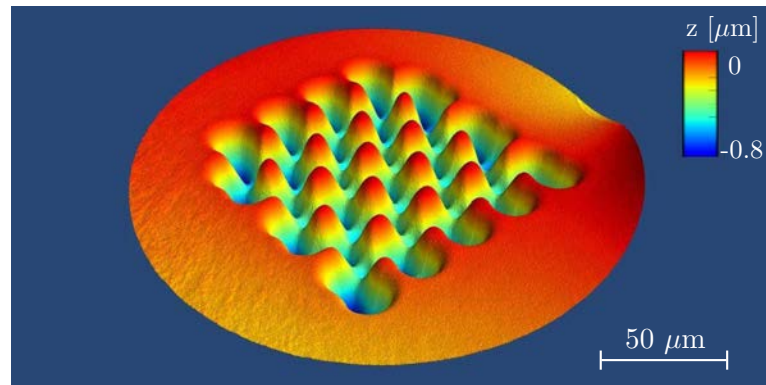


Figure 5.22: 3D profile of the CO₂ machined micro lens array on a MM fiber end facet, shown in Fig. 3.15 c).

- Graded phase mirrors [242] are further, readily realizable, structures that can shape the intra resonator intensity profile. This can be used to obtain exotic resonator modes, such as flattened Gaussian beams [243, 244] which would lead to an increased homogeneity of the atom-resonator coupling and reduce the dependence of the transversal atom-position.

Long FFP resonators:

To fulfill the requirements of the experiment, we have developed a new generation of long FFP resonators. Using the novel CO₂ laser machining method, we could realize the longest FFP resonators to date, which show coating limited high finesse of $\mathcal{F} > 40.000$ at lengths up to $L = 1.4$ mm. High finesse of $\mathcal{F} > 10.000$ was measured even at length $L > 2$ mm.

We have also been able to increase the fiber-resonator coupling by more than a factor of 5, by using for the first time large mode area photonic crystal fibers for FFP resonators. We are optimistic that an even better coupling can be obtained by optimizing the collapsing process. The combination of photonic crystal fibers with the appropriate high reflective coating allows us furthermore the simultaneous operation

at 780 nm and 1560 nm. This makes our cavities the first FFP resonators that span a full octave, further increasing the field of application of FFP resonators.

- The achieved resonator length enables our TACC2 experiment, but the technological advancements regarding long FFP resonators could be of great use in other fields, such as quantum communication. As shown in [245, 246], optical resonators can serve as an efficient interface between single photons and atoms or ions. This was used to realize an elementary quantum network with macroscopic resonators in [82], which can be seen as a first step towards a “quantum Internet” [81]. First proof-of-principle experiments, coupling a FFP resonator to an ion were already carried out [78, 139] and the advantage of direct fiber coupled FFP resonators for network applications is evident. Thus, we hope that our long FFP resonators can be of great use in the ion community, where the ion trapping is impaired by short resonators [147, 247]. This is investigated in our collaborations with the ion community.
- The reduction of the free spectral range with the cavity length brings our resonators into a regime interesting for applications as mode filter.
- A very promising alternative for increasing the mode coupling in the future is the use of mode-matching optics for FFP resonators. The best candidates to adapt the SM fiber mode to the resonator mode are graded index (GRIN) lenses. Here, it is possible to use standard graded index MM fibers to realize the lenses, which does not increase the systems size [248]. Furthermore, the standard fiber processing tools, such as splicers and cleavers, can be used, benefiting from the mature fiber technology. Fig. 5.3.3 shows our first attempts in this direction, where a GRIN lens is spliced to a SM fiber. Combining two fibers terminated

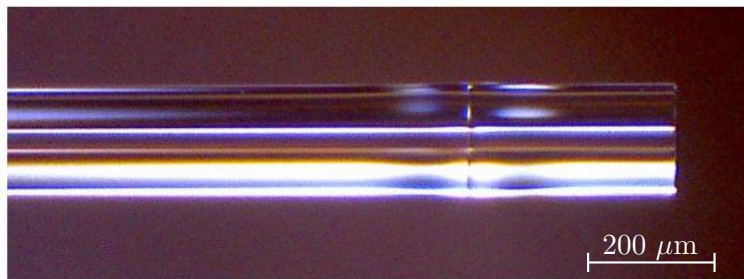


Figure 5.23: Cu800/200 (IVG fibers) SM fiber with a short Cu 50-200 (IVG fibers) MM fiber as a grin lens. The splice parameters are not optimally chosen, which leads to a slight thickening of the fibers at the splice.

with GRIN lenses, we readily achieved SM-fiber to SM-fiber coupling above 85% at fiber end distances of several millimeters (without resonator, for the time being). Furthermore, we tested the compatibility of the GRIN lenses with the CO₂ machining, yielding promising results. Thus, we are ready to implement the next step in FFP resonator technology. The GRIN lenses can still be combined with the advantages of endlessly single mode PC fibers, and grant the bonus of

eliminating the imperfect PC collapsing procedure. The high transmission and a SM input and SM output will increase the area of application of (long) FFP resonators significantly, especially in quantum networks or mode filtering.

We are convinced that the technological progress presented in this thesis, and the work in the FFP resonator community around the globe, will lead to further improvements and applications of FFP resonators, whose potential is far from being fully unlocked.

As a conclusion of this thesis, we come back to the rise of quantum technologies. We hope that the advancements in the FFP resonator technology can support the progress in quantum communication and may find its application in first, small quantum networks. With TACC2, a testbed for quantum effects on metrology is approaching completion and opens the door to many exciting experiments.

A

Appendix

A.1 Calculation of the cavity shift

Calculation of the cavity shift shown in Fig. 2.5. Due to the magnetic bias field along the cavity axis, we are restricted to σ_+ , σ_- transitions. Since the cavity detuning $\Delta = \omega_a/2 \approx 3.4$ GHz is much larger than the hyperfine splitting of the excited state manifold ($5^2P_{3/2}$), we make use of effective couplings for the two clock states with $F=1$ and $F=2$ following [249, 250]:

$$\begin{aligned} \delta\omega_{c,\sigma_-} &= g_{F=1,\sigma_-}^2 \frac{N_{F=1}}{\Delta_{F=1}} + g_{F=2,\sigma_-}^2 \frac{N_{F=2}}{\Delta_{F=2}} \\ g_{F=2} &= \sqrt{\sum_{F'} |\langle F=2, m_F=1 | e\vec{r} | F', m_F=0 \rangle|^2} \cdot g_0 \\ g_{F=1} &= \sqrt{\sum_{F'} |\langle F=1, m_F=-1 | e\vec{r} | F', m_F=-2 \rangle|^2} \cdot g_0 \end{aligned} \quad (\text{A.1.1})$$

with g_0 given in Eq. 2.2.7, but with $\mu_{eq} = 3.58 \cdot 10^{-29}$ Cm being the full electric dipole moment without the reduction $\frac{2J+1}{2J'+1}$. Identical for σ_+ (and π , which cannot be used due to the orientation of the magnetic field parallel to the cavity axis).

A.2 Microclamps fabrication recipe

Here, the recipe for the production of the micro fabricated nickel clamps depicted in Fig. 3.7 is presented.

The recipe, given in [166], is simplified so that the Nickel layer is used as a mask for the wet etch process. This avoids the creation of the SiO₂ layer with thermal oxidation and also one lithography step. This leads to a slight underetch of the nickel (Ni) on the silicon (Si) surface, but no reduced adhesion could be stated.

Two solutions are needed for the process:

Nickel solution, as in [166]:

- 200 ml deionized (DI) water
- 54 g Ni(NH₂ SO₃)₂ 4H₂O
- 6 g H₃BO₃ (add at last to adjust pH value)
- 3 g NiCl₂ 6H₂O
- 0.01-0.02 g C₁₂H₂₅SO₃Na

KOH solution:

- 125 g KOH
- 100 g Isopropanol, VLSI selectipur (IPA)
- 400 g DI water
- the solution is heated to 75°C during the etch process and has to be stirred with a magnet, to avoid air bubbles on the Si-surface.

Step by step instructions:

Seed layer:

- The wafer is cleaned with acetone (ACE) and afterwards with IPA for 5 minutes in an ultra sonic bath (USB).
- Outgassing for 2 h on a heat plate at 210°C. Most likely this is not necessary for Si.
- A layer of ~3 nm chrome and 50-100 nm gold is evaporated on a the Si-Wafer (100 orientation) of thickness $t = 1$ mm. The chrome and gold deposition rate is ~ 0.2 nm/s. When using a thermal evaporator, evaporating first with closed shutter (~10 nm) avoids irregularities in the evaporation, which can appear at the beginning of the evaporation and lead to small droplets on the wafer surface.
- Tips: The bigger the wafer, the smaller the problems due to the photo resist (PR) beads that occur during the spin coating in the next step.
- Tips: The wafer thickness is reduced in the wet etch process by the KOH attacking the backside. It is best to coat the wafer from both sides (chrome on the backside is enough, if backside is polished) to avoid this.

Photolithography:

- Prebake 5 min. on hot plate at 100° C.
- Spin coat PR¹ for 40 s at 3000 rpm, which results in a $\sim 7\ \mu\text{m}$ thick PR layer.
- Remove PR beads at the wafer edge. This is not necessary if the bead is $\sim 10\ \text{mm}$ away from the area to be structured.
- Softbake: 7 min. (1 min./ μm) at 100°C
- Alignment in mask aligner². Make sure that the groove pattern on the mask (cf. Fig. A.1) is parallel or orthogonal to the flat side of the wafer, marking the crystal orientation, which is important for the anisotropic etching) .
- Exposure 100 s.
- Post exposure bake: 70 s at 110°C
- Development³ for 90s
- Check below microscope if PR is well developed. If traces remain in the developed regions, they can be removed with several additional seconds in the developer.
- Tip: Trying to remove the PR residuals by using the developer in the USB will damage the PR-structure
- Plasma cleaner for 3 minutes.

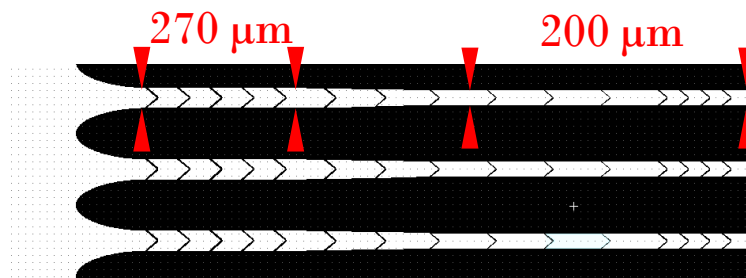


Figure A.1: Mask layout for nickel clamps for fibers of $\varnothing = 125\ \mu\text{m}$. The black region marks the position where later nickel is grown. The wider groove on the left allows to push the fiber in and holds the copper coating with the first 5 clamps.

Nickel plating

- The wafer is attached to a holder made of Teflon. Use the nickel-electrode (home made out of nickel wire fixed on a Teflon-holder) as the anode (+) and the seed layer on the sample as the cathode (-).
- The wafer and the electrode are connected to a current supply with an ampere meter and a resistor (1 k Ω) in series. One electrode should be put in the solution after the power supply is switched on to avoid voltage peaks.
- The solution is constantly stirred with a magnet stirrer.
- Ramp up the current to a current density of $I/A = 20\ \text{mA}/\text{cm}^2$ (value out of the paper mentioned above). Wait until you reach a thickness of 10 – 12 μm of the nickel layer. The grow speed can be calculated [225] or the grow process can be interrupted for a short thickness measurement with an optical microscope or best a surface profiler. The Ni will over grow the PR by 3 – 5 μm , which is not a problem.

¹AZ 2070, MicroChemicals, GmbH, Ulm, Germany

²MJB4, SÜSS microTec

³AZ 726 MIF, MicroChemicals GmbH

- Remove everything in the reverse order.
- The wafer is cleaned with DI water.
- The Ni solution is filtered and put back in the bottle.

Remove photo resist and seed layer

- Place wafer in N-Methyl-2-pyrrolidone (NMP) at 75°C for removing the PR and stir it regularly by hand (25-30 minutes).
- Tip: A syringe can be used to clean areas where the PR does not lift off easily. Therefore the NMP is pulled in the syringe and sprayed with high speed on the critical areas.
- Check the sample under microscope. In case that the PR is still not removed, use hot NMP again.
- Remove Cr/Au seed layer with RIE etching (bombardment with SF₆ ions worked well and removed the seed layer in ~12 min.)

KOH v-groove etching:

- Attach wafer to Teflon holder and put it in the KOH solution at 75°C. The temperature determines the etch speed, as can be seen in Tab. A.1.

Temperature [°C]	Etch rate [$\mu\text{m}/\text{min}$]
45	0.09
55	0.17
75	0.60

Table A.1: Measured etch speed of KOH on Si with (100) crystal orientation.

- Tip: Nylon is not resistant to KOH so Teflon screws should be used for fixing the wafer.
- The IPA concentration will vary from try to try, because of evaporation. Make sure that you have at least 1/3 IPA in the KOH solution to reduce the surface tension, so that the KOH can enter the narrow structures around the nickel clamps.
- Use a magnetic stirrer (highest speed possible, KOH and IPA have to be mixed) and cover the glass
- The speed is also determined by the concentration of your solution. The best way is to check with a surface profiler after one hour, how much silicon was etched.
- With the solution given above, the etch rate is $\sim 0.6 \mu\text{m}/\text{min}$. Since the groove depth is 141 μm , it takes nearly 4 hours to get to the bottom. To get a nice underetch under the Nickel-clamps the etch process takes 6.5 hours in total.
- Filter the KOH solution while pouring it back. Renew the solution frequently (any dirt can stick to the surface and can create unwanted irregularities in the grooves).

A.3 Additional material

In this section we present additional material that did not find its place in the main body. We give the link to the respective paragraphs in the caption.

A.3.1 CO₂ machining with multiple pulses

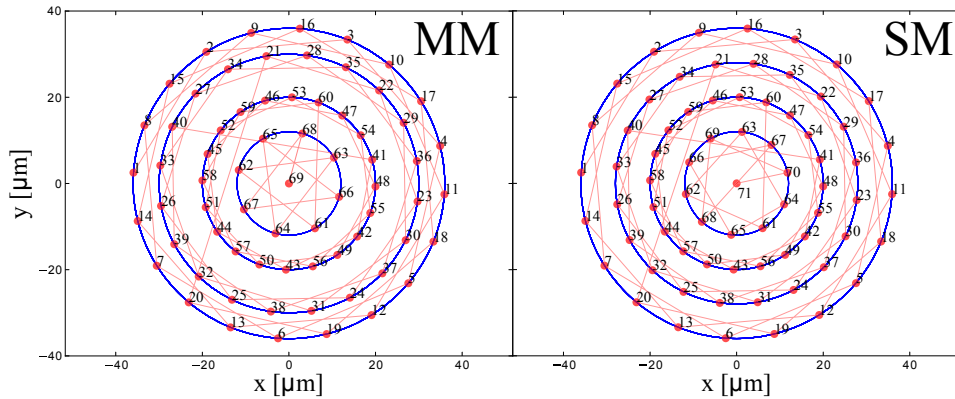


Figure A.2: Shot sequence for SM and MM fiber (cf. 3.4.3). The red circles mark the shot positions, with the shot order noted and visualized with red lines. The radii of the concentric circles for the SM fiber are $r = (36, 28, 20, 12, 0) \mu\text{m}$ with $(20, 20, 20, 10, 1-3)$ shots. For the MM fiber we used $r = (36, 30, 20, 12, 0) \mu\text{m}$ with $(20, 20, 20, 8, 1-3)$ shots. For the PC fiber we used the same pattern as for the MM fiber.

A.3.2 Long fiber Fabry-Pérot resonators

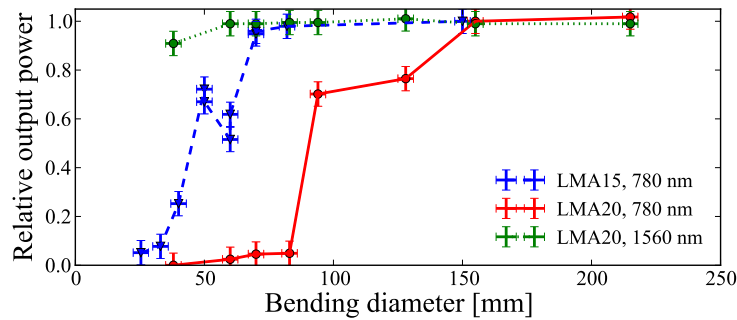


Figure A.3: Bending loss of large mode area PCF (cf. Sec. 4.1.6). The transmitted light was measured for the LMA15 and LMA20 from NKT photonics. A strong dependency of the bending loss on wavelength and effective mode field diameter can be seen. Bending diameter $d < 160$ mm should be avoided to exclude bending loss for the LMA20 at 780 nm. For this reason, we recommend to investigate the fiber-resonator mode coupling with the LMA15 for future large FFPs.

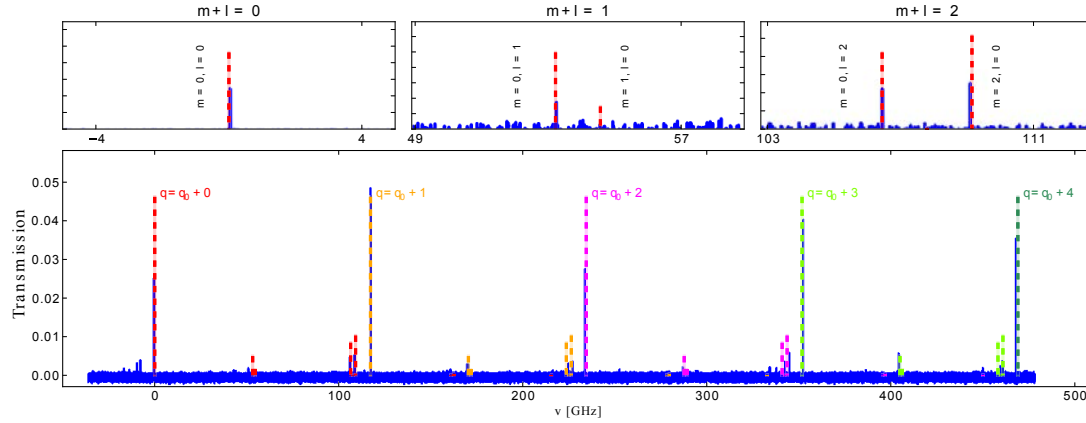


Figure A.4: The bottom row shows a spectrum of the high finesse cavity (blue line), taken as in Fig. 4.13. Due to the high finesse, the scan resolution is too small to resolve the peaks, which results in the strong transmission fluctuation from peak to peak and a systematic underestimation of the transmission. The x-axis was calibrated with the calculated FSR for the cavity length $L = 1.275$ mm, measured with a microscope. The ROCs were chosen (the mirror curvatures were assumed to be identical) to meet the higher order modes. This gives $R_1 = 1490\mu\text{m}$, $R_2 = 1430\mu\text{m}$ in very good agreement with the values measured with the profilometer, see Tab.4.2. The colored dashed lines indicate the calculated frequencies and transmissions for higher order modes, with a collapse length $L_{col} = 50\mu\text{m}$. The overlap of the higher order modes is taken into account as well as transmission reduction due to clipping loss ($r_{clip} = 51\mu\text{m}$). The transmissions for $m, l < 3$ were used to calculate the fiber waist and translation which gives the best fit to the data: $d_x = 1.8\mu\text{m}$, $d_y = 1\mu\text{m}$ and $w_f = 4.88\mu\text{m}$. The top row shows the magnification of each higher order mode of the $q = q_0$ transversal mode. To compensate the length jitter of the cavity, the data was shifted in each subframe to meet the theory by the following values [0, 2, 0.4] GHz.

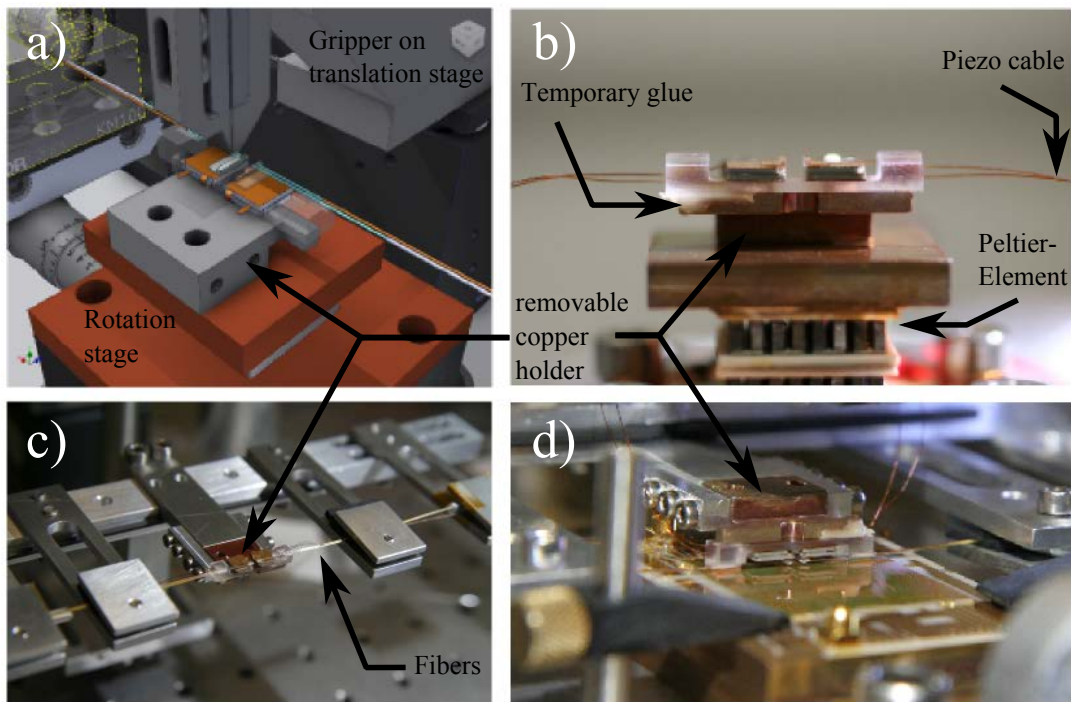


Figure A.5: Resonator gluing setup (cf. Sec. 4.2.7). a) and b) show the resonator mount before the fibers are glued (cf. Sec. 4.2.7). The screws fixing the copper holder are not shown. The mount is only fixed on one side to the copper holder, to avoid stress in the resonator mount. c) shows the transfer of the completed resonator mount to the atom chip. For the transfer, the resonator mount is initially fixed on the removable copper holder. d) shows the resonator mount glued to the atom chip (cf. Sec. 5.3.3). The transfer holder is still in place.

A.3.3 Atom chip for TACC 2

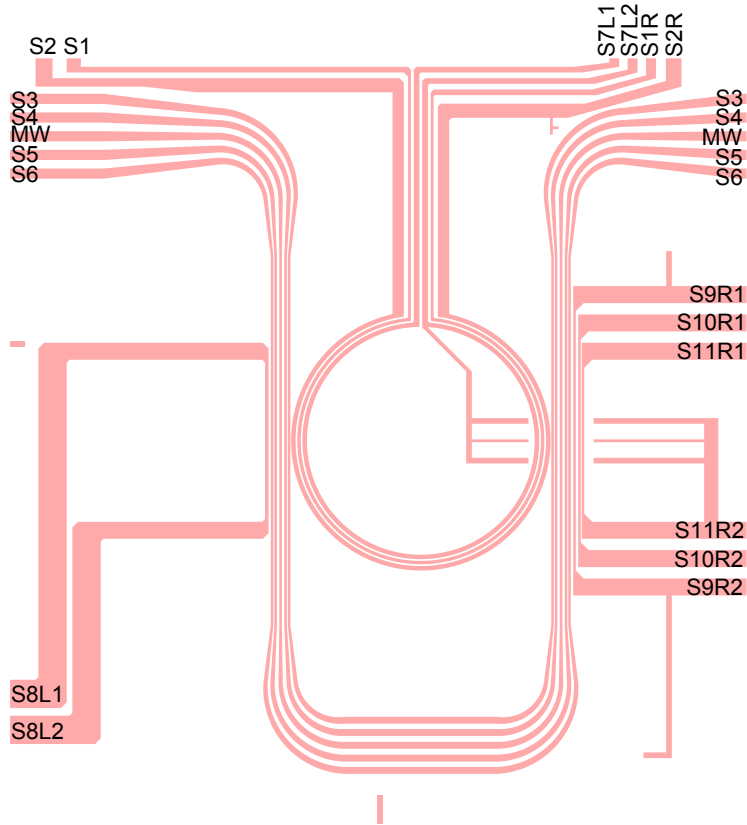


Figure A.6: Labeled science chip (cf. Sec. 5.2).

A.4 Chip fabrication recipe

The recipe given here notes briefly the steps in the chip fabrication. Further details can be found in Sec. 5.3 and [225].

Base chip:

- After laser drilling by A.L.L.: Cleaning with fiber brush.
- Cleaning: 5 min. ACE USB, IPA rinse, 5 min. Piranha ($\text{H}_2\text{SO}_4:\text{H}_2\text{O}_2 = 4 : 1$, as in [225]), Water rinse, 5 min. ACE USB, 3 min. ISO USB.
- Bakeout in oven 1 h at 210°C .
- 5 min. O_2 -plasma cleaner.
- Evaporation (5 nm Ti, 50 nm Au).
- 5 min. O_2 -plasma cleaner.
- 5 min. pre-heat on hotplate at 130°C .
- Spin coating maP-1240, three steps to reduce edge bead formation:
 - 20 s at 600rpm, 30s at 1500 rpm, wipe bead with ACE, hot plate 2 min. at 104°C
 - 20 s at 600rpm, 30s at 1500 rpm, wipe bead with ACE, hot plate 2 min. at 104°C

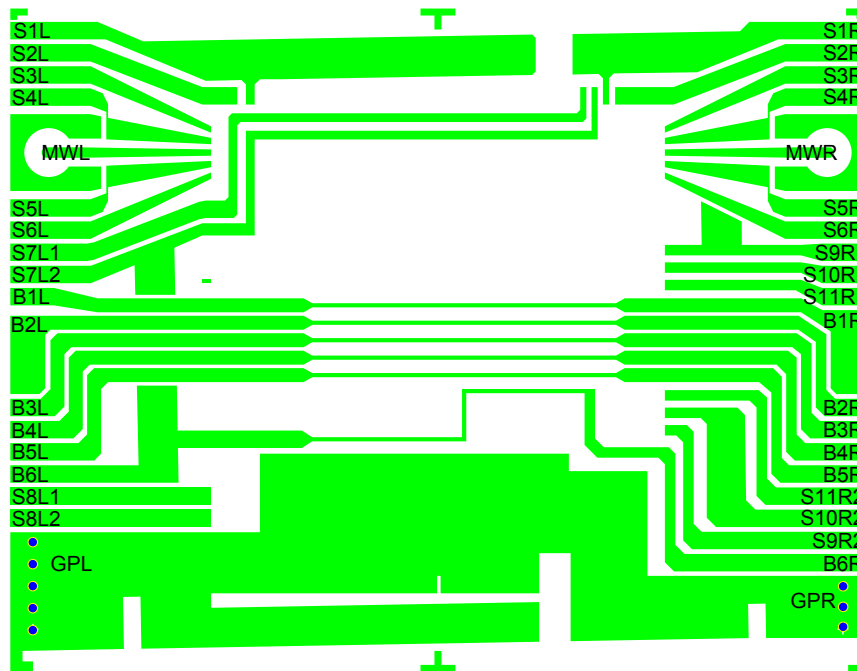


Figure A.7: Labeled base chip (cf. Sec. 5.2).

20 s at 600rpm, 30s at 1500 rpm, wipe bead with ACE, hot plate 5 min. at 104°C

- Exposure 110 s.
- Developer 2 min.
- Electroplating 70 min., with 30 mA → gold thickness $\sim 11 \mu\text{m}$.
- ACE 1 min., new ACE 5 min. at 55°C.
- We did not use Piranha, since no PR residuals could be seen.
- 4 min. RIE with only O₂ plasma (higher power than O₂-plasma cleaner, see Tab. A.2).
- 8 min. NbN-02-5sccm, some gold speckles ($\varnothing < 2 \mu\text{m}$) visible with optical microscope.
- 15 min. add NbN-02-5sccm, gold speckles gone.

Science chip:

We applied a gold backplane on the back side of the science chip, to shield the MW guide on the science chip from the base chip wires. This made a seed layer on both wafer faces necessary.

- The wafer is cleaned as for the base chip. A Ti/Au seed layer is applied on the front and the back side. The front side is then covered with a protection PR (as well ma-P1275) layer and the backside is electroplated as described for the base chip. Higher currents are needed for the large surface of $\sim 25 \text{cm}^2$. We used 20 mA for 60 min. and then 40 mA for 90 min → Au thickness $\sim 9 \mu\text{m}$.
- Prepare front side: cleaning as for base chip.
- 5 min. pre-heat on hotplate at 130°C.

Program name	Unit	Stripping	Plasma O ₂	NbN-02-5sccm
Working Pressure	mTorr	100	50	6
SF6	[sccm]	-	-	25
O2	[sccm]	100	100	5
RF Fwd Power	[W]	30	60	70
RF Load	-	340	365	360
RF Tune	-	2312	2318	2304
maP-1240 etch rate	nm/min	n.a.	160	100
Ti/Au etch rate	nm/min	0	0	11

Table A.2: RIE programs used for chip fabrication. The upper part of the table shows the program parameter for the RIE machine. The lower part shows the etch rate on the photo resist used and Ti/Au.

- Spin coating: we changed to ma-P 1275, 30 s at 1800 rpm → PR thickness $\sim 11.7 \mu\text{m}$.
- Post-exposure bake: 12 min. at 130°C.
- Exposure 35 s.
- Developer AZ 726 MIF: 2 min.
- Electroplating: 65 min. at $I = 20 \text{ mA}$.
- ACE 1 min., new ACE 5 min. at 55°C.
- We did not use Piranha, since no PR residuals could be seen.
- 4 min. RIE with only O₂ plasma (higher power than O₂-plasma cleaner, see Tab. A.2).
- 8 min. NbN-02-5sccm, some gold speckles ($\varnothing < 2 \mu\text{m}$) visible with optical microscope.
- 15 min. add NbN-02-5sccm , gold speckles gone.

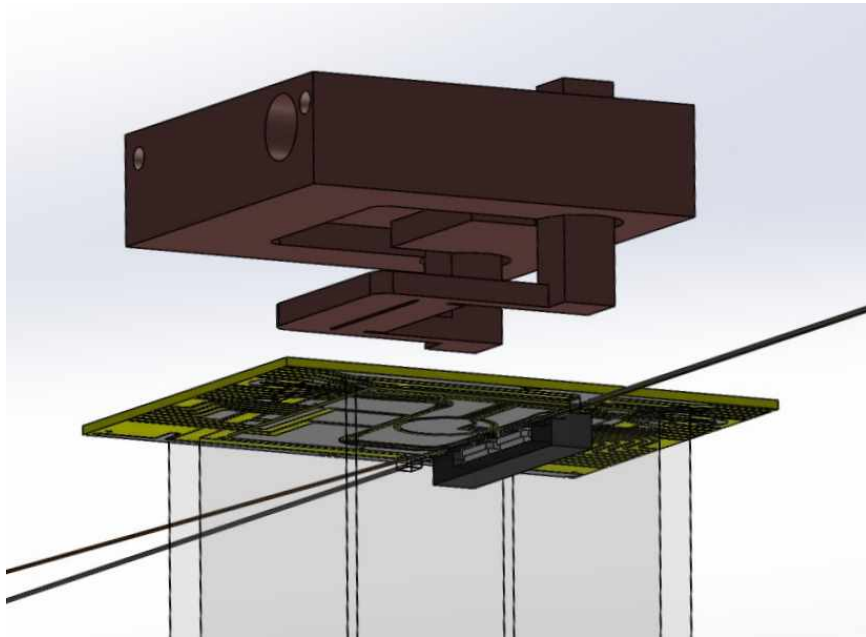


Figure A.8: Macroscopic U with chip assembly (cf. Sec. 5). Shown is the macroscopic U, which lies inside a copper block for water cooling. The small groove in the U center allows to place a wire of $\varnothing = 0.5$ mm, which is named “macroscopic I”.

We did not add a thermo electric cooler (TEC) as in [135], since it was suspected in [251] to be a potential noise source. Switching off the TEC during the Ramsey time of several seconds would considerably hinder the heat transport.

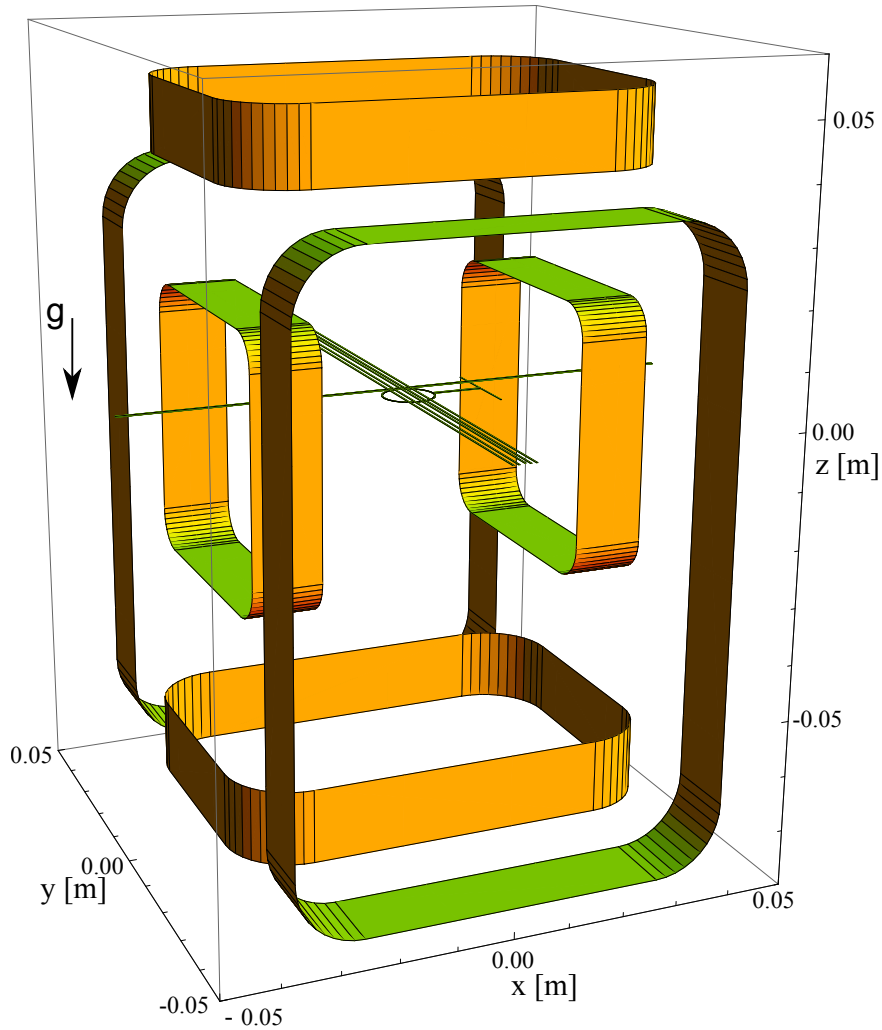


Figure A.9: Coil cage for simulation (cf. Sec. 5). Shown are the coils and central chip wires. The chip wires (beside the Ω -wire) are simplified to straight and long wires since their connections did not have important effects on the simulated trap parameters. The x-coil center is displaced by $\Delta z = -6.66$ mm with respect to the science chip surface. The y-coils by $\Delta z = -19.35$ mm. The lower z-coil has a distance of -65.36 mm to the science chip surface, the upper z coil 46.64 mm.

A.5 French summary

L'objet de cette thèse de doctorat est la conception et la construction d'une horloge atomique réalisée sur un microcircuit à atomes (TACC) et améliorée par l'intrication. Dans ce qui suit, nous allons récapituler les idées principales de chaque chapitre.

A.5.1 Chapter 1: Trapped Atom Clock on a Chip

Les horloges atomiques sont des références de fréquence de haute précision et de grande stabilité, qu'on peut regrouper en deux catégories:

- Des horloges actives comme le MASER [83] à hydrogène, où les atomes émettent un rayonnement à une fréquence bien définie.
- Des horloges passives, comme des fontaines atomiques, où la transition atomique est utilisée pour stabiliser un oscillateur local.

Notre horloge fait partie de la deuxième classe et une description détaillée en français peut être trouvée dans [92]. La particularité de ce système est que les atomes sont piégés pendant le cycle de l'horloge, ce qui confère l'avantage d'utiliser des temps d'interrogation plus longs comparé aux fontaines atomiques entre autres. Augmenter cette durée induit une plus grande stabilité, comme en témoigne l'équation 1.1.6.

Dans notre expérience, les atomes ^{87}Rb sont piégés magnétiquement en exploitant leur moment dipolaire magnétique qui génère un potentiel de piégeage avec un champ magnétique externe comme noté dans l'Eq. 1.3.1.

À côté des avantages comme les longs temps d'interrogation dans un système compact, le piégeage induit un désavantage majeur : des décalages de la fréquence de référence dues d'une part à l'augmentation de la densité atomique et d'autre part à la présence d'un champ magnétique de piégeage (effet Zeeman). En choisissant de bonnes valeurs pour la densité atomique et le champ magnétique (« champ magique ») les effets perturbants peuvent être réduits, comme résumé sur la figure 1.4.

Les champs magnétiques utilisés pour le piégeage sont créés par un microcircuit à atomes qui permet de réaliser des gradients magnétiques très forts et localisés à l'échelle du micromètre. Le principe est illustré sur la figure 1.6 où le champ rayonné par un fil du microcircuit parcouru par un interfère avec un champ externe crée par des bobines macroscopiques, ce qui crée un champ quadrupolaire au-dessus du fil centré à une hauteur z_0 .

En appliquant des champs externes et des courants additionnels dans le microcircuit une multitude de configurations peuvent être trouvées pour créer des pièges 2D ou 3D comme présenté figure 1.7.

Nous utilisons la flexibilité des microcircuits à atomes dans le chapitre 5 pour concevoir un nouveau microcircuit qui permet l'insertion d'un micro-résonateur optique dans le montage expérimental.

A.5.2 Chapter 2: Spin Squeezing for Metrology

L'élément principal de cette nouvelle expérience est un micro-résonateur Fabry Péro (cf. chapitre 4) qui permet la génération d'états atomiques comprimés en spin grâce aux interactions entre la lumière et les atomes. Il a déjà été montré que ces états peuvent améliorer les performances métrologiques des horloges atomiques [48].

Les états comprimés de spin ont la particularité que le bruit de projection quantique [90] est réduit sous la limite quantique standard (LQS) pour une composante de spin alors qu'il est augmenté pour la composante conjuguée, de façon à satisfaire le principe d'incertitude de Heisenberg 2.1.3.

Si l'orientation d'état comprimés de spin est choisi astucieusement, comme présenté figure 2.1 b), et si l'opération ne réduit pas trop le rapport signal sur bruit, le bruit sur la mesure de la fréquence de référence peut être réduit par le facteur de compression donné par l' Eq. 2.1.5.

L'état comprimé de spin peut être créé à l'aide d'un résonateur optique qui réalise un Hamiltonien non linéaire (« one axis twisting hamiltonian ») [123, 128] ou par mesure non destructive [49]. Les deux méthodes profitent du couplage lumière-atome élevé dans un résonateur de haute finesse.

Récemment une réalisation impressionnante de cette méthode fut présentée dans [50] où la limite quantique standard a été dépassé d'un facteur de ~ 100 . Cependant, les expériences ayant permis cette démonstration de principe n'ont pas encore atteint un niveau de précision présentant un intérêt métrologique. C'est précisément l'objectif de la nouvelle configuration expérimentale que nous proposons ici.

A.5.3 Chapter 3: CO₂ machining with multiple pulses

Afin de conserver la compacité et la stabilité de notre installation TACC, nous avons choisi d'utiliser une cavité Fabry-Pérot fibrée (fibered Fabry-Pérot, FFP) comme résonateur optique, dans lequel les miroirs du résonateur sont réalisés sur le bout des fibres optiques. Pour répondre aux exigences de notre expérience, une nouvelle génération de résonateurs FFP a été développée au cours de cette thèse, les plus longs réalisés à ce jour. A cette fin, nous avons développé une procédure d'ablation par tirs multiples à l'aide d'un laser CO₂ focalisé, qui permet la mise en forme des surfaces de silice fondue avec une précision et une polyvalence sans précédent.

La technologie consistant à créer des dépressions concaves sur les facettes des fibres optiques par ablation laser CO₂, développée dans notre équipe [73], permet la création des miroirs avec des rayons de courbure submillimétriques et une qualité de surface excellente. Grâce à la miniaturisation des miroirs et la rugosité de surface de seulement $\sigma_r \sim 0.2$ nm des résonateurs de haute finesse et d'un volume de mode minimal pourrait être réalisés. Cela a rendu une multitude d'expériences d'électrodynamique quantique en cavité possible [72, 74, 75, 79] avec des résonateurs d'une longueur de seulement ~ 40 μm .

Pour notre horloge la longueur du nuage atomique dépasse cette longueur de cavité par un ordre de grandeur et est typiquement ~ 400 μm . Pour assurer que le résonateur fibré soit compatible avec le nuage atomique, nous avons développé une nouvelle génération de longs résonateurs FFP, présenté dans le chapitre 4 qui nécessitent des miroirs d'un diamètre élevé, en comparaison avec les résonateurs précédents.

Pour fabriquer ces miroirs de diamètre plus élevé et s'affranchir de leur forme Gaussienne, typique pour l'ablation avec un tir CO_2 simple, nous avons développé une nouvelle méthode de fabrication en utilisant une multitude des tirs individuels pour contrôler la forme résultante. Dans ce but, nous avons réalisé un nouveau dispositif automatisé pour l'ablation laser et l'analyse de surface. Le dispositif est compatible avec un nouveau type de support pour 42 fibres en parallèle, présenté figure 3.9, qui permet de travailler plusieurs fibres consécutives sans parasiter le flux laminaire qui garantit la propreté de la production. Une description complète du dispositif en français peut être trouvée dans [163].

Une séquence de tirs est présentée figure 3.16 et le miroir ainsi produit figure 3.18. L'écart moyen d'un ajustement sphérique d'un diamètre de $100\ \mu\text{m}$ est inférieur à 12 nm pour un miroir d'un rayon de courbure de 1.5 mm. L'écart maximal est inférieur à 40 nm, qui correspond à un vingtième de la longueur d'onde de 780 nm de la lumière utilisée dans les expériences d'électrodynamique quantique en cavité.

La méthode des tirs multiples permet en plus la fabrication des formes plus complexes que des dépressions concaves. Des essais préliminaires, comme une matrice de lentilles, sont représentés figure 3.15 et promettent une diversification des champs d'application de notre méthode de travail de la silice fondue.

A.5.4 Chapter 4: Long Fiber Fabry-Pérot Resonators

Les miroirs présentés chapitre 3 ont permis de construire des résonateurs FFP de haute finesse, les plus longs réalisés à ce jour. Le chapitre présente des analyses pour deux revêtements réfléchissants différents : un revêtement de haute réflectivité permettant des finesses $\mathcal{F} \sim 50.000$ et un revêtement d'une réflectivité moyenne pour des finesses $\mathcal{F} \sim 3.000$ à une longueur d'onde de 780 nm. Un résonateur est toujours composé de deux fibres avec des structures sphériques sur leurs extrémités, comme expliqué dans le chapitre précédent. Une fibre monomode (à cristal photonique ou standard) est utilisée pour guider la lumière vers le résonateur, ce qui garantit un couplage stable au résonateur. La fibre à la sortie du résonateur est une fibre multimode pour collecter la lumière efficacement.

En utilisant des fibres à cristaux photoniques dont le diamètre de mode est élevé, nous avons pu augmenter le couplage de la fibre au mode du résonateur d'un ordre de grandeur par rapport à des fibres monomodes standards.

La figure 4.5 montre la finesse et la transmission d'un résonateur FFP en fonction de sa longueur. Les données sont consistantes avec une théorie analytique simple (cf. équation 4.1.19) où les miroirs sont modélisés avec des diamètres finis. La figure présente aussi des simulations numériques avec le programme FFT optique OSCAR [194]. Pour la simulation, nous avons fait une reconstruction 3D des miroirs fabriqués comme présenté figure 3.17 par profilométrie optique.

La reconstruction 3D et la simulation numérique permettent d'évaluer la forme d'un miroir sans être obligé de construire un résonateur et même avant l'application d'un revêtement réfléchissant. Cette possibilité raccourcit énormément le procédé de développement et de test de nouvelles formes de miroirs.

La figure 4.13 présente l'excitation des modes transverses du résonateur. Le recouvrement calculé du mode de la fibre et des modes Hermite-Gauss du résonateur sont

en bon accord avec les données, ce qui confirme la modélisation du résonateur FFP par un résonateur Fabry-Pérot idéalisé.

Le revêtement de haute réflectivité choisi est aussi réfléchissant à 1560 nm pour stabiliser la longueur du résonateur avec de la lumière fortement désaccordée et d'avoir aussi la possibilité de piéger les atomes dans un piège dipolaire comme indiqué figure 4.15.

La dernière partie du chapitre 4 présente la construction d'un support compact et stable pour deux résonateurs FFP à une distance de moins de 500 μm comme donné figure 4.19. À cet effet nous avons développé une nouvelle méthode de collage des résonateurs FFP très précise et fiable, esquissée figure 4.24 qui a permis de construire une paire de résonateurs, comme montré figure 4.25 avec des paramètres donnés tableau 4.2.

Au-delà de notre expérience les longs résonateurs FFP développés au cours de cette thèse sont aussi utiles à la communauté d'ions piégés où le potentiel du piégeage est perturbé par la présence des miroirs proches des ions. L'avantage des résonateurs FFP est d'être directement couplé aux fibres optiques ce qui peut être de grand intérêt pour réaliser des réseaux quantiques [81, 82].

A.5.5 Chapter 5: Atom Chip for TACC 2

L'intégration du résonateur optique au dispositif expérimental TACC nécessite une conception nouvelle du microcircuit à atomes, qui doit permettre le transport du nuage atomique jusqu'au résonateur. Nous présenterons alors dans le chapitre 5 la conception et la fabrication de ce microcircuit à atomes. Le catalogue d'exigences pour le nouveau microcircuit est donné au début du chapitre 5 et comprend les points suivants :

- **Performance d'horloge:** Avec l'expérience précédente nous avons trouvé les meilleurs paramètres pour l'horloge comme résumé en [62]. L'objectif principal du nouveau microcircuit est de permettre la même performance qui nécessite des pièges mous de fréquences de seulement quelques Hertz ce qui demande des pistes en or d'une rugosité minimale pour ne pas fragmenter le nuage atomique.
- Pour exciter la transition d'horloge nous utilisons le champ évanescent d'un **guide microonde coplanaire**. Cela donne l'avantage de focaliser la puissance de la microonde sur des dimensions bien plus petites que le λ^2 d'une onde en propagation libre. Malheureusement le guide microonde interdit le croisement des autres pistes conductrices, ce qui ajoute des contraintes pour le dessin du microcircuit.
- Les atomes doivent être transportés et positionnés précisément dans le **résonateur FFP**. Pour minimiser les effets sur le résonateur par chauffage des pistes conductrices tous les courants et résistances doivent être les plus petites possibles.
- **Accès optique :** La surface du microcircuit doit être suffisamment large pour réaliser un piège magnéto-optique à miroir, ce qui est en conflit avec l'idée de monter le support de résonateurs sur cette surface. Une approche très élégante fut trouvée dans [135] où le piège magnéto-optique à miroir est réalisé sur un côté du microcircuit et les expériences d'électrodynamique quantique en cavité sur

l'autre côté. Nous adoptons cette idée principale, ce qui nécessite un transport des atomes de la région du piège magnéto-optique à miroir vers les résonateurs FFP. Nous réalisons ce transport avec une piste en forme de Ω , qu'on va décrire dans la suite.

Le schéma du microcircuit est présenté figure 5.1 où tous les éléments essentiels sont indiqués. Pour être capable de réaliser des pistes croisées malgré le guide microonde, un microcircuit à deux couches superposées est choisi. Les deux couches sont constituées de AlN, une céramique avec une conduction thermique élevée de $180 \text{ Wm}^{-1} \text{ K}^{-1}$, pour évacuer efficacement la chaleur dissipée par les pistes conductrices.

Les pistes en or sont appliquée par électrodéposition comme décrit figure ??, et ont une hauteur de $10 - 12 \mu\text{m}$ avec une rugosité de surface $\rho_r \sim 30 \text{ nm}$.

La caractéristique la plus frappante est la piste en forme de Ω au centre du microcircuit. Elle sert à réaliser le transport des atomes de la région du piège magnéto-optique à miroir vers les résonateurs FFP. La piste Ω avec un champ magnétique externe est une variation du piège en U (cf. figure 1.8) qui permet de déplacer les atomes en tournant la direction du champ magnétique externe, comme réalisé en [219]. La figure 5.5 montre la position simulé du nuage atomique et les gradients de piégeage pendant la rotation du champ magnétique externe.

Dès que les atomes sont arrivés à la position des résonateurs une deuxième séquence de transport est exécutée pour traverser les dernières centaines de micromètres. Le principe est présenté figure 5.6 où les courants dans les pistes avoisinantes sont calculés de manière à minimiser les fluctuations des gradients et de position pendant le trajet.

Les simulations des champs magnétiques ont permis l'analyse de différents types de pièges magnétiques pour l'opération d'horloge. Une option est un piège à trois pistes qui réduit les fluctuations de position et de fréquence du piège, comme résumé tableau 5.2.

Une réalisation intéressante de ce type de piège est un piège « stand-alone » qui ne nécessite pas de champs magnétiques externes, car tous les champs nécessaires sont créés par les pistes du microcircuit. Les paramètres pour ce piège sont présentés tableau 5.4.

La figure 5.20 montre le mariage des microcircuits avec les résonateurs FFP. La monture transparente en silice fondue permet d'aligner les résonateurs précisément avec les pistes conductrices et la réflexion par le miroir du piège magnéto-optique à miroir permet choisir la distance des résonateurs à la surface du microcircuit.

Avec cet assemblage, la nouvelle pièce maîtresse du dispositif expérimental est maintenant complète, ce qui rend une multitude des expériences d'électrodynamique quantique en cavité possible. Nous allons étudier l'interaction des dynamiques de spin en présence des corrélations induites par la lumière intra-cavité et espérons faire les premiers tests d'application d'états comprimé de spin à un niveau de précision présentant un intérêt métrologique.

List of Figures

1.1	Atomic clock schematic	2
1.2	Rabi and Ramsey pulse	3
1.3	Ramsey sequence	3
1.4	Mean field and second order Zeeman shift	6
1.5	Zeeman sub-level diagram of the $5^2S_{1/2}$ manifold	7
1.6	Basic principle of wire traps	9
1.7	Dimple trap	10
1.8	H/U/Z-trap	12
1.9	Effect of gravity on trap depth	13
1.10	Gravitational sag	15
2.1	Coherent and spin-squeezed state on Bloch sphere	18
2.2	Atom-light interaction	20
2.3	Cavity feedback squeezing	25
2.4	Optimal enhancement by QND-measurement squeezing	27
2.5	Cavity shift	28
2.6	Cloud-mirror overlap	29
2.7	Influence of mirror transmission \mathcal{T}	32
3.1	Ridge at the core-cladding interface	35
3.2	CO ₂ dot milling setup	36
3.3	Contrast of the profilometry	38
3.4	Residual depending on profilometry position	38
3.5	Noise reduction due to averaging	39
3.6	Multi fiber holder with v-grooves	41
3.7	Microclamp fabrication	42
3.8	Microfabricated nickel clamps	43
3.9	Multi fiber holder	44
3.10	Cleave and groove angle estimation	45
3.11	Pre-pull method for small cleave angles	46
3.12	Collaps and cleave of a PCF	47
3.13	Effect of doping	48
3.14	Initial tests for multi shots	49
3.15	Mirror and lens array	50
3.16	Multi shot sequence	51

3.17	Large spherical surface machined on a 200 μm diameter SM fiber	52
3.18	Fit and residuals of a spherical profile	52
3.19	Influence of the doped core region	53
4.1	Stability diagram and resonator configuration	56
4.2	FFP resonator	58
4.3	Clipping loss for finite mirror diameters	60
4.4	Power coupling between the incoupling fiber mode and the mode of a symmetric cavity	62
4.5	Length scan of a FFP resonator	66
4.6	Simulated cavity length scan with different numbers of averaged profiles	67
4.7	Simulated losses with different numbers of averaged profiles	68
4.8	Simulated losses depending on grid resolution	69
4.9	Intensity distribution of Hermite-Gauss modes	72
4.10	Mode coupling scheme	73
4.11	Higher order mode coupling	74
4.12	Clipping loss for higher order modes	75
4.13	Spectrum of low finesse cavity	76
4.14	Mode crossing	77
4.15	$\lambda_{780,1560}$ standing wave configuration	79
4.16	Laser setup for 780 nm and 1560 nm	79
4.17	Co-resonant length scan	80
4.18	Length scan of low finesse resonator	81
4.19	Bridge design	83
4.20	Electric field of piezos	84
4.21	Simulated effects of misalignment	86
4.22	Simulated effects of misalignment for different resonator lengths	86
4.23	Gluing of FFP resonators	87
4.24	Channel gluing method	88
4.25	Long FFP resonators for TACC2	89
5.1	Layout of the TACC2 atom chip	95
5.2	Details of science chip	96
5.3	Magnetic field above Ω -wire	97
5.4	Dependence of longitudinal gradient of Ω -wire	98
5.5	Positions and gradients during transport.	99
5.6	Trap properties during parallel park procedure	101
5.7	Three wire trap configuration	103
5.8	Trap position depending on coil cage displacement	105
5.9	Magnetic field of the x-coil pair in xy -plane.	106
5.10	Magnetic field of two wires	108
5.11	Coplanar waveguide and bias-tee	111
5.12	Interdigital capacitor	112
5.13	Chip fabrication process	114
5.14	Au/Ti removal by reactive ion etching	115
5.15	Au surface after RIE etch	116

5.16	Photoresist and Au-Profile	117
5.17	Chip assembly	118
5.18	SEM pictures of SC wire edges	118
5.19	Microscope pictures of the science chip	119
5.20	Cavity mount glued to chip	120
5.21	Chip assembly with cell	121
5.22	3D profile of micro lens array	123
5.23	GRIN lens on SM fiber	124
A.1	Mask layout for nickel clamps	129
A.2	Shot sequence for SM and MM fiber	131
A.3	Bending loss of large mode area PCF	131
A.4	Spectrum of high finesse cavity	132
A.5	Resonator gluing setup	133
A.6	Labeled science chip	134
A.7	Labeled base chip	135
A.8	Macroscopic U with chip assembly	137
A.9	Coil cage for simulation	138

Bibliography

- [1] J. P. Dowling and G. J. Milburn, “Quantum technology: the second quantum revolution,” *Philosophical Transactions of the Royal Society of London A: Mathematical, Physical and Engineering Sciences* **361**, 1655–1674 (2003). ix
- [2] European Commission, “The European Cloud Initiative,” (2016). URL: <https://ec.europa.eu/digital-single-market/en/news/european-commission-will-launch-eu1-billion-quantum-technologies-flagship>. ix
- [3] E. Schrödinger, “An undulatory theory of the mechanics of atoms and molecules,” *Physical Review* **28**, 1049 (1926). ix
- [4] E. Schrödinger, “Die gegenwärtige Situation in der Quantenmechanik,” *Naturwissenschaften* **23**, 807–812 (1935). URL: <http://dx.doi.org/10.1007/BF01491891>. ix
- [5] W. H. Zurek, “Decoherence and the transition from quantum to classical—revisited,” in “Quantum Decoherence,” (Springer, 2006), pp. 1–31. ix
- [6] S. Eibenberger, S. Gerlich, M. Arndt, M. Mayor, and J. Tüxen, “Matter-wave interference of particles selected from a molecular library with masses exceeding 10000 amu,” *Physical Chemistry Chemical Physics* **15**, 14696–14700 (2013). ix
- [7] T. Kovachy, P. Asenbaum, C. Overstreet, C. Donnelly, S. Dickerson, A. Sugarbaker, J. Hogan, and M. Kasevich, “Quantum superposition at the half-metre scale,” *Nature* **528**, 530–533 (2015). ix
- [8] E. Schrödinger, “Discussion of probability relations between separated systems,” in “Mathematical Proceedings of the Cambridge Philosophical Society,” , vol. 31 (Cambridge Univ Press, 1935), vol. 31, pp. 555–563. ix
- [9] A. Einstein, B. Podolsky, and N. Rosen, “Can quantum-mechanical description of physical reality be considered complete?” *Physical review* **47**, 777 (1935). ix
- [10] J. S. Bell, “On the Einstein Podolsky Rosen paradox,” (1964). ix
- [11] A. Aspect, P. Grangier, and G. Roger, “Experimental tests of realistic local theories via Bell’s theorem,” *Phys. Rev. Lett.* **47**, 460–463 (1981). URL: <http://link.aps.org/doi/10.1103/PhysRevLett.47.460>. ix

- [12] B. Hensen, H. Bernien, A. Dréau, A. Reiserer, N. Kalb, M. Blok, J. Ruitenberg, R. Vermeulen, R. Schouten, C. Abellán *et al.*, “Loophole-free Bell inequality violation using electron spins separated by 1.3 kilometres,” *Nature* **526**, 682–686 (2015). ix
- [13] J. S. Bell, “Bertlmann’s socks and the nature of reality,” *Le Journal de Physique Colloques* **42**, C2–41 (1981). ix
- [14] C. H. Bennett and D. P. DiVincenzo, “Quantum information and computation,” *Nature* **404**, 247–255 (2000). x
- [15] C. H. Bennett and G. Brassard, “Quantum cryptography: Public key distribution and coin tossing,” *Theoretical computer science* **560**, 7–11 (2014). x
- [16] “ID Quantique SA, Geneva, Switzerland,” URL: <http://www.idquantique.com>. x
- [17] “MagiQ Technologies, Inc.” URL: <http://www.magiqtech.com>. x
- [18] W. K. Wootters and W. H. Zurek, “A single quantum cannot be cloned,” *Nature* **299**, 802–803 (1982). x
- [19] S. Lloyd, “Universal quantum simulators,” *Science* **273**, 1073 (1996). x
- [20] L. K. Grover, “A fast quantum mechanical algorithm for database search,” in “Proceedings of the twenty-eighth annual ACM symposium on Theory of computing,” (ACM, 1996), pp. 212–219. x
- [21] P. W. Shor, “Polynomial-time algorithms for prime factorization and discrete logarithms on a quantum computer,” *SIAM review* **41**, 303–332 (1999). x
- [22] I. M. Georgescu, S. Ashhab, and F. Nori, “Quantum simulation,” *Rev. Mod. Phys.* **86**, 153–185 (2014). URL: <http://link.aps.org/doi/10.1103/RevModPhys.86.153>. x
- [23] R. P. Feynman, “Quantum mechanical computers,” *Foundations of Physics* **16**, 507–531 (1986). URL: <http://dx.doi.org/10.1007/BF01886518>. x
- [24] M. Aidelsburger, M. Atala, M. Lohse, J. T. Barreiro, B. Paredes, and I. Bloch, “Realization of the Hofstadter Hamiltonian with ultracold atoms in optical lattices,” *Phys. Rev. Lett.* **111**, 185301 (2013). URL: <http://link.aps.org/doi/10.1103/PhysRevLett.111.185301>. x
- [25] B. P. Lanyon, J. D. Whitfield, G. G. Gillett, M. E. Goggin, M. P. Almeida, I. Kassal, J. D. Biamonte, M. Mohseni, B. J. Powell, M. Barbieri *et al.*, “Towards quantum chemistry on a quantum computer,” *Nature Chemistry* **2**, 106–111 (2010). x
- [26] N. C. Menicucci, S. J. Olson, and G. J. Milburn, “Simulating quantum effects of cosmological expansion using a static ion trap,” *New Journal of Physics* **12**, 095019 (2010). URL: <http://stacks.iop.org/1367-2630/12/i=9/a=095019>. x

- [27] “Resolution 1 of the 13th CGPM,” (1967/68). URL: <http://www.bipm.org/en/CGPM/db/13/1/>. x
- [28] H. J. Mamin, M. Kim, M. H. Sherwood, C. T. Rettner, K. Ohno, D. D. Awschalom, and D. Rugar, “Nanoscale nuclear magnetic resonance with a nitrogen-vacancy spin sensor,” *Science* **339**, 557–560 (2013). URL: <http://science.sciencemag.org/content/339/6119/557>. x
- [29] “Muquans, Talence - France,” URL: <http://www.muquans.com>. x, 122
- [30] V. Giovannetti, S. Lloyd, and L. Maccone, “Quantum-enhanced measurements: Beating the standard quantum limit,” *Science* **306**, 1330 (2004). x, xi
- [31] G. Santarelli, P. Laurent, P. Lemonde, A. Clairon, A. G. Mann, S. Chang, A. N. Luiten, and C. Salomon, “Quantum projection noise in an atomic fountain: A high stability cesium frequency standard,” *Phys. Rev. Lett.* **82**, 4619–4622 (1999). xi, 4
- [32] S. Weyers, B. Lipphardt, and H. Schnatz, “Reaching the quantum limit in a fountain clock using a microwave oscillator phase locked to an ultrastable laser,” *Phys. Rev. A* **79**, 031803 (2009). URL: <http://link.aps.org/doi/10.1103/PhysRevA.79.031803>. xi
- [33] J. J. . Bollinger, W. M. Itano, D. J. Wineland, and D. J. Heinzen, “Optimal frequency measurements with maximally correlated states,” *Physical Review A* **54**, R4649–R4652 (1996). URL: <http://link.aps.org/doi/10.1103/PhysRevA.54.R4649>. xi, 17
- [34] M. Zwiery, C. A. Pérez-Delgado, and P. Kok, “General optimality of the Heisenberg limit for quantum metrology,” *Physical review letters* **105**, 180402 (2010). xi
- [35] The LIGO Scientific Collaboration, “A gravitational wave observatory operating beyond the quantum shot-noise limit,” *Nat Phys* **7**, 962–965 (2011). URL: <http://dx.doi.org/10.1038/nphys2083>. xi, 24
- [36] J. Aasi, J. Abadie, B. Abbott, R. Abbott, T. Abbott, M. Abernathy, C. Adams, T. Adams, P. Addesso, R. Adhikari *et al.*, “Enhanced sensitivity of the LIGO gravitational wave detector by using squeezed states of light,” *Nature Photonics* **7**, 613–619 (2013).
- [37] T. L. S. C. et al., “Advanced LIGO,” *Classical and Quantum Gravity* **32**, 074001 (2015). URL: <http://stacks.iop.org/0264-9381/32/i=7/a=074001>. xi
- [38] A. Kuzmich, L. Mandel, and N. P. Bigelow, “Generation of spin squeezing via continuous quantum nondemolition measurement,” *Phys. Rev. Lett.* **85**, 1594–1597 (2000). URL: <http://link.aps.org/doi/10.1103/PhysRevLett.85.1594>. xi

- [39] V. Meyer, M. Rowe, D. Kielpinski, C. Sackett, W. Itano, C. Monroe, and D. Wineland, “Experimental demonstration of entanglement-enhanced rotation angle estimation using trapped ions,” *Physical Review Letters* **86**, 5870 (2001). xi
- [40] J. Esteve, C. Gross, A. Weller, S. Giovanazzi, and M. K. Oberthaler, “Squeezing and entanglement in a Bose-Einstein condensate,” *Nature* **455**, 1216–1219 (2008). xi
- [41] J. Appel, P. J. Windpassinger, D. Oblak, U. B. Hoff, N. Kjærgaard, and E. S. Polzik, “Mesoscopic atomic entanglement for precision measurements beyond the standard quantum limit,” *Proceedings of the National Academy of Sciences* **106**, 10960–10965 (2009). URL: <http://www.pnas.org/content/106/27/10960.abstract>. 23
- [42] T. Takano, M. Fuyama, R. Namiki, and Y. Takahashi, “Spin squeezing of a cold atomic ensemble with the nuclear spin of one-half,” *Phys. Rev. Lett.* **102**, 033601 (2009). URL: <http://link.aps.org/doi/10.1103/PhysRevLett.102.033601>.
- [43] C. Gross, T. Zibold, E. Nicklas, J. Estève, and M. K. Oberthaler, “Nonlinear atom interferometer surpasses classical precision limit,” *Nature* **464**, 1165–1169 (2010). URL: <http://dx.doi.org/10.1038/nature08919>. 23
- [44] M. Koschorreck, M. Napolitano, B. Dubost, and M. W. Mitchell, “Sub-projection-noise sensitivity in broadband atomic magnetometry,” *Phys. Rev. Lett.* **104**, 093602 (2010). URL: <http://link.aps.org/doi/10.1103/PhysRevLett.104.093602>.
- [45] I. D. Leroux, M. H. Schleier-Smith, and V. Vuletić, “Implementation of cavity squeezing of a collective atomic spin,” *Physical Review Letters* **104**, 073602 (2010). URL: <http://link.aps.org/doi/10.1103/PhysRevLett.104.073602>, copyright (C) 2010 The American Physical Society; Please report any problems to prola@aps.org. 23, 24
- [46] M. H. Schleier-Smith, I. D. Leroux, and V. Vuletić, “States of an ensemble of two-level atoms with reduced quantum uncertainty,” *Phys. Rev. Lett.* **104**, 073604 (2010). URL: <http://link.aps.org/doi/10.1103/PhysRevLett.104.073604>. 21, 22, 23, 27, 29, 30, 90
- [47] M. F. Riedel, P. Böhi, Y. Li, T. W. Hänsch, A. Sinatra, and P. Treutlein, “Atom-chip-based generation of entanglement for quantum metrology,” *Nature* **464**, 1170–1173 (2010). URL: <http://dx.doi.org/10.1038/nature08988>. xi, 23
- [48] I. D. Leroux, M. H. Schleier-Smith, and V. Vuletić, “Orientation-dependent entanglement lifetime in a squeezed atomic clock,” *Phys. Rev. Lett.* **104**, 250801 (2010). URL: <http://link.aps.org/doi/10.1103/PhysRevLett.104.250801>. xi, xii, 140
- [49] J. G. Bohnet, K. C. Cox, M. A. Norcia, J. M. Weiner, Z. Chen, and J. K. Thompson, “Reduced spin measurement back-action for a phase sensitivity ten

- times beyond the standard quantum limit,” *Nat Photon* **8**, 731–736 (2014). URL: <http://dx.doi.org/10.1038/nphoton.2014.151>. xi, 23, 26, 27, 140
- [50] O. Hosten, N. J. Engelsen, R. Krishnakumar, and M. A. Kasevich, “Measurement noise 100 times lower than the quantum-projection limit using entangled atoms,” *Nature* **529**, 505–508 (2016). URL: <http://www.nature.com/nature/journal/v529/n7587/full/nature16176.html>. xi, xii, 23, 25, 26, 27, 30, 78, 140
- [51] P. Gill, “Optical frequency standards,” *Metrologia* **42**, S125 (2005). URL: <http://stacks.iop.org/0026-1394/42/i=3/a=S13>. xi, 1
- [52] A. D. Ludlow, M. M. Boyd, J. Ye, E. Peik, and P. O. Schmidt, “Optical atomic clocks,” *Reviews of Modern Physics* **87**, 637 (2015). xi
- [53] P. Gill, “Is the time right for a redefinition of the second by optical atomic clocks?” *Journal of Physics: Conference Series* **723**, 012053 (2016). URL: <http://stacks.iop.org/1742-6596/723/i=1/a=012053>. xi
- [54] J. C. Hafele and R. E. Keating, “Around the world atomic clocks: predicted relativistic time gains,” (American Association for the Advancement of Science, 1972). xii
- [55] G. Tino, L. Cacciapuoti, K. Bongs, C. J. Bordé, P. Bouyer, H. Dittus, W. Ertmer, A. Görlitz, M. Inguscio, A. Landragin *et al.*, “Atom interferometers and optical atomic clocks: New quantum sensors for fundamental physics experiments in space,” *Nuclear Physics B-Proceedings Supplements* **166**, 159–165 (2007). xii
- [56] L. Cacciapuoti and C. Salomon, “Space clocks and fundamental tests: The ACES experiment,” *The European Physical Journal Special Topics* **172**, 57–68 (2009). URL: <http://dx.doi.org/10.1140/epjst/e2009-01041-7>. xii
- [57] EMRP, “Compact microwave clocks for industrial applications, Call 2012 – Open Excellence, Industry and SI Broader Scope,” (2012). [Www.emrponline.eu](http://www.emrponline.eu). xii
- [58] F. Esnault, N. Rossetto, D. Holleville, J. Delporte, and N. Dimarcq, “Horace: A compact cold atom clock for Galileo,” *Advances in Space Research* **47**, 854–858 (2011). xii
- [59] S. Micalizio, C. E. Calosso, A. Godone, and F. Levi, “Metrological characterization of the pulsed Rb clock with optical detection,” *Metrologia* **49**, 425–436 (2012).
- [60] F. Tricot, P. Yun, B. Francois, S. Mejri, J. Danet, M. Lours, S. Guerandel, and E. de Clercq, “Progress on a pulsed CPT clock: Reduction of the main noise source contributions,” in “2016 European Frequency and Time Forum (EFTF),” (IEEE, 2016), pp. 1–3.
- [61] R. L. Tjoelker, J. D. Prestage, E. A. Burt, P. Chen, Y. J. Chong, S. K. Chung, W. Diener, T. Ely, D. G. Enzer, H. Mojaradi, C. Okino, M. Pauken, D. Robison,

- B. L. Swenson, B. Tucker, and R. Wang, “Mercury ion clock for a NASA technology demonstration mission,” *IEEE Transactions on Ultrasonics, Ferroelectrics, and Frequency Control* **63**, 1034–1043 (2016).
- [62] R. Szmuk, V. Dugrain, W. Maineult, J. Reichel, and P. Rosenbusch, “Stability of a trapped-atom clock on a chip,” *Phys. Rev. A* **92**, 012106 (2015). URL: <http://link.aps.org/doi/10.1103/PhysRevA.92.012106>. xii, 27, 93, 103, 142
- [63] P. Treutlein, P. Hommelhoff, T. Steinmetz, T. W. Hänsch, and J. Reichel, “Coherence in microchip traps,” *Phys. Rev. Lett.* **92**, 203005– (2004). URL: <http://link.aps.org/abstract/PRL/v92/e203005>. xii
- [64] J. Reichel and V. Vuletic, *Atom Chips* (Wiley-VCH, 2011). xii, 9, 94
- [65] C. Deutsch, F. Ramirez-Martinez, C. Lacroûte, F. Reinhard, T. Schneider, J. Fuchs, F. Piéchon, F. Laloë, J. Reichel, and P. Rosenbusch, “Spin self-rephasing and very long coherence times in a trapped atomic ensemble,” *Physical Review Letters* **105**, 020401 (2010). xii, 6, 94, 121
- [66] W. Maineult, C. Deutsch, K. Gibble, J. Reichel, and P. Rosenbusch, “Spin waves and collisional frequency shifts of a trapped-atom clock,” *Phys. Rev. Lett.* **109**, 020407 (2012). URL: <http://link.aps.org/doi/10.1103/PhysRevLett.109.020407>. xii
- [67] C. Lacroûte, F. Reinhard, F. Ramirez-Martinez, C. Deutsch, T. Schneider, J. Reichel, and P. Rosenbusch, “Preliminary results of the trapped atom clock on a chip,” *IEEE Transactions on Ultrasonics, Ferroelectrics and Frequency Control* **57**, 106–110 (2010). xii
- [68] F. Ramírez-Martínez, C. Lacroûte, P. Rosenbusch, F. Reinhard, C. Deutsch, T. Schneider, and J. Reichel, “Compact frequency standard using atoms trapped on a chip,” *Advances in Space Research* **47**, 247 – 252 (2011). URL: <http://www.sciencedirect.com/science/article/pii/S0273117710002553>. xii
- [69] J. Lodewyck, P. Westergaard, and P. Lemonde, “Nondestructive measurement of the transition probability in a Sr optical lattice clock,” *Phys. Rev. A* **79**, 061401 (2009). xii
- [70] N. Shiga and M. Takeuchi, “Locking the local oscillator phase to the atomic phase via weak measurement,” *New Journal of Physics* **14**, 023034 (2012). xii
- [71] T. Vanderbruggen, R. Kohlhaas, A. Bertoldi, S. Bernon, A. Aspect, A. Landragin, and P. Bouyer, “Feedback control of trapped coherent atomic ensembles,” *Physical review letters* **110**, 210503 (2013). xii
- [72] Y. Colombe, T. Steinmetz, G. Dubois, F. Linke, D. Hunger, and J. Reichel, “Strong atom-field coupling for Bose-Einstein condensates in an optical cavity on a chip,” *Nature* **450**, 272–276 (2007). URL: <http://dx.doi.org/10.1038/nature06331>. xii, 28, 30, 31, 33, 140

- [73] D. Hunger, T. Steinmetz, Y. Colombe, C. Deutsch, T. W. Hänsch, and J. Reichel, “A fiber Fabry-Perot cavity with high finesse,” *New Journal of Physics* **12**, 065038 (2010). URL: <http://stacks.iop.org/1367-2630/12/i=6/a=065038>. xii, 33, 34, 36, 58, 61, 62, 69, 140
- [74] F. Haas, J. Volz, R. Gehr, J. Reichel, and J. Estève, “Entangled states of more than 40 atoms in an optical fiber cavity,” *Science* **344**, 180 (2014). xiii, 140
- [75] G. Barontini, L. Hohmann, F. Haas, J. Estève, and J. Reichel, “Deterministic generation of multiparticle entanglement by quantum Zeno dynamics,” *Science* **349**, 1317–1321 (2015). URL: <http://science.sciencemag.org/content/349/6254/1317>. xiii, 22, 140
- [76] S. Stapfner, L. Ost, D. Hunger, J. Reichel, I. Favero, and E. M. Weig, “Cavity-enhanced optical detection of carbon nanotube Brownian motion,” *Applied Physics Letters* **102**, 151910 (2013). xiii
- [77] M. Mader, J. Reichel, T. W. Hänsch, and D. Hunger, “A scanning cavity microscope,” *Nat Commun* **6** (2015). URL: <http://dx.doi.org/10.1038/ncomms8249>. 33
- [78] H. M. Meyer, R. Stockill, M. Steiner, C. Le Gall, C. Matthiesen, E. Clarke, A. Ludwig, J. Reichel, M. Atatüre, and M. Köhl, “Direct photonic coupling of a semiconductor quantum dot and a trapped ion,” *Phys. Rev. Lett.* **114**, 123001 (2015). URL: <http://link.aps.org/doi/10.1103/PhysRevLett.114.123001>. xiii, 28, 33, 124
- [79] J. Volz, R. Gehr, G. Dubois, J. Estève, and J. Reichel, “Measurement of the internal state of a single atom without energy exchange,” *Nature* **475**, 210–213 (2011). xiii, 140
- [80] K. Ott, S. Garcia, R. Kohlhaas, K. Schüppert, P. Rosenbusch, R. Long, and J. Reichel, “Millimeter-long fiber Fabry-Perot cavities,” *Opt. Express* **24**, 9839–9853 (2016). URL: <http://www.opticsexpress.org/abstract.cfm?URI=oe-24-9-9839>. xiii, 33, 62
- [81] H. J. Kimble, “The quantum internet,” *Nature* **453**, 1023 (2008). xiii, 124, 142
- [82] S. Ritter, C. Nolleke, C. Hahn, A. Reiserer, A. Neuzner, M. Uphoff, M. Mücke, E. Figueroa, J. Bochmann, and G. Rempe, “An elementary quantum network of single atoms in optical cavities,” *Nature* **484**, 195–200 (2012). URL: <http://dx.doi.org/10.1038/nature11023>. xiii, 124, 142
- [83] L.-G. Bernier, P. Rochat *et al.*, “Active hydrogen maser atomic frequency standard,” (1998). US Patent 5,838,206. 1, 139
- [84] M. Fischer, N. Kolachevsky, M. Zimmermann, R. Holzwarth, T. Udem, T. W. Hänsch, M. Abgrall, J. Grünert, I. Maksimovic, S. Bize, H. Marion, F. P. D. Santos, P. Lemonde, G. Santarelli, P. Laurent, A. Clairon, C. Salomon, M. Haas, U. D. Jentschura, and C. H. Keitel, “New limits on the drift of fundamental

- constants from laboratory measurements,” *Phys. Rev. Lett.* **92**, 230802 (2004). URL: <http://link.aps.org/doi/10.1103/PhysRevLett.92.230802>. 1
- [85] T. Rosenband, D. Hume, P. Schmidt, C. Chou, A. Brusch, L. Lorini, W. Oskay, R. Drullinger, T. Fortier, J. Stalnaker *et al.*, “Frequency ratio of Al⁺ and Hg⁺ single-ion optical clocks; metrology at the 17th decimal place,” *Science* **319**, 1808–1812 (2008). 1
- [86] F. Bloch, “Nuclear induction,” *Phys. Rev.* **70**, 460–474 (1946). URL: <http://link.aps.org/doi/10.1103/PhysRev.70.460>. 2, 17
- [87] J. Vanier and C. Audoin, *The quantum physics of atomic frequency standards* (Adam Hilger, 1989). 2
- [88] C. Gerry and P. Knight, *Introductory Quantum Optics* (Cambridge Univ. Press, 2005). 2, 20
- [89] C. Deutsch, “Trapped atom clock on a chip. Identical spin rotation effects in an ultracold trapped atomic clock,” Ph.D. thesis, Université Paris VI (2011). 3, 5, 96, 100, 102
- [90] W. M. Itano, J. C. Bergquist, J. J. Bollinger, J. M. Gilligan, D. J. Heinzen, F. L. Moore, M. G. Raizen, and D. J. Wineland, “Quantum projection noise: Population fluctuations in two-level systems,” *Physical Review A* **47**, 3554 (1993). URL: <http://link.aps.org/abstract/PRA/v47/p3554>, copyright (C) 2009 The American Physical Society; Please report any problems to prola@aps.org. 4, 18, 140
- [91] F. Reinhard, “Design and construction of an atomic clock on an atom chip,” Ph.D. thesis, Université Paris VI (2009). 5, 7, 9, 13, 16, 93, 95, 110, 111
- [92] C. Lacroûte, “Développement d’une horloge atomique sur puce à atomes : optimisation de la durée de cohérence et caractérisation préliminaire.” Ph.D. thesis, Université Pierre et Marie Curie, Paris (2010). 5, 96, 139
- [93] L. Yi, S. Mejri, J. J. McFerran, Y. Le Coq, and S. Bize, “Optical lattice trapping of ¹⁹⁹Hg and determination of the magic wavelength for the ultraviolet $^1s_0 \leftrightarrow ^3p_0$ clock transition,” *Phys. Rev. Lett.* **106**, 073005 (2011). URL: <http://link.aps.org/doi/10.1103/PhysRevLett.106.073005>. 5
- [94] H. J. Lewandowski, D. M. Harber, D. L. Whitaker, and E. A. Cornell, “Observation of anomalous spin-state segregation in a trapped ultracold vapor,” *Physical Review Letters* **88**, 070403 (2002). URL: <http://link.aps.org/abstract/PRL/v88/e070403>. 5
- [95] D. Harber, H. Lewandowski, J. McGuirk, and E. Cornell, “Effect of cold collisions on spin coherence and resonance shifts in a magnetically trapped ultracold gas,” *Physical Review A* **66**, 053616 (2002). 5, 6

- [96] V. Dugrain, “Metrology with trapped atoms on a chip using non-degenerate and degenerate quantum gases,” Ph.D. thesis, Université Pierre et Marie Curie (2012). 5
- [97] P. Rosenbusch, “Magnetically trapped atoms for compact atomic clocks,” *Applied Physics B: Lasers and Optics* **95**, 227–235 (2009). 6
- [98] X. Du, L. Luo, B. Clancy, and J. E. Thomas, “Observation of anomalous spin segregation in a trapped Fermi gas,” *Phys. Rev. Lett.* **101**, 150401 (2008). URL: <http://link.aps.org/doi/10.1103/PhysRevLett.101.150401>. 6
- [99] Y. Sortais, S. Bize, C. Nicolas, G. Santarelli, G. S. C. Salomon, and A. Clairon, “ ^{87}Rb versus ^{133}Cs in cold atom fountains: a comparison,” *IEEE Transactions on Ultrasonics, Ferroelectrics, and Frequency Control* **47**, 1093–1097 (2000). 6
- [100] “Recommendation 2 (ci-2015) updates to the list of standard frequencies,” (2015). URL: <http://www.bipm.org/jsp/en/CIPMRecommendations.jsp>. 6
- [101] D. A. Steck, *Rubidium 87 D Line Data Version 2.1.5* (2010). URL: <http://steck.us/alkalidata/>. 7, 21, 27, 90
- [102] Hänsel, “Magnetische Mikrofallen für Rubidiumatome,” Ph.D. thesis, Ludwig-Maximilians-Universität München (2000). 8, 10, 12, 14, 95
- [103] W. H. Wing, “On neutral particle trapping in quasistatic electromagnetic fields,” *Progress in Quantum Electronics* **8**, 181 – 199 (1984). URL: <http://www.sciencedirect.com/science/article/pii/0079672784900120>. 8
- [104] W. Ketterle, D. Durfee, and D. Stamper-Kurn, “Making, probing and understanding Bose-Einstein condensates,” in “Bose-Einstein condensation in atomic gases,” , vol. 140 of *Proceedings of the international school of physics Enrico Fermi*, Inguscio, Stringari and Wieman, ed. (IOS Press, 1999), vol. 140 of *Proceedings of the international school of physics Enrico Fermi*, pp. 67–176. 8, 27, 96
- [105] Y.-J. Lin, A. R. Perry, R. L. Compton, I. B. Spielman, and J. V. Porto, “Rapid production of ^{87}Rb Bose-Einstein condensates in a combined magnetic and optical potential,” *Phys. Rev. A* **79**, 063631 (2009). URL: <http://link.aps.org/doi/10.1103/PhysRevA.79.063631>. 8
- [106] W. Petrich, M. H. Anderson, J. R. Ensher, and E. A. Cornell, “Stable, tightly confining magnetic trap for evaporative cooling of neutral atoms,” *Phys. Rev. Lett.* **74**, 3352–3355 (1995). URL: <http://link.aps.org/doi/10.1103/PhysRevLett.74.3352>. 8
- [107] M. Keil, O. Amit, S. Zhou, D. Groswasser, Y. Japha, and R. Folman, “Fifteen years of cold matter on the atom chip: promise, realizations, and prospects,” *Journal of Modern Optics* pp. 1–46 (2016). 9

- [108] A. L. Migdall, J. V. Prodan, W. D. Phillips, T. H. Bergeman, and H. J. Metcalf, “First observation of magnetically trapped neutral atoms,” *Phys. Rev. Lett.* **54**, 2596–2599 (1985). URL: <http://link.aps.org/doi/10.1103/PhysRevLett.54.2596>. 9
- [109] J. Reichel, W. Hänsel, P. Hommelhoff, and T. W. Hänsch, “Applications of integrated magnetic microtraps,” *Applied Physics B: Lasers and Optics* **72**, 81–89 (2001). URL: <http://dx.doi.org/10.1007/s003400000460>. 10
- [110] T. van Zoest, N. Gaaloul, Y. Singh, H. Ahlers, W. Herr, S. T. Seidel, W. Ertmer, E. Rasel, M. Eckart, E. Kajari, S. Arnold, G. Nandi, W. P. Schleich, R. Walser, A. Vogel, K. Sengstock, K. Bongs, W. Lewoczko-Adamczyk, M. Schiemangk, T. Schuldt, A. Peters, T. Konemann, H. Muntinga, C. Lammerzahl, H. Dittus, T. Steinmetz, T. W. Hansch, and J. Reichel, “Bose-Einstein condensation in microgravity,” *Science* **328**, 1540–1543 (2010). URL: <http://www.sciencemag.org/cgi/content/abstract/328/5985/1540>. 16
- [111] D. Leibfried, M. D. Barrett, T. Schaetz, J. Britton, J. Chiaverini, W. M. Itano, J. D. Jost, C. Langer, and D. J. Wineland, “Toward Heisenberg-limited spectroscopy with multiparticle entangled states,” *Science* **304**, 1476–1478 (2004). URL: <http://dx.doi.org/10.1126/science.1097576>. 17
- [112] F. T. Arecchi, E. Courtens, R. Gilmore, and H. Thomas, “Atomic coherent states in quantum optics,” *Phys. Rev. A* **6**, 2211–2237 (1972). URL: <http://link.aps.org/doi/10.1103/PhysRevA.6.2211>. 17
- [113] D. J. Wineland, J. J. Bollinger, W. M. Itano, F. L. Moore, and D. J. Heinzen, “Spin squeezing and reduced quantum noise in spectroscopy,” *Phys. Rev. A* **46**, R6797–R6800 (1992). URL: <http://link.aps.org/doi/10.1103/PhysRevA.46.R6797>. 19
- [114] A. Sorensen, L.-M. Duan, J. I. Cirac, and P. Zoller, “Many-particle entanglement with Bose–Einstein condensates,” *Nature* pp. 63–66 (2001). 19
- [115] C. Cohen-Tannoudji, J. Dupont-Roc, and G. Grynberg, *Processus d’interaction entre photons et atomes* (Editions du CNRS, 1988). 20
- [116] E. Brion, L. H. Pedersen, and K. Molmer, “Adiabatic elimination in a lambda system,” *Journal of Physics A: Mathematical and Theoretical* **40**, 1033 (2007). URL: <http://stacks.iop.org/1751-8121/40/i=5/a=011>. 20
- [117] E. T. Jaynes and F. W. Cummings, “Comparison of quantum and semiclassical radiation theories with application to the beam maser,” *Proceedings of the IEEE* **51**, 89–109 (1963). 20
- [118] D. Braak, “Integrability of the Rabi model,” *Phys. Rev. Lett.* **107**, 100401 (2011). URL: <http://link.aps.org/doi/10.1103/PhysRevLett.107.100401>. 21
- [119] M. H. Schleier-Smith, “Cavity-enabled spin squeezing for a quantum-enhanced atomic clock,” Ph.D. thesis, Harvard University (2011). 21

- [120] H. J. Kimble, “Strong interactions of single atoms and photons in cavity QED,” *Physica Scripta* **1998**, 127 (1998). URL: <http://iopscience.iop.org/article/10.1238/Physica.Topical.076a00127/meta>. 22
- [121] H. Uys, M. Biercuk, A. VanDevender, C. Ospelkaus, D. Meiser, R. Ozeri, and J. Bollinger, “Decoherence due to elastic Rayleigh scattering,” *Physical review letters* **105**, 200401 (2010). 23
- [122] R. Ozeri, C. Langer, J. Jost, B. DeMarco, A. Ben-Kish, B. Blakestad, J. Britton, J. Chiaverini, W. Itano, D. Hume *et al.*, “Hyperfine coherence in the presence of spontaneous photon scattering,” *Physical review letters* **95**, 030403 (2005). 23
- [123] M. H. Schleier-Smith, I. D. Leroux, and V. Vuletić, “Squeezing the collective spin of a dilute atomic ensemble by cavity feedback,” *Phys. Rev. A* **81**, 021804 (2010). URL: <http://link.aps.org/doi/10.1103/PhysRevA.81.021804>. 23, 24, 25, 26, 140
- [124] K. Pawłowski, J. érôme Est‘eve, J. Reichel, and A. Sinatra, “Limits of atomic entanglement by cavity feedback: From weak to strong coupling,” *EPL (Europhysics Letters)* **113**, 34005 (2016). URL: <http://stacks.iop.org/0295-5075/113/i=3/a=34005>. 23, 24
- [125] C. D. Hamley, C. S. Gerving, T. M. Hoang, E. M. Bookjans, and M. S. Chapman, “Spin-nematic squeezed vacuum in a quantum gas,” *Nat Phys* **8**, 305–308 (2012). URL: <http://dx.doi.org/10.1038/nphys2245>. 23
- [126] R. J. Sewell, M. Koschorreck, M. Napolitano, B. Dubost, N. Behbood, and M. W. Mitchell, “Magnetic sensitivity beyond the projection noise limit by spin squeezing,” *Phys. Rev. Lett.* **109**, 253605 (2012). URL: <http://link.aps.org/doi/10.1103/PhysRevLett.109.253605>. 23
- [127] R. Friedberg and J. Manassah, “Dicke states and Bloch states,” *Laser Physics Letters* **4**, 900 (2007). 24
- [128] M. Kitagawa and M. Ueda, “Squeezed spin states,” *Phys. Rev. A* **47**, 5138–5143 (1993). URL: <http://link.aps.org/doi/10.1103/PhysRevA.47.5138>. 25, 140
- [129] I. D. Leroux, “Squeezing collective atomic spin with an optical resonator,” Ph.D. thesis, Massachusetts Institute of Technology (2011). 25, 26
- [130] M. Takeuchi, S. Ichihara, T. Takano, M. Kumakura, T. Yabuzaki, and Y. Takahashi, “Spin squeezing via one-axis twisting with coherent light,” *Phys. Rev. Lett.* **94**, 023003 (2005). URL: <http://link.aps.org/doi/10.1103/PhysRevLett.94.023003>. 25
- [131] Z. Chen, J. G. Bohnet, J. M. Weiner, K. C. Cox, and J. K. Thompson, “Cavity-aided nondemolition measurements for atom counting and spin squeezing,” *Phys. Rev. A* **89**, 043837 (2014). URL: <http://link.aps.org/doi/10.1103/PhysRevA.89.043837>. 26

- [132] R. Gehr, J. Volz, G. Dubois, T. Steinmetz, Y. Colombe, B. L. Lev, R. Long, J. Estève, and J. Reichel, “Cavity-based single atom preparation and high-fidelity hyperfine state readout,” *Physical Review Letters* **104**, 203602 (2010). URL: <http://link.aps.org/doi/10.1103/PhysRevLett.104.203602>. 28
- [133] J. Reichel, W. Hänsel, and T. W. Hänsch, “Atomic micromanipulation with magnetic surface traps,” *Phys. Rev. Lett.* **83**, 3398–3401 (1999). URL: <http://dx.doi.org/10.1103/PhysRevLett.83.3398>. 28, 94
- [134] D. M. Harber, J. M. McGuirk, J. M. Obrecht, and E. A. Cornell, “Thermally induced losses in ultra-cold atoms magnetically trapped near room-temperature surfaces,” *Journal of Low Temperature Physics* **133**, 229–238 (2003). URL: <http://dx.doi.org/10.1023/A:1026084606385>.
- [135] T. Steinmetz, “Resonator-Quantenelektrodynamik auf einem Mikrofallenchip,” Ph.D. thesis, Ludwig–Maximilians–Universität München (2008). 28, 30, 56, 82, 85, 87, 94, 96, 98, 120, 137, 142
- [136] J. D. Miller, R. A. Cline, and D. J. Heinzen, “Far-off-resonance optical trapping of atoms,” *Phys. Rev. A* **47**, R4567–R4570 (1993). URL: <http://link.aps.org/doi/10.1103/PhysRevA.47.R4567>. 30
- [137] J.-P. Brantut, J.-F. Clément, M. R. de Saint Vincent, G. Varoquaux, R. A. Nyman, A. Aspect, T. Bourdel, and P. Bouyer, “Light-shift tomography in an optical-dipole trap for neutral atoms,” *Physical Review A* **78**, 031401 (2008). 30
- [138] C. Toninelli, Y. Delley, T. Stöferle, A. Renn, S. Götzinger, and V. Sandoghdar, “A scanning microcavity for in-situ control of single-molecule emission,” *Applied Physics Letters* **97**, 021107 (2010). 33
- [139] M. Steiner, H. M. Meyer, C. Deutsch, J. Reichel, and M. Köhl, “Single ion coupled to an optical fiber cavity,” *Phys. Rev. Lett.* **110**, 043003 (2013). URL: <http://link.aps.org/doi/10.1103/PhysRevLett.110.043003>. 124
- [140] R. Albrecht, A. Bommer, C. Deutsch, J. Reichel, and C. Becher, “Coupling of a single nitrogen-vacancy center in diamond to a fiber-based microcavity,” *Physical Review Letters* **110**, 243602 (2013).
- [141] M. Miguel-Sánchez, A. Reinhard, E. Togan, T. Volz, A. Imamoğlu, B. Besga, J. Reichel, and J. Estève, “Cavity quantum electrodynamics with charge-controlled quantum dots coupled to a fiber Fabry-Perot cavity,” *NJP* **15**, 045002 (2013).
- [142] B. Besga, C. Vaneph, J. Reichel, J. Estève, A. Reinhard, J. Miguel-Sánchez, A. Imamoğlu, and T. Volz, “Polariton boxes in a tunable fiber cavity,” *Phys. Rev. Applied* **3**, 014008 (2015). 33
- [143] N. E. Flowers-Jacobs, S. W. Hoch, J. C. Sankey, A. Kashkanova, A. M. Jayich, C. Deutsch, J. Reichel, and J. G. E. Harris, “Fiber-cavity-based optomechanical device,” *APL* **101**, 221109 (2012). 33

- [144] B. Petrak, N. Djeu, and A. Muller, “Purcell-enhanced Raman scattering from atmospheric gases in a high-finesse microcavity,” *Phys. Rev. A* **89**, 023811 (2014). URL: <http://link.aps.org/doi/10.1103/PhysRevA.89.023811>. 33
- [145] B. Brandstätter, A. McClung, K. Schüppert, B. Casabone, K. Friebe, A. Stute, P. O. Schmidt, C. Deutsch, J. Reichel, R. Blatt, and T. E. Northup, “Integrated fiber-mirror ion trap for strong ion-cavity coupling,” *RSI* **84**, 123104 (2013). 33, 34, 62, 63, 64, 69
- [146] H. Takahashi, J. Morphey, F. Oručević, A. Noguchi, E. Kassa, and M. Keller, “Novel laser machining of optical fibers for long cavities with low birefringence,” *Optics express* **22**, 31317 (2014). 33, 34, 35, 53, 63, 64
- [147] A. Márquez Seco, H. Takahashi, and M. Keller, “Novel ion trap design for strong ion-cavity coupling,” *Atoms* **4**, 15 (2016). 33, 124
- [148] C. Miller and F. Janniello, “Passively temperature-compensated fibre Fabry-Perot filter and its application in wavelength division multiple access computer network,” *Electronics letters* **26**, 2122–2123 (1990). 33
- [149] R. Kitamura, L. Pilon, and M. Jonasz, “Optical constants of silica glass from extreme ultraviolet to far infrared at near room temperature,” *Applied optics* **46**, 8118–8133 (2007). 34
- [150] E. Mendez, K. M. Nowak, H. J. Baker, F. J. Villarreal, and D. R. Hall, “Localized CO₂ laser damage repair of fused silica optics,” *Appl. Opt.* **45**, 5358–5367 (2006). 34
- [151] F. Laguarda, N. Lupon, and J. Armengol, “Optical glass polishing by controlled laser surface-heat treatment,” *Appl. Opt.* **33**, 6508–6513 (1994). URL: <https://www.osapublishing.org/ao/abstract.cfm?uri=ao-33-27-6508>.
- [152] K. M. Nowak, H. J. Baker, and D. R. Hall, “Efficient laser polishing of silica micro-optic components,” *Appl. Opt.* **45**, 162–171 (2006). 34, 48
- [153] D. Hunger, C. Deutsch, R. J. Barbour, R. J. Warburton, and J. Reichel, “Laser micro-fabrication of concave, low-roughness features in silica,” *AIP Advances* **2**, 012119 (2012). URL: <http://scitation.aip.org/content/aip/journal/adv/2/1/10.1063/1.3679721>. 34, 36, 39, 47, 59
- [154] U. Paek and A. Weaver, “Formation of a spherical lens at optical fiber ends with a CO₂ laser,” *Applied optics* **14**, 294–298 (1975). URL: <https://www.osapublishing.org/ao/abstract.cfm?uri=ao-14-2-294>. 34
- [155] D. K. Armani, T. J. Kippenberg, S. M. Spillane, and K. J. Vahala, “Ultra-high-Q toroid microcavity on a chip,” *Nature* **421**, 925–928 (2003). URL: <http://dx.doi.org/10.1038/nature01371>. 34
- [156] M. Salz, “Optimierung einer segmentierten Paulfalle mit optischer Schnittstelle,” Master’s thesis, Johannes Gutenberg-Universität Mainz (2013). 34, 47

- [157] A. A. Trichet, P. R. Dolan, D. M. Coles, G. M. Hughes, and J. M. Smith, “Topographic control of open-access microcavities at the nanometer scale,” *Optics express* **23**, 17205–17216 (2015). 34
- [158] M. Shaheen, J. Gagnon, and B. Fryer, “Femtosecond laser ablation behavior of gold, crystalline silicon, and fused silica: a comparative study,” *Laser Physics* **24**, 106102 (2014). URL: <http://iopscience.iop.org/article/10.1088/1054-660X/24/10/106102/meta>. 34
- [159] R. Albrecht, A. Bommer, C. Pauly, F. Mücklich, A. W. Schell, P. Engel, T. Schröder, O. Benson, J. Reichel, and C. Becher, “Narrow-band single photon emission at room temperature based on a single nitrogen-vacancy center coupled to an all-fiber-cavity,” *Applied Physics Letters* **105**, 073113 (2014). 34
- [160] G. Rempe, R. J. Thompson, H. J. Kimble, and R. Lalezari, “Measurement of ultralow losses in an optical interferometer,” **17**, 363–365 (1992). 34
- [161] M. Uphoff, M. Brekenfeld, G. Rempe, and S. Ritter, “Frequency splitting of polarization eigenmodes in microscopic Fabry-Perot cavities,” (2015). 34, 53, 91
- [162] J. Benedikter, T. Hämmer, M. Mader, B. Schlederer, J. Reichel, T. W. Hänsch, and D. Hunger, “Transverse-mode coupling and diffraction loss in tunable Fabry-Perot microcavities,” *New Journal of Physics* **17**, 053051 (2015). URL: <http://stacks.iop.org/1367-2630/17/i=5/a=053051>. 34, 64, 71, 76, 77
- [163] S. Garcia, “Interfaces fibrées entre atomes uniques et photons uniques,” Ph.D. thesis, Ecole normale supérieure (2015). 36, 42, 63, 78, 80, 85, 141
- [164] J. Schmit and J. Creath, “Extended averaging technique for derivation of error-compensating algorithms in phase-shifting interferometry,” *Appl. Opt.* **34**, 3610 (1995). 36, 37
- [165] M. Gad-el Hak, *The MEMS handbook* (CRC press, 2001). 41
- [166] X. Dai, X. Zhao, G. Ding, H. Wang, and B. Cai, “Packaging of optical fibers using microfabricated nickel clamps,” *Journal of Micro/Nanolithography, MEMS, and MOEMS* **7**, 010501–010501–3 (2008). URL: <http://dx.doi.org/10.1117/1.2896082>. 41, 128
- [167] H. Klank, J. P. Kutter, and O. Geschke, “CO₂-laser micromachining and back-end processing for rapid production of PMMA-based microfluidic systems,” *Lab Chip* **2**, 242–246 (2002). URL: <http://dx.doi.org/10.1039/B206409J>. 44
- [168] J. N. Gonsalves and W. W. Duley, “Cutting thin metal sheets with the cw CO₂ laser,” *Journal of Applied Physics* **43**, 4684–4687 (1972). URL: <http://scitation.aip.org/content/aip/journal/jap/43/11/10.1063/1.1660989>. 44

- [169] K. Boyd, S. Rees, N. Simakov, J. M. O. Daniel, R. Swain, E. Mies, A. Hemming, W. A. Clarkson, and J. Haub, “High precision 9.6 μm CO₂ laser end-face processing of optical fibres,” *Opt. Express* **23**, 15065–15071 (2015). URL: <http://www.opticsexpress.org/abstract.cfm?URI=oe-23-11-15065>. 46, 48
- [170] Y. Colombe, D. H. Slichter, A. C. Wilson, D. Leibfried, and D. J. Wineland, “Single-mode optical fiber for high-power, low-loss UV transmission,” *Optics express* **22**, 19783 (2014). 46
- [171] K. M. Nowak, H. J. Baker, and D. R. Hall, “Analytical model for CO₂ laser ablation of fused quartz,” *Appl. Opt.* **54**, 8653–8663 (2015). URL: <http://ao.osa.org/abstract.cfm?URI=ao-54-29-8653>. 47
- [172] T. Doualle, L. Gallais, P. Cormont, D. Hébert, P. Combis, and J.-L. Rullier, “Thermo-mechanical simulations of CO₂ laser-fused silica interactions,” *Journal of Applied Physics* **119**, 113106 (2016). URL: <http://scitation.aip.org/content/aip/journal/jap/119/11/10.1063/1.4944435>. 47
- [173] L. Flatten, A. Trichet, and J. Smith, “Spectral engineering of coupled open-access microcavities,” *Laser & Photonics Reviews* (2015). 47
- [174] F. Fang, X. Zhang, A. Weckenmann, G. Zhang, and C. Evans, “Manufacturing and measurement of freeform optics,” *CIRP Annals - Manufacturing Technology* **62**, 823 – 846 (2013). URL: <http://www.sciencedirect.com/science/article/pii/S0007850613001935>. 48
- [175] J. F. Dynes, S. J. Kindness, S. W.-B. Tam, A. Plews, A. W. Sharpe, M. Lucamarini, B. Fröhlich, Z. L. Yuan, R. V. Penty, and A. J. Shields, “Quantum key distribution over multicore fiber,” *Opt. Express* **24**, 8081–8087 (2016). URL: <http://www.opticsexpress.org/abstract.cfm?URI=oe-24-8-8081>. 50
- [176] I. N. Papadopoulos, S. Farahi, C. Moser, and D. Psaltis, “High-resolution, lensless endoscope based on digital scanning through a multimode optical fiber,” *Biomed. Opt. Ex.* **4**, 260 (2013). 50, 62
- [177] P. Cormont, P. Combis, L. Gallais, C. Hecquet, L. Lamaignère, and J. L. Rullier, “Removal of scratches on fused silica optics by using a CO₂ laser,” *Opt. Express* **21**, 28272–28289 (2013). URL: <http://www.opticsexpress.org/abstract.cfm?URI=oe-21-23-28272>. 48
- [178] K. Imen, C. H. Lee, Y. Y. Yang, S. D. Allen, and A. K. Ghosh, “Laser-fabricated fiber optical taps for interconnects and optical data processing devices,” (1991). URL: <http://dx.doi.org/10.1117/12.24661>. 48
- [179] K. M. Nowak, H. J. Baker, and D. R. Hall, “Pulsed-laser machining and polishing of silica micro-optical components using a co₂ laser and an acousto-optic modulator,” in “*Photonics Fabrication Europe*,” (International Society for Optics and Photonics, 2003), pp. 107–111.

- [180] G. A. Markillie, H. J. Baker, F. J. Villarreal, and D. R. Hall, “Effect of vaporization and melt ejection on laser machining of silica glass micro-optical components,” *Appl. Opt.* **41**, 5660 (2002).
- [181] J. F. Monjardin, K. M. Nowak, H. J. Baker, and D. R. Hall, “Correction of beam errors in high power laser diode bars and stacks,” *Opt. Exp.* **14**, No. **18**, 8178–8183 (2006).
- [182] G. Vázquez, A. Harhira, R. Kashyap, and R. Bosisio, “Micromachining by CO₂ laser ablation: Building blocks for a multiport integrated device,” *Optics Communications* **283**, 2824 – 2828 (2010). URL: <http://www.sciencedirect.com/science/article/pii/S0030401810002683>.
- [183] S. Heidrich, A. Richmann, and E. Willenborg, “Development of a laser-based process chain for manufacturing free form optics,” (2012). URL: <http://dx.doi.org/10.1117/12.922407>. 48
- [184] “Heating power feedback control for [co₂,” . 48
- [185] C. Fabry and A. Pérot, “Sur les franges des lames minces argentées et leur application à la mesure de petites épaisseurs d’air,” *Ann. Chim. Phys* **12**, 459–501 (1897). 55
- [186] K. J. Vahala, “Optical microcavities,” *Nature* **424**, 839–846 (2003). URL: <http://dx.doi.org/10.1038/nature01939>. 55
- [187] H. Kogelnik and T. Li, “Laser beams and resonators,” *Applied optics* **5**, 1550–1567 (1966). 55
- [188] B. E. Saleh and M. C. Teich, *Fundamentals of Photonics* (Wiley, 2007). 57, 70
- [189] M. Pöllinger, D. O’Shea, F. Warken, and A. Rauschenbeutel, “Ultrahigh-Q tunable whispering-gallery-mode microresonator,” *Phys. Rev. Lett.* **103**, 053901 (2009). URL: <http://link.aps.org/doi/10.1103/PhysRevLett.103.053901>. 58
- [190] The VIRGO Collaboration, “The VIRGO large mirrors: a challenge for low loss coatings,” *Classical and Quantum Gravity* **21**, S935 (2004). URL: <http://stacks.iop.org/0264-9381/21/i=5/a=083>. 59
- [191] J. M. Bennett, “Recent developments in surface roughness characterization,” *Measurement Science and Technology* **3**, 1119 (1992). URL: <http://stacks.iop.org/0957-0233/3/i=12/a=001>. 59
- [192] W. B. Joyce and B. C. DeLoach, “Alignment of Gaussian beams,” *Appl. Opt.* **23**, 4187–4196 (1984). URL: <http://ao.osa.org/abstract.cfm?URI=ao-23-23-4187>. 61, 71, 73
- [193] T. A. Birks, J. C. Knight, and P. S. J. Russell, “Endlessly single-mode photonic crystal fiber,” *Opt. Lett.* **22**, 961–963 (1997). URL: <http://ol.osa.org/abstract.cfm?URI=ol-22-13-961>. 63

- [194] J. Degallaix, “Oscar, a Matlab-based optical FFT code,” *J. Phys.: Conf. Ser.* **228**, 012021 (2010). 67, 141
- [195] A. Roy and M. D. Barrett, “Fabrication of glass micro-cavities for cavity quantum electrodynamics experiments,” *Applied Physics Letters* **99**, 171112 (2011). 69
- [196] W. B. Joyce and B. DeLoach, “Alignment of Gaussian beams,” *Appl. Opt.* **23**, 4187–4196 (1984). 70
- [197] R. A. Boudreau and S. M. Boudreau, *Passive micro-optical alignment methods* (CRC Press, 2005). 71
- [198] D. Kleckner, W. T. M. Irvine, S. S. R. Oemrawsingh, and D. Bouwmeester, “Diffraction-limited high-finesse optical cavities,” *Phys. Rev. A* **81**, 043814 (2010). URL: <http://link.aps.org/doi/10.1103/PhysRevA.81.043814>. 76
- [199] C. Lebouteiller, “Dispositif pour le chargement rapide d’une cavité miniaturisée : vers un registre de qubits atomiques,” Ph.D. thesis, Université Pierre et Marie Curie (2016). 78, 87
- [200] A. Franzen (2009). URL: <http://www.gwoptics.org/ComponentLibrary/>. 79
- [201] D. McCarron, S. King, and S. Cornish, “Modulation transfer spectroscopy in atomic rubidium,” *Measurement science and technology* **19**, 105601 (2008). 78
- [202] C. Nshii, M. Vangeleyn, J. Cotter, P. Griffin, E. Hinds, C. Ironside, P. See, A. Sinclair, E. Riis, and A. Arnold, “A surface-patterned chip as a strong source of ultracold atoms for quantum technologies,” *Nature nanotechnology* **8**, 321–324 (2013). 82, 122
- [203] J. R. Mowat, “Stark effect in alkali-metal ground-state hyperfine structure,” *Phys. Rev. A* **5**, 1059–1062 (1972). URL: <http://link.aps.org/doi/10.1103/PhysRevA.5.1059>. 83
- [204] W. M. Itano, L. L. Lewis, and D. J. Wineland, “Shift of $^2S_{1/2}$ hyperfine splittings due to blackbody radiation,” *Phys. Rev. A* **25**, 1233–1235 (1982). URL: <http://link.aps.org/doi/10.1103/PhysRevA.25.1233>. 83
- [205] H. Gould, E. Lipworth, and M. C. Weisskopf, “Quadratic stark shift between Zeeman substates in Cs^{133} , Rb^{87} , Rb^{85} , K^{39} , and Na^{23} ,” *Phys. Rev.* **188**, 24–29 (1969). URL: <http://link.aps.org/doi/10.1103/PhysRev.188.24>. 83
- [206] J. Gallego, S. Ghosh, S. K. Alavi, W. Alt, M. Martinez-Dorantes, D. Meschede, and L. Ratschbacher, “High-finesse fiber fabry–perot cavities: stabilization and mode matching analysis,” *Applied Physics B* **122**, 1–14 (2016). URL: <http://dx.doi.org/10.1007/s00340-015-6281-z>. 85, 87
- [207] A. Bick, C. Staarmann, P. Christoph, O. Hellmig, J. Heinze, K. Sengstock, and C. Becker, “The role of mode match in fiber cavities,” *Review of Scientific Instruments* **87**, 013102 (2016). URL: <http://scitation.aip.org/content/aip/journal/rsi/87/1/10.1063/1.4939046>. 85

- [208] R. R. Braga, R. Y. Ballester, and J. L. Ferracane, “Factors involved in the development of polymerization shrinkage stress in resin-composites: a systematic review,” *Dental Materials* **21**, 962–970 (2005). 87
- [209] G. Q. d. M. Monteiro and M. A. J. R. Montes, “Evaluation of linear polymerization shrinkage, flexural strength and modulus of elasticity of dental composites,” *Materials Research* **13**, 51–55 (2010).
- [210] L. C. C. Boaro, F. Gonçalves, T. C. Guimarães, J. L. Ferracane, A. Versluis, and R. R. Braga, “Polymerization stress, shrinkage and elastic modulus of current low-shrinkage restorative composites,” *Dental Materials* **26**, 1144–1150 (2010).
- [211] K. Karthick, K. Sivakumar, P. Geetha Priya, and S. Shankar, “Polymerization shrinkage of composites—a review,” *JIADS* **2**, 32–36 (2011). 87
- [212] F. Ferri, “In preparation,” Ph.D. thesis, Ecole normale supérieure (2017). 87
- [213] S. K. Sheem and T. G. Giallorenzi, “Two-dimensional silicon grooves for longitudinal alignment in fiber end-butt coupling,” *Optics letters* **3**, 73–75 (1978). 87
- [214] C. Bulmer, S. Sheem, R. Moeller, and W. Burns, “Fabrication of flip-chip optical couplers between single-mode fibers and LiNbO₃ channel waveguides,” *IEEE Transactions on Components, Hybrids, and Manufacturing Technology* **4**, 350–355 (1981).
- [215] E. J. Murphy, “Fiber attachment for guided wave devices,” *Journal of lightwave technology* **6**, 862–871 (1988).
- [216] D. Albares and T. Trask, “Optical fiber to waveguide coupling technique,” Tech. rep., DTIC Document (1990). 87
- [217] K. L. Moore, “Ultracold atoms, circular waveguides, and cavity QED with millimeter-scale electromagnetic traps,” Ph.D. thesis, Citeseer (2007). 89
- [218] S. Wildermuth, P. Krüger, C. Becker, M. Brajdic, S. Haupt, A. Kasper, R. Folman, and J. Schmiedmayer, “Optimized magneto-optical trap for experiments with ultracold atoms near surfaces,” *Phys. Rev. A* **69**, 030901 (2004). URL: <http://link.aps.org/doi/10.1103/PhysRevA.69.030901>. 95
- [219] R. Long, T. Rom, W. Hänsel, W. T. Hänsch, and J. Reichel, “Long distance magnetic conveyor for precise positioning of ultracold atoms,” *The European Physical Journal D - Atomic, Molecular, Optical and Plasma Physics* **35**, 125–133 (2005). URL: <http://dx.doi.org/10.1140/epjd/e2005-00177-6>. 97, 98, 143
- [220] R. Long, “Couplage d’une microsphère accordable et d’une puce à atomes,” Ph.D. thesis, Université Pierre et Marie Curie (2003). 97, 98

- [221] M. Dupont-Nivet, M. Casiulis, T. Laudat, C. I. Westbrook, and S. Schwartz, “Microwave-stimulated Raman adiabatic passage in a Bose-Einstein condensate on an atom chip,” *Phys. Rev. A* **91**, 053420 (2015). URL: <http://link.aps.org/doi/10.1103/PhysRevA.91.053420>. 98
- [222] F. J. Harris, “On the use of windows for harmonic analysis with the discrete Fourier transform,” *Proceedings of the IEEE* **66**, 51–83 (1978). 100
- [223] J.-B. Trebbia, C. L. Garrido Alzar, R. Cornelussen, C. I. Westbrook, and I. Bouchoule, “Roughness suppression via rapid current modulation on an atom chip,” *Phys. Rev. Lett.* **98**, 263201 (2007). URL: <http://link.aps.org/doi/10.1103/PhysRevLett.98.263201>. 103
- [224] S. J. Orfanidis, *Electromagnetic Waves and Antennas* (1999). URL: <http://www.ece.rutgers.edu/~orfanidi/ewa/>. 110
- [225] P. Treutlein, “Coherent manipulation of ultracold atoms on atom chips,” Ph.D. thesis, Ludwig-Maximilians-Universität München (2008). 111, 114, 115, 129, 134
- [226] V. Guarrera, R. Szmuk, J. Reichel, and P. Rosenbusch, “Microwave-dressed state-selective potentials for atom interferometry,” *New Journal of Physics* **17**, 083022 (2015). URL: <http://stacks.iop.org/1367-2630/17/i=8/a=083022>. 112
- [227] T. Schumm, S. Hofferberth, L. M. Andersson, S. Wildermuth, S. Groth, I. Bar-Joseph, J. Schmiedmayer, and P. Krüger, “Matter-wave interferometry in a double well on an atom chip,” *Nature Physics* **1**, 57–62 (2005). URL: <https://docweb.lrz-muenchen.de/cgi-bin/doc/nph-webdoc.cgi/000110A/http/www.nature.com/nphys/journal/v1/n1/abs/nphys125.html>. 112
- [228] P. A. Böhi, “Coherent manipulation of ultracold atoms with microwave near-fields,” PhD thesis, Ludwig-Maximilians-Universität München, München (2010). 112, 113, 117
- [229] S. S. Gevorgian, T. Martinsson, P. L. J. Linner, and E. L. Kollberg, “CAD models for multilayered substrate interdigital capacitors,” *IEEE Transactions on Microwave Theory and Techniques* **44**, 896–904 (1996). 113
- [230] B. Mussler and D. Brunner, “Aluminiumnitridkeramik,” *Technische Keramische Werkstoffe (DKG)* (2001). 113
- [231] T. Schneider, “Chip fabrication report for atomic clock on chip experiment,” Tech. rep., Ecole Normale Supérieure (2007). 114, 118
- [232] F. Haas, “Création d’états intriqués d’un ensemble d’atomes dans une cavité optique,” Ph.D. thesis, Université Pierre et Marie Curie (2014). 114
- [233] F. Haas, “Chip fabrication report for the FFP experiment,” Tech. rep., École normale supérieure (2013). 115

- [234] T. Schumm, J. Estève, C. Figl, J.-B. Trebbia, C. Aussibal, H. Nguyen, D. Mailly, I. Bouchoule, I. C. Westbrook, and A. Aspect, “Atom chips in the real world: the effects of wire corrugation,” *The European Physical Journal D - Atomic, Molecular, Optical and Plasma Physics* **32**, 171–180 (2005). URL: <http://dx.doi.org/10.1140/epjd/e2005-00016-x>. 118
- [235] microresist, “Personal communications with customer support of micro resist technology,” (2016). 119
- [236] Epotek, “Techtip 6, minimum bond line (cure and thickness),” Tech. rep. (2009). 119
- [237] M. Vangeleyn, P. F. Griffin, E. Riis, and A. S. Arnold, “Laser cooling with a single laser beam and a planar diffractor,” *Optics letters* **35**, 3453–3455 (2010). 122
- [238] C. L. G. Alzar, W. Yan, and A. Landragin, “Towards high sensitivity rotation sensing using an atom chip,” *High Intensity Lasers and High Field Phenomena*, pages JT2A–10. Optical Society of America (2012). 122
- [239] M. Ammar, M. Dupont-Nivet, L. Huet, J.-P. Pocholle, P. Rosenbusch, I. Bouchoule, C. I. Westbrook, J. Estève, J. Reichel, C. Guerlin *et al.*, “Symmetric microwave potentials for interferometry with thermal atoms on a chip,” *Physical Review A* **91**, 053623 (2015). 122
- [240] R. Dumke, M. Volk, T. Mütter, F. Buchkremer, G. Birkl, and W. Ertmer, “Micro-optical realization of arrays of selectively addressable dipole traps: a scalable configuration for quantum computation with atomic qubits,” *Physical review letters* **89**, 097903 (2002). 123
- [241] G. Birkl, F. Buchkremer, R. Dumke, and W. Ertmer, “Atom optics with micro-fabricated optical elements,” *Optics Communications* **191**, 67–81 (2001). 123
- [242] P.-A. Belanger, R. L. Lachance, and C. Pare, “Super-Gaussian output from a CO2 laser by using a graded-phase mirror resonator,” *Optics letters* **17**, 739–741 (1992). 123
- [243] F. Gori, “Flattened Gaussian beams,” *Optics Communications* **107**, 335–341 (1994). 123
- [244] M. Bondarescu and K. S. Thorne, “New family of light beams and mirror shapes for future LIGO interferometers,” *Phys. Rev. D* **74**, 082003 (2006). URL: <http://link.aps.org/doi/10.1103/PhysRevD.74.082003>. 123
- [245] J. McKeever, A. Boca, A. D. Boozer, R. Miller, J. R. Buck, A. Kuzmich, and H. J. Kimble, “Deterministic generation of single photons from one atom trapped in a cavity,” *Science* **303**, 1992–1994 (2004). URL: <http://science.sciencemag.org/content/303/5666/1992>. 124

- [246] M. Keller, B. Lange, K. Hayasaka, W. Lange, and H. Walther, “Continuous generation of single photons with controlled waveform in an ion-trap cavity system,” *Nature* **431**, 1075–1078 (2004). URL: <http://dx.doi.org/10.1038/nature02961>. 124
- [247] T. E. Northup, B. Casabone, K. Friebe, K. Schüppert, F. R. Ong, M. Lee, D. Fioretto, K. Ott, S. Garcia, J. Reichel *et al.*, “An ion-cavity interface for quantum networks,” in “SPIE Optical Engineering+ Applications,” (International Society for Optics and Photonics, 2015), pp. 961506–961506. 124
- [248] W. Emkey and C. Jack, “Analysis and evaluation of graded-index fiber lenses,” *Journal of Lightwave Technology* **5**, 1156–1164 (1987). 124
- [249] F. Brennecke, T. Donner, S. Ritter, T. Bourdel, M. Kohl, and T. Esslinger, “Cavity QED with a Bose-Einstein condensate,” *Nature* **450**, 268–271 (2007). URL: <http://dx.doi.org/10.1038/nature06120>. 127
- [250] K. J. Arnold, “Collective dispersive interaction of atoms and light in a high finesse cavity,” Ph.D. thesis, National University of Singapore (2012). 127
- [251] S. L. Hohmann, “Using optical fibre cavities to create multi-atom entanglement by quantum Zeno dynamics,” Ph.D. thesis, Université Pierre et Marie Curie (2015). 137

Acknowledgments

To begin with, I would like to thank Jakob Reichel for welcoming me to his team and for offering his generous support throughout my time as a Ph.D. candidate. His outstanding intuition served, more than once, to guide our project on the right path. I am deeply impressed by his dynamic approach in the lab and his scientific thoroughness. I very much appreciated our many walks from the Observatoire to the LKB, discussing everything from physics, to politics, to music. Thank you for being, not only my supervisor, but my mentor.

I also thank my co-supervisor, Peter Rosenbusch, for trusting me with the planning and construction of the next generation of his experiment. Our weekly meetings at the Observatoire and his input were invaluable to this project.

My work has been free of financial stress thanks to the C.N.E.S. and the D.G.A., who support their Ph.D. candidates in an exceptional way. Their support allowed me to attend many interesting meetings and conferences that broadened my horizon beyond cold atom physics.

I appreciate the scientific input of all the jury members at my defense and in their reports. Thank you to Agnès Maître, Philippe Bouyer, Matthias Keller, François-Xavier Esnault, Tilo Steinmetz, and Jean-Marc Lesage.

I would also like to thank the entire staff at the Laboratoire Kastler Brossel and the SYRTE, beginning with their directors Antoine Heidmann and Arnaud Landragin. Thank you to Thierry Tardieu and his team for patiently managing most of my administrative tasks. I also benefited greatly from the atelier mécanique of the LKB under the direction of Jean-Michel Isac. He managed all long term and last minute demands kindly and he created an amicable atmosphere for discussion. I'd like to also mention Arnaud Leclercq, Allan Hourdry, Thierry Bastien, and Florence Thibout who built most of the parts necessary for my work. Extra thanks to Nabil Garroum, who offered valuable tips on precision machining and engineering.

As for the workshop, the clean room was of crucial importance for my project. I received much help and many suggestions from the clean room supervisors at the ENS, Michael Rosticher and Jose Palomo, as well as at Université Paris 7 with Christophe Manquest et Stéphane Suffit. I want to thank, in particular, Thibaut Vacelet for his precision work with the dicing saw and for his numerous tips on micro assembly and clean room methods.

There is a “new tradition” at the LKB which provides the Ph.D. students with a mentor. Through this program, I had the opportunity to get to know Samuel Deléglise, who helped advise me through the various issues we face as Ph.D. candidates.

Of course, the most important people in a the lab are the teammates you work with every day. I had the luck to be part of a fantastic group, where I was happy to find not only kind colleagues, but good friends.

First, there were the two great Co-Ph.D. candidates Florian Haas (a kreizbrava Mo) and Leander Hohmann who introduced me to the work with fibers, the clean room basics, and the life as a German greenhorn in Paris. Even though we did not always share the same opinion on movies (I mostly like my movies in color), I enjoyed very much the discussions. I especially want to thank Leander for his patience and optimism, which kept up the spirit in the lab during the tough first round of fiber cavity gluing trials.

Next, there was the SAROCEMA experiment under the supervision of Romain “Mad/Relax Max” Long. With his calm nature and depth of experience, Romain was always a helpful guide. Most of my lab and break time was shared with his great team, including Claire Leboutteiller, Sébastien Garcia, and Francesco Ferri.

Sébastien personifies for me the physicist you want to have in your lab, from his hands-on experience with screwdriver and hammer, to his vast theoretical knowledge. We worked often and very well together on the fiber mirror production, and I learned a great deal from and with him. At this point, I also want to thank Klemens Schüppert, who was a big help with the “CO₂ software” and was always a very welcome guest in Paris. Aside from Klemens, I had the chance to speak, from time to time, with Yves Colombe, who had insightful tips on PCF handling and fibers in general. So big thanks to Innsbruck.

I am especially happy to have crossed paths with Claire. Our endless discussions on physics and everything around often helped to clarify my views or led to necessary changes in perspective. I am also thankful for the many soirées, good food, and open minded discussions with her and Adrien.

I met Francesco as an infinitely kind and helpful Master’s student, eager for knowledge. Over our time together, he evolved into an infinitely kind and helpful friend and Ph.D. student, full of knowledge. Thanks for the teamwork and for the evenings of delicious Italian cuisine with your congenial flat mates.

During my time as a Ph.D. student, many great masters students worked in our labs: Torben Pöpplau, Eckhard Wallis, Gregoire Vallet, Mohamed Baghdad, and Samarth Vadia, who were always icredibly helpful. I am very happy that Torben continued in our team as a Ph.D. student, and we could continue our discussions on fibers, Brezel, and Amerikaner.

The Solid-State cavity QED team with Jean Hare, Jérôme Estève, Benjamin Besga, and Cyril Vaneph was a further source of knowledge and interesting discussions over lunch. Jean was, moreover, an irreplaceable help in dealing with the impressive and oppressive French bureaucracy. Merci beaucoup.

We often shared equipment and experiences with our lab neighbours. Thank you to the teams of Christophe Salomon, Jean Dalibard, Antoine Heidmann, and Serge Haroche, especially to my fellow Ph.D. students Mihail Rabinovic and Leonhard Neuhaus.

Over the time at the LKB many groups visited our lab for fiber machining. I enjoyed the input and questions those teams brought. I want to thank the Yale team, including Anna Kashkanova and Scott Hoch, as well as the Oxford/Bonn teams, with Hendrik-Marten Meyer, Matthias Steiner and Christian Schilz.

Finally, I arrive at my own group, the notorious TACC team. Even though I did not work extensively on the old experiment, I was lucky to have worked with Wilfried Mainault, Vincent Dugrain, and Ramon Szmuk and to have found in them an endless know-how about atomic clocks and cold atom physics. While my overlap with Vincent and Wilfried was rather short, I have really appreciated Ramon's presence at the Observatoire over the years and, of course, the delightful dinners with him and his wife, Ira.

Later on, the team was joined by the postdocs Ralf Kohlhaas and Vera Guarrera and the Ph.D. students Théo Laudat and Mengzi Huang. Ralf pushed the experiment with his productive restlessness and taught me a lot about how to approach critical decisions in the planning phase. More importantly, his cheerful character made the work more pleasurable, even if it was late at night and food was running low.

Vera was always available for questions of any sort and her (not so northern) Italian temperament was clearly a plus when the theory was a bit dry. Along with Vera I got to know Giovanni Barontini, another phenomenal postdoc from Italy (or should I say Kaiserslautern) and evenings spent with them were always fun.

Théo was basically my last social contact during the jam-packed writing phase. If you take helpfulness, perseverance, and French cuisine and leave it in the "cocotte" for a while, you will end up with this great colleague.

The latest newcomer on the TACC experiment was Mengzi, who was an excellent companion in the clean room and in building the final fiber cavities. I am grateful for his important support from the first day on. His skillfulness and the necessary carefulness have enabled him to quickly take over the experiment. I am sure that with Théo and Mengzi the experiment is in the most capable of hands. To both of you, I wish the best of luck and I thank you all for your help.

Apart from my team, I also want to thank all the people at the Observatoire for creating a very special working environment. Thanks to David Holleville, Bertrand Venon, Florence Cornu, Marine Pailler, Francia Decostier, Christel Comte, Pascal Blondé, Gilles Sakoun and many more.

The camaraderie among the Observatoire Ph.D. students and the IACI team is exceptional for a group of that size, and I thank you all for helpful or just enjoyable conversations. Thanks to Satya Bade, Marc-Antoine Buchet, Cyrille Solaro, Bess Fang, Carlos Garrido Alzar, Pierre Gillot, Rémi Geiger, Franck Pereira dos Santos, Pacôme Delva, Mehdi Langlois, Denis Savoie, the beautiful Maxime Favier, Rinat Tyumenev, Ouali Acef, Olivier Gobron, Sébastien Bize, Nicolas Miélec, Jean-Marc Martin, Louis Amand, and of course, the great Indranil Dutta.

During my time in Paris, I had the opportunity to make music with a lot of marvelous people, and I appreciated the counterbalance to and diversion from the lab work. Thanks to the lovely BeePeez with Clémence, Sarah, Renaud and Jérémy and to Franz, Maxime, David, Mathias, Kévin, Sandra and Edward for the awesome Jam-sessions.

Next to my “music friends”, I want to especially thank Brittany, Pedro, Eva, and Friedemann for excellent evenings all over Paris.

Since I missed the chance to write acknowledgments in my Diplomarbeit, I would like to make up for this lapse and thank the people that strongly influenced the beginning of my life as a physicist. Thanks to Mirko Emmel, Eike Venzmer, Marco Dillmann, Philip Ketterer, Daniel Rost, Ulrich Poschinger, Andreas Walther, Frank Ziesel, Max Hettrich, Georg Jacob, Stefan Ulm, Julian Naber, Alex Wiens, Michael Schnorr, Thomas Ruster, Stefan Weidlich, Claudia Warschburger, Tim Lindner, Henning Kaufmann, Thomas Feldker, Christian Schmiegelow, Ferdinand Schmidt-Kaler, and especially, Andreas Nink, who is a great teacher and friend.

Going even further back to the roots, I want to thank my awesome friends and family back in Wiesbaden. They cheered me up when the experiment followed its own mysterious ways, and were happy for me, when it followed my own mysterious ways. A heartfelt “thank you” for the years long friendships and the familial backing.

I want to thank especially my parents who were and still are my strongest supporters. They inspired in me the curiosity, perseverance, and creativity that motivated me to start and enabled me to finish my Ph.D. project. I am deeply grateful to them, to my siblings, and to my grandparents and hope to give back, with time, even a thousandth of the support I have received.

But most of all I want to thank my wonderful wife. For her patience, her support, and her love. Thank you.

Sujet : Towards a squeezing-enhanced atomic clock on a chip

Résumé : L'objet de cette thèse de doctorat est la conception et la construction d'une horloge atomique réalisée sur un microcircuit à atomes (TACC) et améliorée par l'intrication. L'élément principal de cette nouvelle expérience est un micro-résonateur Fabry Pérót qui permet la génération d'états de spin comprimés de l'ensemble atomique grâce aux interactions entre la lumière et les atomes. Il a déjà été montré que ces états peuvent améliorer les performances métrologiques des horloges atomiques. Cependant, les expériences ayant permis cette démonstration de principe n'ont pas encore atteint un niveau de précision présentant un intérêt métrologique. C'est précisément l'objectif de la nouvelle configuration expérimentale que nous proposons ici. L'intégration du résonateur optique au dispositif expérimental TACC nécessite une conception nouvelle du microcircuit à atomes, qui doit permettre le transport du nuage atomique jusqu'au résonateur. Nous présenterons donc la conception et la fabrication de ce microcircuit à atomes. Afin de conserver la compacité et la stabilité de notre installation, nous avons choisi d'utiliser une cavité Fabry-Pérót fibrée (fibred Fabry-Pérót, FFP) comme résonateur optique, dans lequel les miroirs du résonateur sont réalisés sur la pointe de fibres optiques. Pour répondre aux exigences de notre expérience, une nouvelle génération de résonateurs FFP a été développée au cours de cette thèse, les plus longs réalisés à ce jour. A cette fin, nous avons développé une procédure d'ablation par tirs multiples à l'aide d'un laser CO₂ focalisé, qui permet la mise en forme des surfaces de silice fondue avec une précision et une polyvalence sans précédent.

Mots clés : Horloge atomique, états de spin comprimés, microcircuit à atomes, cavité Fabry-Pérót fibrée

Subject : Towards a squeezing-enhanced atomic clock on a chip

Abstract: This thesis describes the conception and construction of an “entanglement-enhanced” trapped atom clock on an atom chip (TACC). The key feature of this new experiment is the integration of two optical Fabry-Pérot micro resonators which enable generation of spin-squeezed states of the atomic ensemble via atom-light interactions and nondestructive detection of the atomic state.

It has been shown before that spin-squeezed states can enhance the metrological performance of atomic clocks, but existing proof-of-principle experiments have not yet reached a metrologically relevant level of precision. This is the first goal of the new setup.

To retain the compactness and stability of our setup, we chose the optical resonator to be a fiber Fabry-Pérot (FFP) resonator where the resonator mirrors are realized on the tip of optical fibers. To meet the requirements of our experiment, a new generation of FFP resonators was developed in the context of this thesis, demonstrating the longest FFP resonators to date. For this purpose, we developed a “dot milling” procedure using a focused CO₂-laser that allows shaping of fused silica surfaces with unprecedented precision and versatility. Beyond the TACC experiment these long FFP resonators open up new applications in other fields as in the ion trapping community or for frequency filtering.

Incorporating optical resonators in the TACC system necessitates a new atom chip design, allowing transportation of the atom cloud into the resonator. We present the design and the fabrication of this atom chip.

The completed setup will enable investigations of the interplay of spin-dynamics in presence of light mediated correlations and spin-squeezing at a metrologically relevant stability level of 10^{-13} at 1 s.

Keywords : fiber Fabry-Pérot resonator; micro resonator; atomic clock; spin squeezed states; quantum metrology; atom chip